Simulation of air-conditioning loads in electrical power systems

Ibrahim, Sherine Taher Mahmoud

Award date:
1997

Awarding institution:
University of Bath

Simulation Of Air-Conditioning Loads in Electrical Power Systems

Submitted by

Sherine Taher Mahmoud Ibrahim

B.Sc. (Alexandria, Egypt)

For the degree of Ph.D.

of the University of Bath

1997

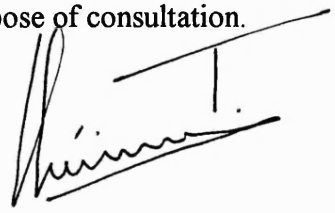

Sherine Taher Mahmoud Ibrahim

ProQuest LLC
789 East Eisenhower Parkway
P.O. Box 1346
Ann Arbor, MI 48106-1346

To My Father In Heaven Taher

To My Beloved Mother Nadia

And To My Dearest Son Amro

Soras From Quran

Sora Fatir (XXXV) : 28

" Those Truly Fear God, Among His Servants, Who Have Knowledge."

Sora Al-Israa (XVII) : 85

" Of Knowledge It Is Only A Little That Is Communicated To You men."

Sora Al-Ahqaf (XLVI) : 23

" He Said: The Knowledge Is Only With God."

(Wholly truth is the words of God)

Acknowledgments

To the Almighty God, who guided me along the right path, and helped me to accomplish this work, I am wholeheartedly thankful and always pray to him for his endless care and mercy.

I greatly acknowledge the loving and endless support of my dear mother while this research work was in progress, as well as all people who afforded me with their knowledge, time, assistance and encouragement.

I like to express my deepest thanks and gratitude to Professor A.T. Johns, Head of School of Electronic and Electrical Engineering, University of Bath - UK, who spent much of his valuable time in supporting and guiding me while pursuing my research work.

I deeply recognise the great support and encouragement of Dr. Darwish M.K. Al-Gobaisi, Director General of Power and Desalination Plants, Water and Electricity Department - Government of Abu Dhabi, in order to achieve this work.

I will be forever grateful to my elder brother, Dr. Mohammed H. El-Banhawy of Power System Group, WED, for his continuous and invaluable assistance and encouragement. His excellent attitude has greatly influenced my performance while achieving this research work.

Also, I present my thanks to the engineers at ABB Control, Baden - Switzerland, who supplied the necessary equipment to accomplish this research work.

Summary

Summer load, in Abu Dhabi as well as in other hot countries, includes a large percentage of single-phase air-conditioning (A/C) load. The air-conditioner load slows down considerably during voltage transients, because of its fluid coolant pressurized circuit and low inertia compressor. Then, after clearing the fault and during consequent voltage recovery, the A/C load imposes large low power factor starting currents on the network. Accordingly, it was emphasized to build an efficient single-phase A/C load model to simulate the impact of A/C load on the system during abnormal conditions.

Towards such goal, laboratory tests were performed on a selected group of single-phase A/C compressors in order to investigate such dynamic load behavior under low-voltage conditions. Based on the transient simulation test data, a relationship was derived relating the low terminal voltage and the maximum fault clearing time (t_{max}) needed to avoid the stalling of single-phase A/C compressor load. The distribution system reactance (X_d), which was added to the test circuit, and the thermal overload relay equipped inside the A/C compressor, have showed a distinctive impact on the low-voltage dynamic behavior of the A/C load. Test results have mainly showed that the compressor load active power was nearly constant during transients. Accordingly, a new definition method was derived in this thesis for the identification of single-phase A/C load mechanical torque characteristics.

Summary

The new A/C load model was simulated by using a commercial mathematical software, where the model dynamic simulations greatly matched the recorded test results, proving the accuracy of the newly defined A/C load mechanical torque characteristics. Afterwards, the new dynamic load model was adopted in a transient stability program, where the results have satisfactorily matched the system records of two selected major fault cases. Based on the stability analysis, it was concluded that the combined impact of a large number of stalled A/C units and relatively longer fault clearing time has led to small power system instability. The static VAR compensator showed a favorable impact on system stability, where it has increased the voltage support on load busbars during faults, and consequently, has reduced the number of stalling A/C compressors and low-inertia motors.

According to test results and stability analysis, an adaptive under-voltage load shedding scheme was proposed herein to reduce the adverse impact of stalling motors on the system stability, and enhance the restoration of voltage stability following faults. The proposed scheme was based on the criteria of reactive power consumed by the aggregated dynamic load connected at each load feeder in the system during faults. Conclusions and recommendations for further work, mainly aimed to improve the power system stability and performance, are detailed and discussed at the end of the thesis.

Keywords: Single-phase air-conditioning (A/C) load, dynamic load modeling, transient simulation test, single-phase A/C load mechanical torque characteristics, transient stability analysis, fast fault clearing, A/C load percentage, under-voltage load shedding scheme.

Table of contents

List of symbols

P	Load active power at the bus, per unit
P_o	Initial load active power at the bus, pu
P_{a1}	Frequency-dependent fraction of active power load
KPV1	Voltage exponent for frequency-dependent active power load
KPV2	Voltage exponent for non-frequency-dependent active power load
KPF1	Frequency sensitivity coefficient for active power load
Δf	Frequency deviation from nominal value, pu
V	Bus voltage, pu
V_o	Initial bus voltage, pu
Q	Load reactive power at the bus, pu
Q_o	Initial load reactive power at the bus, pu
Q_{a1}	Reactive load coefficient - ratio of initial uncompensated reactive load to total initial active power load (P_o)
KQV1	Voltage exponent for the uncompensated reactive power load
KQV2	Voltage exponent for the reactive compensation term
KQF1	Frequency sensitivity coefficient for the uncompensated reactive power load

KQF2	Frequency sensitivity coefficient for the reactive compensation term
IM	Induction motor
Tm	Load mechanical torque, pu
Te	Motor electrical torque, pu
S	Motor slip
H	Load inertia constant, pu
r_1	Stator resistance, pu
x_1	Stator reactance, pu
R_c	Core loss resistance, pu
X_m	Magnetizing reactance, pu
r_2	Rotor resistance, pu
x_2	Rotor reactance, pu
V_{ph}	Stator terminal phase voltage, pu
V_{tth}	Thevenin equivalent source voltage, pu
Z_{oo}	Open-circuit motor impedance, pu
Z_{tth}	Thevenin equivalent motor impedance, pu
R_{tth}	Thevenin equivalent stator resistance - real part of Z_{th}, pu
X_{tth}	Thevenin equivalent stator reactance - imaginary part of Z_{th}, pu

ω_s	Synchronous angular velocity, radian/second or pu
A	Quadratic mechanical torque coefficient, pu
B	Linear mechanical torque coefficient, pu
C	Constant mechanical torque coefficient, pu
KVA	Total rating capacity of motor, kilo-volt amperes
dP/dV	Rate of change of motor active power to the terminal voltage
dQ/dV	Rate of change of motor reactive power to the terminal voltage
λ	Eigen value, pu
CT	Current transformer
VT	Voltage transformer
μF	Capacitance, micro-Farad
φ	Phase-shift angle
I_{st}	Starting winding current, amperes
I_{main}	Main winding current, amperes
DC	Direct current, amperes
AC	Alternating current, amperes
V_{ac}	AC voltage, pu

I_{ac}	AC current, pu
V_{dc}	DC voltage, pu
I_{dc}	DC current, pu
V_{nl}	No-load voltage, pu
I_{nl}	No-load current, pu
P_{nl}	No-load motor active power, pu
I_c	Iron core current, pu
I_m	Magnetizing current, pu
V_{br}	Locked-rotor voltage, pu
I_{br}	Locked-rotor current, pu
P_{br}	locked-rotor motor active power, pu
X_{br}	Locked-rotor motor reactance, pu
I_1	Stator current, pu
I_2	Rotor current, pu
P_{in}	Compressor input active power, pu
P_g	Total power transferred across the air-gap from the stator, pu
BTU	British Thermal Unit
hr	hour

EER	Energy Efficiency Ratio
G	Weight of rotating parts, kilograms
D	Effective diameter of gyration, meter
rpm	Motor speed, revolution per minute
X_d	Distribution system reactance, pu
t_{max}	Maximum fault clearing time, milliseconds
mcb	Miniature circuit breaker
R_T	Resistance of transformer secondary winding, Ω
Z_T	Impedance of transformer secondary winding, Ω
V_{cr}	Compressor critical voltage, pu
Te_{max}	Maximum motor developed electrical torque, pu
K_1	Constant for calculating (t_{max})
K_2	Constant for calculating (t_{max})
di_1/dt	Rate of change of compressor stator current with time
di_2/dt	Rate of change of compressor rotor current with time
t	time, seconds
l_{o1}-l_{o4} , k_{o1}-k_{o4}	Initial constants of Runge-Kutta method

l_{n1}-l_{n4} , k_{n1}-k_{n4} Constants of Runge-Kutta method

E_n Local truncation error of Runge-Kutta method

R_n Round-off error of Runge-Kutta method

h Step size of Runge-Kutta method

t_c Fault clearing time, milliseconds or cycles

MW Total 3-phase active power of voltage source or load, Mega-watt

MVAR Total 3-phase reactive power of voltage source or load, Mega-volt amperes reactive

kV System voltage, kilo-volts

Hz System frequency, Hertz

UFLSS Under-frequency load shedding scheme

SVC Static VAR compensator

OHL Overhead transmission line

UAN Um Al-Nar power station

WATH Al-Wathba substation

AIN Al-Ain power station

ADPS Abu Dhabi power station

TAW Taweelah power station

E18	East substation # 18
W13	West substation # 13
W16	West substation # 16
W24	West substation # 24

CHAPTER 1

Introduction

1.1- Problem statement:

In recent years, much more attention has been devoted to load modeling, since load characteristics often significantly affect the static and dynamic behavior of a power system. Proper representation of loads is important in system stability analysis, which is the main evaluation tool of power system performance.

In order to study a dynamic load impact on power system performance, extensive tests are often performed on individual loads in order to investigate the steady-state and transient dynamic behaviour. This will lead to the accurate identification of load model parameters, which can be used efficiently in power system stability analysis.

The main problem in load modeling is not building complex models, but it is obtaining reliable load data for use in simple models [45]. Power utilities worldwide have used different approaches in order to construct their own load models, whether they are component-based or measurement-based [23,47].

The measurement-based load model represents the combined effect of all load components at a particular load feeder at a specific time. When used in stability analysis,

such a model does not afford significant data regarding the impact of a particular load on the overall power system performance [46].

In the case of a small and isolated power system, abnormal operating conditions and disturbances can badly affect the system stability. The problem becomes more severe when a highly concentrated dynamic load exists in a small system. Therefore, the necessity for an improved load model is very strong in order to ensure qualitative results of stability analysis, which will allow a refined estimation of system stability limits [14].

For example, the major part of Abu Dhabi system summer load is composed of single-phase air-conditioners. Subsequent to system faults, the A/C compressors slow down considerably because of their low inertia constants [26]. Due to reduced supply voltage, the electrical torque developed by the A/C compressors is much less than the required mechanical torque, which results from the back pressure of refrigerant gas. In this case, most of the air-conditioner compressors will stall, and draw high locked-rotor currents. Since most single-phase A/C compressors are not supplied by contactors, then, they will be disconnected from the system by their thermal overload protective device after a few seconds time delay.

The stability problem is considered more severe in the case of highly reduced system voltage during transients, or a relatively longer fault clearing time. This results in

an extended cascade stalling of compressors, causing a delayed post-fault recovery of the system voltage. Therefore, if the power system is not strong enough, where it can supply the reactive power needed to re-accelerate the stalled compressor loads, the system voltage will be more depressed and continue to decay until total voltage collapse is reached [14,15,26].

1.2- Background:

According to the above stated problem, load modeling is a highly and increasingly important topic. An efficient load model can simulate, through stability analysis, the impact of dynamic load on the system performance. Many references recommended the performance of further laboratory tests on samples of individual important loads in order to improve the load characteristic database available for load modeling task [16,23-26,45,46,47]. Accordingly, the Abu Dhabi power utility has encouraged the performance of such tests (measurement-based modeling) on the single-phase air-conditioning load, which is highly-concentrated in the system during summer time.

A review of current load modeling techniques enabled the researcher to define his strategy in order to construct an efficient dynamic load model. Following this, three models of single-phase air-conditioners, equipped with single-piston reciprocating-type compressors of different refrigeration capacities, were selected to undergo laboratory tests for the following purposes:

1) Identification of the compressors electrical and mechanical characteristics.

2) Recording the compressors response when subjected to simulated low-voltage transients.

According to the transient simulation test results, a new method was proposed herein to define the mechanical torque characteristics of the single-phase A/C compressor load. Also, the electrical characteristics of single-phase A/C compressor load were identified. Test procedures and related instrumentation are detailed in the thesis.

The new dynamic load model, including the newly-defined mechanical torque characteristics of A/C compressor load, was adopted in the transient stability analysis in order to simulate two selected major disturbance events, which have occurred in Abu Dhabi power system in recent years. Accordingly, the system variables recorded during these events were compared to the system simulations for the validation of the new dynamic load model.

Sensitivity analysis of the system and load variables have led to useful conclusions regarding the reliability of the new load model, and their impact on the system stability and performance. Conclusions and recommendations for further work, which are aimed to enhance the power system performance and security, are discussed at the end of the thesis.

1.3- Thesis preview:

Chapter 2 includes a general review of load modeling current techniques.

Chapter 3 includes the procedure for the transient simulation test, and the analysis of test results.

Chapter 4 includes the procedure for laboratory tests performed for electrical parameters identification of the single-phase A/C compressor load. The chapter also includes the details of a new method for identifying the mechanical torque characteristics of the single-phase A/C compressor load.

Chapter 5 includes the simulation of transient simulation test circuit by using a commercial software (MathCAD 5). Sensitivity analysis of the A/C compressor model parameters are performed to check their impact on the model dynamic simulations, and hence, on the model reliability.

Chapter 6 includes the discussion and analysis of the system fault simulations to validate the new dynamic load model, which was implemented in the transient stability analysis. It also includes the discussion of sensitivity analysis performed on the system and load variables, and their impact on the system stability.

Chapter 7 includes findings and conclusions regarding the improvements achieved in the new dynamic load model, as well as the recommendations for future work needed to enhance the power system performance and stability.

CHAPTER 2

Review of Load Modeling Techniques

2.1- Introduction :

For many years, the subject of load modeling has received less attention than it deserves, and continues to be an area of considerable uncertainty. Many studies have shown that load modeling has a significant impact on stability analysis results. Electric power utilities have contributed much effort in recent years in order to improve load modeling [15,23]. In this chapter, current techniques of load modeling techniques and related monitoring equipment are reviewed.

2.2- Methods of load modeling:

In this section, the *"component-based"* and *"measurement-based"* load modeling methods are detailed [16,17,18]:

2.2.1 - Component-based load modeling method:

The component-based method builds up the load model from available data of all load components connected to a particular load bus. Essentially, there are three types of data which need to be collected for building load models:

1) *Load class mix data* - which describe the percentage contribution of each load class to the total active power (P) at the bus. This data must be specified for each bus in the system. Most power utilities maintain records of their energy consumption by each load class.

2) *Load composition data* - which describe the percentage contribution of each load component to the active power consumption of a particular load class. This data is a function of daily and seasonal cycles as well as local climate and weather. Power utilities are developing load composition data tailored to their own systems.

3) *Load characteristics data* - which describe the electrical and mechanical characteristics of each load component. Typical load component characteristics can be defined by information from published tests and analysis [25]. This data may be used in all power utilities since all individual loads have the same characteristics. Figure (2.1) shows the procedure of component-based load modeling, where gathered data on load components is used to construct the load model. Figure (2.2) illustrates a table of default characteristics data for static and dynamic loads published in EPRI final report of research project 849-7 [30].

Basically, the component-based modeling method has the following advantages:

1) It does not require any power system measurements.

2) Since load characteristics and load composition data should not vary widely over a particular system, they can be developed once for the entire system. Only the load class mix data needs to be prepared for each bus or area, and modified for changes in the system load.

2.2.1.1 - Load model aggregation:

Load model aggregation is the grouping of various load data in a suitable form to be used in power flow and stability analysis. The objective of load model aggregation is to represent the combined effect of all load components and the intervening system in producing (P) and (Q) changes at a certain bus, in response to changes in voltage and frequency at the same bus. Model aggregation includes the aggregation of static as well as dynamic loads connected to each bus in the system [16,20,25].

Static aggregation:

The aggregation of static loads involves the following steps:

1) Determine the bus load composition (fraction of each load component at a particular bus) by combining the load class mix and the load composition data.

2) Use the bus load composition fractions as weighting factors to compute average sensitivity factors for the individual components, which when aggregated can be used as exponents in the general load model.

The active power formula, which is given in equation (2.1), has two terms each exponential in voltage, which are used to aggregate the following load components:

1) Frequency dependent loads, such as motors and fluorescent lights.

2) Non-frequency dependent loads, such as heaters and incandescent lamps.

$$\frac{P}{P_o} = P_{a1} * \left(\frac{V}{V_o}\right)^{KPV1} * \left(1 + KPF1 * \Delta f\right) + \left(1 - P_{a1}\right) * \left(\frac{V}{V_o}\right)^{KPV2} \qquad (2.1)$$

Parameters in the active power formula are defined as follows:

P - bus load active power.

P_o - initial bus load active power, from power flow base case.

P_{a1} - frequency dependent fraction of active power load.

KPV1 - voltage exponent for frequency dependent active power load.

KPV2 - voltage exponent for non-frequency dependent active power load.

KPF1 - frequency sensitivity coefficient for active power load.

Δf - per unit frequency deviation from nominal value.

V - per unit bus voltage.

V_o - initial bus voltage, from power flow base case.

The reactive power formula, which is given in equation (2.2), has also two terms, but is defined differently from the active power formula as follows:

1) Reactive power consumption of all load components, by using their power factors.

2) Approximate reactive compensation and losses in the sub-transmission and distribution system between the bus and various connected loads. This term is based on the difference between total reactive power consumption and the initial reactive power at the bus as specified in the power flow data.

$$\frac{Q}{P_o} = Q_{a1} * \left(\frac{V}{V_o}\right)^{KQV1} * \left(1 + KQF1 * \Delta f\right) + \left(\frac{Q_o}{P_o} - Q_{a1}\right) * \left(\frac{V}{V_o}\right)^{KQV2} * \left(1 + KQF2 * \Delta f\right)$$

(2.2)

Parameters in the reactive power formula are defined as follows:

Q - bus load reactive power.

Q_o - initial bus load reactive power, from power flow base case.

Q_{a1} - reactive load coefficient (ratio of initial uncompensated reactive load to total initial active power load (P_o)).

KQV1 - voltage exponent for the uncompensated reactive power load.

KQV2 - voltage exponent for reactive compensation term.

KQF1 - frequency sensitivity coefficient for uncompensated reactive power load.

KQF2 - frequency sensitivity coefficient for reactive compensation term.

The reactive power formula is normalized to (P_o) rather than (Q_o) in order to avoid problems in the case where (Q_o) equals zero, due to the cancellation of the load reactive consumption and reactive losses by means of shunt capacitance or static VAR compensators (SVC).

Dynamic aggregation:

The objective of dynamic load aggregation is to combine the parameters of different motors into a single motor model using the conventional induction motor equivalent circuit shown in figure (2.3) and the following dynamic equation (2.3):

$$\frac{dS}{dt} = \frac{T_m - T_e}{2 * H} \qquad (2.3)$$

where $T_m = \left[A*(1-S)^2 + B*(1-S) + C\right]$

and $$T_e = \frac{1}{\omega_s} * \frac{V_{th}^2 * \left(\frac{r_2}{S}\right)}{\left(R_{th} + \frac{r_2}{S}\right)^2 + \left(X_{th} + x_2\right)^2}$$

and $$V_{th} = V_{ph} * \frac{jX_m}{r_1 + j\left(X_m + x_1\right)}$$

r_1 - stator resistance (pu) x_1 - stator reactance (pu)

X_m - magnetizing reactance (pu)

r_2 - rotor resistance (pu) x_2 - rotor reactance (pu)

V_{ph} - stator terminal voltage (pu)

V_{th} -Thevenin equivalent source voltage (pu)

R_{th} - Thevenin equivalent stator resistance (pu)

X_{th} - Thevenin equivalent stator reactance (pu)

ω_s - synchronous angular velocity, $\frac{4*\pi*f}{poles}$ (radian/second or pu)

A - quadratic mechanical torque coefficient (pu)

B - linear mechanical torque coefficient (pu)

C - constant torque coefficient (pu)

H - inertia constant (pu torque/pu speed)

Tm - load mechanical torque (pu)

Te - motor electrical torque (pu)

S - motor slip.

The following aggregation methods are used for building up dynamic load models:

1) Aggregation method (A) is based on the kVA weighted average of the individual motor parameters.

2) Aggregation method (B) is based on the kVA weighted average of the motor's branch admittance.

In reference [16], EPRI has recommended the second aggregation method (B) since the approach of weighted branch admittance is similar to the parallel connection of motors, and reducing them into a single equivalent motor load.

2.2.1.2 - Segregation of motors [16,23]:

Generally, high inertia motors with large rotor resistance are considered as *"robust"* motors, while low inertia motors with small rotor resistance are considered as *"prone-to-stall"* motors. The following methods are used to segregate different types of motors into *"robust"* and *"prone-to-stall"* motor groups:

1) Method (A) is based on the comparison of magnitude and phase characteristics of (dP/dV) and (dQ/dV) transfer functions of individual motors. All motors having similar characteristics are gathered into one group.

2) Method (B) is based on the comparison of the Eigen values for individual motors. The third order model of an induction motor produces one complex pair of Eigen values representing the rotor electrical dynamics, and one real negative Eigen value representing the rotor mechanical dynamics.

Based on the second segregation method and for ease of calculation, EPRI has proposed the following simple equation (2.4) in order to calculate an approximate real negative Eigen value for any type of motors:

$$\lambda = -\left(\frac{1}{2 * r_2 * H}\right) \qquad (2.4)$$

where

r_2 = rotor resistance (pu).

H = motor inertia constant (pu).

2.2.1.3 - Aggregated 2-motor model [16]:

EPRI had proposed an aggregated 2-motor model, which represents two groups of motors having different parameters. The 2-motor model has an improved accuracy over the conventional 1-motor model, and it allows an independent monitoring of the behavior of each motor group.

It has been proved through EPRI tests that if the relative rating of either motor group is less than 15% of the total load power consumption, then the aggregated 2-motor model will not significantly improve the modeling accuracy over the conventional 1-motor model. This percentage was defined by comparing stability analysis when using the conventional 1-motor model and the aggregated 2-motor model.

Appendix (A) includes a sample data of combined residential and commercial motor loads, which are used to build up 1-motor, 2-motor, and composite load models. When comparing the torque-speed characteristic curves of the conventional 1-motor model and aggregated 2-motor model illustrated in figure (2.4), it is clear that the T-S curve of the 2-motor model is closer to the T-S curve of the composite motor model.

2.2.2 - Measurement-based load modeling method [17,18,19,22]:

The measurement-based load modeling method involves placing monitoring equipment at various load buses in order to obtain on-line records of load variables under various system operating conditions.

This method has the advantage of direct measurement of actual load behavior and can yield load models directly. On the other hand, this modeling method has the following disadvantages:

1) Application of load data gathered at one substation to other substations' models will induce errors in stability analysis. This may be possible only in case of identical loads at different substations, which is unusual.

2) Voltage and frequency changes of any appreciable magnitude are practically impossible to make in the system [46].

3) Variation of load characteristics, due to daily and seasonal weather changes and end-user needs, requires continuous system on-line measurements.

4) Unless buses will have fairly different loads composition, there will be no understanding of the results, so that they can be extrapolated to different system conditions.

Records of load variables can be obtained either in case of small disturbances due to routine system operations, such as capacitor switching or transformer tap changing, or in case of severe transients. *SCADA* (Supervisory Control and Data Acquisition) and digital disturbance recorders are considered as the most important data acquisition means, which monitor and record power system variables during steady-state and transient conditions.

In any monitoring system, some basic requirements must be available such as the automatic triggering of recording equipment, time synchronization and security of recorded disturbance data, reliability and ease of maintenance of monitoring equipment, automated retrieval of disturbance data to a central computer for evaluation and further analysis.

Based on the recorded load variables, load model parameters can be identified by using a commercially developed software. Figure (2.5) illustrates a typical scheme for measuring load characteristics in substations. Appendix (B) includes the description of a typical digital disturbance recorder used for system on-line measurements.

2.3 - Load model validation and testing:

The topic of load model validation and testing against the real system is important, time consuming and complex. Two methods for load model testing are considered herein, the *"system variables"* and *"load model identification"* monitoring method [16,18,22].

2.3.1 - System variables monitoring:

This type of monitoring consists of installing digital disturbance recorders to record the system dynamic response to significant disturbances. Then, the recorded system variables are compared with a system simulation during the disturbance by using the proposed load model. If the recorded system response show good agreement when compared to the simulated response, the proposed load model is validated. However, if both responses of the system do not match, then the whole system model has to be checked, including the proposed load model.

2.3.2 - Load model identification monitoring:

As in the previous method, load and system variables are recorded during disturbances. Then, a specially developed commercial software can identify the best values of load model parameters in order to match the measured system response.

This method has the advantage of eliminating some of the other model uncertainties, such as the transmission and generation system model. However, it has the following disadvantages:

1) It validate the load model only at specific locations rather than for the whole power system.

2) The identified load model parameters change with daily and seasonal weather variations.

2.4 - Conclusions:

Most power utilities worldwide are adopting two methods for load representation. The component-based load modeling method consists of building-up load models based on the available data of load components connected to a particular bus in the system. The measurement-based load modeling method employs on-line measurements of load variables at various load buses under various system operating conditions. Both methods were developed by EPRI and published in their research project report 849-7.

The component-based method combines the percentage contribution of each individual load component to the active power consumption at a specific load bus, with the characteristics data of such load component. Static and dynamic loads are aggregated in a general load model used in system simulations. Dynamic loads are aggregated into two different groups of motors, where the higher inertia motors belong to the *"robust"* motors group, and the lower inertia motors belong to the *"prone-to-stall"* motors group.

The measurement-based method uses the load variables recorded during disturbances by means of digital disturbance recorders. Then, based on such records, a commercially developed software can identify the load model parameters.

Power utilities test their developed load models before adopting them in system simulations through two methods, the *"system variables"* and the *"load model identification"* method. In either case, stability analysis using load models under test are compared with actual system transient response. If the simulated system response matched the actual recorded system transient response, then the load model is validated and can be applied efficiently in different system analysis.

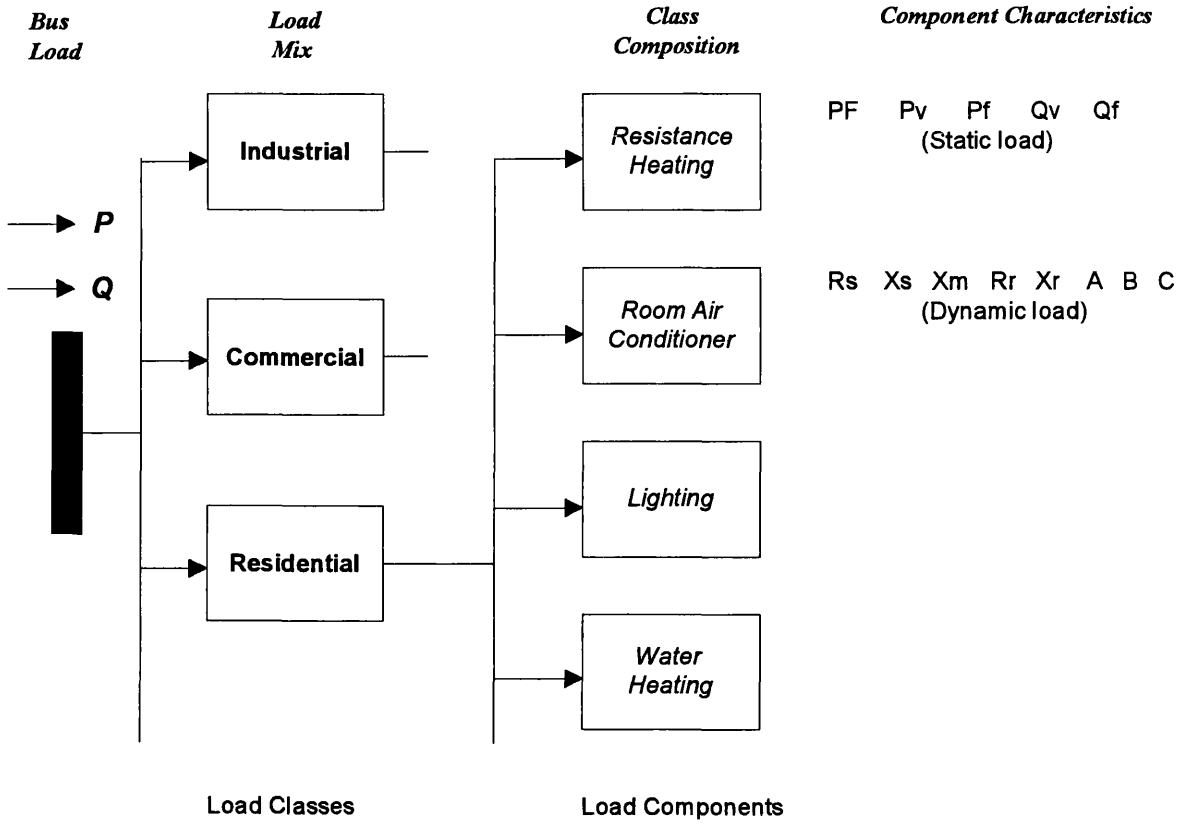

Figure (2.1) Component-based load modeling.

Component	Static characteristics											Dynamic Characteristics								
	PF	P_V	P_f	Q_V	Q_f	N_p	PF_m	P_{V_m}	P_{f_m}	Q_{V_m}	Q_{f_m}	R_t	X_t	T_{3_t}	R_t	X_t	A	B	E	LF_s
Resistance space heater	1.0	2.0	0.0	0.0	0.0	0.0	-	-	-	-	-	-	-	-	-	-	-	-	-	-
Heat pump space heating	0.84	0.2	0.9	2.5	-1.3	0.9	1.0	2.0	0.	0.	0.	.33	.076	2.4	.048	.062	0.2	0.	0.28	0.6
Heat pump central air cond.	0.81	0.2	0.9	2.5	-2.7	1.0	-	-	-	-	-	.33	.076	2.4	.048	.062	0.2	0.	0.28	0.6
Central air conditioner	0.81	0.2	0.9	2.2	-2.7	1.0	-	-	-	-	-	.33	.076	2.4	.048	.062	0.2	0.	0.28	0.6
Room air conditioner	0.76	0.6	0.6	2.6	-2.8	1.0	-	-	-	-	-	.10	.10	1.8	.09	.06	0.2	0.	0.28	0.6
Water heater	1.0	2.0	0.0	0.0	0.0	0.0	-	-	-	-	-	-	-	-	-	-	-	-	-	-
Range	1.0	2.0	0.0	0.0	0.0	0.0	-	-	-	-	-	-	-	-	-	-	-	-	-	-
Refrigerator and freezer	0.84	0.8	0.6	2.6	-1.4	0.8	1.0	2.0	0.	0.	0.	.056	.087	2.4	.053	.082	0.2	0.	0.28	0.6
Dishwasher	0.89	1.8	0.0	3.6	-1.4	0.8	1.0	2.0	0.	0.	0.	.11	.14	2.6	.11	.066	1.0	0.	0.28	0.6
Clothes washer	0.85	0.08	2.9	1.6	1.8	1.0	-	-	-	-	-	.11	.12	2.0	.11	.13	1.0	0.	0.69	0.4
Incandescent lighting	1.0	1.84	0.0	0.0	0.0	0.0	-	-	-	-	-	-	-	-	-	-	-	-	-	-
Clothes dryer	0.99	2.0	0.0	3.3	-2.6	0.2	1.0	2.0	0.	0.	0.	.12	.16	1.9	.13	.14	1.0	0.	0.11	0.4
Colored television	0.77	2.0	0.0	5.2	-4.6	0.0	-	-	-	-	-	-	-	-	-	-	-	-	-	-
Furnace fan	0.73	0.08	2.9	1.6	1.8	1.0	-	-	-	-	-	-	-	-	-	-	-	-	-	-
Commercial heat pump	0.84	0.1	1.0	2.5	-1.3	0.9	1.0	2.0	0.	0.	0.	.83	.83	1.9	.036	.068	0.2	0.	0.28	0.6
Heat pump commercial A/C	0.81	0.1	1.0	2.5	-1.3	1.0	-	-	-	-	-	.83	.83	1.9	.036	.068	0.2	0.	0.28	0.6
Commercial central A/C	0.76	0.1	1.0	2.5	-1.3	1.0	-	-	-	-	-	.83	.83	1.9	.036	.068	0.2	0.	0.28	0.6
Commercial room A/C	0.76	0.6	0.6	2.5	-2.8	1.0	-	-	-	-	-	.10	.10	1.8	.09	.06	0.2	0.	0.28	0.6
Fluorescent lighting	0.90	1.0	1.0	3.0	-2.8	0.0	-	-	-	-	-	-	-	-	-	-	-	-	-	-
Pumps, fans, other motors	0.87	0.08	2.9	1.6	1.8	1.0	-	-	-	-	-	.079	.12	3.2	.052	.12	1.0	0.	0.7	0.7
Electrolysis	0.90	1.8	-0.9	2.2	0.8	0.0	-	-	-	-	-	-	-	-	-	-	-	-	-	-
Arc furnace	0.72	2.3	-1.0	1.61	-1.0	0.0	-	-	-	-	-	-	-	-	-	-	-	-	-	-
Small industrial motors	0.83	0.1	2.9	0.6	-1.8	1.0	-	-	-	-	-	.031	.10	3.2	.018	.18	1.0	0.	0.7	0.6
Large industrial motors	0.89	0.05	1.9	0.6	1.2	1.0	-	-	-	-	-	.013	.067	3.8	.009	.17	1.0	0.	1.5	0.8
Agricultural water pumps	0.86	1.4	5.6	1.4	4.2	1.0	-	-	-	-	-	.025	.088	3.2	.016	.17	1.0	0.	0.8	0.7
Power plant auxiliaries	0.80	0.08	2.9	1.6	1.8	1.0	-	-	-	-	-	.013	.14	2.4	.009	.12	1.0	0.	1.5	0.7

Figure (2.2) EPRI characteristics data for static and dynamic loads.

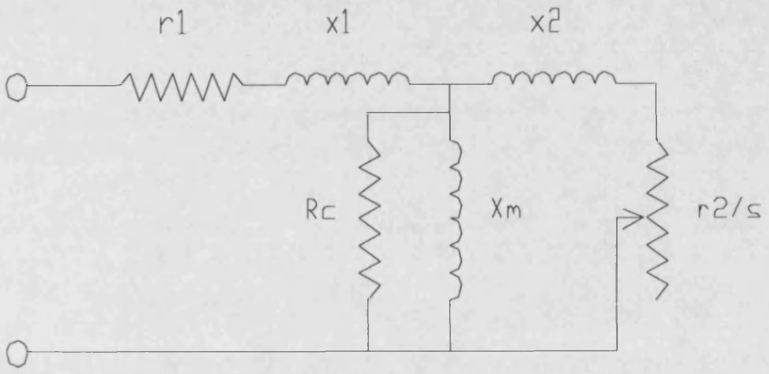

Figure (2.3) Induction motor equivalent circuit.

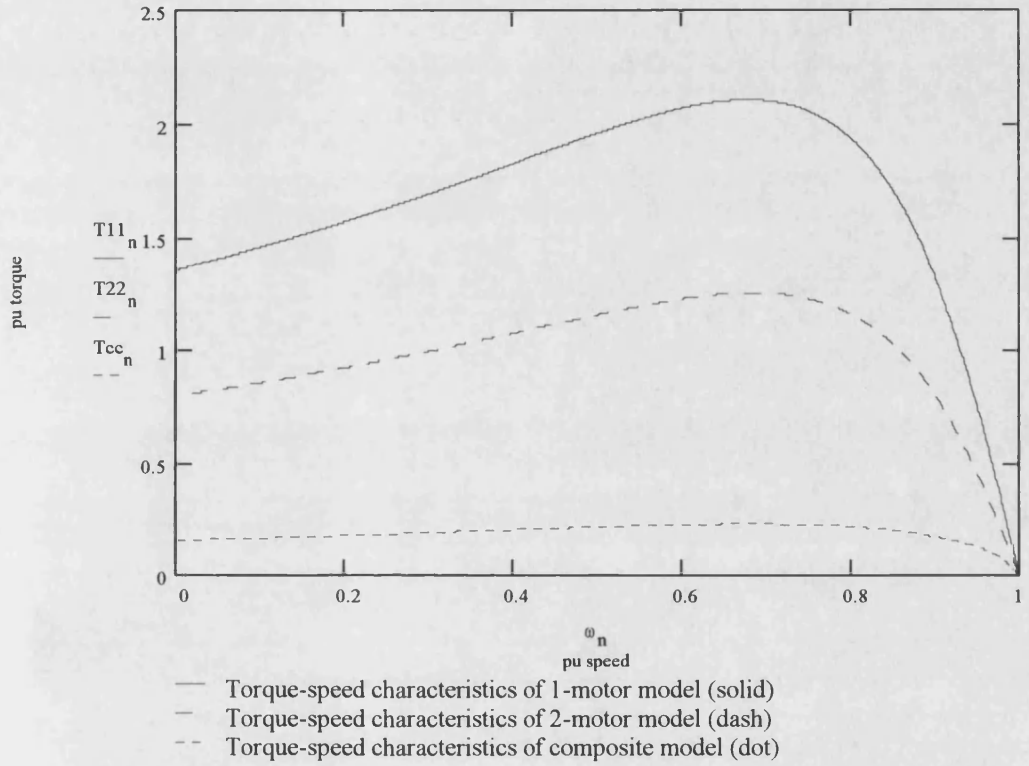

Figure (2.4) Electrical torque-speed characteristics of 1-motor, 2-motor, and the composite motor models.

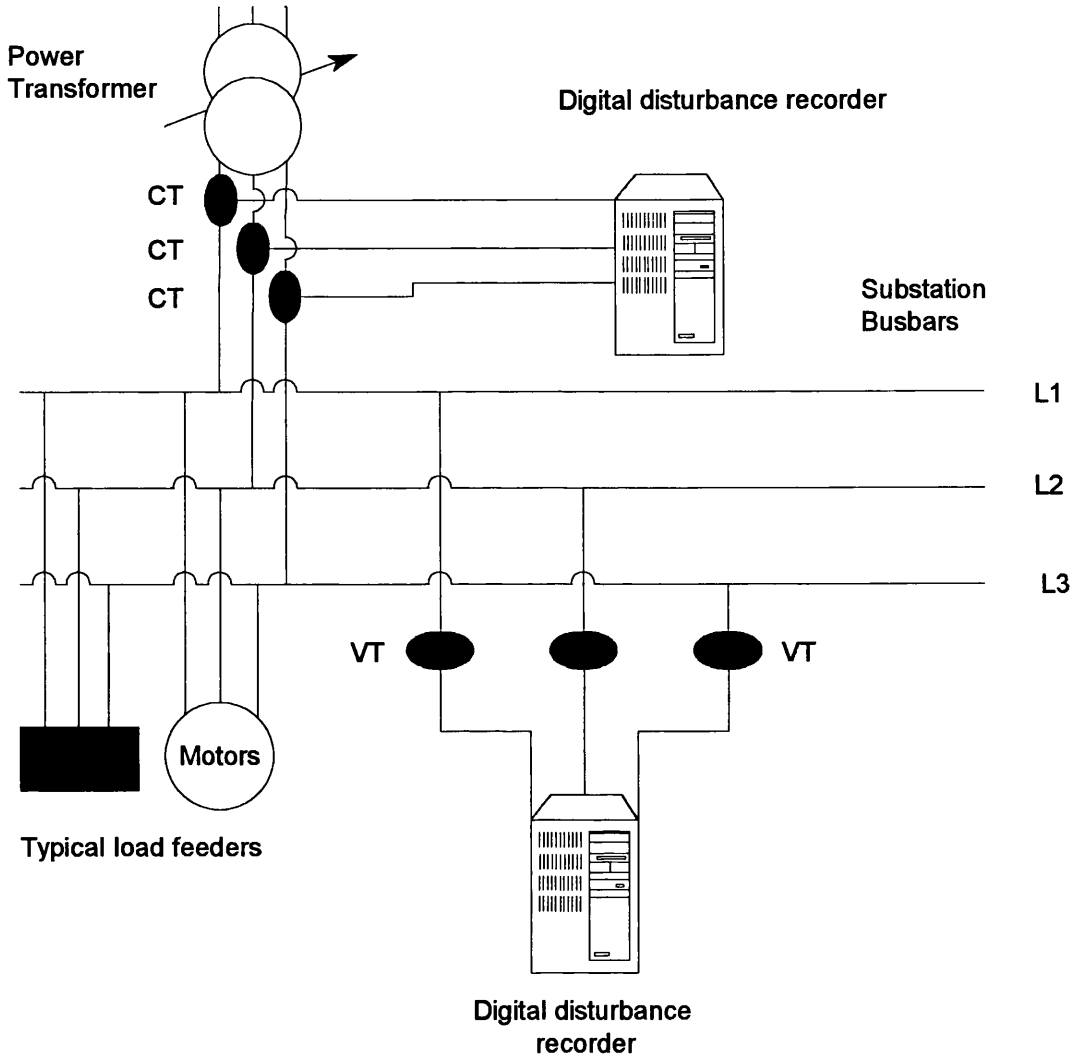

Figure (2.5) Typical scheme of load characteristics measurements at substations.

CHAPTER 3

Transient Simulation Results

3.1 - Test objectives:

The main purpose of transient simulation test is to monitor and record the transient response of single-phase A/C compressor load, for better understanding of its dynamic behavior under abnormal system operating conditions. One of the important questions, in induction motors stability studies, is whether motors will reaccelerate or stall following fault clearing [23].

Three different models of single-phase A/C units, having different refrigeration capacities of 17600, 18330, and 21000 BTU/hr respectively, were selected to undergo the transient simulation test. They were subjected to simulated low-voltage transients, where their voltage and current signals were recorded by means of a digital disturbance recorder.

The analysis of test results were aimed at shedding more light on the low-voltage characteristics of the single-phase A/C compressor load, including the following issues:

1) Determination of the system low-voltage level, below which the single-phase A/C compressor would stall.
2) Determination of the maximum fault clearing time, which is essential to avoid the compressor stalling when subjected to a reduced system voltage.

3) Investigation of the distribution system reactance (X_d) impact, when simulated in the test circuit, on the compressor low-voltage dynamic behavior, and on the maximum fault clearing time (t_{max}).

4) Investigation of the thermal overload relay impact on the compressor low-voltage dynamic behavior.

Therefore, by having good analysis of reliable test data, system planners will be able to reach satisfactory countermeasures to disturbance impact, which affect the power system performance and stability.

3.2 - Configuration of test circuit:

To achieve the above mentioned objectives, a transient simulation test circuit was built as illustrated in figure (3.1), which includes the following components:

No.	Designation	Quantity
1	Single-phase auto-transformer (10 A)	3
2	20 A fuse	3
3	Fuse holder	1
4	Bridge rectifier	1
5	Rheostat - 5000Ω	1
6	Universal digital timer	1
7	Push-button switch	1
8	Thermal overload relay	1
9	Current transformer (ratio 100:1)	1
10	240 v mcb	2
11	380 / 24 v transformer	3
12	Three poles power contactor	1
13	Data acquisition unit (digital disturbance recorder)	1

3.2.1 - Power supply:

The test circuit input terminals are supplied with terminal voltage, as well as with reduced voltage levels during test, through three banks of single-phase auto-transformer connected in parallel. The auto-transformer banks are connected to the main supply by means of a miniature circuit breaker (mcb), which serves as a main switching device for the test circuit.

3.2.2 - Line fuses :

The auto-transformer secondary terminals are connected to the test circuit and the compressor under test through three line fuses. They are mainly used to protect the test circuit in case of sustained severe faults. The selected fuses will not disturb the transient simulation process during the test, since they are comparatively slow tripping devices.

According to the compressor manufacturer data, the maximum current rating of line fuses must not exceed 225% of the compressor rated current [43]. The average rated current of the selected compressors is 10 Amperes, therefore, the three selected fuses are rated 20 Amperes each.

As shown in figure (3.1), the first fuse connects between the main output terminal of the auto-transformer and the normal-close auxiliary contact of the three-poles power contactor, while the second fuse connects between the auto-transformer slider terminal and the normal-open auxiliary contact of the power contactor. The third fuse connects

between the auto-transformer neutral terminal and the common terminal of the compressor under test.

3.2.3 - Three-poles power contactor:

The compressor under test is supplied with full and reduced terminal voltage simultaneously during the test through the auxiliary contacts of a three-pole power contactor. Full terminal voltage is supplied to the compressor under test through the normal-close auxiliary contact of the power contactor, while the reduced terminal voltage is supplied to the compressor through the normal-open auxiliary contact of the power contactor, when auxiliary contacts changeover during the test. The auxiliary contacts of the power contactor can withstand the compressor rated current during normal operation, as well as the compressor locked-rotor current if stalled during the test.

3.2.4 - Digital timer relay:

The digital timer relay in the test circuit is mainly used to set the fault clearing time, or in other words, to define the time duration of the simulated transient. It can provide very accurate time settings with small steps of 10 milliseconds each.

As shown in figure (3.1), a miniature circuit breaker (mcb) supplies the digital timer relay with AC voltage through a push-button switch. In parallel, the same mcb supplies the pick-up coil of the power contactor through the normal-open auxiliary contact of the digital timer relay. The timer relay is de-energized after the set time is elapsed, or when the timer main supply is interrupted, even before the set time has elapsed.

3.2.5 - Thermal overload relay:

The thermal overload relay in the test circuit is used to backup the compressor internal thermal relay in case of sustained severe fault during the test. The thermal relay will not interrupt the compressor operation, since its current setting is higher than the compressor starting as well as rated current. Similarly, the thermal overload relay will not disturb the transient simulation test, due to its slow response to the high transient current.

3.2.6 -Data acquisition unit:

The data acquisition unit used in the test circuit is a digital disturbance recorder, which has been detailed in Appendix (B). The recorder is used to record the compressor voltage and current signals during the test. The recorded compressor data will be used in further analysis, aimed for the investigation of such load dynamic behavior at low-voltage conditions.

A 100:1 external current transformer (CT) is connected in series with the compressor main winding in order to measure the compressor stator current during steady-state and transient conditions. The measured current signal is further reduced when it is fed to the recorder internal current transformer. The voltage across the compressor main winding terminals is directly measured by the recorder internal voltage transformer.

The terminals of the normal-close contact of the power contactor are connected in parallel to the input terminals of a variable resistance (rheostat). Consequently, the

rheostat output terminals are connected to the input terminals of a rectifier bridge, which in turn, it feeds its DC output signal to an internal digital channel (optocoupler) of the disturbance recorder.

The DC signal will be generated only during the simulated transients, where it will appear as a constant-amplitude pulse on the test records. This pulse is the time reference, which exactly indicates the start and end boundaries of the recorded transients during test.

3.2.7 - Distribution system reactance:

To simulate the effect of distribution system reactance (X_d) in this test, the secondary winding of a low-voltage transformer is connected in series with the compressor main winding. Both the resistance (R_T) and impedance (Z_T) of the transformer secondary winding are evaluated by injecting DC and AC currents respectively at reduced voltages. Therefore, the winding resistance (R_T) and impedance (Z_T) are given by the following equations (3.1):

$$R_T = \frac{V_{dc}}{I_{dc}} \qquad Z_T = \frac{V_{ac}}{I_{ac}} \qquad (3.1)$$

and the winding reactance (X_d) is given by equation (3.2):

$$X_d = \sqrt{Z_T^{\,2} - R_T^{\,2}} \qquad (3.2)$$

The winding reactance (X_d) is calculated in per-unit value, based on the compressor rated voltage and current. The following table includes different values of the distribution system reactance (X_d), simulated in the test circuit. The reactance values depend on the number of parallel-connected transformer secondary windings, which in turn, are connected in series with the main winding of compressor under test.

Transformer windings connection	Reactance (X_d)
One transformer secondary winding in series with the compressor	0.200 pu
Two parallel winding in series with the compressor main winding	0.100 pu
Three parallel windings in series with the compressor main winding	0.067 pu

3.3 - Test procedure:

The transient simulation test was performed by subjecting a single-phase air-conditioner to a reduced terminal voltage for short duration. Voltage and current signals of the single-phase compressor, equipped in the A/C unit, were recorded by means of a digital disturbance recorder. The recorded test data were used in further analysis in order to investigate the compressor dynamic behavior at low-voltage conditions.

Mainly, there are three major parameters which influence the test results, the transient voltage, the duration of simulated transients, and the value of simulated distribution system reactance (X_d) added in series to the compressor circuit. Prior to each test run, the terminal voltage was adjusted to the desired reduced level by means of the auto-transformer, while the duration of the simulated transient was set by means of the digital timer relay.

Each test run was repeated while varying the value of distribution reactance (X_d), as previously detailed in section (3.2.7), in order to investigate its impact on the compressor dynamic behavior during simulated transients. Before the test starts, the refrigerant gas pressure was adjusted to a pre-specified value by the manufacturer. This is to ensure a standard operating status for all compressors selected for testing, in order to avoid large tolerances in test results due to variable machines efficiencies and aging effects.

To begin the test, the compressor was allowed to start, where it was supplied with full terminal voltage through the normal-close auxiliary contact of the power contactor. To initiate a transient simulation, the push-button switch was pressed, and the digital timer relay was energized, which in turn, has energized the contactor pick-up coil.

Consequently, when the power contactor was energized, its normal-close auxiliary contact has opened, and the compressor main supply was interrupted. Simultaneously, the normal-open auxiliary contact was closed, and the compressor was supplied with the pre-adjusted auto-transformer output (reduced terminal voltage), simulating the fault situation.

When the normal-close auxiliary contact was opened, the nominal rated voltage across its terminals was fed to the rheostat, which in turn, has fed its varied AC output to the rectifier bridge. The rheostat output voltage was adjusted, so that when it was directed

to the rectifier bridge, the DC output signal was equal to 110 v. The DC signal is directly fed, as a binary input, to the internal digital channel of the disturbance recorder, which has created a constant-amplitude pulse, appearing on the recorded event as the time boundaries of the simulated transient.

The major factor, which was of great consideration in this test circuit, was the accuracy of the simulated transients, where the exact duration of recorded transients was compared to the corresponding digital timer settings.

By running different tests, it was found that the recorded transients duration were always greater than the corresponding digital timer settings by a small value, typically in the range of 10 milliseconds. Therefore, the time elapsed during the changeover of the contactor auxiliary contacts was negligible, and the principle of contactor-switching adopted in this test circuit could be practically accepted. Figure (3.2) illustrates the differences between various timer settings and the corresponding recorded transients duration, extracted from the test data of the 21,000 BTU/hr single-phase A/C compressor.

The first goal to be reached through the transient simulation test was to determine the low-voltage level below which the single-phase A/C compressor would stall. The auto-transformer output voltage was set at 0.8 pu of nominal terminal voltage during the first test run, and the digital timer relay was set at an arbitrary value of 0.5 seconds. This means

that the compressor under test was subjected to a low-voltage transient of 0.8 pu, which has lasted for half-second. If the compressor under test did not stall, the test voltage was further reduced down with a step of 0.01 pu, by re-adjusting the auto-transformer output setting. This procedure was repeated until the compressor under test would stall, and the corresponding low-voltage level reached in this case was called the *compressor critical voltage (V_{cr}).*

Subsequently, the second goal of this test was to determine the maximum fault clearing time (t_{max}), which was needed to avoid the compressor stalling when subjected to a low-voltage transient. Accordingly, the following test steps were performed:

1) The auto-transformer secondary output was adjusted to a lower voltage level than the pre-determined critical voltage of the compressor under test.

2) The digital timer relay was set at an arbitrary value of 0.2 seconds, which was less than the initial timer setting (0.5 seconds) used earlier while determining the compressor critical voltage.

3) If the compressor did not stall during the first test run, then, the timer setting was increased by a step of 10 milliseconds in order to prolong the simulated transient. This step was repeated until the compressor would have stalled.

4) Similarly, if the compressor had stalled during the first test run at the setting of 0.2 seconds, then, the timer setting was further decreased by the same time

step of 10 milliseconds. This test step was similarly repeated until the compressor would have stalled.

The main concern herein was the timer setting of the last two test runs, whether in step (3) or (4), where the compressor had stalled during one test run, and where it did not stall during the other. Therefore, the maximum fault clearing time (t_{max}) needed to avoid the compressor stalling at this particular low voltage level was limited between these timer settings.

Since it is impossible to change the timer setting by a step smaller than 10 milliseconds, therefore, the maximum fault clearing time (t_{max}) was taken as the average value of the recorded transient duration in both above mentioned test cases. The above test procedure was repeated at different low-voltage levels below the compressor critical voltage, in order to determine the corresponding (t_{max}) at each level.

The third test goal was to investigate the impact of the simulated distribution system reactance (X_d) on the compressor dynamic behavior at low-voltage conditions. It was important to determine such impact in order to decide the need to include (X_d) in the power system dynamic simulations.

To simulate the impact of (X_d) on the compressor dynamic behavior, the above detailed test procedure was identically repeated while connecting the secondary winding of a low-voltage transformer in series to the compressor main winding. As previously mentioned in section (3.2.7), different connections of the transformer windings will simulate various values of the distribution system reactance (X_d). The impact of distribution reactance (X_d) on the compressor dynamic behavior will be evaluated, based on the analysis of test results.

3.4 - Analysis of test results:

The above detailed test procedure was repeated for the three selected single-phase A/C compressors respectively. Appendix (E) includes the analysis of test results, which are represented in the table shown in figure (3.3). Such analysis have enabled better definition of the compressor dynamic behavior at low-voltage conditions, according to the earlier mentioned test objectives.

3.4.1 - Compressor critical voltage:

For a given system voltage, there is a maximum electrical torque (pullout torque) that an induction motor can develop. If the load mechanical torque exceeds this value, due to an increase in the load or due to a low system voltage, the motor would stall and reduce the system voltage further [15]. Therefore, the compressor critical voltage (V_{cr}) can be defined as the terminal voltage developing a decreased electrical torque, which is not matching with the minimum required load mechanical torque, and consequently, the compressor load will stall.

According to test results, when the tested compressors were subjected to low-voltage levels in the range between 0.72 pu and 0.8 pu, their speed decreased due to the mechanical overload, but they did not stall and resumed normal operation after fault clearance. On the other hand, the three tested compressors have stalled at the same reduced terminal voltage of 0.72 pu during the test, despite the differences in their refrigeration capacities. Regarding the condenser fan motor, it has never stalled when its terminal voltage was reduced during the test because of its light shaft load.

For any induction motor, the maximum developed electrical torque (Te_{max}) is given by equation (3.3) [32]:

$$Te_{\max} = \frac{0.5 * V^2}{R_{th} + \sqrt{R_{th}^2 + (X_{th} + x_2)^2}} \qquad (3.3)$$

By defining the voltage in the above equation as the critical voltage (V_{cr}), then, it can be given by equation (3.4):

$$V_{cr} = \sqrt{\frac{\left[R_{th} + \sqrt{R_{th}^2 + (X_{th} + x_2)^2}\right] * Te_{\max}}{0.5}} \qquad (3.4)$$

where Z_s - stator impedance = $r_1 + jx_1$

Z_m - magnetizing reactance = X_m

x_2 - rotor reactance.

Te_{max} - maximum developed electrical torque of A/C compressor.

Z_{th} - Thevenin equivalent impedance = $\frac{Z_s * Z_m}{Z_s + Z_m}$

R_{th} - Thevenin equivalent resistance.

X_{th} - Thevenin equivalent reactance.

In order to simulate a compressor critical voltage of 0.72 pu, as actually depicted from test results, sensitivity analysis of equation (3.4) showed that the maximum developed electrical torque (Te_{max}) of the tested compressors might have the values included in the following table:

Compressor model	**Max. torque (Te_{max})**	**Calculated (V_{cr})**
17,600 BTU/hr	1.33	0.719
18,330 BTU/hr	1.00	0.717
21,000 BTU/hr	1.36	0.719
Agg. compressor	1.23	0.719

The maximum electrical torque (Te_{max}) of the aggregate compressor is taken as the average of the maximum electrical torque of the three tested compressors. Accordingly, based on the above analysis, it was found that the compressor critical voltage (0.72 pu) is the reduced terminal voltage which developed an average maximum electrical torque *(Te_{max}) of 1.23 pu of the nominal load mechanical torque*.

In other words, the compressor maximum developed electrical torque (Te_{max}) must be equal or greater than 1.23 pu , in order to avoid the compressor stalling phenomena, caused by the reduced terminal voltage and excessive load mechanical torque during transients.

3.4.2 - Maximum fault clearing time:

The second objective of transient simulation test is to determine the threshold fault clearing time, above which the single-phase compressor would stall, when subjected to a low-voltage transient. This time limit is defined as the *maximum fault clearing time (t_{max}).*

According to test results, it was found that the maximum fault clearing time (t_{max}) is a function of the reduced terminal voltage, and the distribution system reactance (X_d). Figures (3.4a), (3.4b), and (3.4c) graphically illustrate the test data of all compressors. Each plotted curve in these figures relates the maximum fault clearing time (t_{max}) with the reduced terminal voltage for different values of simulated distribution reactance (X_d).

Equation (3.5) represents the general relationship between the clearing time (t_{max}) and the reduced terminal voltage (V), where its exponential output curve is matching with the actual test data :

$$V = K_1 * \left[e^{t_{max}} - 1 \right]^{K_2} \qquad (3.5)$$

Therefore, the following equation (3.6) results when moving (t_{max}) in the above equation (3.5) to the left hand side:

$$t_{max} = \ln \left[\left(\frac{V}{K_1} \right)^{\frac{1}{K_2}} + 1 \right] \qquad (3.6)$$

The constants (K_1) and (K_2) of equation (3.6) vary with the distribution system reactance (X_d). For each value of (X_d) and for every tested compressor, these constants are tuned so that the output curve of equation (3.6) will match the corresponding curve of the actual test data. Then, an average value of each constant is calculated, based on the defined constants of the three tested compressors, and corresponding to each value of the simulated reactance (X_d).

The average values of constants (K_1) and (K_2) are determined to represent the aggregated single-phase A/C compressor load. Figure (3.5) illustrates the relationship

between the distribution reactance (X_d) and the corresponding constants (K_1) and (K_2) respectively, which are represented by the following equations (3.7) and (3.8):

$$K_1 = 0.75 + 1.14 * X_d \qquad (3.7)$$

$$K_2 = 0.07 + 0.36 * X_d \qquad (3.8)$$

Therefore, the constants (K_1) and (K_2) can be calculated by substituting the value of (X_d) in equations (3.7) and (3.8). And, by substituting these constants in equation (3.6), the maximum fault clearing time (t_{max}) can be determined for the single-phase A/C compressor load at any reduced terminal voltage. Figure (3.6) illustrates the general relationship between the terminal voltage and the maximum fault clearing time (t_{max}), for different values of simulated distribution system reactance (X_d).

As shown in figure (3.6), if the terminal voltage is reduced down to 0.6 pu, the maximum fault clearing time (t_{max}) becomes very small, typically in the range of 30 to 40 milliseconds. Therefore, equation (3.6) is considered effective for any reduced terminal voltage ranging between 0.6 pu and 0.72 pu.

3.4.3 - Distribution system reactance:

As clearly shown in the previous section, the distribution system reactance (X_d) has greatly affected the compressor dynamic behavior when it was simulated in the test circuit. As shown in figure (3.6), the compressor will not stall ($t_{max} = \infty$) if the terminal voltage is

reduced down to 0.72 pu, in case of no added distribution reactance ($X_d = 0$). This aspect complies with the actual test result, which was previously detailed in section (3.4.1).

Meanwhile, when the reactance (X_d) was increased up to 0.067 pu or higher values, it was found that (t_{max}) must be less than 0.2 second in order to avoid the compressor stalling at the same voltage level of 0.72 pu. This large difference in (t_{max}) in both cases shows the extreme impact of the distribution reactance (X_d) on the compressor dynamic behavior at low-voltage conditions.

Figure (3.7) illustrates the relationship between (X_d) and (t_{max}), and shows the impact of (X_d) on the 17,600 BTU/hr compressor low-voltage dynamic behavior, which was subjected to low terminal voltage of 0.72, 0.70, 0.67 pu respectively. As depicted from this figure, the maximum fault clearing time (t_{max}) has heavily decreased when the simulated distribution reactance (X_d) was slightly increased up to 0.067 pu. On the other hand, when the distribution reactance (X_d) was increased to a value greater than 0.067 pu, the maximum fault clearing time (t_{max}) has reasonably decreased.

3.4.4 - Variation of P and Q:

During low-voltage transients, the dynamic load power requirements are changing in order to keep the load stable. In this section, two typical cases are selected for the stalling and non-stalling compressor during transient simulation test, in order to investigate the transient characteristics of the compressor load active and reactive power.

The voltage and current signals of the compressor under test were recorded, and the corresponding active and reactive power were calculated. The dynamic locus of compressor load active and reactive power at both cases are illustrated in figures (3.8-a) and (3.8-b) respectively. As shown in these figures, during the transient limits in both cases, the compressor load active power (P) was nearly constant. Therefore, it can be concluded that the single-phase A/C compressor is a constant-power load.

In these test case, the 17,600 BTU/hr compressor was subjected to a low-voltage transient of 0.7 pu, and a distribution system reactance (X_d) of 0.1 pu was simulated in the test circuit. The fault clearing time was 0.242 second in the non-stalling case, and 0.256 second in the stalling case.

In the non-stalling case, the compressor reactive power (Q) has crossed the active power limit, then after fault clearance, it has stabilized again at its pre-fault value. While in the stalling case, the compressor reactive power (Q) has largely increased, and sustained at a high post-fault value, nearly four times the compressor active power (P). This large difference, observed in the compressor dynamic behavior at both cases, clearly indicates the necessity of fast fault clearing.

Therefore, it can be depicted that the aggregated dynamic load of a particular load feeder will be affected during low-voltage transients, so that the total load reactive power may have a similar trend as shown in these figures, depending on the following factors:

1) fault clearing time.

2) fault location relative to the load feeder.

3) low voltage reached during transient.

4) load composition of the load feeder at the time of fault.

3.4.5 - Thermal overload protection:

There are other dynamic load characteristics, which deserve more attention and investigation, such as the characteristics of the thermal overload relays equipped inside compressors. Very little information was available from previous tests, regarding the tripping function of thermal overload relay [26,46].

According to test observations, the single-phase compressor was disconnected from the main supply after stalling by means of its internal thermal overload relay in nearly 10 seconds. Meanwhile, the compressor gas bleeding-off process required three to five minutes after stalling. The following characteristics of thermal overload relay were noticed during the test:

1) Delayed tripping, which allowed the stalled compressor to withdraw high reactive power from the system.

2) The thermal overload relay was reset after one minute of tripping the stalled compressor. Accordingly, it automatically reconnected the stalled compressor to the main supply, while the internal gas pressure was not released yet.

The relay reset and consecutive compressor reconnection process may occur two to three times during the five minutes period, which is required to release the compressor internal gas pressure. Even when the terminal voltage was fully restored after fault clearance, the single-phase compressor failed to restart or re-accelerate every time it was reconnected to the main supply. This phenomena occurred because the compressor could not develop enough electrical torque in order to overcome the excessive load mechanical torque, resulting from the non-released gas pressure.

Therefore, the thermal overload relay characteristics will have a disturbing effect on the system stability, since it enhances the high reactive power requirements of the single-phase compressor load during faults.

3.5 - Conclusions:

The transient simulation test circuit was built to investigate the dynamic behavior of the single-phase A/C compressor under low-voltage conditions. The principle of simulating low-voltage transients, adopted in this test circuit, has depended on the changeover of the three-poles power contactor auxiliary contacts, which supplies the compressor under test with nominal and reduced terminal voltage simultaneously. This

changeover technique has proved its reliability in simulating high-accuracy low-voltage transients during the test. The configuration of the test circuit as well as the test procedure are detailed in this chapter.

Different values of the distribution system reactance (X_d) were simulated in the test circuit by connecting, one or more secondary winding of a low-voltage transformer as detailed in section (3.2.7), in series with the main winding of the compressor under test. Voltage and current signals of the single-phase compressor under test were recorded by a digital disturbance recorder, where the test data have undergone further analysis for the evaluation of the compressor low-voltage dynamic behavior.

Based on test results, all tested compressors have stalled when the terminal voltage was reduced to 0.72 pu during the test. According to test results analysis, the compressor maximum electrical torque (Te_{max}) developed at this voltage level, was about 1.23 pu of the nominal load mechanical torque, which is the minimum required torque to avoid the compressor stalling. In contrast, the condenser fan motor did not stall during the test, due to the great difference between its load mechanical characteristics and that of the single-phase A/C compressor.

According to test results, the maximum fault clearing time (t_{max}) has mainly depended on the transient voltage , and the simulated distribution system reactance (X_d).

Therefore, the system protection relays can be set at a suitable value of 100 milliseconds, in order to safeguard the power system stability against the severe impact of compressor stalling phenomena during faults.

The distribution system reactance (X_d) showed a significant impact on the single-phase A/C compressor low-voltage dynamic behavior, when simulated in the test circuit. It has largely decreased the operational stability limits of the compressor load. Based on test results, it was found that the maximum fault clearing time (t_{max}) is inversely proportional to the simulated distribution system reactance (X_d). At any low-voltage level, (t_{max}) has largely decreased when the simulated reactance (X_d) was slightly increased. Therefore, it is important to include the distribution system reactance (X_d) in the power system dynamic simulations.

In a typical stalling and non-stalling test case, it was observed that the compressor load active power (P) was nearly constant, therefore, the A/C compressor was assumed to be a constant-power load. On the other hand, the reactive power (Q) has highly increased in the case of compressor stalling because of its delayed tripping. Accordingly, the necessity of fast fault clearing is confirmed in order to avoid the severe impact of the stalling compressor high reactive power requirements on the system stability during faults.

According to test observations, the slow-acting thermal overload relay had a disturbing impact on the power system stability, since it allowed the stalled compressor to withdraw high reactive power from the system before being tripped. It was found that the delayed tripping and the consecutive reconnection of the stalled compressor to the system, were the main reasons causing the delayed recovery of the post-fault system voltage. Therefore, the necessity to fast fault clearing is more stressed, and the fast and complete tripping of the stalled compressors is urged.

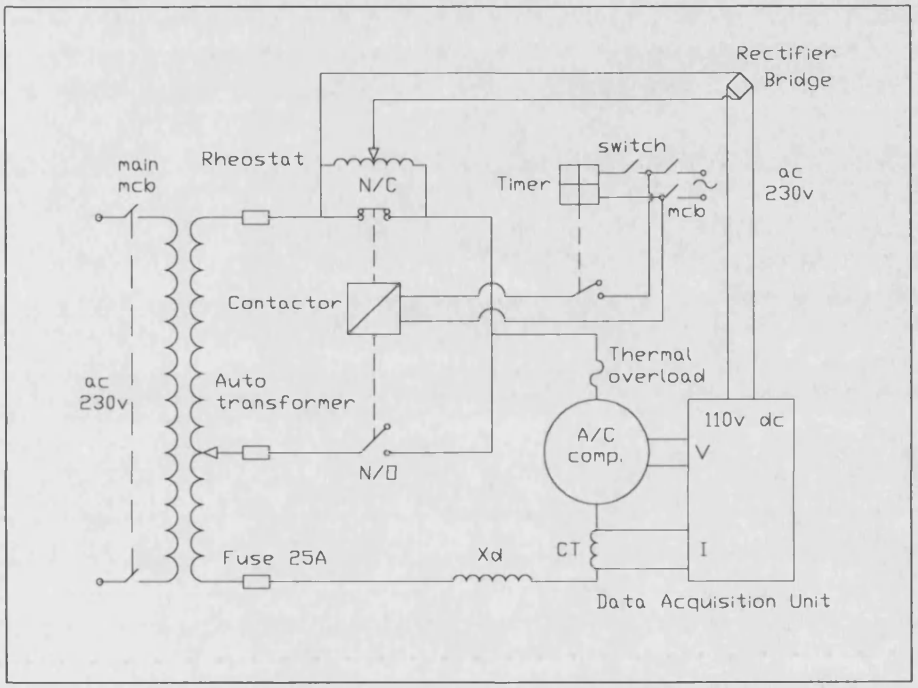

Fig (3.1) Transient simulation test circuit.

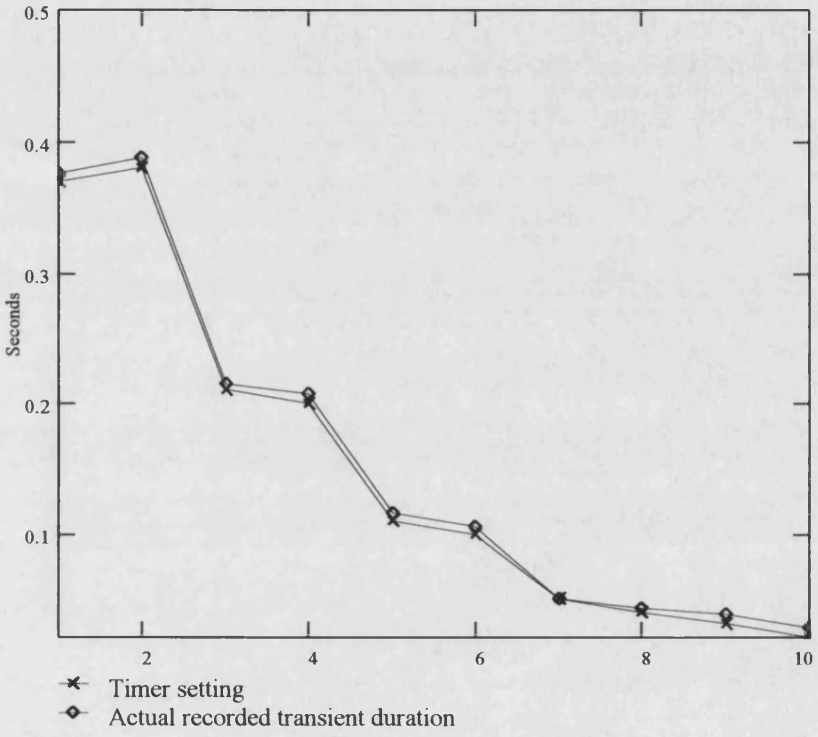

Fig (3.2) Difference between the digital timer settings and the corresponding actual transient duration when testing 21,000 BTU/hr compressor ($X_d = 0$).

Compressor capacity	Test voltage (pu)	Distribution reactance (X_d)	Timer setting (sec)	Transient duration (sec)	Event file name	Comp. blocked ?	Max. fault clearing time (t_{max})
17,600 BTU	0.67	0	0.250	0.256	RE001.414	N	0.261
			0.260	0.266	RE001.415	Y	
	0.64	0	0.220	0.228	RE001.425	N	0.232
			0.230	0.236	RE001.426	Y	
	0.60	0	0.120	0.128	RE001.427	Y	0.123
			0.110	0.118	RE001.429	N	
	0.57	0	0.100	0.100	RE001.430	N	0.109
			0.110	0.118	RE001.431	Y	
	0.54	0	0.110	0.120	RE001.435	N	0.124
			0.120	0.128	RE001.436	Y	
	0.50	0	0.100	0.096	RE001.437	N	0.105
			0.110	0.114	RE001.438	Y	
	0.47	0	0.080	0.088	RE001.439	Y	0.084
			0.070	0.080	RE001.440	N	
	0.44	0	0.070	0.080	RE001.441	N	0.082
			0.080	0.084	RE001.442	Y	
	0.72	0.2	0.180	0.190	RE001.465	N	0.193
			0.190	0.196	RE001.466	Y	
	0.70	0.2	0.170	0.180	RE001.536	N	0.184
			0.180	0.188	RE001.537	Y	
	0.67	0.2	0.120	0.128	RE001.545	N	0.133
			0.130	0.138	RE001.546	Y	
	0.72	0.1	0.250	0.256	RE001.488	Y	0.249
			0.240	0.242	RE001.491	N	
	0.70	0.1	0.200	0.208	RE001.530	N	0.213
			0.210	0.218	RE001.531	Y	
	0.67	0.1	0.140	0.146	RE001.553	N	0.151
			0.150	0.156	RE001.554	Y	
	0.72	0.067	0.310	0.314	RE001.510	Y	0.308
			0.300	0.302	RE001.513	N	
	0.70	0.067	0.220	0.223	RE001.521	N	0.231
			0.230	0.238	RE001.522	Y	
	0.67	0.067	0.140	0.148	RE001.560	N	0.153
			0.150	0.158	RE001.561	Y	
18,330 BTU	0.72	0	0.390	0.400	RE001.278	Y	0.394
			0.380	0.388	RE001.280	N	
	0.70	0	0.200	0.204	RE001.283	N	0.211
			0.210	0.218	RE001.284	Y	
	0.67	0	0.080	0.088	RE001.310	N	0.093
			0.090	0.098	RE001.311	Y	
	0.64	0	0.050	0.056	RE001.303	N	0.057
			0.060	0.058	RE001.304	Y	
	0.60	0	0.040	0.046	RE001.306	N	0.052
			0.050	0.058	RE001.307	Y	

	0.72	0.2	0.070	0.078	RE001.318	N	0.083
			0.080	0.088	RE001.319	Y	
	0.70	0.2	0.060	0.068	RE001.352	N	0.069
			0.070	0.070	RE001.353	Y	
	0.67	0.2	0.040	0.048	RE001.357	Y	0.043
			0.030	0.038	RE001.359	N	
	0.72	0.1	0.100	0.106	RE001.326	Y	0.096
			0.090	0.086	RE001.328	N	
	0.70	0.1	0.060	0.068	RE001.370	Y	0.064
			0.050	0.060	RE001.372	N	
	0.67	0.1	0.040	0.050	RE001.386	N	0.054
			0.050	0.058	RE001.387	Y	
	0.72	0.067	0.100	0.108	RE001.334	N	0.113
			0.110	0.118	RE001.335	Y	
	0.70	0.067	0.070	0.070	RE001.379	N	0.079
			0.080	0.088	RE001.380	Y	
	0.67	0.067	0.040	0.048	RE001.382	N	0.058
			0.060	0.068	RE001.384	Y	
21,000 BTU	0.72	0	0.370	0.376	RE001.157	N	0.377
			0.380	0.388	RE001.158	Y	
	0.70	0	0.210	0.215	RE001.124	Y	0.212
			0.200	0.208	RE001.125	N	
	0.67	0	0.110	0.116	RE001.162	Y	0.111
			0.100	0.106	RE001.163	N	
	0.64	0	0.050	0.050	RE001.166	Y	0.046
			0.040	0.042	RE001.167	N	
	0.60	0	0.020	0.028	RE001.131	N	0.033
			0.030	0.038	RE001.132	Y	
	0.72	0.2	0.050	0.058	RE001.176	Y	0.048
			0.040	0.038	RE001.182	N	
	0.70	0.2	0.040	0.042	RE001.211	Y	0.033
			0.030	0.024	RE001.212	N	
	0.67	0.2	0.030	0.033	RE001.216	Y	0.025
			0.020	0.017	RE001.218	N	
	0.72	0.1	0.080	0.084	RE001.214	N	0.091
			0.090	0.096	RE001.215	Y	
	0.70	0.1	0.040	0.050	RE001.263	N	0.053
			0.050	0.056	RE001.264	Y	
	0.67	0.1	0.050	0.050	RE001.227	Y	0.045
			0.040	0.040	RE001.239	N	
	0.72	0.067	0.100	0.102	RE001.222	Y	0.100
			0.090	0.098	RE001.223	N	
	0.70	0.067	0.080	0.055	RE001.251	N	0.062
			0.090	0.068	RE001.249	Y	
	0.67	0.067	0.050	0.066	RE001.243	Y	0.054
			0.040	0.042	RE001.246	N	

Figure (3.3) Data of transient simulation test.

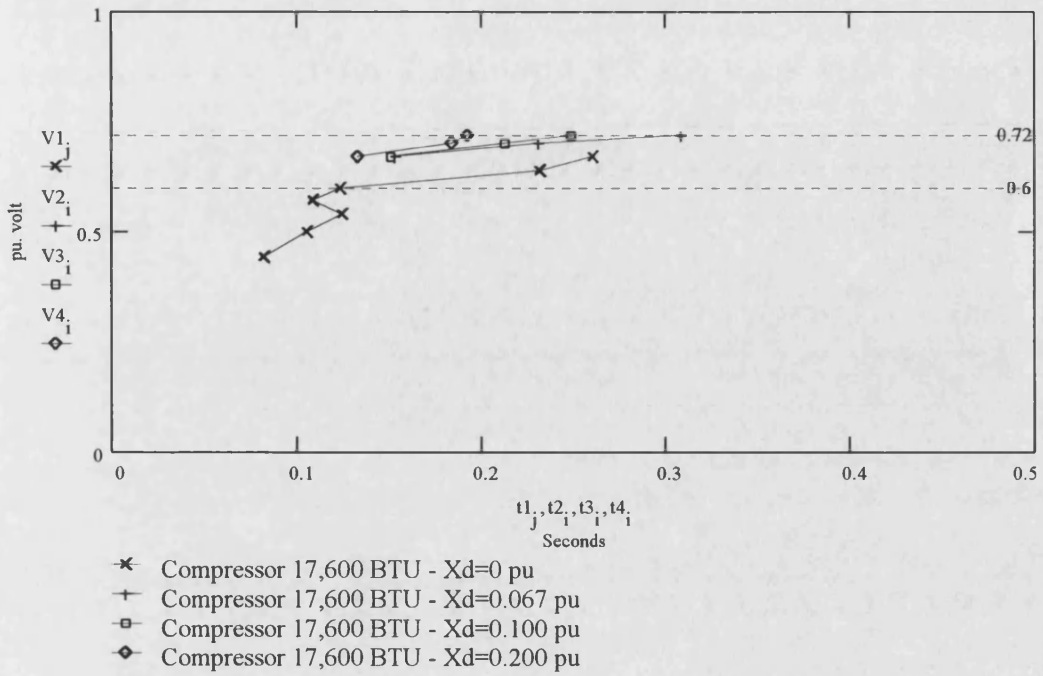

Fig (3.4-a) Data of transient simulation test performed on 17,600 BTU/hr compressor.

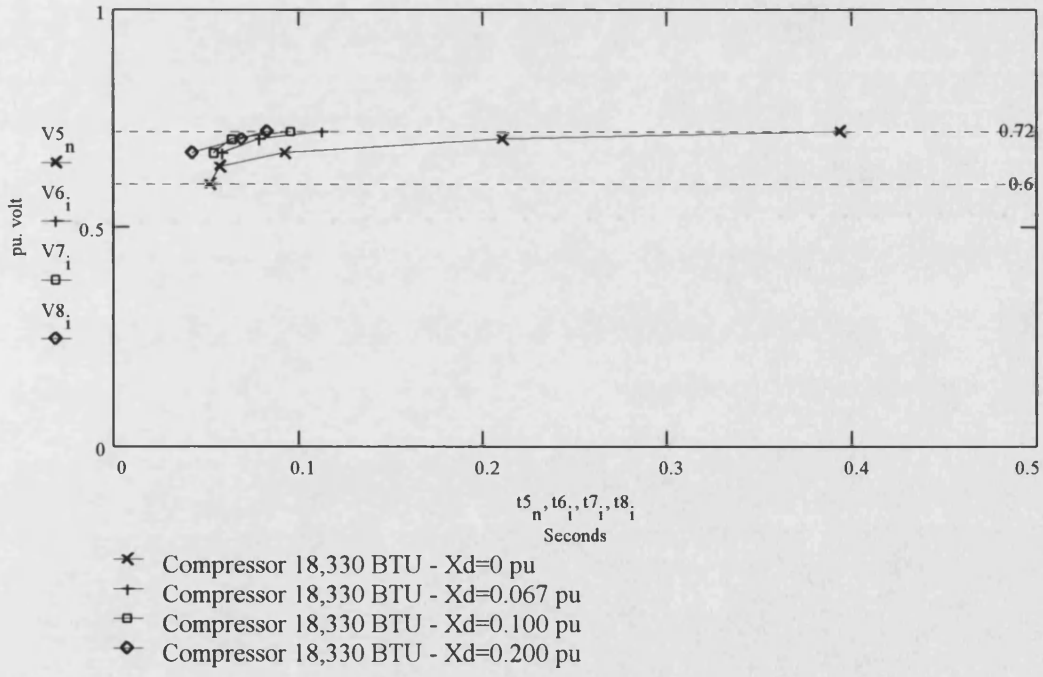

Fig (3.4-b) Data of transient simulation test performed on 18,330 BTU/hr compressor.

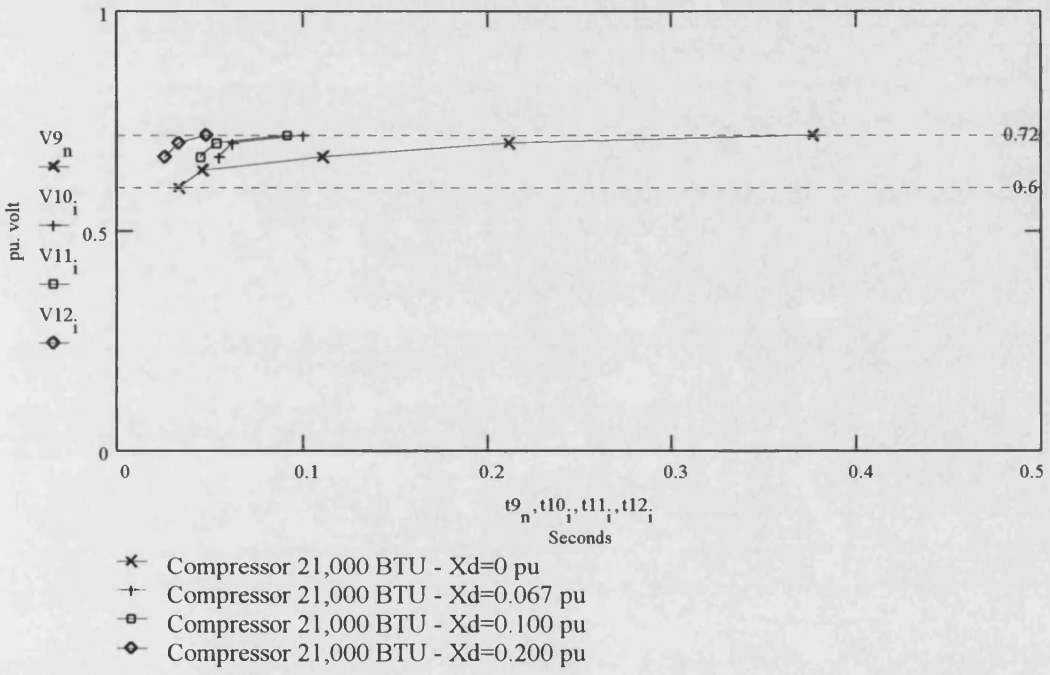

Fig (3.4-c) Data of transient simulation test performed on 21,000 BTU/hr compressor.

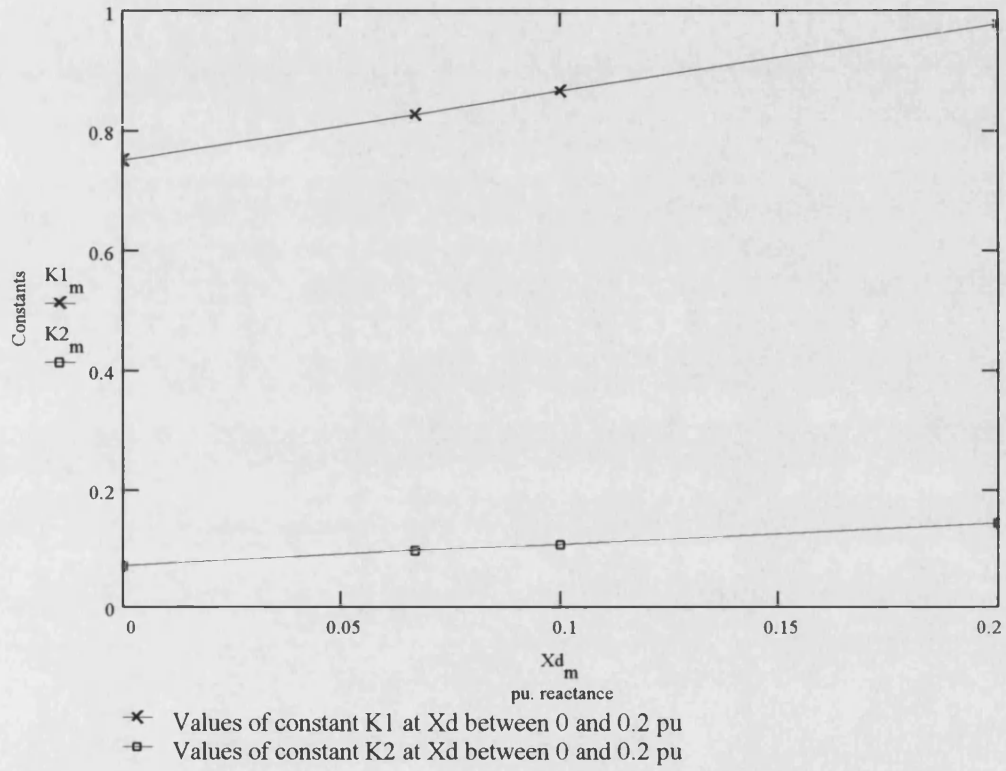

Fig (3.5) Relationship between the tuning constants K_1 and K_2 and the simulated distribution system reactance (X_d).

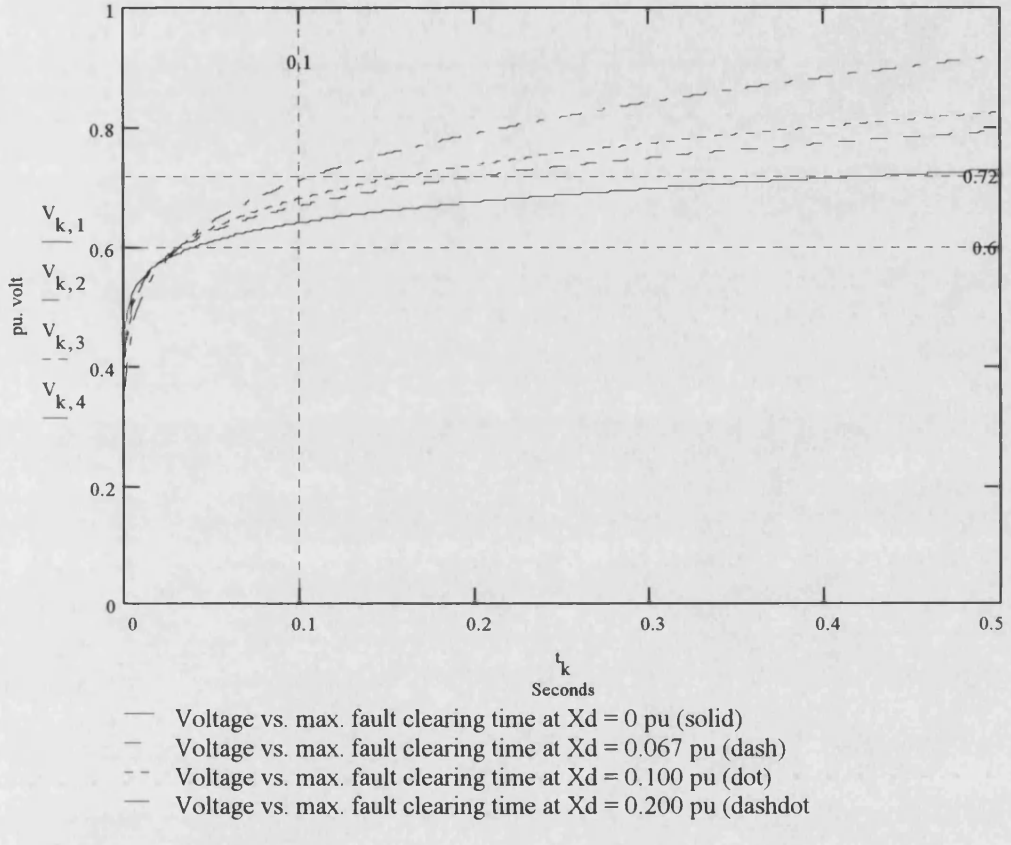

Fig (3.6) General relationship between the terminal voltage and the maximum fault clearing time (t_{max}) of the single-phase A/C compressor load, for different values of simulated distribution system reactance (X_d).

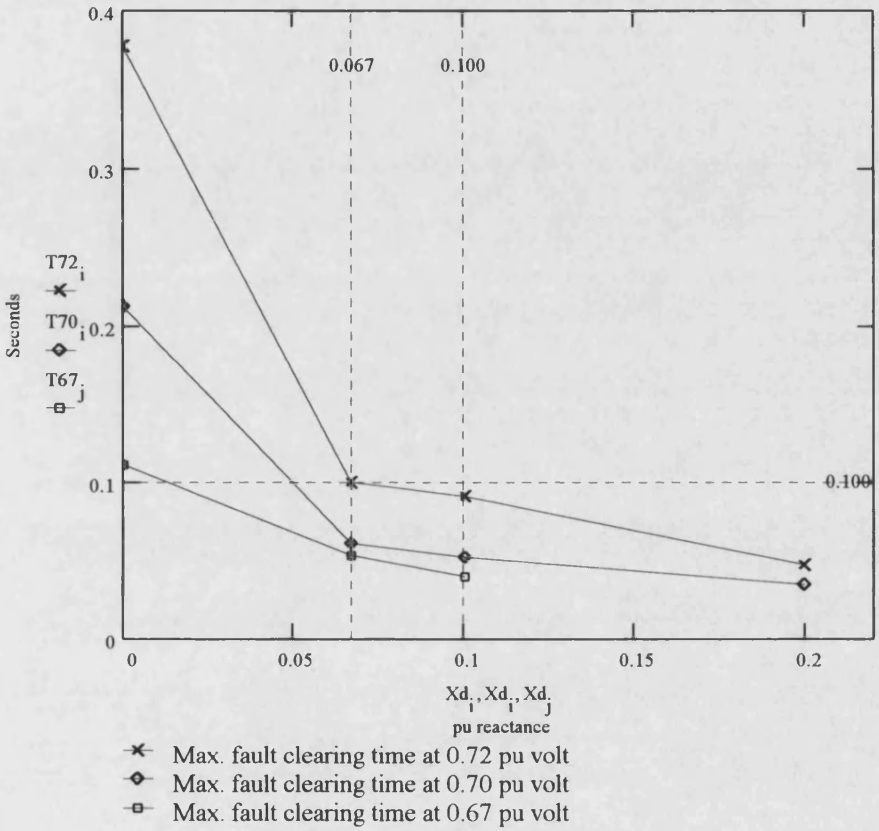

Fig (3.7) Relationship between the maximum fault clearing time (t_{max}) and variable simulated distribution system reactance (X_d), when testing the 17,600 BTU/hr single-phase A/C compressor load at different low voltage levels.

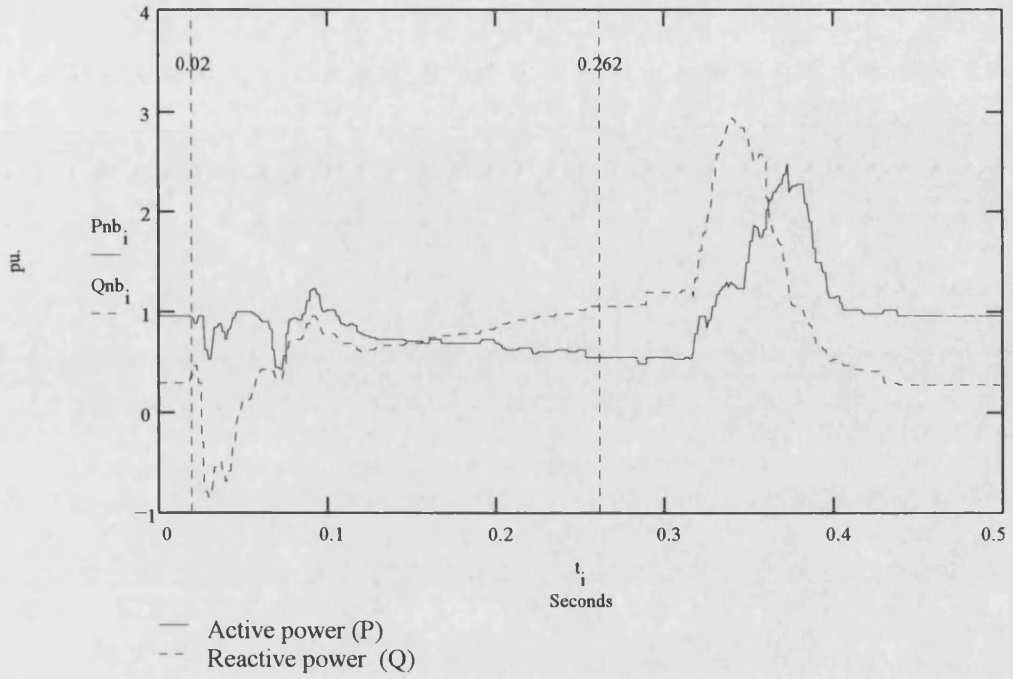

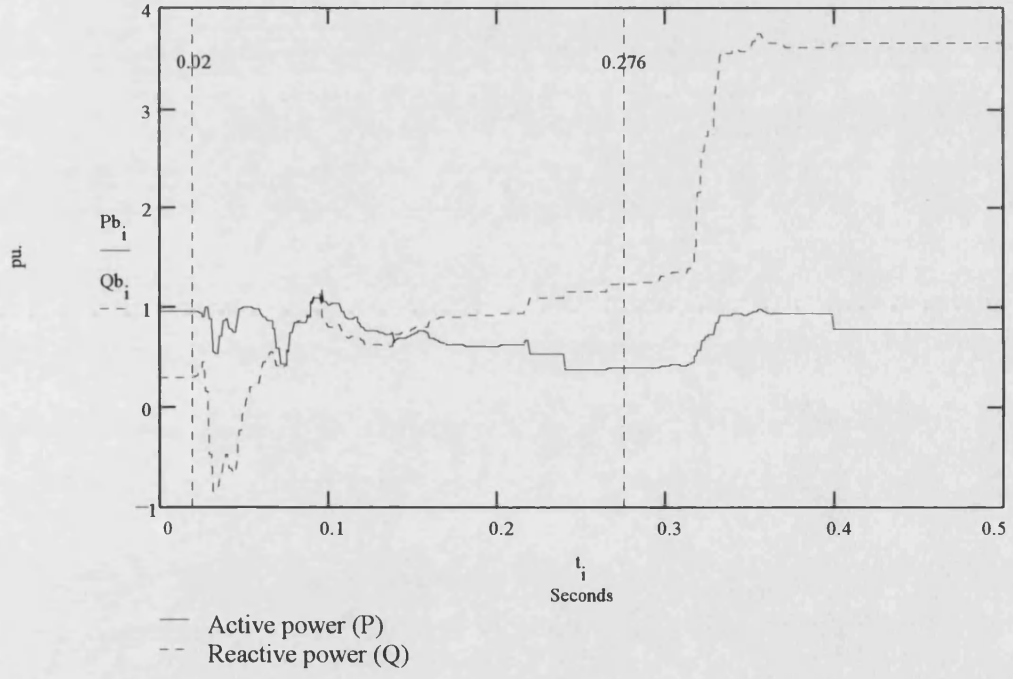

Fig (4.7-a & b) Active and reactive power of the typical non-stalling and stalling test cases for the 17,600 BTU/hr single-phase A/C compressor.

CHAPTER 4

Parameters Identification of Single- phase A/C Compressor Load

4.1 - Introduction:

In order to build up an efficient load model for load flow and transient stability analysis, useful load data is needed. The electrical parameters of the single-phase A/C compressor load were identified through laboratory tests. This chapter includes the identification procedure of electrical parameters, and results were compared to earlier published A/C load model data [16].

The mechanical torque-speed characteristics in loads with compressors such as refrigerators and air-conditioners is significantly different from the load torque-speed characteristics of other appliances which do not include compressors such as washing machines, fans, or dishwashers [27]. Accordingly, this chapter also includes the details of a new identification method for the mechanical torque characteristics of the single-phase A/C compressor load. Advantages and shortcomings of the new methodology were discussed herein as well.

4.2 - Compressor design:

The hermetic single-phase air-conditioning reciprocating compressor is one of the most important direct-drive motor applications, that typically employ a 4-pole 1500 rpm split-phase induction motor [38]. Figure (4.1) illustrates the hermetic single-phase

compressor. This design permits a compact well-suited arrangement of single-phase window-type air-conditioning units widely offered by the industry [39].

Single-phase A/C compressors are considered as a hard-to-start loads, which are equipped with split-phase induction motors of Design Class "C", and an internal thermal overload protective device [41]. The thermal overload relay will break the circuit after a certain time delay, which is variable with the motor locked-rotor current. Typically, the split-phase compressor motor has a full-load slip of less than 5%, and a starting current which does not exceed five to six times the rated current [41,42].

In practice, the split-phase compressor motor has two windings, a high-resistance starting winding, and a low-resistance main winding. A capacitor, typically rated at 35 μF, is connected in series with the starting winding in order to increase the phase shift (φ) between the starting winding current (I_{st}) and main winding current (I_{main}), resulting in a higher compressor starting torque. Figure (4.2) illustrates a typical schematic wiring diagram of the single-phase A/C compressor [43].

4.3 - Identification of electrical parameters:

The equivalent circuit of a single-phase induction motor previously illustrated in figure (2.3) includes a stator resistance (r_1) and leakage reactance (x_1), connected in series with the rotor resistance (r_2) and leakage reactance (x_2), referred to the stator. The

magnetizing reactance (X_m) is represented as a shunt reactance in parallel with the core loss (R_c) [41,42].

The no-load, locked-rotor, and DC tests were employed to evaluate the induction motor resistive and reactive parameters. The locked-rotor test was performed for short duration and at a reduced voltage in order to avoid overheating, since the winding resistance vary with temperature.

4.3.1 - DC test:

Figure (4.3) illustrates the DC test circuit. With a direct current flowing in the stator winding, the stator magnetic field is fixed in space. If no external torque turns the shaft, the flux linkages with the rotor circuit are constant in time. As a result, no voltages are induced in the rotor, and no electrical torque is developed.

Therefore, the rotor circuit has no electrical effect on those of the stator, and the stator resistance (r_1) can be calculated independently of the rotor impedance by the following equation (4.1)[41]:

$$r_1 = \frac{V_{dc}}{I_{dc}} \qquad (4.1)$$

4.3.2 - No-load test:

The no-load test was carried out at synchronous speed and rated supply voltage with zero rotor current. In case of single-phase compressor, it was supplied with rated

voltage and allowed to run for a short time while it's empty of refrigerant gas, until no-load current and power were measured. Figure (4.4) illustrates the no-load test circuit.

The input impedance corresponds to the stator impedance ($r_1 + jx_1$) in series with the magnetizing branch comprising the core loss (R_c) in parallel with the magnetizing reactance (X_m). The stator resistance (r_1) can be neglected since it is much less than the core loss (R_c), which is given by equation (4.2) [41,42]:

$$R_c = \frac{V_{nl}^2}{P_{nl}} \qquad (4.2)$$

Neglecting the small voltage drop on the stator impedance, the iron core current is given by equation (4.3):

$$I_c = \frac{V_{nl}}{R_c} \qquad (4.3)$$

Therefore, the magnetizing current (I_m) is given by the following equation (4.4):

$$I_m = \sqrt{I_{nl}^2 - I_c^2} \qquad (4.4)$$

and consequently, the magnetizing reactance (X_m) is given by equation (4.5):

$$X_m = \frac{V_{nl}}{I_m} \qquad (4.5)$$

4.3.3 - Locked-rotor test:

For any machine, the locked-rotor test is achieved by clamping its shaft so that it cannot run. In case of the hermetic sealed single-phase A/C compressor, it was not possible to reach the rotor in order to block it. Therefore, the compressor rotor was prevented from rotating by suddenly disconnecting the compressor supply while running. The sudden brake resulting from the internal gas pressure has blocked the compressor rotor from rotating. Then, a reduced supply voltage was instantly applied to the compressor terminals so as to permit an approximate rated current to flow in the compressor main winding. Figure (4.5) illustrates the locked-rotor test circuit.

The rotor resistance (r_2) and leakage reactance (x_2), referred to the stator winding, are calculated while neglecting the magnetizing reactance (X_m), which is typically much higher than the magnitude of rotor impedance ($r_2 + jx_2$). Therefore, the rotor resistance (r_2) is given by equation (4.6), and the locked-rotor reactance (X_{br}) is given by the following equation (4.7) [41,42]:

$$r_2 = \frac{P_{br}}{I_{br}^2} - r_1 \qquad (4.6)$$

$$X_{br} = \sqrt{\left(\frac{V_{br}}{I_{br}}\right)^2 - (r_1 + r_2)^2} \qquad (4.7)$$

The following table shows how the locked-rotor reactance (X_{br}) approximately divides between stator reactance (x_1) and rotor reactance (x_2) for rotors of different designs:

Rotor	X_1	X_2
Wound	0.5 X_{BR}	0.5 X_{BR}
Design A	0.5 X_{BR}	0.5 X_{BR}
Design B	0.4 X_{BR}	0.6 X_{BR}
Design C	0.3 X_{BR}	0.7 X_{BR}
Design D	0.5 X_{BR}	0.5 X_{BR}

Then, (x_1) and (x_2) of the Design Class C compressor motor are given by the following equation (4.8) [41]:

$$x_1 = 0.3 * X_{br}$$
$$x_2 = 0.7 * X_{br} \qquad (4.8)$$

4.3.4 - Nominal slip:

Since it was impossible to measure the actual speed of the hermetic single-phase A/C compressor, a proposed method is presented herein to calculate an approximate and satisfactory value of the compressor nominal slip. The induction motor equivalent circuit has been approximated by moving the magnetizing branch forward to the input terminals, as shown in figure (4.6). Therefore, the rotor current (I_2) is given by equation (4.9):

$$I_2 = \frac{V_{ph}}{r_1 + \frac{r_2}{S} + j(x_1 + x_2)} \qquad (4.9)$$

The total input power (P_g) transferred across the air-gap from the stator is given by equation (4.10) [32]:

$$P_g = I_2^2 * \frac{r_2}{S} \qquad (4.10)$$

The compressor input power can also be calculated from equation (4.11), where the *Energy Efficiency Ratio* (EER) and the refrigeration capacity in BTU/hr of different compressors were extracted from the manufacturer data [43]:

$$P_{in} = \frac{BTU/hr}{EER} \qquad (4.11)$$

Neglecting the compressor core and stator copper losses, (P_g) is assumed to be equal to (P_{in}). Therefore, equation (4.12) results from substituting equations (4.9) and (4.11) into equation (4.10):

$$\frac{\left[r_1 + \frac{r_2}{S} + j(x_1 + x_2)\right]^2}{\frac{r_2}{S}} = \frac{V_{ph}^2}{P_{in}} \qquad (4.12)$$

Neglecting the small imaginary term in the above equation (4.12), then, the approximate compressor slip can be given by equation (4.13):

$$S = \frac{-\left(2 * r_1 - \frac{V_{ph}^2}{P_{in}}\right) - \sqrt{\left(2 * r_1 - \frac{V_{ph}^2}{P_{in}}\right)^2 - 4 * r_1^2}}{2 * \frac{r_1^2}{r_2}} \qquad (4.13)$$

4.3.5 - Inertia constant:

The inertia constant (H) is the kilowatt-seconds of the mechanical stored energy at synchronous speed divided by the machine rated kVA [39]. The mechanical stored energy or inertia torque is commonly expressed as (GD^2), where (G) is the weight of rotating parts in kilograms, and (D) is the effective diameter of gyration in meters [56].

In case of the hermetic single-phase A/C compressor, it was not possible to specify (G) and (D) exactly. Therefore, the weight of compressor rotor and coupled cam shaft and piston (G) was estimated as 40% of the compressor total weight, and the gyration diameter (D) was estimated as 0.12 meters. Accordingly, the compressor inertia constant (H) is given by the following equation (4.14):

$$H = \frac{1.386 * 10^{-6} * \left(G\ D^2\right) * (rpm)^2}{kVA} \qquad (4.14)$$

4.3.6 - Tests data:

Three different models of single-phase A/C units, having different refrigeration capacities of 17600, 18330, and 21000 BTU/hr respectively, were selected in order to identify the electrical parameters of their compressors and condenser fan motors. The selected units are currently the most available single-phase air-conditioner models used in Abu Dhabi residential and commercial buildings.

The typically used condenser fan motor in all A/C units is a single-phase fractional horsepower split-phase motor. This type of motors has three stator windings in order to

provide a range of high, medium, and low fan speed. Appendix (C) includes all tests data and parameters of the three selected compressors as well as of a typical condenser fan motor. Figure (4.7) illustrates the simulated electrical torque-speed characteristics of the above mentioned compressors and condenser fan motor, compared to an earlier published A/C model [16]. The identified parameters herein were used to build up the new A/C load model, while neglecting the fan motor parameters, which do not concern the A/C load under investigation in this work.

4.4 - Compressor mechanical torque characteristics:

The mechanical torque characteristics of single-phase A/C compressor load has a great impact on its steady-state and transient behavior. Accordingly, it is important to define such characteristics accurately in order to build up an efficient dynamic load model for the system dynamic simulations. A new graphical method was developed herein in order to determine the mechanical torque coefficients of single-phase A/C compressor load, based on the induction motor dynamic equation.

4.4.1 - Methodology:

The first step is to calculate the dynamic slip of the single-phase compressor under test based on its starting current. The starting current is recorded by means of a digital disturbance recorder, as detailed in Appendix (B). As earlier proved in Chapter 3, the A/C compressor load is assumed to be a constant-power load since the active power was nearly constant during transients, where the power can be given by equation (4.15):

$$P = (I_2)^2 * \frac{r_2}{S} \qquad (4.15)$$

where P = compressor active power = 1 pu.

I_2 = compressor rotor current.

r_2 = rotor resistance.

S = compressor slip.

The compressor rotor current (I_2) can be calculated from the recorded compressor stator current during starting (I_1), which is divided in proportion to the magnetizing reactance (X_m) and rotor impedance $\left(\frac{r_2}{S}+x_2\right)$ of the compressor induction motor. Therefore, the compressor rotor current (I_2) is given by equation (4.16):

$$I_2 = I_1 * \frac{X_m}{X_m + x_2 + \frac{r_2}{S}} \qquad (4.16)$$

By substituting equation (4.16) in (4.15), the compressor active power is given by the following equation (4.17):

$$P = \left[I_1 * \frac{X_m}{X_m + x_2 + \frac{r_2}{S}} \right]^2 * \frac{r_2}{S} \qquad (4.17)$$

By substituting the dynamic values of the recorded compressor stator current during starting in equation (4.17), the corresponding dynamic values of compressor slip can be calculated. Figures (4.8), (4.9), and (4.10) illustrate the dynamic slip curves of 17600, 18330, and 21000 BTU/hr compressors respectively.

The second step is to determine the slopes of each plotted dynamic slip curves at three specific points, where the compressor slip equals unity (at standstill), critical slip, and nominal steady-state slip. For each compressor under test, three equations were obtained when applying three values of slope $\left(\frac{dS}{dt}\right)$, electrical torque ($T_e$), and slip (S) in the following dynamic equation (4.18):

$$\frac{dS}{dt} = \frac{\left[A*(1-S)^2 + B*(1-S) + C\right] - T_e}{2*H} \qquad (4.18)$$

where A = quadratic mechanical torque coefficient (pu).

B = linear mechanical torque coefficient (pu).

C = constant mechanical torque coefficient (pu).

H = compressor load inertia constant (pu).

T_e = compressor electrical torque.

At the same above mentioned slip values, the corresponding compressor electrical torque values are calculated from the following equation (4.19), based on the electrical parameters of each tested compressor:

$$T_e = \frac{\left(\frac{X_m}{|Z_o|}\right)^2 * \frac{r_2}{S} * V_{ph}^{\ 2}}{\left(R_{th} + \frac{r_2}{S}\right)^2 + \left(X_{th} + x_2\right)^2} \qquad (4.19)$$

where V_{ph} = terminal phase voltage = 1 pu.

Z_o = open-circuit impedance = $r_1 + (x_1 + X_m)$

Z_{th} = Thevenin equivalent impedance = $[(r_1 + x_1)* X_m]/ (r_1 + x_1 + X_m)$

R_{th} = real part of Z_{th}

X_{th} = imaginary part of Z_{th}

The electrical torque can also be graphically extracted from the electrical torque-speed characteristics of each compressor. By solving the resulting three equations simultaneously, the mechanical torque coefficients (A, B, and C) were obtained for each compressor under test. Figures (4.11), (4.12), and (4.13) illustrate the electrical and mechanical torque-speed characteristics of the 17600, 18330, and 21000 BTU/hr compressors respectively.

An average value of each coefficient was calculated based on the defined torque coefficients of the above mentioned compressors in order to represent the mechanical torque characteristics of the aggregated single-phase A/C compressor. Figure (4.14) illustrates the mechanical torque-speed characteristics of the individual compressors as well as for the aggregated compressor model. Appendix (D-2) includes the calculation procedure and details of the above definition method.

4.4.2 - Advantages and shortcomings:

The above detailed method is simple, efficient, and can generally be applied to any type of motor-driven mechanical load, such as pumps and fans, etc. On the other hand, this method has a major disadvantage, where the slopes of different dynamic slip curves at similar slip values may widely vary. Mainly, this is due to variations in performance efficiencies, related to design parameters, refrigeration capacities, and aging effects.

This criteria was found true in case of similar A/C compressor models under test as well. If two motors are originally built for identical shaft loads, they may show very different characteristics because of aging effects [46]. Therefore, while practicing the new method, the following considerations were found necessary in order to ensure best precision of obtained results:

1) All dynamic slip curves must be plotted to the same scale.

2) The starting current must be recorded for several compressors of the same model. Then, the average of similar slopes' values is calculated to minimize possible tolerances in results due to the above mentioned reasons.

4.4.3 - Results analysis:

At unity and critical slip, slopes of dynamic slip curves have negative values, since the compressor slip is decreasing at starting until it reaches nominal steady-state. However, the compressor slip may not reach unity at starting. Therefore, as an approximation, the curve slope (dS/dt) was set to equal zero in the dynamic equation at unity slip. The resulting mechanical torque coefficients of single-phase compressor load were close in their magnitude but with different signs (A negative, B positive), whereas the constant torque coefficient (C) was less than unity. The mechanical torque coefficients of the aggregated compressor model may be tuned through sensitivity analysis, so as the nominal mechanical torque (T_m) equals 1 pu.

A *reverse* dynamic slip curve can be obtained based on the recorded compressor current when it is switched-off. In this case, the compressor dynamic slip will increase from steady-state value until it reaches unity at complete stop, and curve slopes can be determined as detailed in the previous section.

It was found that the reverse dynamic slip curve cannot be used instead of the dynamic slip curve obtained from the compressor starting to determine its mechanical torque coefficients due to the following reasons:

1) The mechanical torque characteristics of compressor load must be determined in steady-state condition, as in case of compressor starting.

2) The magnitude of slip increase rate while switching-off the compressor is quite different and higher than the magnitude of slip decrease rate during starting. This is due to the large difference in the internal gas pressure during both starting and switching-off cases.

3) It is physically accepted to apply the compressor starting electrical torque (T_e) in the dynamic equation only in case of the compressor starting (S = 1), but not in the switching-off case.

Earlier references assumed that the dynamic load mechanical torque is constant during steady-state and transient conditions [24,25,26,27]. In Chapter 3, it was shown in figures (3.8-a & b) that the calculated compressor load active power (P), based on current and voltage measurement during transient simulation test, was nearly constant. Accordingly, the compressor mechanical torque increases during transients since it is inversely proportional to the decreased compressor speed.

On the other hand, the compressor electrical torque decreases due to its dependence on the reduced system voltage. This large difference between both mechanical and electrical torque clearly justifies the sudden braking effect exerted on the compressor load during transients, and which would not occur if the compressor mechanical torque was constant as stated in earlier references.

Figure (4.15) illustrates the electrical and mechanical torque-speed characteristics of the new aggregated compressor model and an earlier published EPRI single-phase A/C load model. Accordingly, it was found that the mechanical torque characteristics of the EPRI model is not matching with the actual transient load response. Therefore, the earlier dynamic load model induces distinctive errors in the system dynamic simulations.

4.5 - Proposal for a new dynamic load model:

In hot areas, single-phase A/C compressors form a large percentage of dynamic load connected to the power system. Therefore, it is proposed to build up a new 3-motor model in order to be used in system simulations. The new model has a similar structure to the earlier detailed 2-motor model with one modification only, where the *"prone-to-stall"* motors group is further divided into *"compressor"* and *"non-compressor"* sub-groups of motors.

The *"compressor"* sub-group will include low-inertia motors of compressor type, such as refrigerators, freezers, and air-conditioners. The *"non-compressor"* sub-group will include other types of low-inertia motors like dishwashers, washing machines, fans, etc. Appendix (A) includes the building-up procedure of the newly proposed 3-motor model. Figure (4.16) illustrates the simulated electrical torque-speed characteristics of different models, where the proposed 3-motor model showed an improved accuracy over other models towards the composite motor model.

4.6 - Conclusions:

The design of single-phase A/C compressor load was detailed in this chapter, as one of the most important and highly concentrated dynamic loads in warm countries. Electrical parameters of three different single-phase A/C compressors were determined in laboratory by means of DC, no-load, and locked-rotor tests.

Since it was impossible to measure the actual speed of hermetic compressor, therefore, a mathematical formula was derived in order to determine an approximate and satisfactory value of the compressor slip. Comparison between the simulated electrical torque-speed characteristics of the above mentioned compressors and an earlier published A/C load model showed similarity in their design, and proved accuracy of their identified parameters.

The most important topic covered in this chapter was the description of a new method for the definition of mechanical torque characteristics of the single-phase A/C compressor load. Advantages and shortcomings of the new methodology were discussed, where the newly defined mechanical torque characteristics was satisfactorily matching with the actual behavior of the single-phase compressor load during steady-state and transient conditions. The newly defined compressor mechanical torque characteristics will be included in a new dynamic load model in order to simulate specific disturbance events, which have occurred in the Abu Dhabi power system in recent years.

Chapter 4

Due to the high percentage contribution of the single-phase A/C compressor load in hot areas, and due to the unique mechanical torque characteristics of such load compared to other motor-driven mechanical loads, a new 3-motor model is proposed in this chapter. The new dynamic model is based on the segregation of low-inertia motors, called as *"prone-to-stall"* motors in the earlier published 2-motor model, into *"compressor"* and *"non-compressor"* sub-groups of motors.

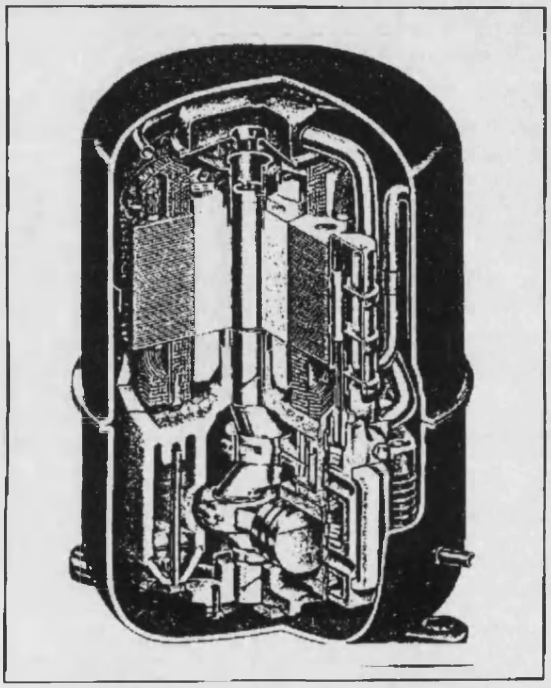

Figure (4.1) Hermetic single-phase A/C compressor.

(Courtesy of *Tecumseh Products Co.*)

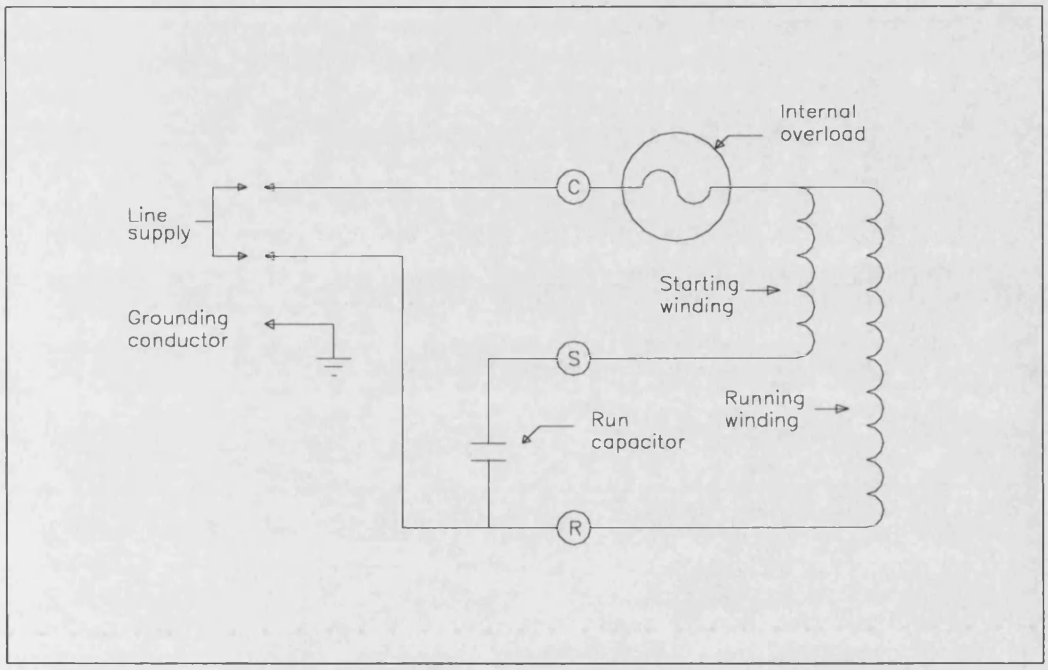

Fig (4.2) Typical schematic wiring diagram of the single-phase A/C compressor.

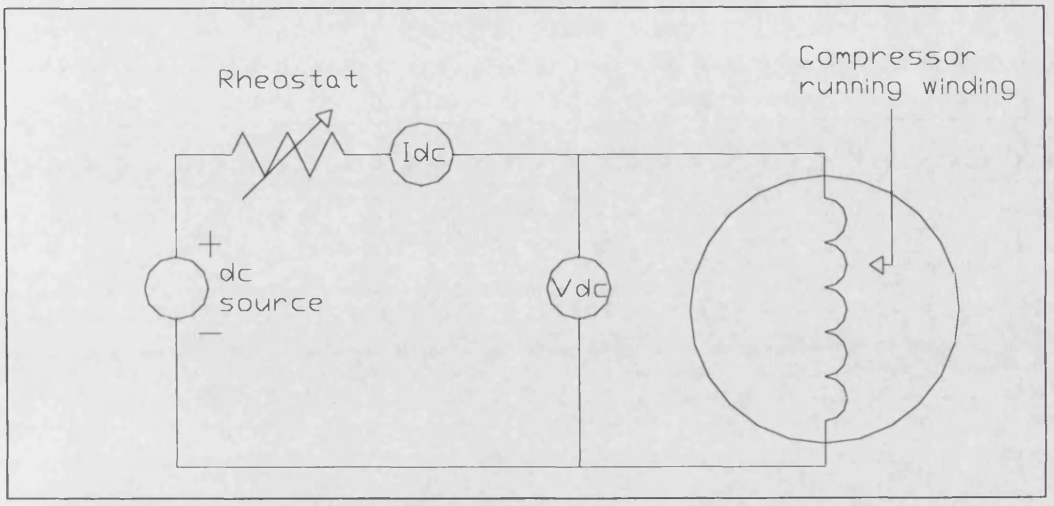

Fig (4.3) DC test circuit.

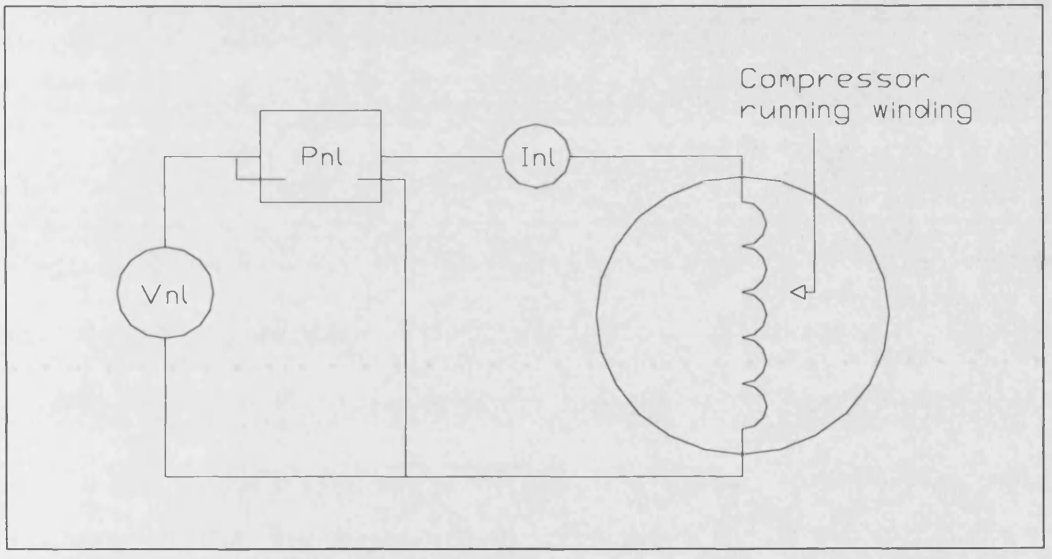

Fig (4.4) No-load test circuit.

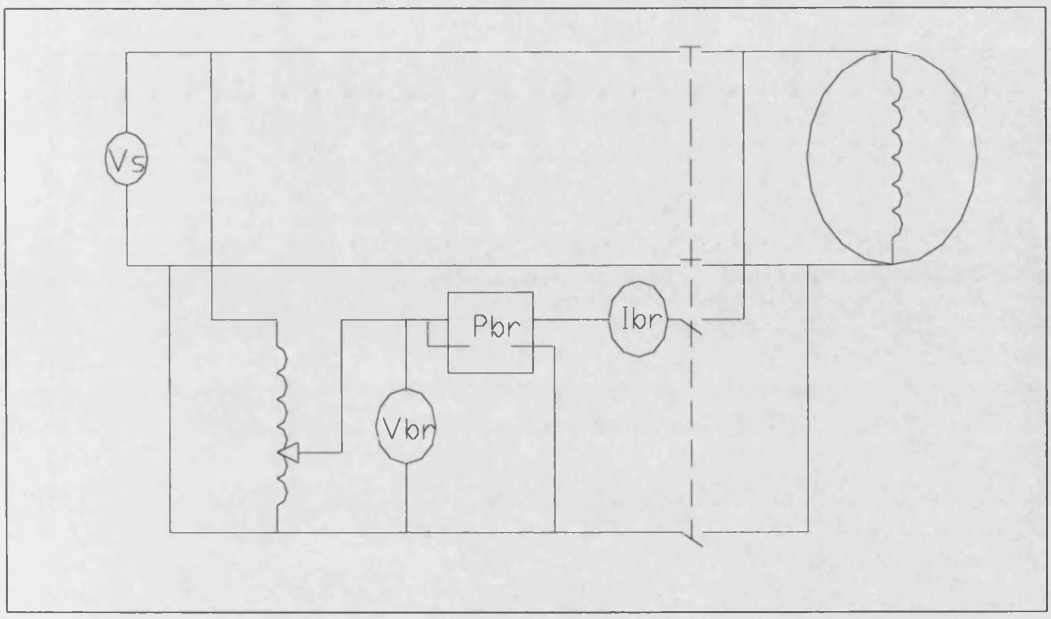

Fig (4.5) Locked-rotor test circuit.

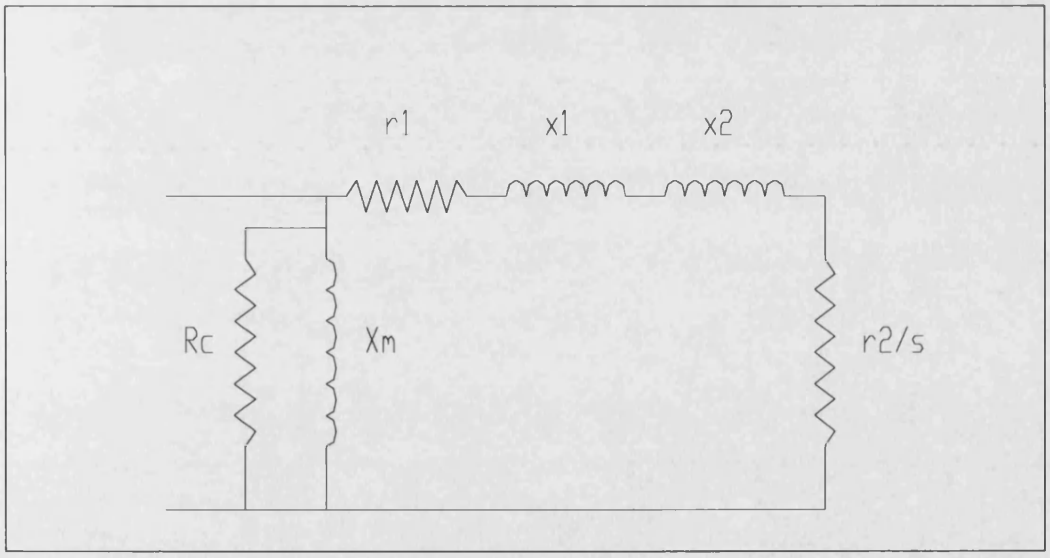

Fig (4.6) Approximate induction motor equivalent circuit.

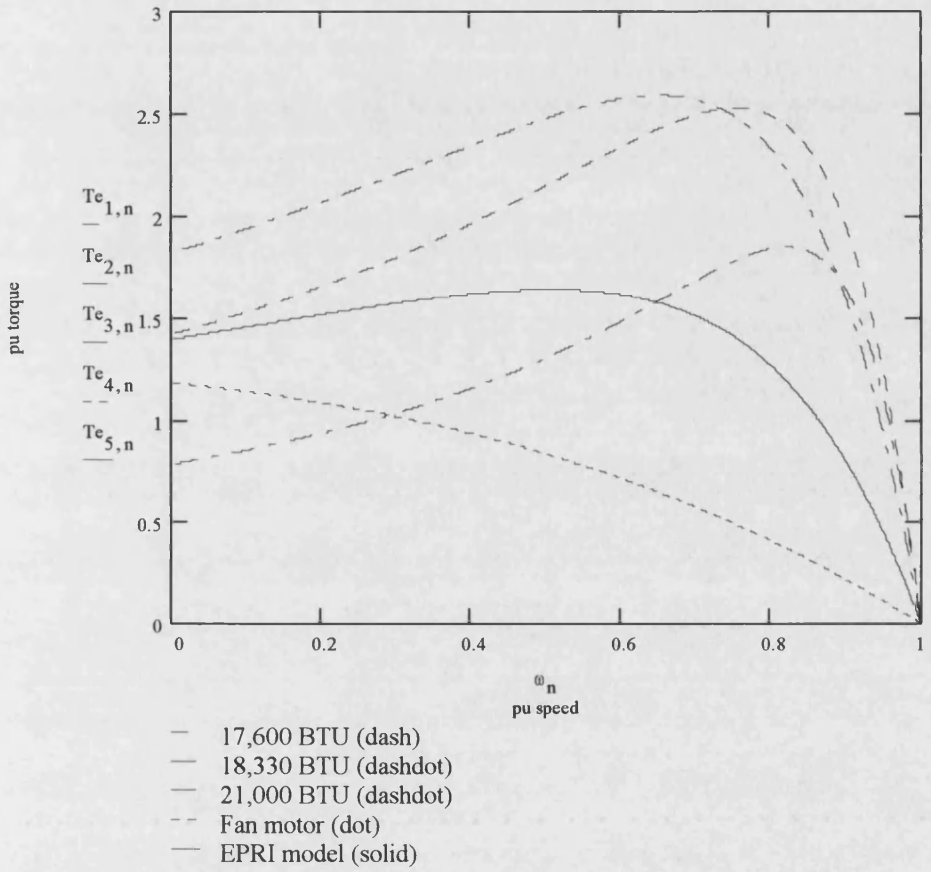

Fig (4.7) Electrical torque-speed characteristics of the three tested compressors, the condenser fan motor, and EPRI single-phase A/C model.

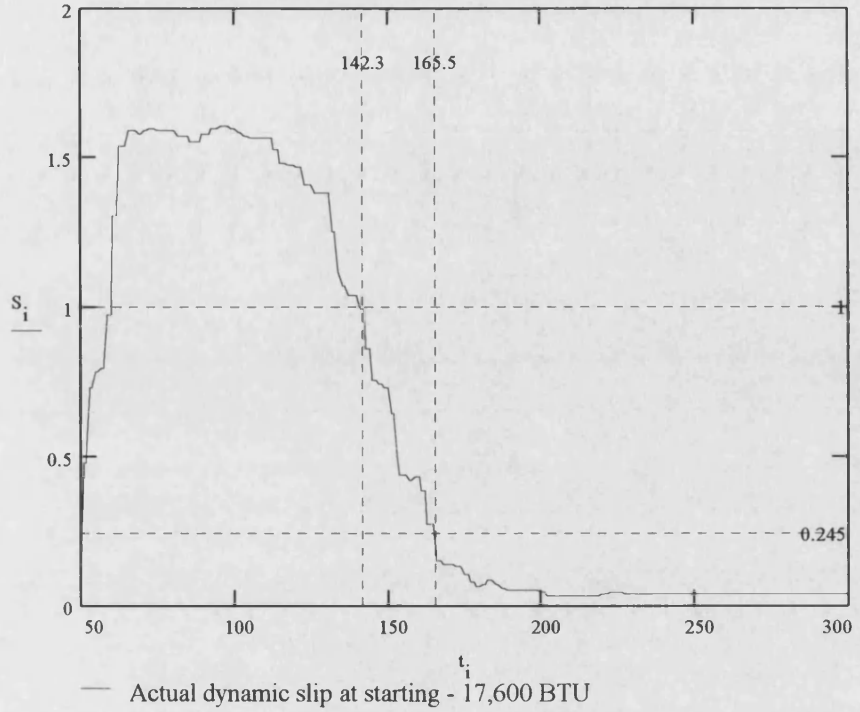

Fig (4.8) Dynamic slip curve at starting of 17,600 BTU/hr compressor.

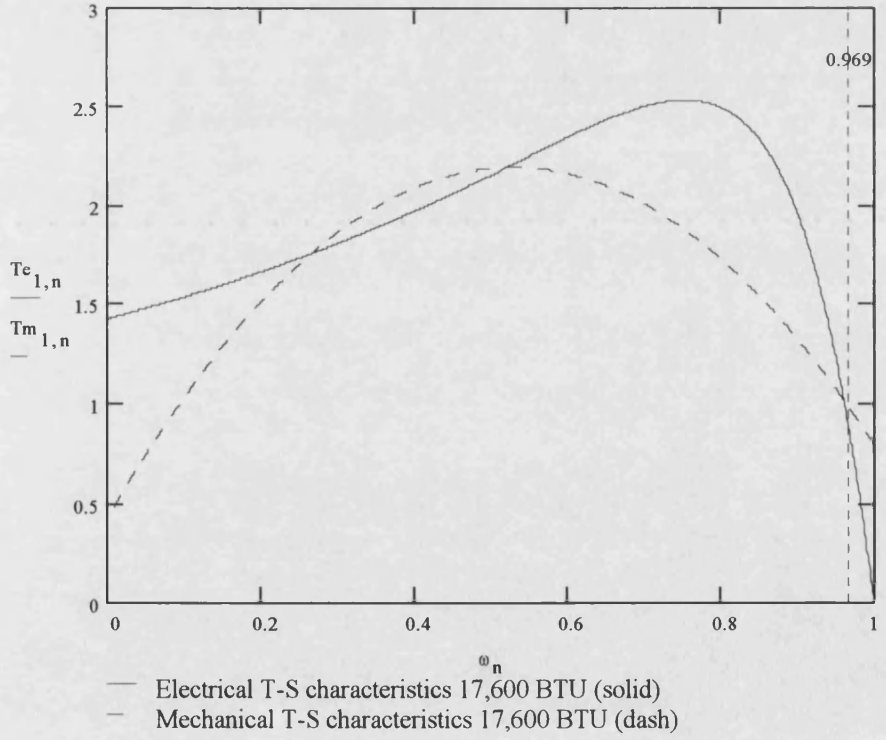

Fig (4.11) Electrical and mechanical T-S characteristics of 17,600 BTU/hr compressor.

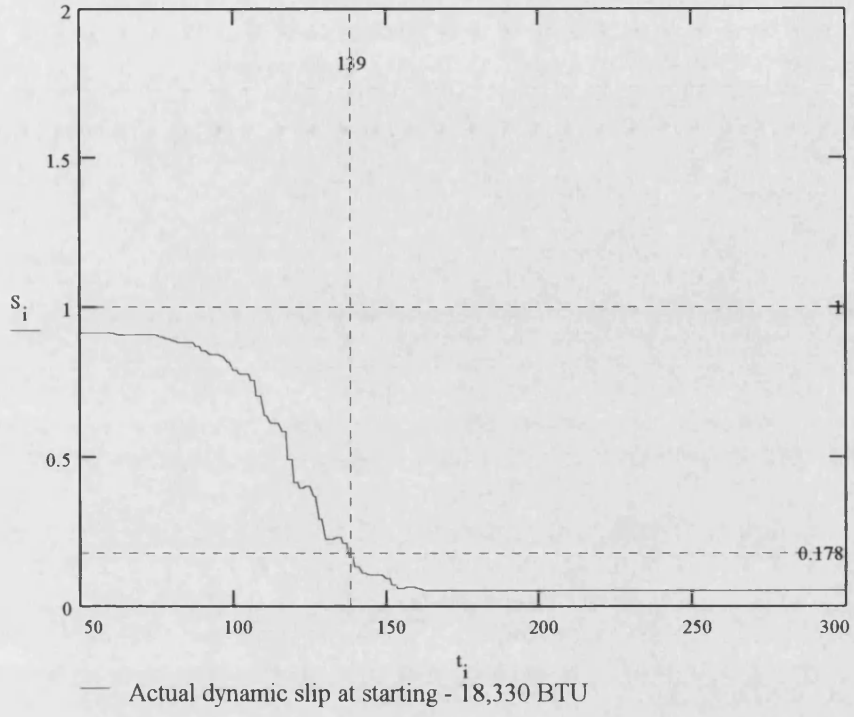

Fig (4.9) Dynamic slip curve at starting of 18,330 BTU/hr compressor.

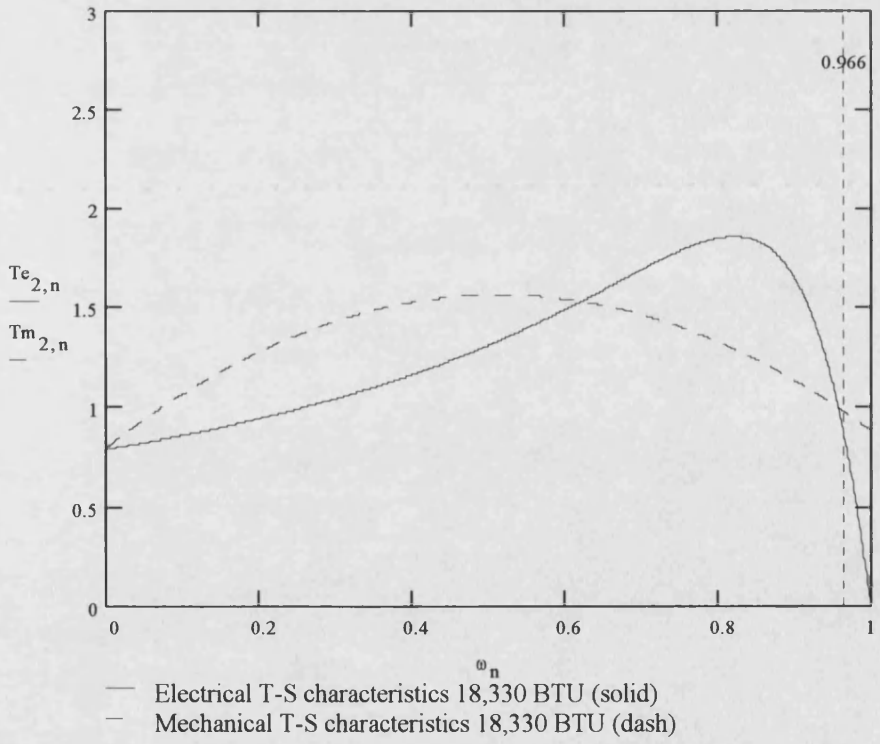

Fig (4.12) Electrical and mechanical T-S characteristics of 18,330 BTU/hr compressor.

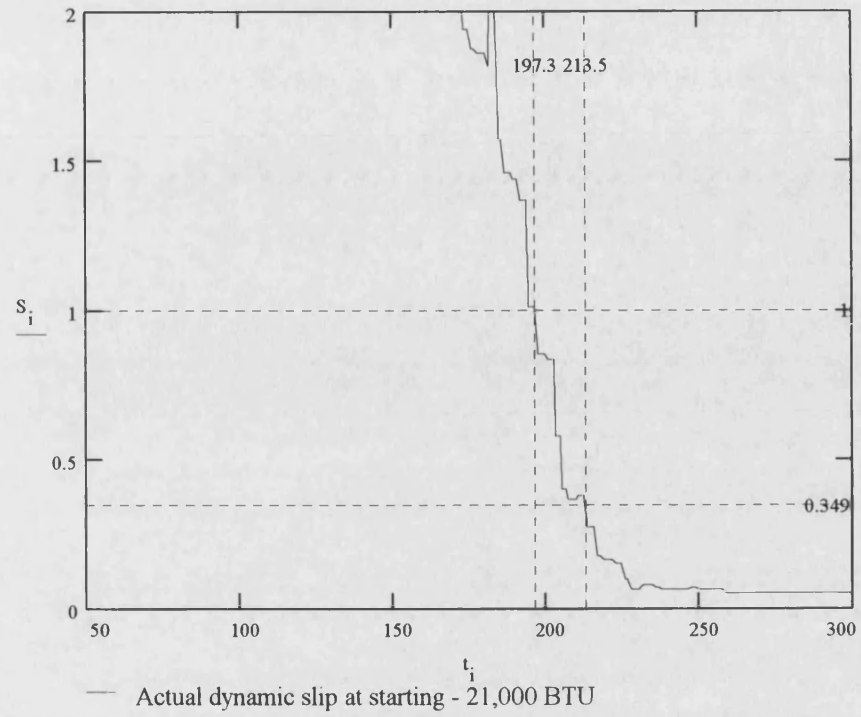

Fig (4.10) Dynamic slip curve at starting of 21,000 BTU/hr compressor.

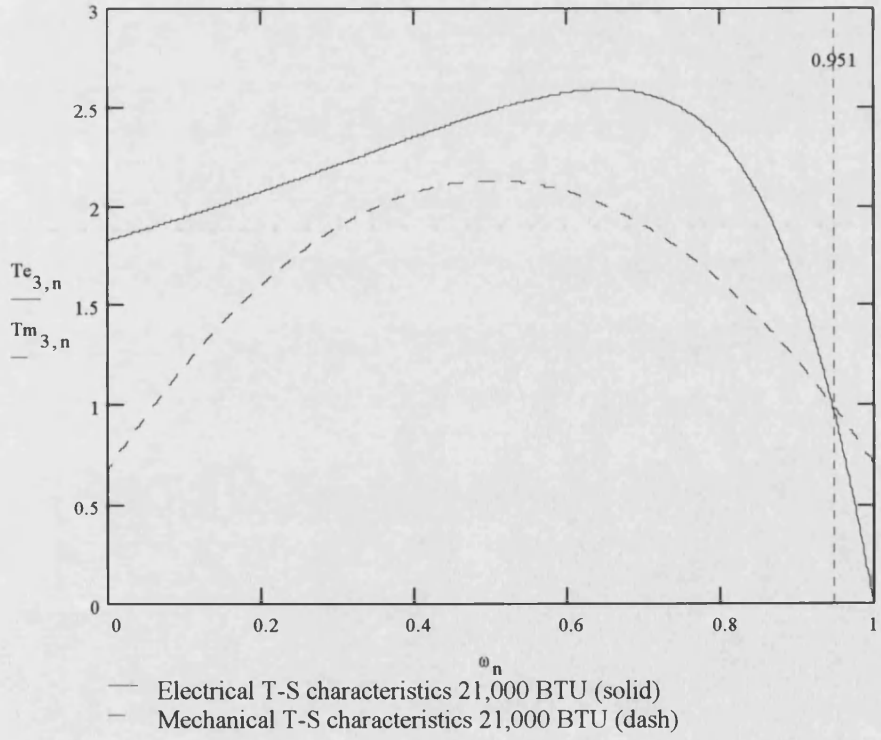

Fig (4.13) Electrical and mechanical T-S characteristics of 21,000 BTU/hr compressor.

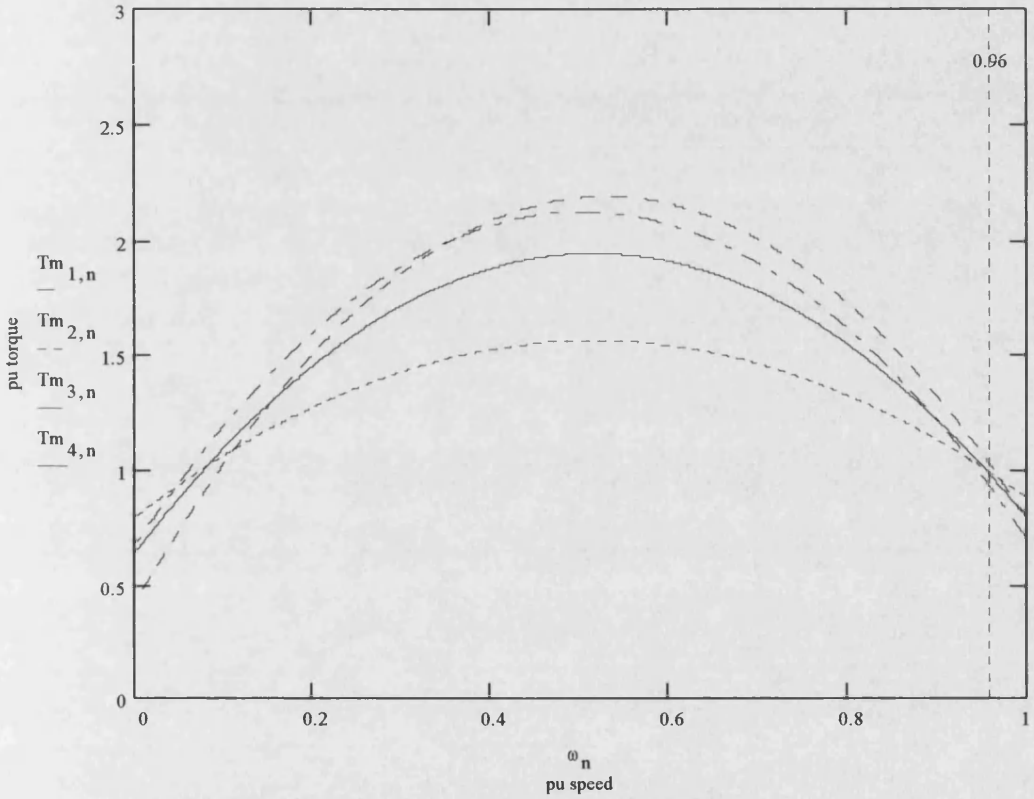

Fig (4.14) Mechanical torque-speed characteristics of the tested and aggregated compressors.

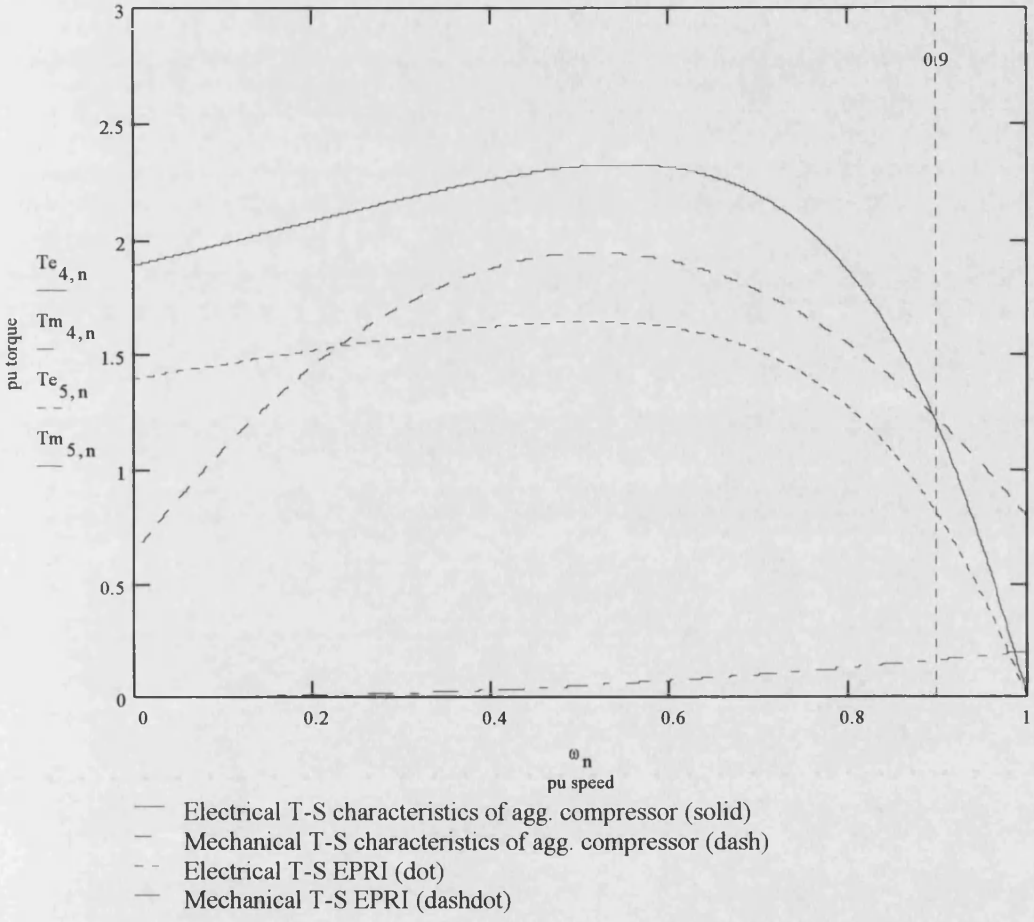

Fig (4.15) Electrical and mechanical T-S characteristics of the aggregated compressor and EPRI single-phase A/C model.

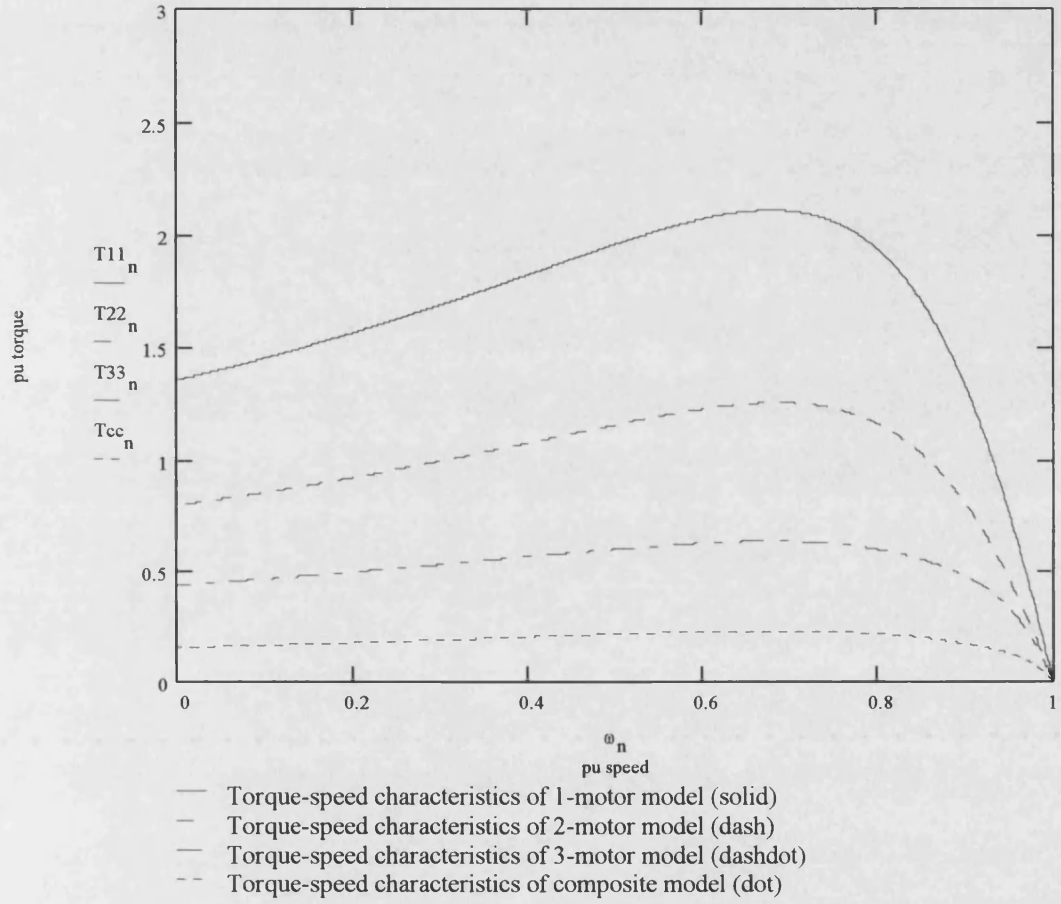

Fig(4.16) Electrical T-S characteristics of 1-motor, 2-motor, 3-motor, and the composite motor model.

CHAPTER 5

Simulation of Test Circuit

5.1 - Introduction :

Dynamic characteristics of motor load can be reasonably represented by ordinary nonlinear differential equations [46]. The mathematical model of single-phase compressor load consists of two nonlinear first-order differential equations, which are based on the induction motor equivalent circuit.

The single input to the compressor induction motor model is the recorded compressor voltage, which is the forcing function exerting dynamic variations in this system, while the two unknown model outputs are the compressor stator current and its motor slip. The commercial mathematical software (Mathcad 5.0) was used herein to analyze the test results, by simulating the transient simulation test circuit and object, and therefore, to produce comparable results to the original test data.

The compressor stator current, which is one of the model outputs, is compared with the recorded compressor current during the test. Sensitivity analysis is conducted in this chapter to prove the compressor motor model parameters, including the simulation of the newly-defined compressor mechanical torque characteristics. The compressor motor model, simulated herein, will be further utilized in the fully-pledged stability analysis program.

5.2 - Dynamic model of single-phase compressor:

5.2.1- Differential equations:

The following differential equations (5.1) and (5.2), representing the single-phase A/C compressor load, are derived herein based on the IM equivalent circuit illustrated in figure (5.1):

$$r_1 * i_1 + (x_1 + X_m) * \frac{di_1}{dt} - X_m * \frac{di_2}{dt} = V \qquad (5.1)$$

$$\frac{r_2}{S} * i_2 - X_m * \frac{di_1}{dt} + (x_2 + X_m) * \frac{di_2}{dt} = 0 \qquad (5.2)$$

where i_1 = stator current. r_1= stator resistance.

i_2 = rotor current. x_1= stator reactance.

V= compressor terminal voltage. r_2= rotor resistance.

X_m= magnetizing reactance. x_2= rotor reactance.

From equation (5.2), $\left(\frac{di_2}{dt}\right)$ is given by equation (5.3):

$$(x_2 + X_m) * \frac{di_2}{dt} = X_m * \frac{di_1}{dt} - \frac{r_2}{S} * i_2$$

$$\therefore \frac{di_2}{dt} = \frac{X_m}{(x_2 + X_m)} * \frac{di_1}{dt} - \left(\frac{r_2/S}{x_2 + X_m}\right) * i_2 \qquad (5.3)$$

Substituting $\left(\frac{di_2}{dt}\right)$ of equation (5.3) in equation (5.1), we get equation (5.4):

$$r_1 * i_1 + (x_1 + X_m) * \frac{di_1}{dt} - X_m * \left[\frac{X_m}{x_2 + X_m} * \frac{di_1}{dt} - \frac{r_2/S}{x_2 + X_m} * i_2\right] = V$$

$$\therefore r_1 * i_1 + \left[x_1 + X_m - \frac{X_m^2}{x_2 + X_m}\right] * \frac{di_1}{dt} + \frac{X_m * r_2/S}{x_2 + X_m} * i_2 = V \qquad (5.4)$$

where the compressor rotor current is given by equation (5.5):

$$i_2 = i_1 * \frac{X_m}{X_m + x_2 + r_2/S} \qquad (5.5)$$

By substituting (i_2) of equation (5.5) in (5.4), then, $\left(\frac{di_1}{dt}\right)$ is given by equation (5.6):

$$\therefore \left[x_1 + X_m - \frac{X_m^2}{x_2 + X_m}\right] * \frac{di_1}{dt} + \left[r_1 + \frac{X_m^2 * r_2/S}{(x_2 + X_m) * (x_2 + X_m + r_2/S)}\right] * i_1 = V$$

$$\frac{di_1}{dt} = \frac{-\left[r_1 + \frac{X_m^2 * r_2/S}{(x_2 + X_m) * (x_2 + X_m + r_2/S)}\right]}{\left[x_1 + X_m - \frac{X_m^2}{x_2 + X_m}\right]} * i_1 + \frac{1}{\left[x_1 + X_m - \frac{X_m^2}{x_2 + X_m}\right]} * V \quad (5.6$$

Equation (5.6) is the first differential equation governing the single-phase

compressor load. The second differential equation representing the compressor load is the following IM dynamic equation (5.7):

$$\frac{dS}{dt} = \frac{T_m - T_e}{2 * H} \qquad (5.7)$$

where the compressor mechanical torque is given by equation (5.8):

$$T_m = A * (1-S)^2 + B * (1-S) + C \qquad (5.8)$$

and the compressor electrical torque is given by equation (5.9):

$$T_e = i_2^2 * r_2/S = \left[i_1 * \frac{X_m}{X_m + x_2 + r_2/S} \right]^2 * r_2/S \qquad (5.9)$$

By substituting equations (5.8) and (5.9) in equation (5.7), then, $\left(\frac{dS}{dt}\right)$ is given by the following equation (5.10):

$$\frac{dS}{dt} = \frac{\left[A * (1-S)^2 + B * (1-S) + C \right] - \left[i_1 * \frac{X_m}{x_2 + X_m + \frac{r_2}{S}} \right]^2 * \frac{r_2}{S}}{2 * H} \qquad (5.10)$$

5.2.2 - Runge-Kutta solution:

The compressor load model is represented by the above differential equations (5.6) and (5.10), which are functions of the compressor electrical parameters, the mechanical torque coefficients, and the compressor load inertia, which were previously identified in Chapter 3. The compressor terminal voltage is the model input, while the compressor motor slip, and the stator current are the model outputs.

Both differential equations are solved herein by using the 4th order Runge-Kutta method, which is generally considered by the following two first-order nonlinear differential equations [50,51]:

$$x' = f(t,x,y),$$
$$y' = g(t,x,y),$$

and where the initial conditions are:

$$x(t_o) = x_o$$

$$y(t_o) = y_o$$

The Runge-Kutta equations involve a weighted average of the values of $f(x,y)$ and $g(x,y)$ taken at different points in the interval $t_n \le t \le t_{n+1}$, which are given by the following equations (5.11) and (5.12)

$$x_{n+1} = x_n + \frac{h}{6} * [k_{n1} + 2 * k_{n2} + 2 * k_{n3} + k_{n4}] \qquad (5.11)$$

$$y_{n+1} = y_n + \frac{h}{6} * [l_{n1} + 2 * l_{n2} + 2 * l_{n3} + l_{n4}] \qquad (5.12)$$

Therefore, by substituting (x) and (y) in the above equations (5.11) and (5.12) with the compressor stator current (i_1) and motor slip (S), the Runge-Kutta solution of the compressor system differential equations (5.6) and (5.10) are given by equations (5.13) and (5.14):

$$i_{n+1} = i_n + \frac{h}{6} * [k_{n1} + 2 * k_{n2} + 2 * k_{n3} + k_{n4}] \qquad (5.13)$$

$$S_{n+1} = S_n + \frac{h}{6} * [l_{n1} + 2 * l_{n2} + 2 * l_{n3} + l_{n4}] \qquad (5.14)$$

The initial weighted average constants (k_{01}) to (k_{04}) and (l_{01}) to (l_{04}) are calculated, based on equations (5.6) and (5.10) respectively. Then, (i_{n+1}) and (S_{n+1}) are calculated, based on the calculated initial constants (k_{01}) to (k_{04}) and (l_{01}) to (l_{04}), and on the initial values of the compressor stator current and slip. The iteration step size (h) is set at 0.001 in order to match the sampling rate of the digitized recorded compressor voltage and current signals during the test.

The compressor terminal voltage recorded during the test, which is the forcing function in these equations, is fed to the mathematical software as a digital input recorded in a spreadsheet form. The digital values of the recorded compressor current are similarly fed to the software, so that its plotted dynamic curve is compared with that of the simulated compressor stator current. Appendix (F) includes the solution procedure of the compressor model differential equations, as well as the comparison between the recorded and model simulated compressor stator current.

5.2.3 - Calculation errors:

There are two fundamental sources of error in solving an initial value problem numerically [50,51]. The first is the *local truncation error* (E_n), which is the difference between the exact and approximate solution of the initial value problem. This error arises from using an approximate formula at each solution step. The second is the *round-off error* (R_n), which is the difference between the exact and actually computed solution given by the numerical procedure. This error arises due to the lack of computational accuracy. The total error resulting from the numerical procedure is bounded by the sum of the absolute values of the truncation and round-off errors.

When the 4th order Runge-Kutta method is used, the local truncation error (E_n), accumulated over a finite time interval, is proportional to h^5. Therefore, if the iteration step size (h) is decreased, the accumulated truncation error (E_n) will be decreased. However, if the step size (h) is too small, too many steps will be required to cover a fixed interval, and the accumulated round-off error (R_n) may be larger than the accumulated truncation error (E_n) . Accordingly, the round-off error (R_n) is inversely proportional to the step size (h).

The step size (h) is optimum when both local truncation error and round-off error are approximately equal in magnitude, as shown in figure (5.2). In this solution procedure, the iteration step size (h) is set at 0.001, so that the simulated compressor stator current values will correspond to the recorded compressor current values, sampled at a rate of 0.001 second.

5.3 - Simulation results:

The *"seeded iteration"* feature of MathCAD software is a recursive technique used for solving difference equations [52]. This technique is used in Appendix (F) to obtain approximate solutions for the above mentioned differential equations of the single-phase A/C compressor model. In a seeded iteration, the first element of an array is specified, and then, successive elements are computed, based on the first element.

The MathCAD vector notation is used to iterate several variables simultaneously, which are in this case, the weighted average constants of Runge-Kutta method (k_1) to (k_4) and (l_1) to (l_4), the compressor stator current (I_1), and the slip (S). This variation in simple seeded iteration is a powerful method for solving a system of simultaneous difference equations. When several variables are iterated, each step computes the value of the variables from all of their previous values.

The initial values of these variables are defined as the zeroth elements of the seed values array, which is a (10 x 1) vector, and the variables equations are grouped in a matrix form to be solved simultaneously. The most important thing about this technique is that all variables with (i+1) subscripts are on the left-hand side of the matrix equation, while the right-hand side contains only variables with subscript (i). The mathematical software evaluates all the expressions on the right-hand side before performing any assignments to the left-hand side. This means that nothing on the right-hand side can depend on something of the left-hand side of the matrix equation.

The following six test cases were selected for simulation from the 17,600 BTU/hr compressor test data, comprising three stalling cases and the corresponding three non-stalling cases:

Test case #	*Compressor status*	*Test voltage (V) pu*	*Dist. reactance (X_d) pu*	*Clearing time (t) seconds*
465	non-stalling	0.72	0.2	0.190
466	stalling	0.72	0.2	0.196
491	non-stalling	0.72	0.1	0.242
488	stalling	0.72	0.1	0.256
530	non-stalling	0.70	0.1	0.208
531	stalling	0.70	0.1	0.218

For each of the above mentioned six cases, the simulated compressor stator current, is dynamically plotted for comparison against the recorded compressor stator current. Figures (5.3) to (5.8) illustrate the dynamic curves of the simulated and recorded compressor current for the six selected cases.

From the illustrated simulations of the above cases, it was found that the model function has slowly varied during the 80 milliseconds period following the instant of fault occurrence, while the recorded compressor current has quickly overshot to higher values and returned to 1.5 pu of its initial value during the same period.

During the period between 150 and 400 milliseconds of the dynamic simulation, the model function has varied faster than in earlier period, while the recorded current has varied at a slower rate. Both simulated and recorded current are satisfactorily matching each other during this period.

In the stalling cases, the simulated compressor current has greatly matched the recorded current during the test. However, in the non-stalling cases, the simulated compressor current has slowly changed during the post-fault period. It has stabilized to its initial pre-fault value of 1 pu after a time delay of nearly 100 milliseconds, when compared to the recorded compressor current, which has directly stabilized after fault clearance.

The above mentioned differences between the simulated and recorded compressor current were observed due to the following reasons:

1) The total error resulting from the Runge-Kutta solution method.

2) The iteration step size (h).

3) The approximate solution of seeded iteration method.

5.4 - Sensitivity analysis:

One typical non-stalling compressor test case is selected in this section to perform sensitivity analysis on the model parameters to investigate their impact on the model simulation *(Case # 465: non-stalling compressor - $V = 0.72$ pu & $X_d = 0.2$ pu).*

5.4.1 - Variation of the compressor electrical parameters:

In the previous chapter, the compressors electrical parameters were identified through laboratory tests. The stator and rotor resistance were identified from DC and blocked-rotor tests, while the stator and rotor reactance were identified as a proportion of the blocked-rotor reactance (X_{br}), based on the design class of the compressor split-phase motor. As been stated previously, the compressor split-phase motor is of design class "C", where the stator reactance is given as ($x_1 = 0.3 * X_{br}$) and the rotor reactance is given as ($x_2 = 0.7 * X_{br}$) respectively. The values of both reactance are changed to other proportions of (X_{br}) corresponding to different motor design classes as follows:

Stator reactance (x_1)	*Rotor reactance (x_2)*
$0.4 * X_{br}$	$0.6 * X_{br}$
$0.5 * X_{br}$	$0.5 * X_{br}$

Figures (5.9) and (5.10) illustrate the dynamic simulation of case # 465, while varying the stator and rotor reactance according to the above values in the table. Regarding the magnetizing reactance (X_m), it was identified while considering the core resistance (R_c). Therefore, in case of neglecting such resistance, the changed value of (X_m) is used in the test model, and figure (5.11) illustrates the dynamic simulation of the same case while using the new value of (X_m). Therefore, according to the above figures, the variations made in (x_1), (x_2), and (X_m) had no significant impact on the test model dynamic simulations.

5.4.2 - Variation of the compressor load inertia constant:

The compressor load inertia constant (H = 0.251 pu) was calculated previously, based on the approximate values of the weight of compressor rotating part, as well as its radius of gyration. Figure (5.12) and (5.13) illustrate the dynamic simulation of the above mentioned test case, while setting (H) at 0.2 pu and 0.3 pu in the test model respectively. According to these simulations, while setting (H = 0.2 pu) in the test model, the simulated compressor current has largely increased and did not stabilize to its initial pre-fault value after fault clearance. On the other hand, while setting (H = 0.3 pu) in the test model, the simulated compressor current has satisfactorily matched the recorded current curve. Therefore, it was concluded that changing the inertia constant (H) by ± 0.5 pu will have a distinctive impact on the model simulation, whether in contrasting or complying with the recorded test data.

5.4.3 - Variation of the compressor mechanical torque coefficients:

The newly-defined mechanical torque coefficients (A, B, and C) of the single-phase compressor load were varied one at a time in order to investigate their impact on the test model simulations.

5.4.3.1 - Variation of coefficient (A):

When the magnitude of the negative constant (A) was increased by 1% of its value, an improvement was observed in the test model simulation illustrated in figure (5.14), when compared to the reference case 465 simulation illustrated in figure (5.3). In this case, the simulated compressor current has stabilized faster than the recorded compressor current.

However, when the coefficient (A) was increased by 3% of its value, the simulated current curve shown in figure (5.15) has become more steeper, where it stabilized faster than in the former case of 1% increment.

5.4.3.2 - Variation of coefficient (B):

Figures (5.16) and (5.17) illustrate the case 465 simulations, where the coefficient (B) was decreased by 1% and 3% of its value respectively. These simulations corresponded to the above simulations illustrated in figures (5.14) and (5.15), where by increasing the coefficient (A) by 1% of its value had the same impact on the test model simulation as decreasing the coefficient (B) by 1% of its value. Similarly, increasing the coefficient (A) by 3% of its value had the same impact on the test model simulation as decreasing the coefficient (B) by 3% of its value.

5.4.3.3 - Variation of coefficient (C):

Figures (5.18) and (5.19) illustrate the case 465 simulation, while varying the coefficient (C) by ± 5% respectively. As depicted from figure (5.18), when the coefficient (C) was increased by 5% of its value, the simulated compressor current has stabilized in a slower rate, compared to the simulated current of the reference case illustrated in figure (5.3). However, when the coefficient (C) was decreased by 5% of its value, the simulated current has shown an improved behaviour in figure (5.19), compared to the simulated current of the reference case illustrated in figure (5.3).

Figure (5.20) illustrates the same case 465 simulation, while using an earlier published mechanical torque coefficients [16] where A = 0.2 pu and B = C = 0. The simulated compressor current shown in this figure has totally mismatched the recorded

current. Therefore, the earlier published mechanical torque coefficients will definitely induce large errors when used in the system dynamic analysis.

5.4.4 - Variation of the Runge-Kutta step size:

The step size (h) was varied in the Runge-Kutta solution of the model differential equations in order to investigate its impact on the dynamic model simulations. Figures (5.21) to (5.24) illustrate the model simulations while setting (h) at 0.01, 0.005, 0.001, and 0.0001 respectively.

Figures (5.21) and (5.22) showed that the simulated compressor current has totally mismatched the recorded current during the test. The step size (h) of 0.01 and 0.005, which were used in these simulations, has enforced a faster rate of change of the model function, where the simulated current in both cases has continuously increased, while the recorded current has shown a different behavior.

In figure (5.23), the step size (h) was set at 0.001 as in the earlier mentioned reference case # 465. The simulated current has shown a great similarity compared to the recorded current, and the only difference observed was the instantaneous overshoot of the recorded current during the 20 milliseconds period following the instant of fault occurrence. However, the simulated current has shown a very small disturbance during the same period before starting its gradual increase, and then matching with the recorded current curve. In figure (5.24), the step size (h) was set at 0.0001, where the model simulation has totally mismatched the recorded test data, since (h) was too small and induced large errors in the model simulation.

5.5 - Conclusions:

In this chapter, the single-phase A/C compressor load model was described by two nonlinear differential equations. The first equation was derived from the induction motor equivalent circuit as a function in the compressor stator current and its derivative. The second differential equation was the IM dynamic equation, which was a function in the compressor electrical and mechanical torque. The compressor electrical torque was expressed in terms of its stator current, slip, and electrical parameters, while the compressor mechanical torque was a function in its slip and the new mechanical torque coefficients defined earlier in Chapter 3.

The two model equations were solved simultaneously by using the 4^{th} order Runge-Kutta method, where the compressor terminal voltage was the forcing function exerting dynamic variations in the model, and the compressor stator current and slip were the model outputs. The *"seeded iteration"* technique of MathCAD software was used to solve the model equations, and the simulations of the test circuit and compressor were compared to the data of six selected test cases. The test circuit model has proved its reliability in producing satisfactory simulations matching with the actual recorded test data, compared to simulations obtained from an earlier published dynamic model [16].

A sensitivity analysis was performed to investigate the impact of model parameters on the test model simulations. The variation of the compressor electrical parameters had no significant impact on the test model simulations, while the

compressor inertia constant (H) improved the model simulation when it was increased, proving that the high-inertia motors have good impact on the system stability, since they are robust enough and do not require high power during transients.

It was also found that the test model simulations have further improved when the mechanical torque coefficients were slightly tuned. The improvement in simulations were observed in case the mechanical torque coefficient (A) was increased by 1% of its value, or the coefficient (B) was decreased by 1% of its value, or the coefficient (C) was decreased by 5% of its value. The sensitivity analysis has also proved that the step size (h = 0.001) adopted herein was optimally chosen, so that it has reduced the total error of the Runge-Kutta solution and has produced a satisfactory model simulations compared to the test recorded data.

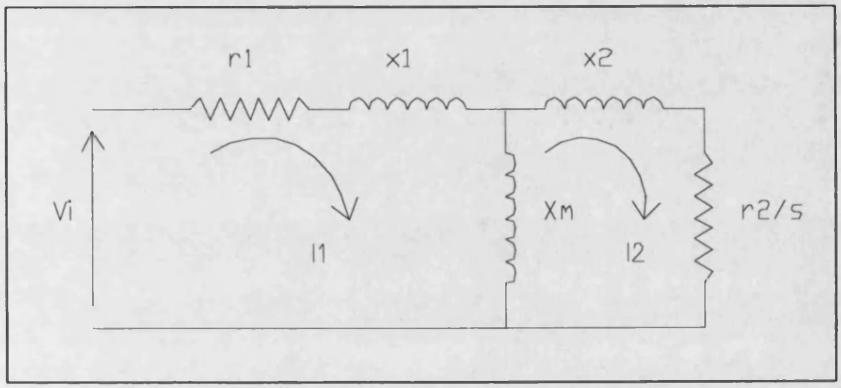

Fig(5.1) IM equivalent circuit.

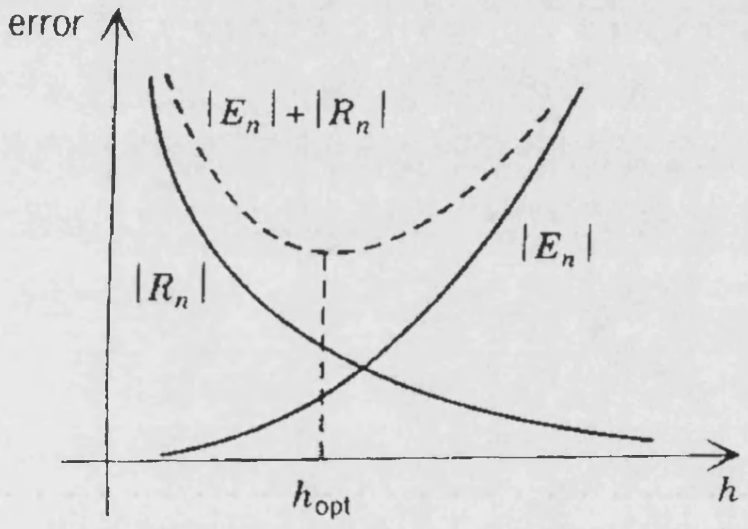

Fig(5.2) The dependence of truncation and round-off errors on the step size (h).

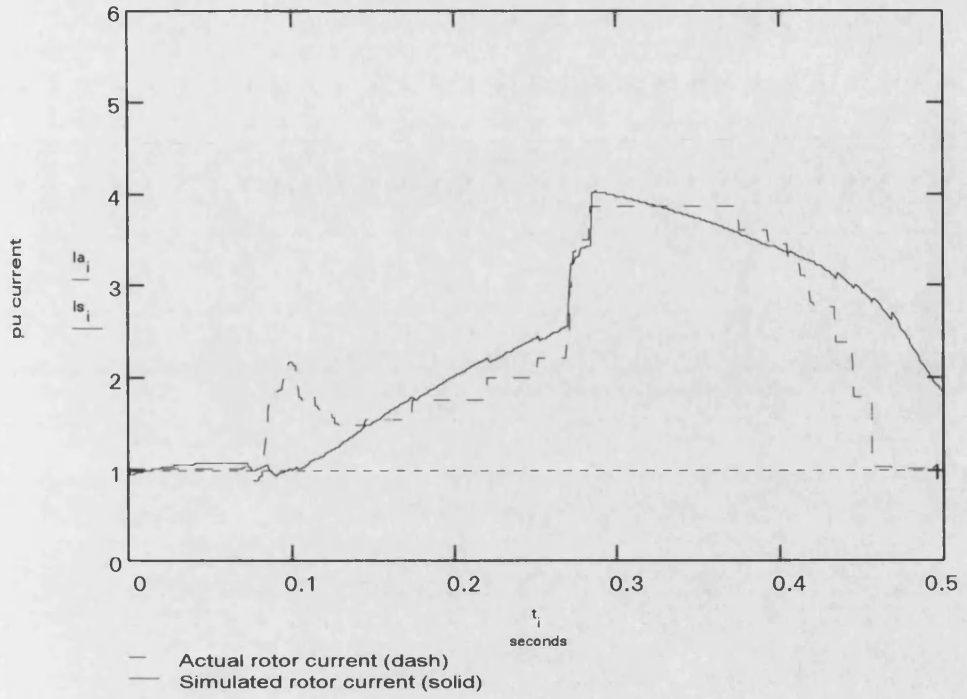

Figure (5.3) Test case # 465 - non-blocked compressor at V = 0.72 pu & X_d = 0.2 pu.

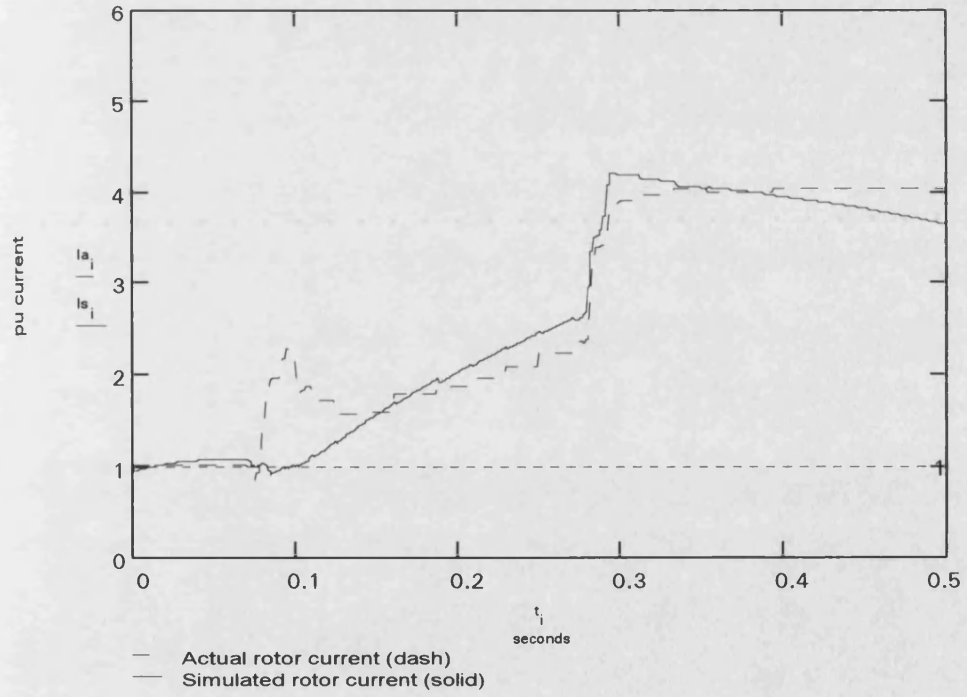

Figure (5.4) Test case # 466 - blocked compressor at V = 0.72 pu & X_d = 0.2 pu.

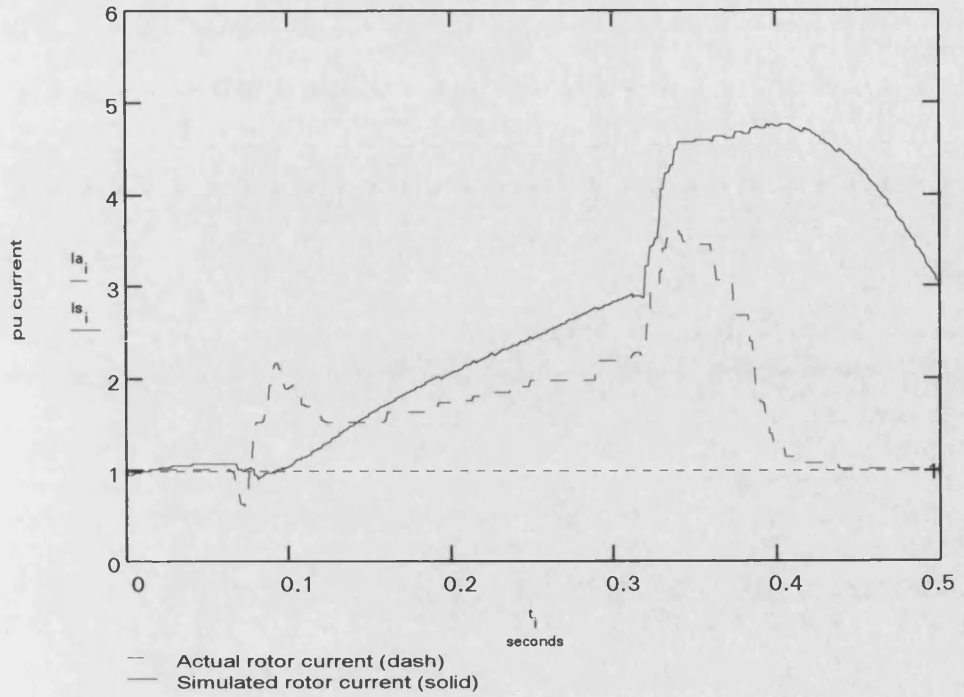

Figure (5.5) Test case # 491 - non-blocked compressor at V = 0.72 pu & X_d = 0.1 pu.

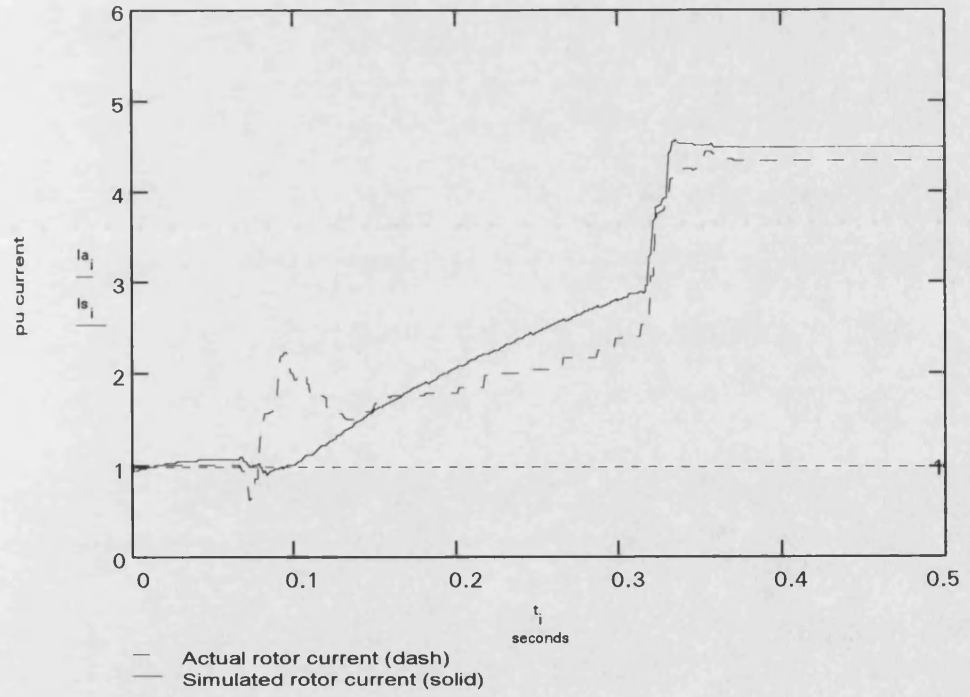

Figure (5.6) Test case # 488 - blocked compressor at V = 0.72 pu & X_d = 0.1 pu.

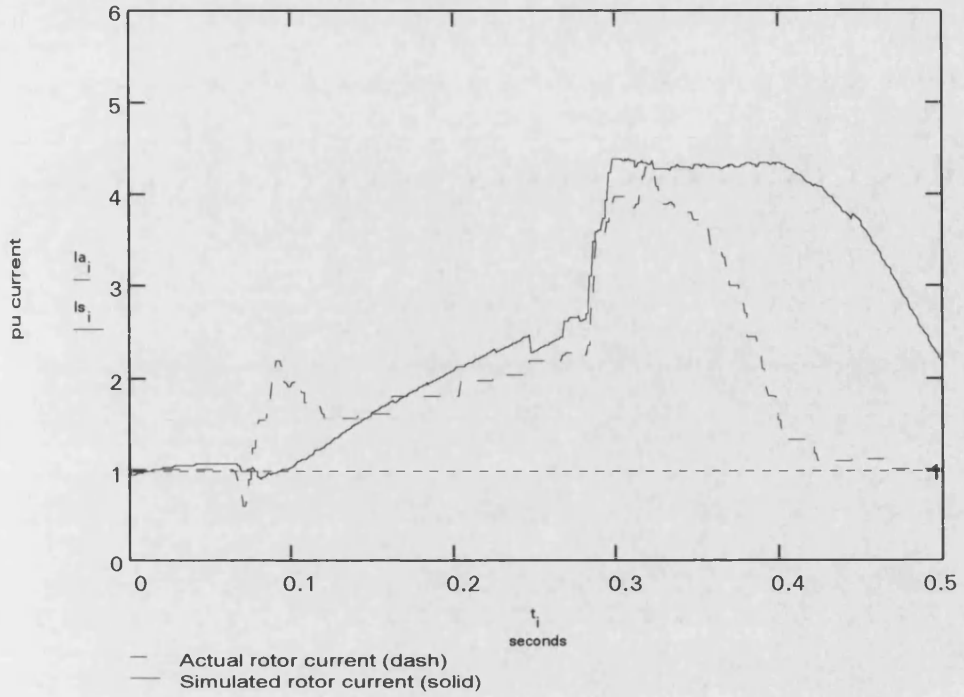

Figure (5.7) Test case # 530 - non-blocked compressor at V = 0.70 pu & X_d = 0.1 pu.

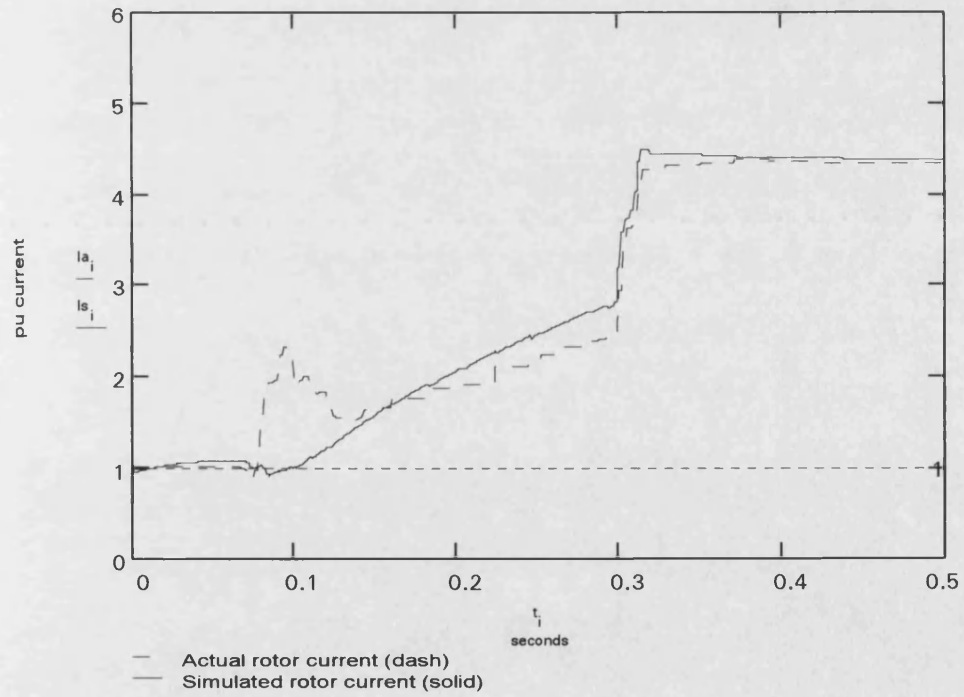

Figure (5.8) Test case # 531 - blocked compressor at V = 0.70 pu & X_d = 0.1 pu.

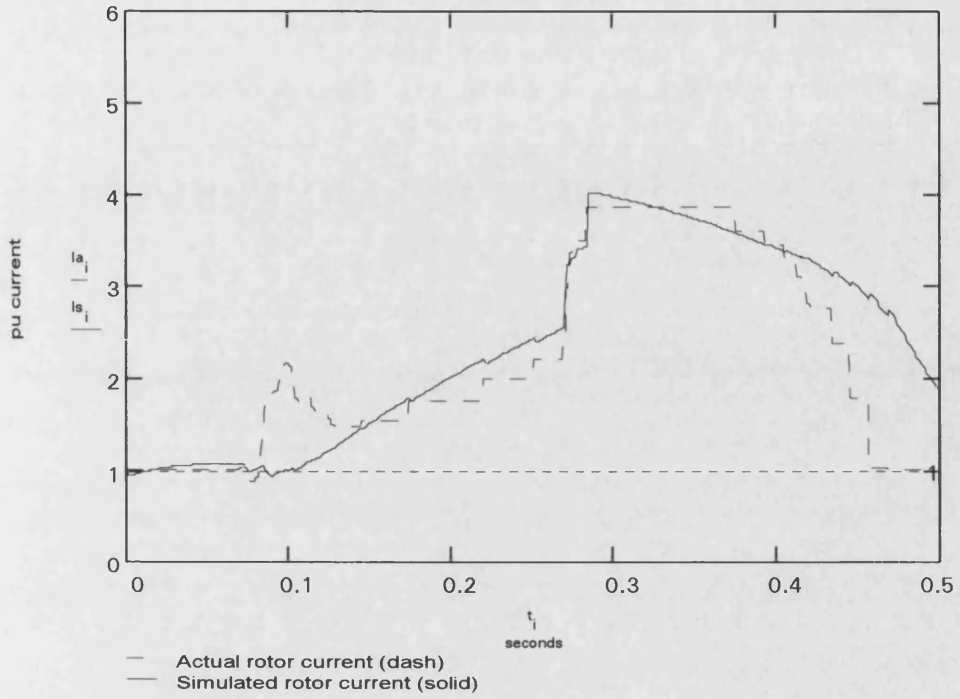

Figure (5.9) Test case # 465 - non-blocked comp. with $x_1 = 0.4*X_{br}$ & $x_2 = 0.6*X_{br}$.

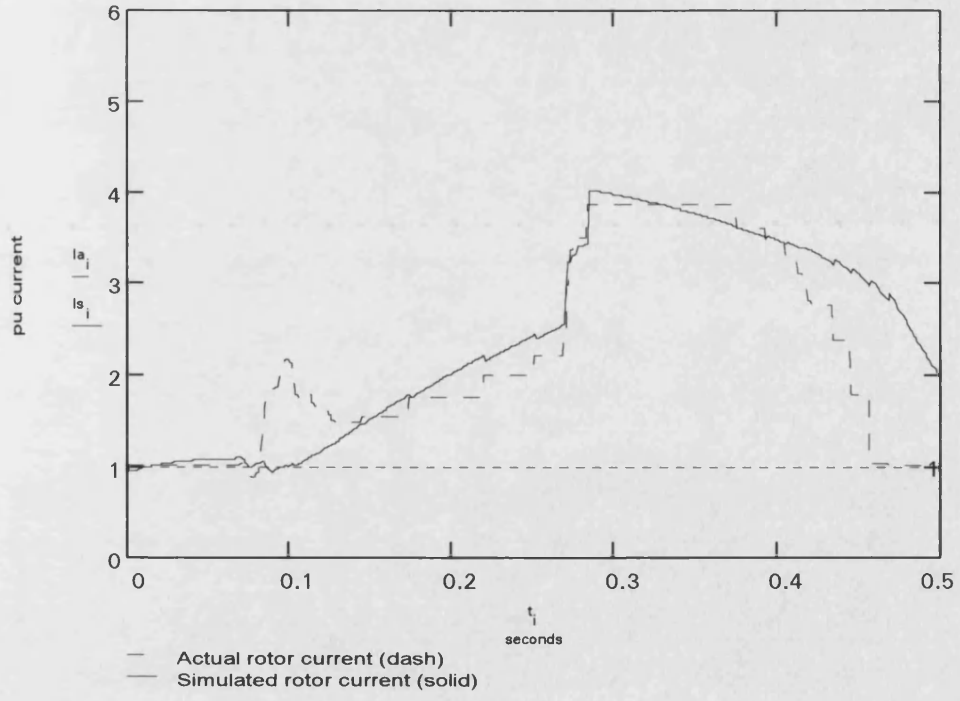

Figure (5.10) Test case # 465 - non-blocked comp. with $x_1 = 0.5*X_{br}$ & $x_2 = 0.5*X_{br}$.

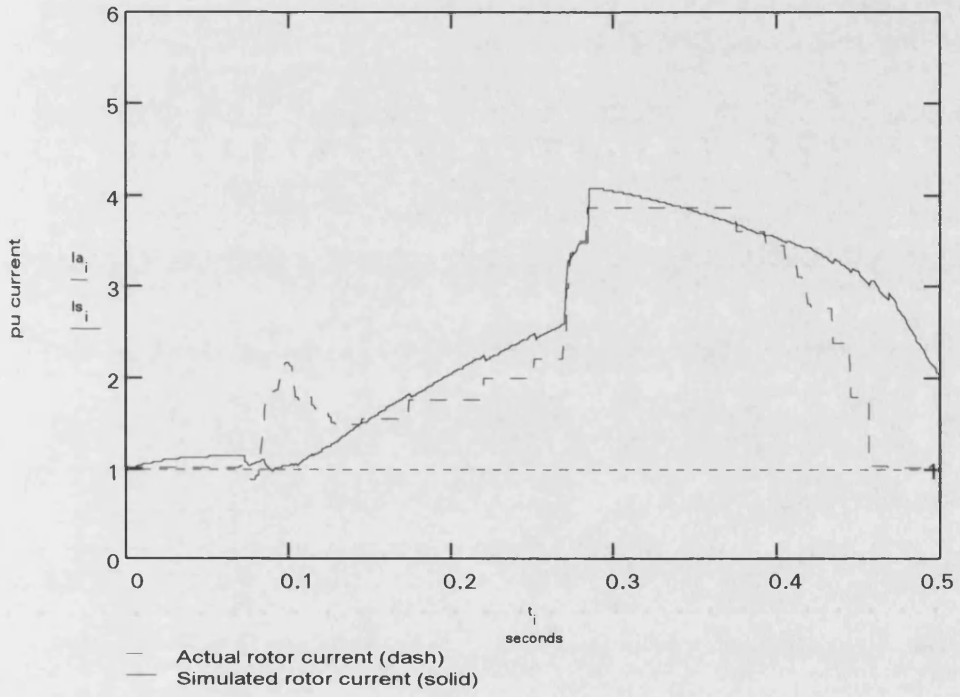

Figure (5.11) Test case # 465 - non-blocked comp. with X_m = 2.535 pu.

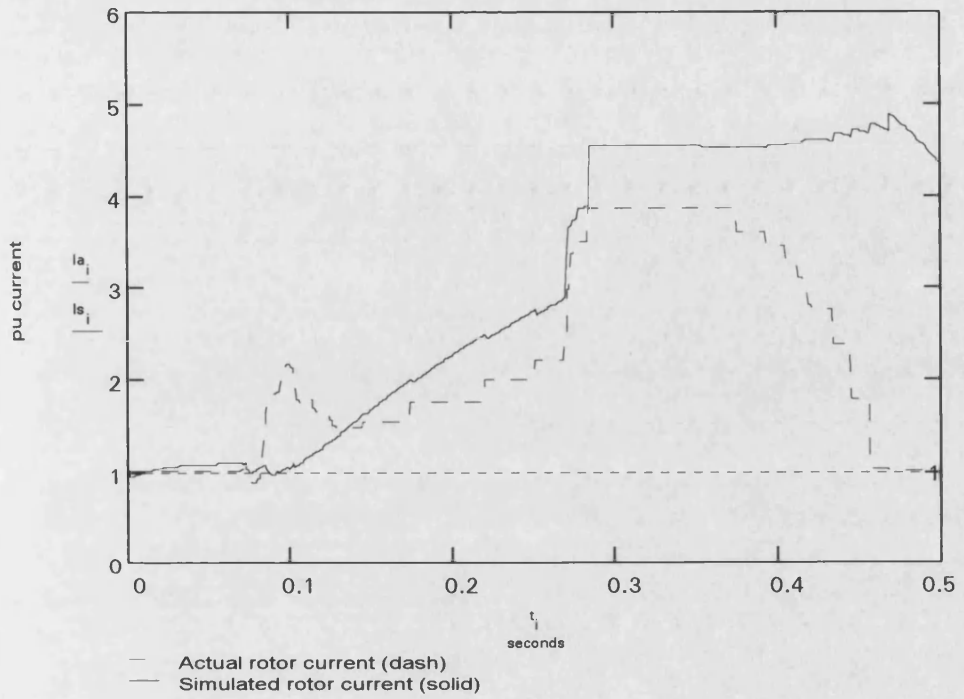

Figure (5.12) Test case # 465 - non-blocked comp. with H = 0.2 pu.

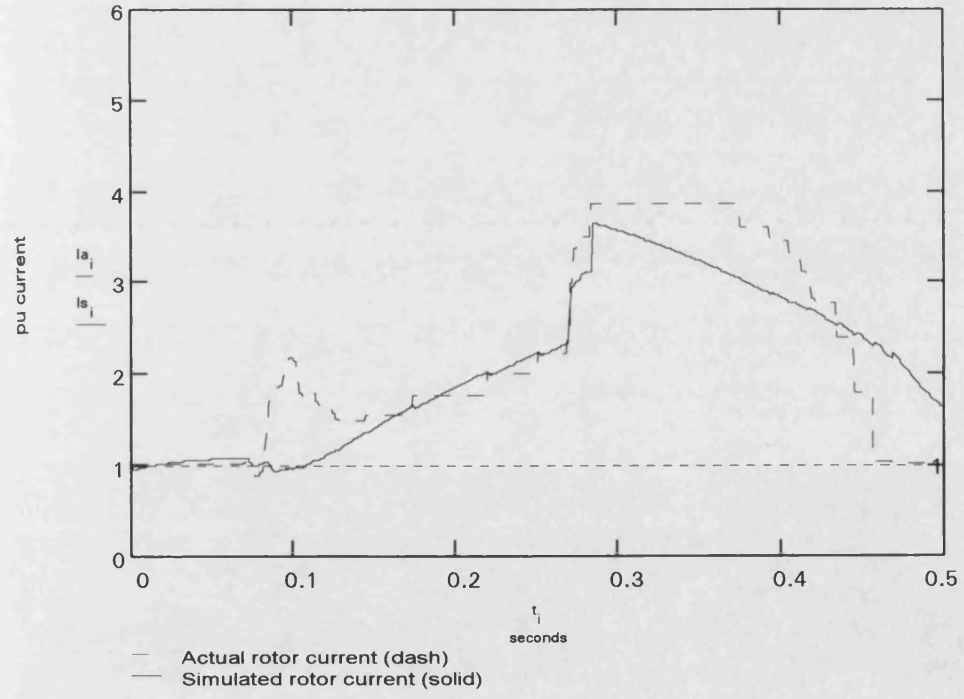

Figure (5.13) Test case # 465 - non-blocked comp. with H = 0.3 pu.

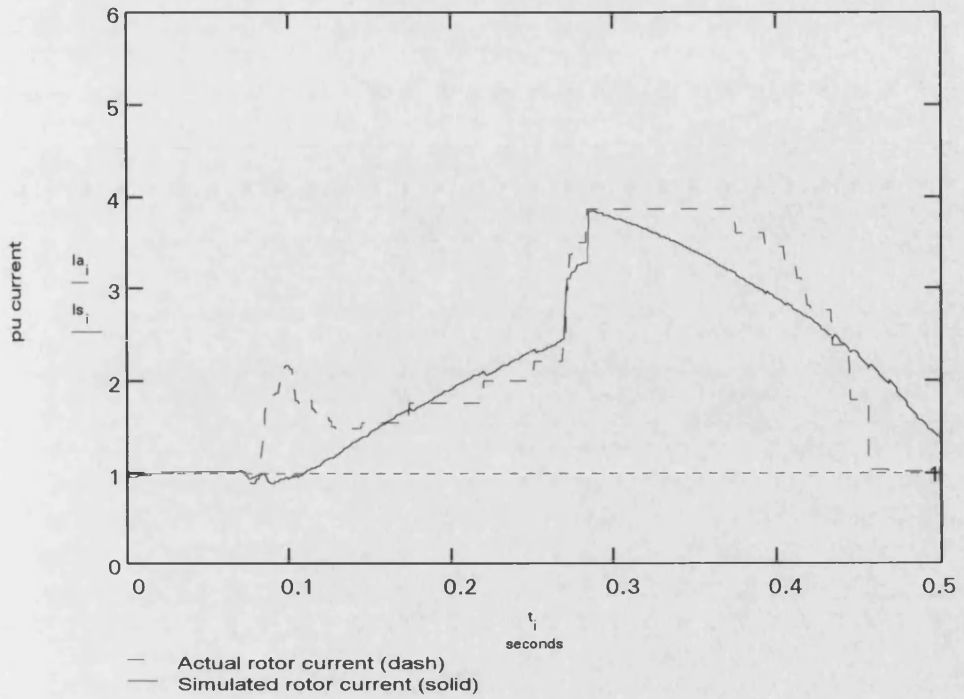

Figure (5.14) Test case # 465 - non-blocked comp. with A increased by 1%.

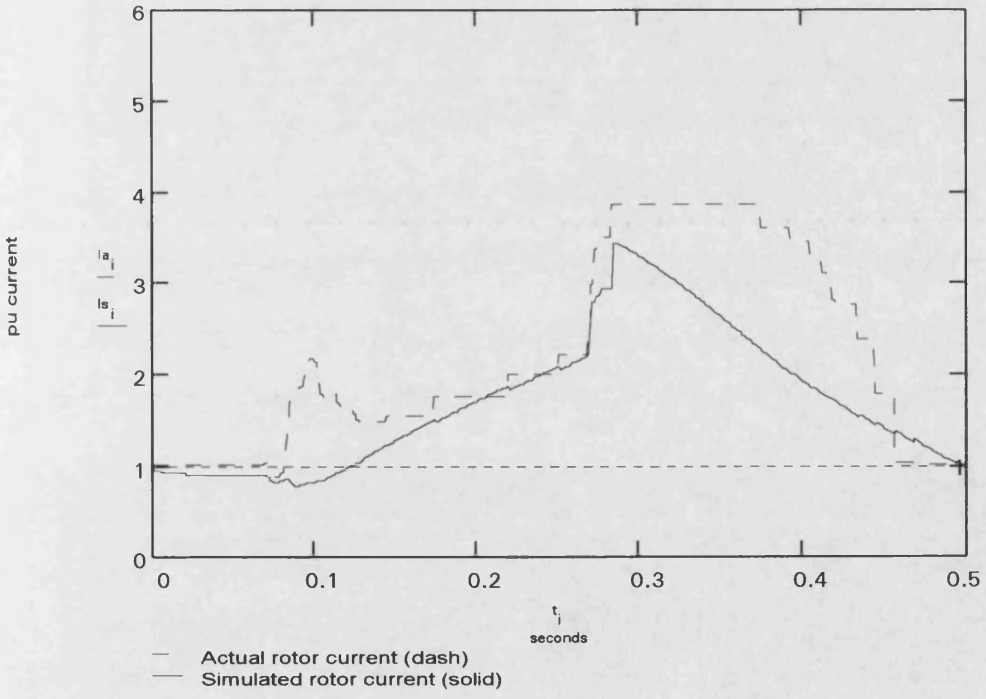

Figure (5.15) Test case # 465 - non-blocked comp. with A increased by 3%.

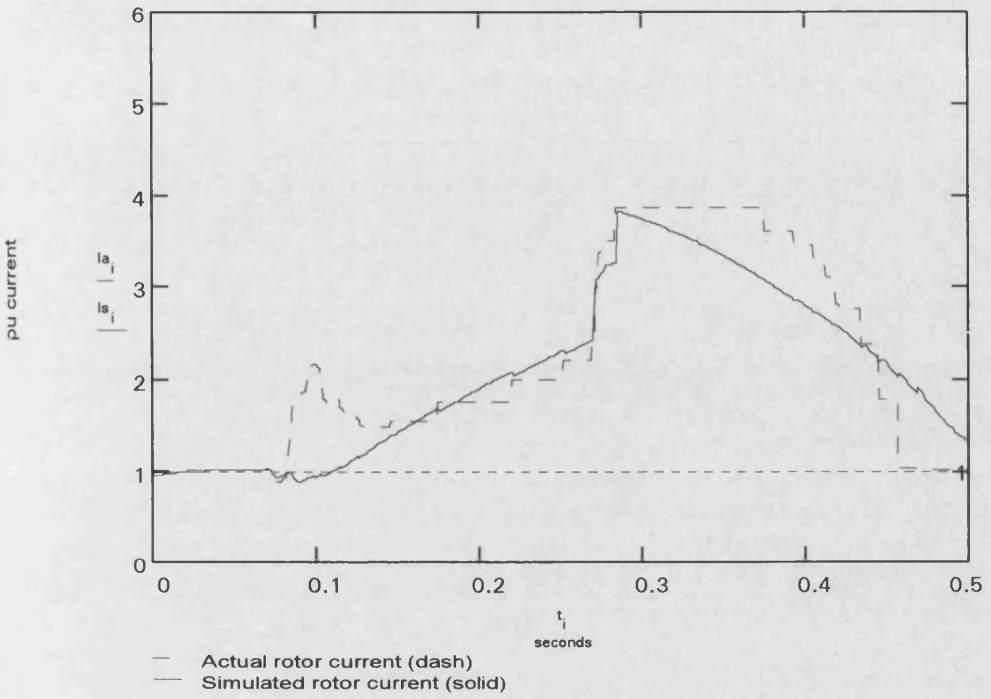

Figure (5.16) Test case # 465 - non-blocked comp. with B decreased by 1%.

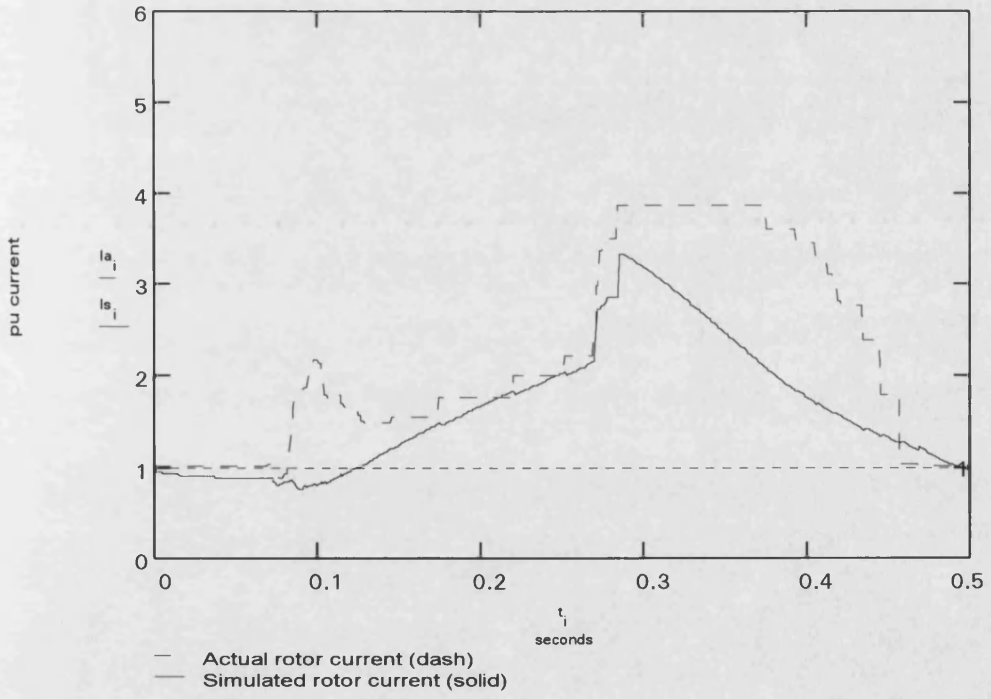

Figure (5.17) Test case # 465 - non-blocked comp. with B decreased by 3%.

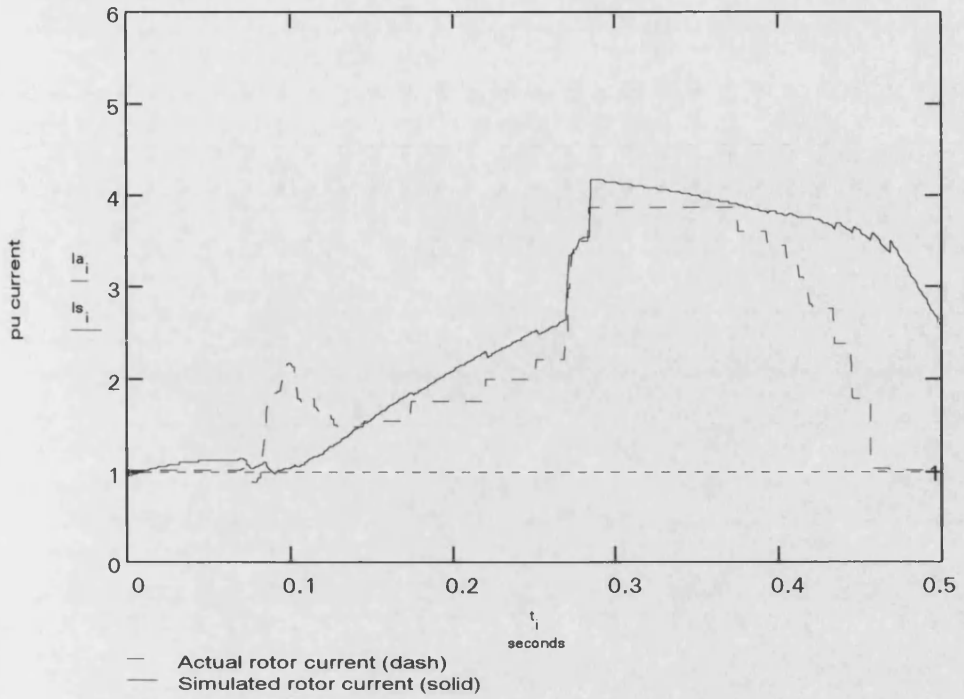

Figure (5.18) Test case # 465 - non-blocked comp. with C increased by 5%.

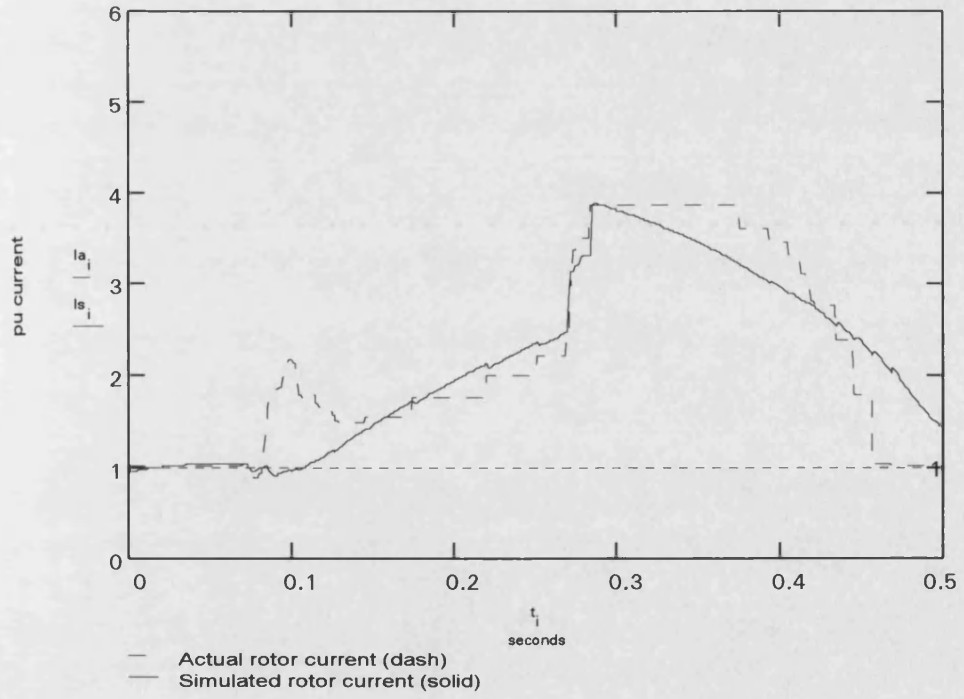

Figure (5.19) Test case # 465 - non-blocked comp. with C decreased by 5%.

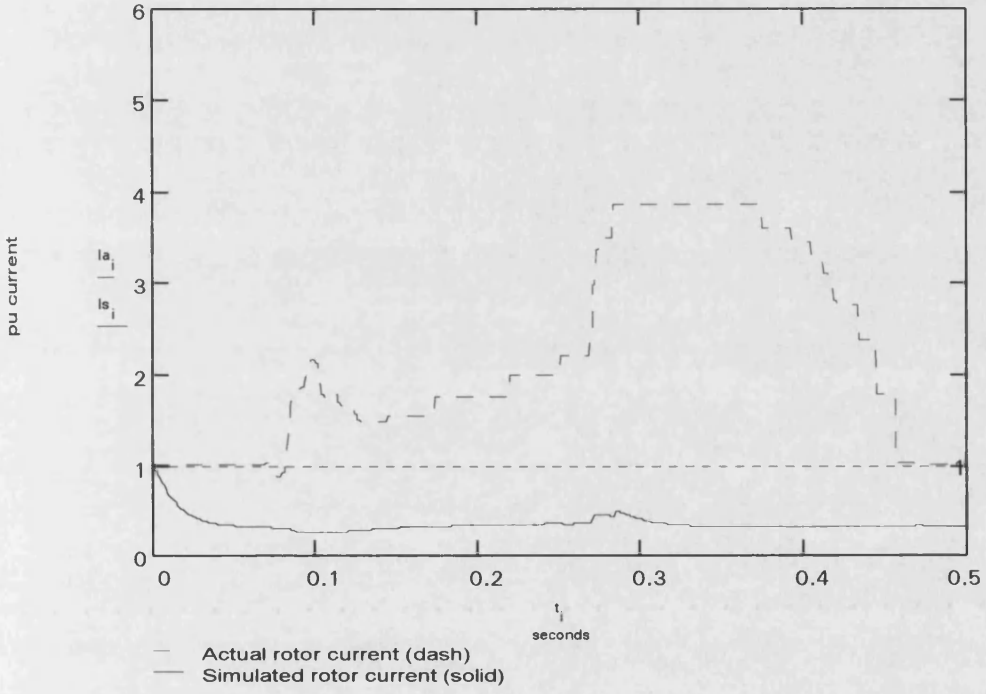

Figure (5.20) Test case # 465 - non-blocked comp. with A = 0.2, B = C = 0.

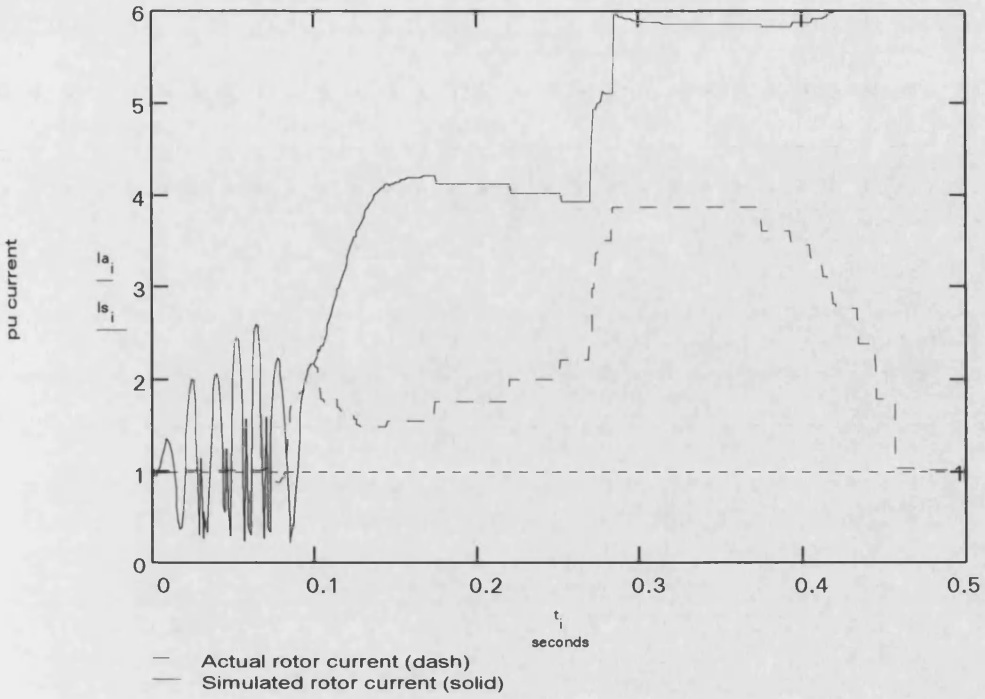

Figure (5.21) Test case # 465 - non-blocked comp. with h = 0.01

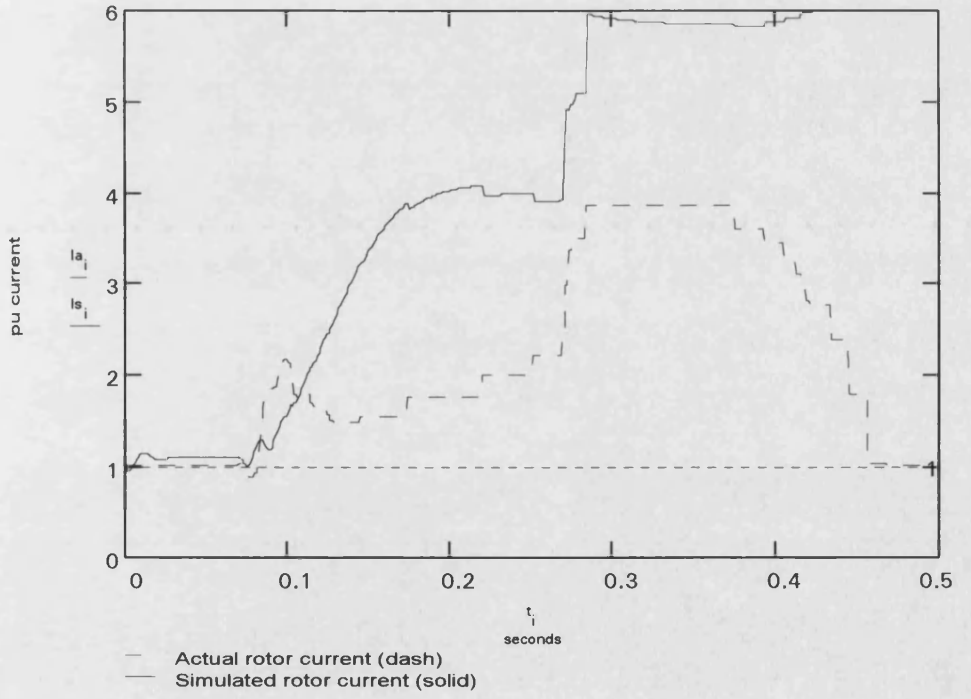

Figure (5.22) Test case # 465 - non-blocked comp. with h = 0.005

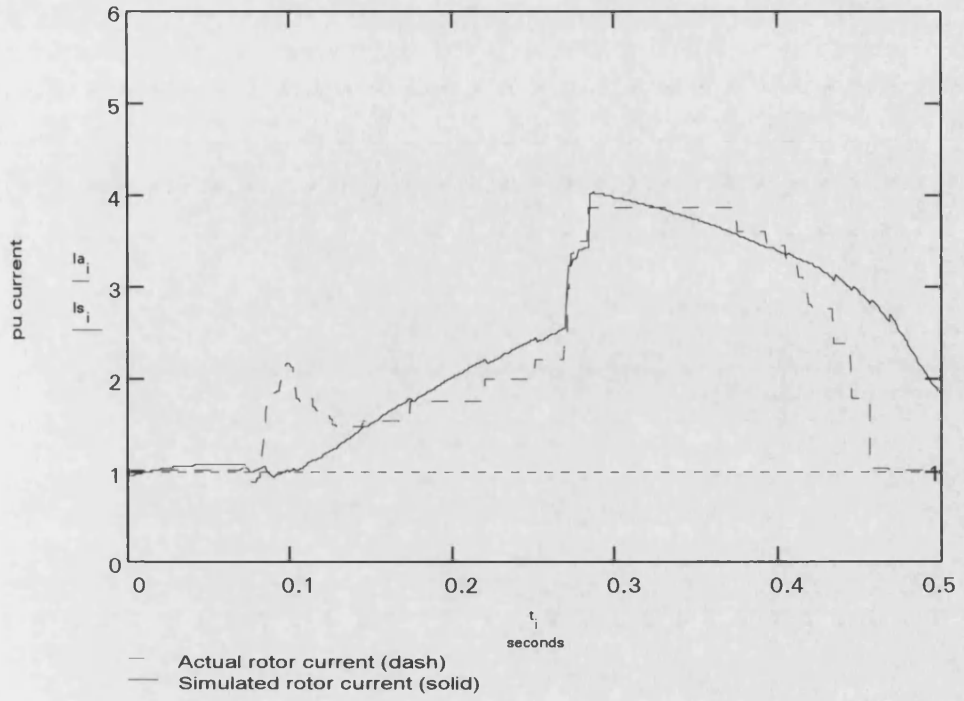

Figure (5.23) Test case # 465 - non-blocked comp. with h = 0.001 (reference case)

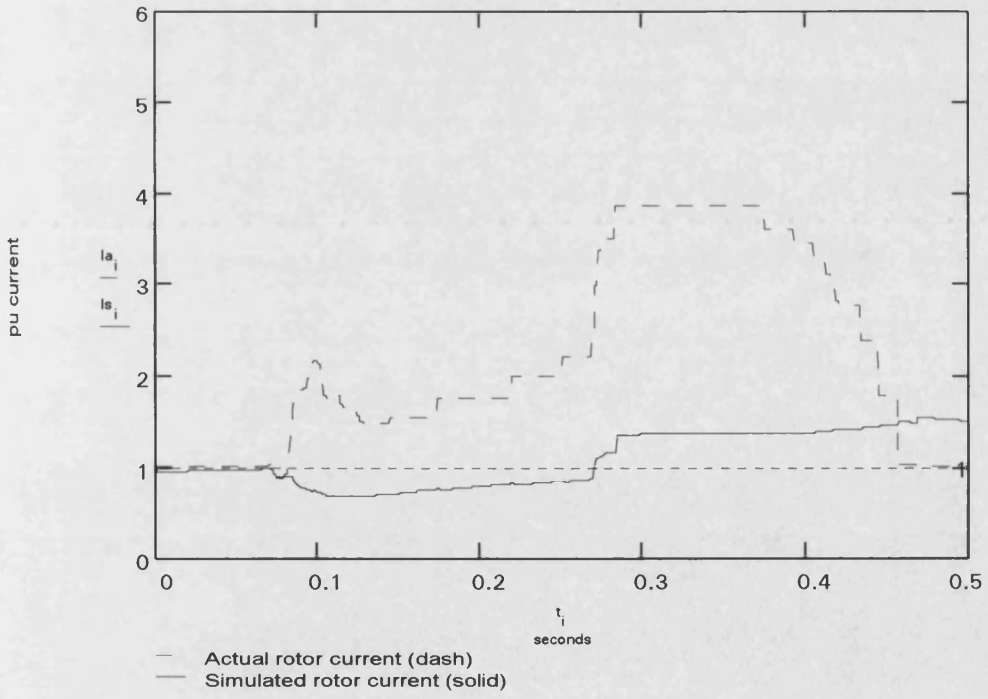

Figure (5.24) Test case # 465 - non-blocked compressor with h = 0.0001

CHAPTER 6

Transient Stability Analysis using the New Dynamic Load Model

6.1 - Introduction:

In this chapter, two major fault cases, which have occurred in Abu Dhabi power system in recent years, are described. The new dynamic load model was tested by using the system variables monitoring technique. First, the new model was adopted in the transient stability analysis to simulate the system variables (frequency and voltage) of these two fault cases. Then, simulations of the new model and an earlier published model were compared to the actual system variables fault records. The new dynamic load model was validated, and sensitivity analysis were performed to show the impact of fault clearing time (t_c) and the A/C load percentage of the total load on the system stability.

6.2 - Description of system fault cases:

6.2.1 - Case # 1: Fault at 220 kV OHL between Um Al-Nar power station & Al-Wathba substation [53]:

At 0229 hours on August 3rd, 1988, a single phase-to-earth fault has occurred on the 220 kV over-head line # 2 linking Um Al-Nar power station (UAN) and Al-Wathba substation (WATH). The fault was cleared after 116 milliseconds, and was followed by a successful single pole auto-reclosure of the circuit breakers at both ends.

After fault clearance, the system frequency has dropped down to 49.4 Hz, causing the first stage of under-frequency load shedding scheme (UFLSS) to shed 12.5% of the

system load in Abu Dhabi and Al-Ain cities. The total system load was nearly 1020 MW at that time, and therefore, it was estimated that nearly 120 MW of system load was shed due to under-frequency relaying. Thereafter, the system frequency has increased up to 50.6 Hz, and three Diesel engine generators of 39 MW total power have tripped in Al-Ain power station (AIN).

At 0231 hours of the same day, 2 minutes later after the first incident, another fault occurred on the 220 kV over-head line # 1, and the fault was cleared after 104 milliseconds. At (WATH) substation, one phase of the circuit breaker opened and auto-reclosed, but at (UAN) power station, the remaining two poles of the circuit breaker opened after 1.8 seconds by the "enforced three poles coupling trip" feature, and the breaker did not auto-reclose. Therefore, the line remained energized from (WATH) substation end without carrying any load, and the system frequency has dropped from 50.2 Hz down to 49.65 Hz, and then increased again up to 50.45 Hz.

At (UAN) power station, GT3 (45 MW) has tripped and there was no further under-frequency load shedding. At 0315 hours, the line was put in service again by closing the circuit breaker manually at (UAN) end. The load which has been shed in Al-Ain city was fully restored after 12 minutes and in Abu Dhabi city after about one hour. The atmosphere was very humid in that area at the time of both incidents, which could be considered as complete fog causing flashovers on the lines. Figure (6.1) illustrates the system frequency recorded at the 220 kV busbar of (UAN) power station.

Readings taken 30 minutes before both incidents can be considered as being fairly close to the system loading conditions at the time when these incidents have occurred. The total power generation of different stations in the system are given in the following table:

Station	Power generation
UAN - East	220 MW
UAN - West	635 MW
Abu Dhabi	88 MW
Baniyas	15 MW
Al-Ain	70 MW
Total	**1028 MW**

By 0300 hours, 25 minutes after the 2nd incident, the total system load was nearly 212 MW less than it would have been without the fault, although the (UFLSS) has only shed 120 MW of the total system load. Accordingly, a major probable cause for the extra load loss was the cascade tripping of many motors, such as the chillers of large A/C systems and the compressors of single-phase A/C units.

The following table shows the comparison of system loads on the 2nd and 3rd of August, 1988:

Time	Actual load 2nd August	Actual load 3rd August	Estimated load without load shedding	Loss of load
01	1083	1088		
02	1033	1028		
03	1018	803	1015	212
04	1003	908	1000	92
05	988	915	980	65
06	948	895	940	45
07	958	925	940	15

6.2.2 - Case # 2: Fault at 132 kV cable of 132/33 kV Interbus transformer at Abu Dhabi power station [54]:

At 0816 hours on July 19th, 1993, a single phase-to-earth fault occurred on the 132 kV cable connecting the 80 MVA interbus transformer #1 with the 132 kV busbars at Abu Dhabi power station (ADPS). The fault was caused by a contractor excavating a trench for the new Gas Turbine extension inside (ADPS). The total power generation in different stations in the system are given in the following table:

Station	Power generation
UAN	840 MW
Taweelah	225 MW
Abu Dhabi	192 MW
Al-Ain	185 MW
Al-Ain SVC plant	134 MVAR
Total	**1576 MW + 134 MVAR**

Figure (6.6) illustrates the system frequency as recorded on the 132kV busbar at (UAN) during the fault. As shown in figure, the system frequency had fluctuated down to 49.55 Hz during the first post-fault swing, then it increased up to 50.5 Hz before stabilizing after nearly 5 minutes.

In the 132 kV network, two main feeders (Sport City-E18 and W13-W24) have tripped due to the operation of distance relays. The loss of such central feeders in the network had affected the reactive power flow from (UAN) power station to Abu Dhabi island, causing the voltage level to rise at (UAN) side and to drop at Abu Dhabi side, as shown in figure (6.11). The fault was cleared after nearly 120 milliseconds due to the tripping of 132 kV circuit breaker directly supplying the interbus transformer, as shown in figure (6.12).

The total system load at 0800 hours at that day was 1446 MW, while the minimum load day at 0800 hours in February 1993 was 503 MW. Based on these data and considering weather conditions at that day, it was estimated that between 65% and 70% of the system load were induction motors driving A/C compressors, where this percentage will be considered in the stability analysis.

6.3 - Transient stability analysis:

The new mechanical torque characteristics of the single-phase A/C compressor load was included in the new dynamic load model, which was adopted in the stability analysis detailed herein. Dynamic simulations of the new model and the earlier published EPRI model [16] were compared to the recorded system transient response in the above detailed fault cases, in order to validate the new dynamic load model, and to show the impact of stalling A/C compressors on the system stability.

6.3.1 - System frequency:

1) The first part of fault case #1 was simulated by setting a fault duration of 5 cycles, and the 220 kV OHL # 1 between (UAN) power station and (WATH) substation was dropped from the system, which was followed by a successful auto-reclosure of the line. The system frequency recorded at (UAN) 220 kV busbar (bus 22), shown in figure (6.1), was compared to the system frequency simulation using both EPRI and the new model, as illustrated in figures (6.2) and (6.3) respectively. The system frequency simulation using EPRI model has slightly fluctuated before quickly reaching stability limits, while the new model frequency simulation has dropped down to nearly

49.4 Hz during the first post-fault swing, and rose up to nearly 50.6 Hz. Therefore, the new load model simulation has closely matched the system frequency recorded during the fault, despite the small tolerance between the actual (116 ms) and simulated (100 ms) fault clearing time.

2) As earlier described in the fault case # 2, the estimated A/C load percentage was varying between 65% and 70% of the total system load. Accordingly, the following aspects were concluded by comparing both models simulations, for an estimated 70% A/C load percentage, as shown in figures (6.7) and (6.8) respectively, and the recorded system frequency during fault shown in figure (6.6):

   - The EPRI model frequency simulation has stabilized right after fault clearance, while the recorded system frequency has deeply fluctuated and reached stability after nearly 5 minutes of fault clearance.

   - The new model frequency simulation has satisfactorily matched the recorded system frequency, despite the difference between the actual (120 ms) and simulated fault clearing time (100 ms). The simulated and recorded system frequency have both dropped down to the same level of nearly 49.55 Hz during the first post-fault swing, then, rose up to 50.5 Hz. It was believed that the impact of 20 ms difference between actual and simulated fault clearing time was compensated by simulating the system frequency at the higher estimated limit of A/C load percentage (70%), instead of (65%).

6.3.2 - System voltage:

Figure (6.4), (6.5), (6.9), and (6.10) illustrates the system voltage simulations using EPRI and the new load model respectively at the same bus for both fault cases. The EPRI model simulation has shown a fast restoration of the system post-fault voltage, while the new model simulation has shown a post-fault voltage recovery delayed by nearly 1.5 seconds. This was due to the impact of high reactive power required by the dynamic load during the fault. Therefore, it was concluded that there was no significant differences observed between both models voltage simulations.

6.3.3 - Dynamic load active and reactive power:

Figures (6.13) and (6.14) illustrate respectively the active and reactive power simulations of a selected group of motors for the fault case # 1 by using the new dynamic load model. These motors were connected to the 11 kV load feeders supplied from the central (E18) substation, which is located in the heart of Abu Dhabi city, while the tripped (OHL) in this case is located in the city suburb, in the same direction of the main 220 KV (OHL) linking Abu Dhabi and Al-Ain cities.

According to these figures, some motors have imposed large power requirements after fault clearance, causing the delay of system stability restoration. Such high power consumption exerted on the system has sustained the system post-fault voltage at lower level for some time, and consequently, have caused the cascade tripping of many other motors, which was the extra load loss mentioned earlier in the fault case # 1.

6.3.4 - Motors speed:

Figures (6.15) illustrates the new model speed simulation of the same motors group mentioned above for the fault case # 1. As shown in figure, some motors have experienced speed variations ranging between 20% and 50%. The speed variation for each motor has mainly depended on its inertia constant, power consumption, and on its relative location to the fault. Motors experiencing large speed excursions were considered as stalling, or at least taking longer time to reaccelerate, which consequently, have badly affected the system stability.

6.4 - Sensitivity analysis:

6.4.1 - Variation of the fault clearing time (t_c):

The fault clearing time has a very important role in stability analysis, specially for small power systems comprising large percentage of dynamic load. Sensitivity analysis was performed herein to investigate the impact of fault clearing time on the system variables transient response.

6.4.1.1 - Impact of (t_c) on the system frequency:

1) Figure (6.16) illustrates the system frequency simulation for the fault case # 1, where the fault was cleared after 140, 120, 100, and 80 milliseconds respectively:

   - As shown in figure, when the fault was cleared after 140 ms, the system frequency has sharply dropped and continued to decay leading to a total system collapse, even with the presence of under-frequency load shedding scheme.

- When the fault was cleared after 120 ms, the system frequency has experienced large excursions for several seconds, without reaching stability limit during the simulation period.

- When the fault was cleared after 100 ms, the system frequency has dropped down to 49.4 Hz during the first post-fault swing, following the same trend of the recorded system frequency during transient.

- When the fault was cleared after 80, the simulated system frequency has reached stability limit more faster than in former cases of relatively longer fault clearing. Generally, this case had a close response to that of 100 ms fault clearing time.

2) Figure (6.17) illustrates the system frequency simulation for the fault case # 2 with an estimated (70%) A/C load percentage, where the fault was cleared after 140, 120, 100, and 80 milliseconds respectively:

   - As shown in figure, when the fault was cleared after 7 cycles (140 ms), the simulated system frequency has dropped down to 48.4 Hz and fluctuated for several seconds before reaching instability, and the system collapsed.

   - When the fault was cleared after 6 cycles (120 ms), the simulated system frequency has dropped down to 49.2 Hz during the first post-fault swing, while it has dropped to 49.4 Hz when the fault was cleared after 5 cycles (100 ms).

Therefore, it was concluded that the slight increase of the fault clearing time may adversely affect the system frequency transient response, and consequently, the system stability.

6.4.1.2 - Impact of (t_c) on the system voltage:

1) Figure (6.18) illustrates the system voltage simulation for the fault case # 1 at Abu Dhabi (E18) substation, and figure (6.19) illustrates the system voltage simulation at Al-Ain substation, where the fault was cleared after 140, 120, 100, and 80 milliseconds respectively:

- When the fault was cleared after 140 ms, the post-fault system voltage at (E18) was sustained at nearly 70%, while it has reached stability limit after few seconds in Al-Ain substation. The sustained post-fault low voltage in Abu Dhabi was due to the prolonged fault clearing time, in addition to the concentration of dynamic loads in Abu Dhabi area, which have caused the stalling and cascade tripping of many low-inertia motors, and consequently, delaying the post-fault voltage recovery.
- When the fault was cleared after 120 ms, the post-fault voltage at (E18) substation as well as at Al-Ain has reached stability limit after nearly 5 seconds.
- When the fault was cleared after 80 ms and 100 ms respectively, the post-fault system voltage has reached stability much faster than in the former cases.

2) Figure (6.20) illustrates the system voltage simulation for the fault case # 2, for an estimated 70% A/C load percentage.

   - When the fault was cleared after 7 cycles (140 ms), the system voltage has decayed until it has totally collapsed.
   - However, when the fault was cleared after 5cycles (100 ms) and 6 cycles (120 ms) respectively, the system voltage has quickly recovered in both cases.

Therefore, the above aspects has confirmed the necessity and favorable impact of fast fault clearing on the system stability, since it has definitely improved the system post-fault voltage recovery, and consequently, enhanced the fast restoration of system stability.

6.4.2 - Variation of A/C load percentage:

The presence of certain load types can, under some system transmission and generation conditions, lead to system instability in the form of uncontrolled voltage oscillations or transient voltage collapse [48]. Induction motors driving A/C compressors are of such load types as they show a fast increase of reactive power demand following system faults. Accordingly, the following sensitivity analysis is performed to investigate the impact of A/C load percentage on the system variables transient response.

6.4.2.1 - Impact of A/C load percentage on the system frequency:

Figure (6.21) illustrates the system frequency simulation for the fault case # 2, for different A/C load percentage ranging between 50% and 70% of the total load. As shown in figure, the system frequency has deeply dropped down during the first post-fault swing

and stabilized in a longer time, in case of high A/C load percentage. The system frequency response was better enhanced every time the A/C load percentage was decreased by (5%).

It was earlier defined, in the fault case # 2 data, that the A/C load percentage was ranging between 65% and 70% of the total load. The exact definition of such load percentage has produced a frequency simulation matching with the system frequency recorded during transient.

6.4.2.2 - Impact of A/C load percentage on the system voltage:

Figure (6.22) illustrates the system voltage simulation of the fault case # 2, for the same different levels of A/C load percentage. As shown in figure, the variation of A/C load percentage had no significant impact on the system voltage simulation, except only in case of (70%) A/C load, where the post-fault system voltage has stabilized after nearly two seconds of fault clearance.

6.4.2.3 - Impact of A/C load percentage on the dynamic load active and reactive power:

The active and reactive power required by a selected group of motors connected to the system were simulated for the fault case # 2, where the fault clearing time and the A/C load percentage were varied according to the following table:

Figures	Power	Fault clearing time	A/C load %
(6.23)	MW	5 cycles	50%
(6.24)	MVAR	5 cycles	50%
(6.25)	MW	5 cycles	70%
(6.26)	MVAR	5 cycles	70%
(6.27)	MW	7 cycles	70%
(6.28)	MVAR	7 cycles	70%

- As shown in figures (6.23) and (6.24), the active and reactive power for all motors have quickly stabilized when the fault was cleared after 5 cycles and in case of (50%) A/C load percentage.
- However, figures (6.25) and (6.26) illustrated the high active and reactive power withdrawn by the stalling motor (103) in case of 5 cycles fault clearing time and (70%) A/C load percentage.
- In case of 7 cycles fault clearing time and (70%) A/C load percentage, the active and reactive power required by all motors have sustained at high levels for few seconds after fault clearance, as shown in figures (6.27) and (6.28).

Therefore, it was concluded that the large A/C load percentage combined with a relatively longer fault clearing time have a severe impact on the system stability, since the motors active and reactive power have highly increased during transient.

6.5 - Impact of SVC on the system frequency [55]:

The static VAR compensator (SVC) installed at Al-Ain 220 kV busbar was simulated for the fault case # 1, as shown in figure (6.29), in order to investigate its impact on stabilizing the system frequency. It was assumed that the whole (SVC) capacity (180 MVAR) was available in the system, which is not considered as normal operation procedure, but to illustrate the maximum possible (SVC) impact on the system, i.e. zero MVAR injection as initial condition.

Previous publication has evidenced that the system stability was improved by the synchronous condensers and static reactive power compensators, which tend to stabilize the system voltage [46]. The result was as expected and the (SVC) has caused better system frequency recovery. Practically, the system has suffered the frequency dip following the fault as in the fault case recorded frequency, but less minimum frequency was reached during the first post-fault swing, due to the increased MVAR capacity injected in the system than in the actual case.

6.6 - Conclusions:

According to the transient stability simulations, it can be concluded that the new A/C load model has produced comparable results with the actual system transient records. The main difference between the new model and earlier published model [16,25] was the

new mechanical torque characteristics of the single-phase A/C compressor load, which was earlier defined in Chapter 4.

In the first fault case, the new model system frequency simulation has matched with the recorded system frequency, despite the slight tolerance between the actual and simulated fault clearing time, where it has dropped down to 49.4 Hz during the first post-fault swing. In the second fault case, the A/C load percentage was estimated between 65% and 70% during the fault, based on the difference between the total system load at that day and the minimum system load during winter time. Similarly, the new model system frequency simulation at this loading condition has satisfactorily matched the recorded system frequency, when it has dropped down to nearly 49.55 Hz during the first post-fault swing.

Therefore, it was concluded that there was a significant improvement in the new model simulations when compared to the earlier published model, due to the impact of the newly defined mechanical torque characteristics of the single-phase A/C compressor load.

According to sensitivity analysis, it was concluded that the fault clearing time (t_c) had an important impact on the system stability, and has to be carefully considered in stability studies. For an increased fault clearing time, the system post-fault voltage was sustained at low level for some time, causing the cascade stalling of A/C compressors and

other low-inertia motors. Consequently, the power requirements of such stalling motors have highly increased, and were heavily imposed on the system and affecting its stability. Therefore, fast fault clearing has a great necessity in small power systems comprising high percentage of A/C load.

In hot countries, the A/C load percentage of the total system load is always increasing during the summer peak load, specially with the continuous development and expansions taking place in small societies. Accordingly, sensitivity analysis proved that the increased A/C load percentage had a severe impact on the system stability due to the A/C load dynamic behavior during transients. Mainly, for a high percentage of A/C load, the system frequency has deeply fluctuated and the A/C load power have highly increased during faults. According to sensitivity analysis, it can be concluded that the worst impact exerted on the system stability during faults is expected when a high percentage of A/C load is combined with an increased fault clearing time.

The fast-acting reactive power compensator (SVC) provides the additional reactive power needed to boost the post-fault system voltage. Such equipment increases the voltage support on load busbars, re-accelerates the *"robust"* motors, reduces the number of stalling low-inertia motors caused by faults, and eventually enhances the power system stability.

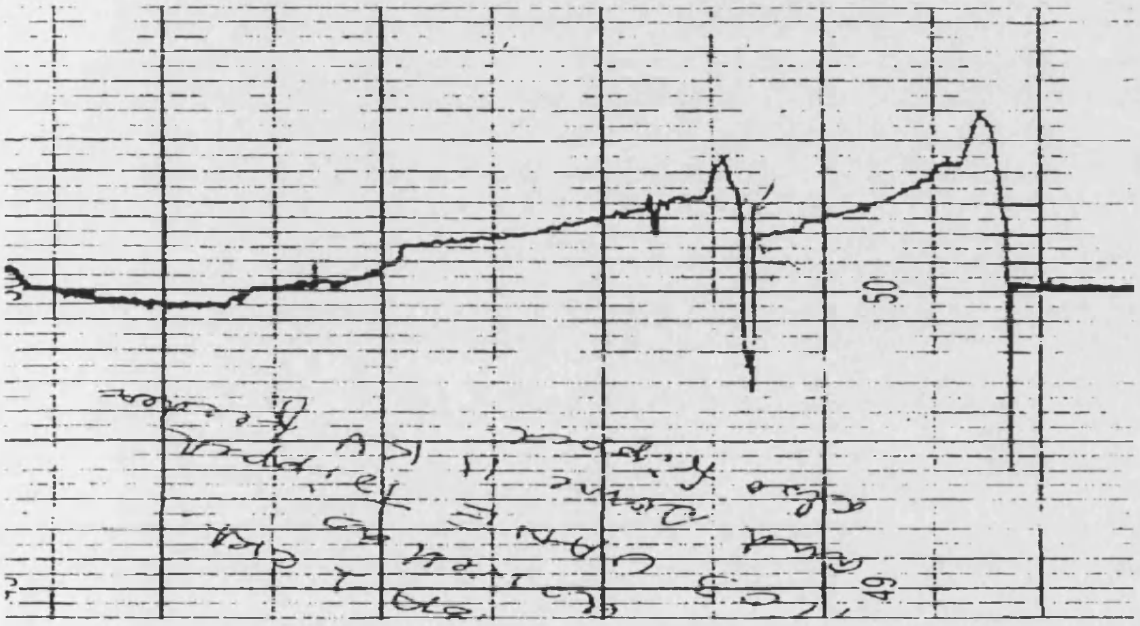

Figure (6.1) Case # 1 - System frequency record on 3/8/1988.

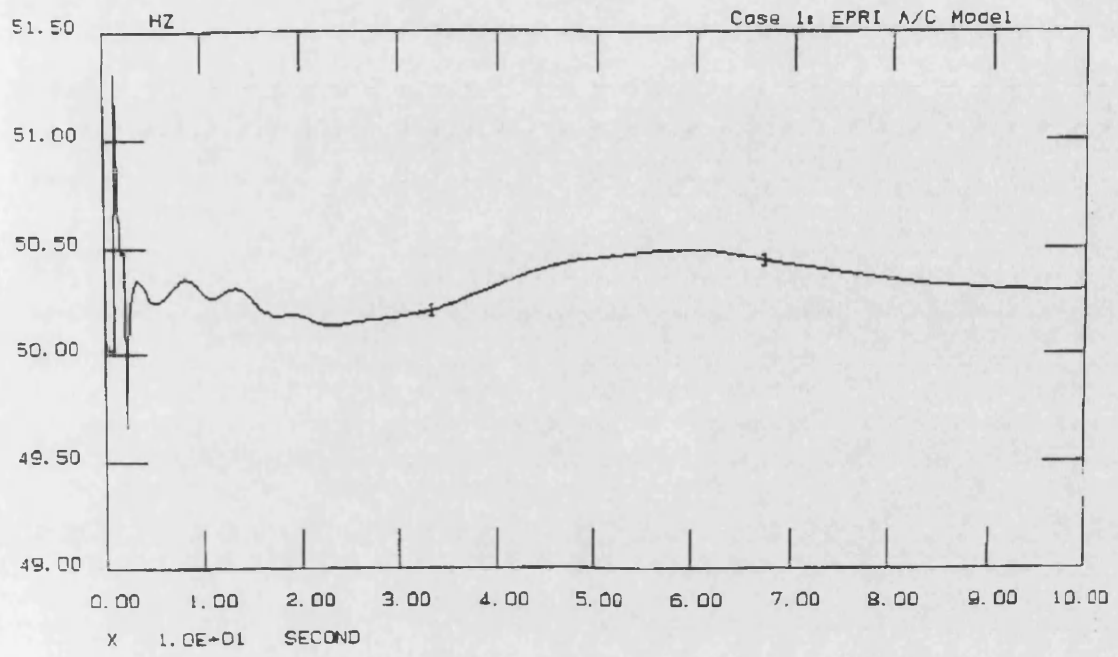

Figure (6.2) Case # 1 - Frequency simulation using the EPRI model.

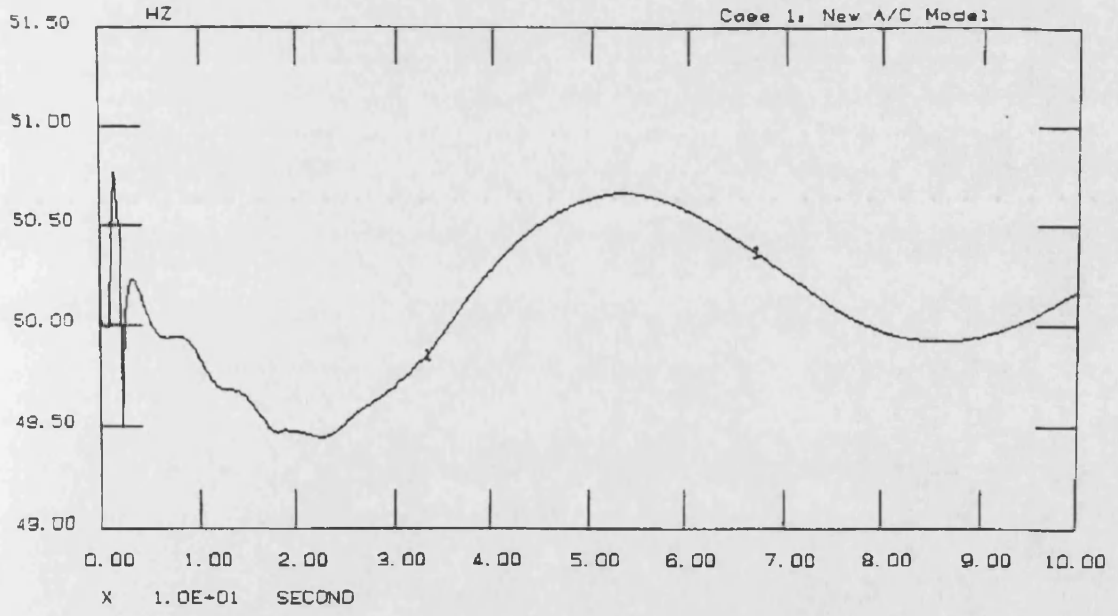

Figure (6.3) Case # 1 - Frequency simulation using the new model.

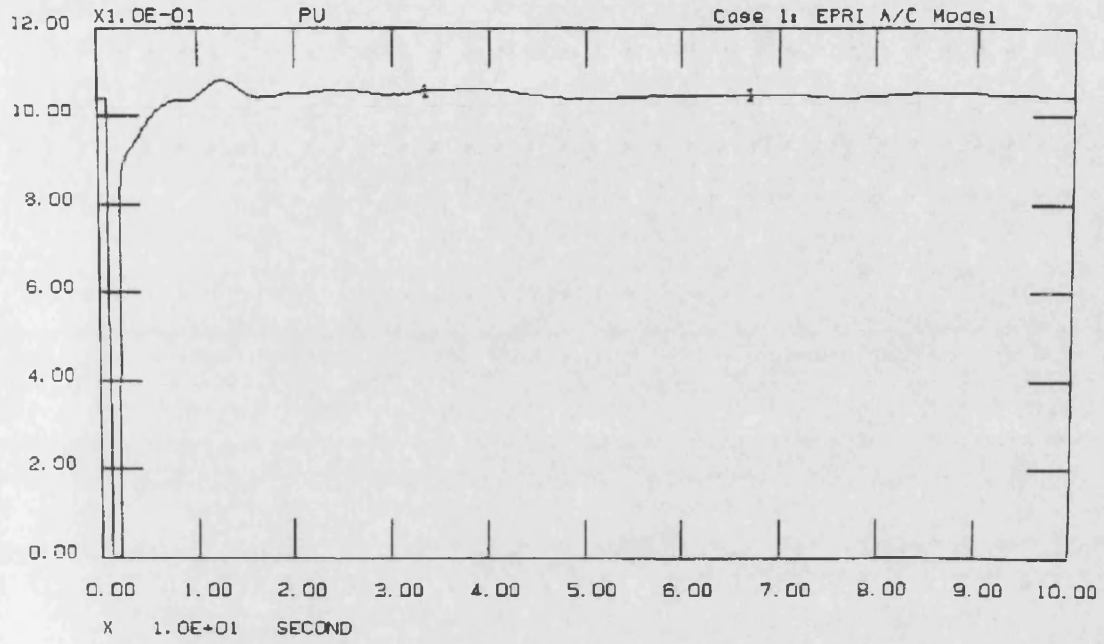

Figure (6.4) Case # 1 - Voltage simulation using the EPRI model.

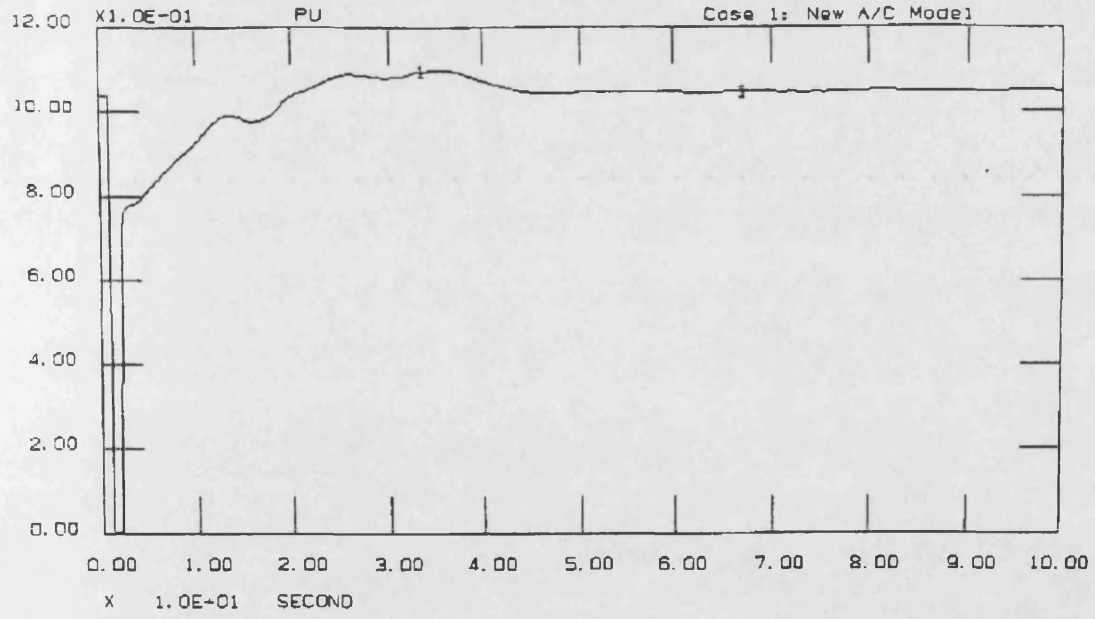

Figure (6.5) Case # 1 - Voltage simulation using the new model.

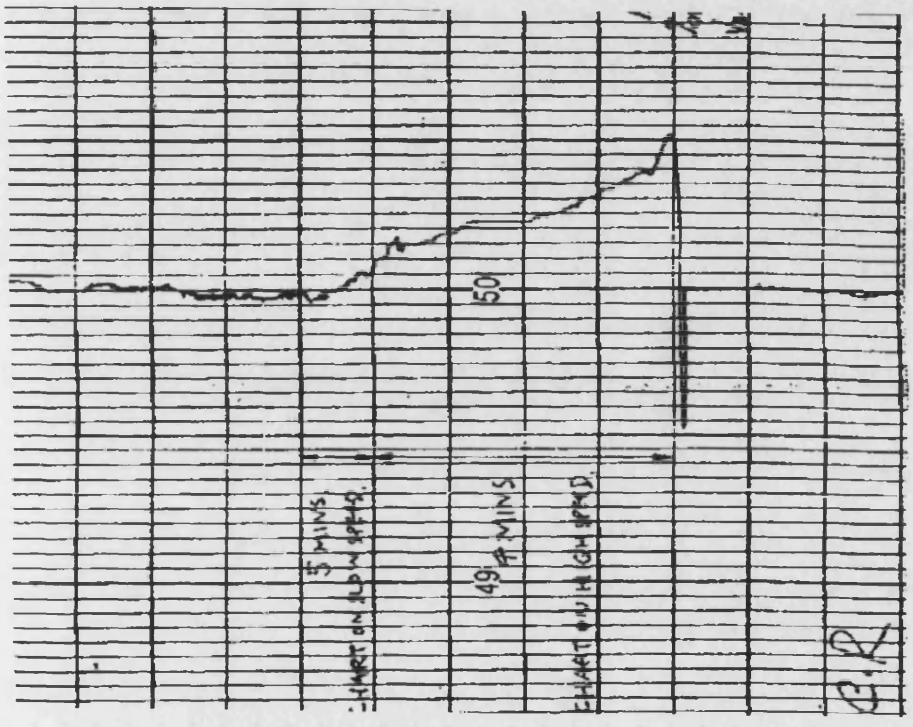

Figure (6.6) Case # 2 - System frequency record on 19/7/1993.

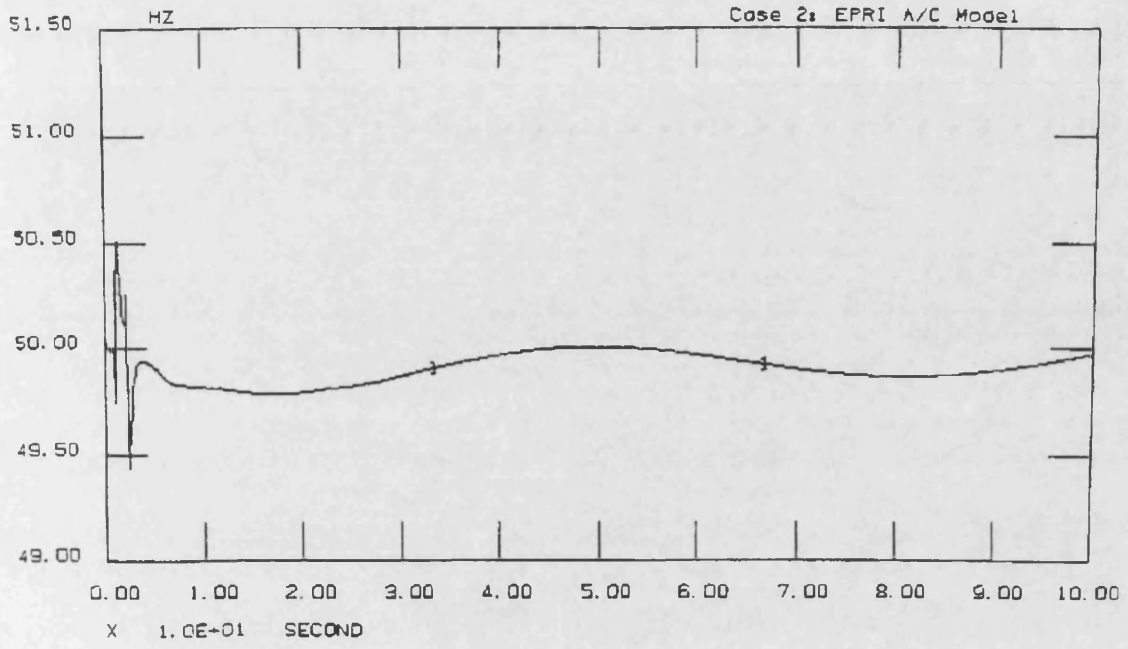

Figure (6.7) Case # 2 - Frequency simulation using the EPRI model.

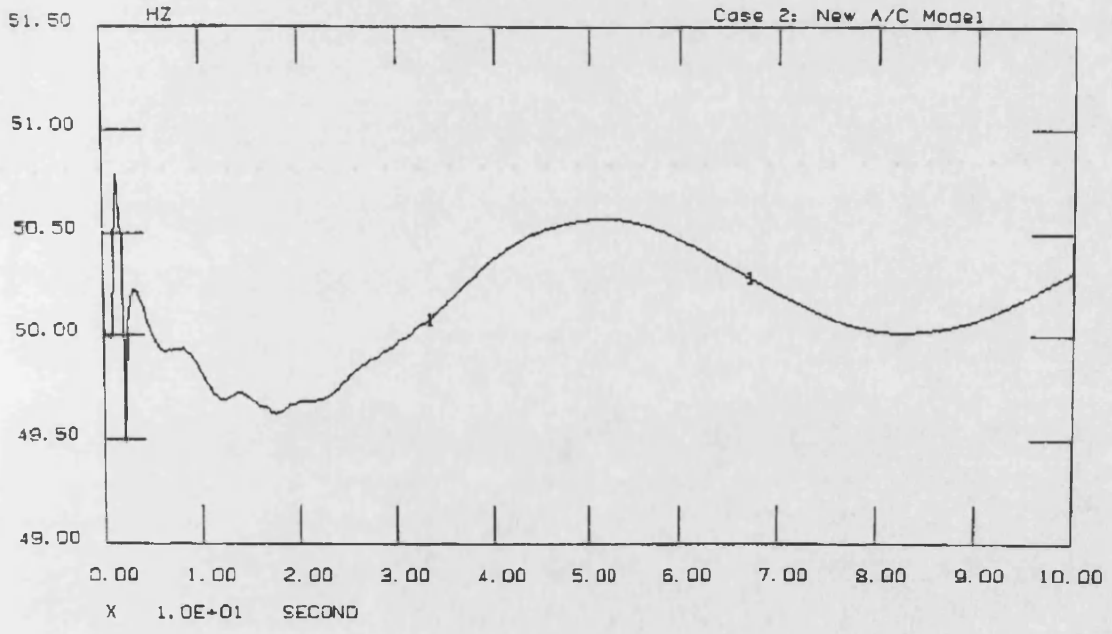

Figure (6.8) Case # 2 - Frequency simulation using the new model.

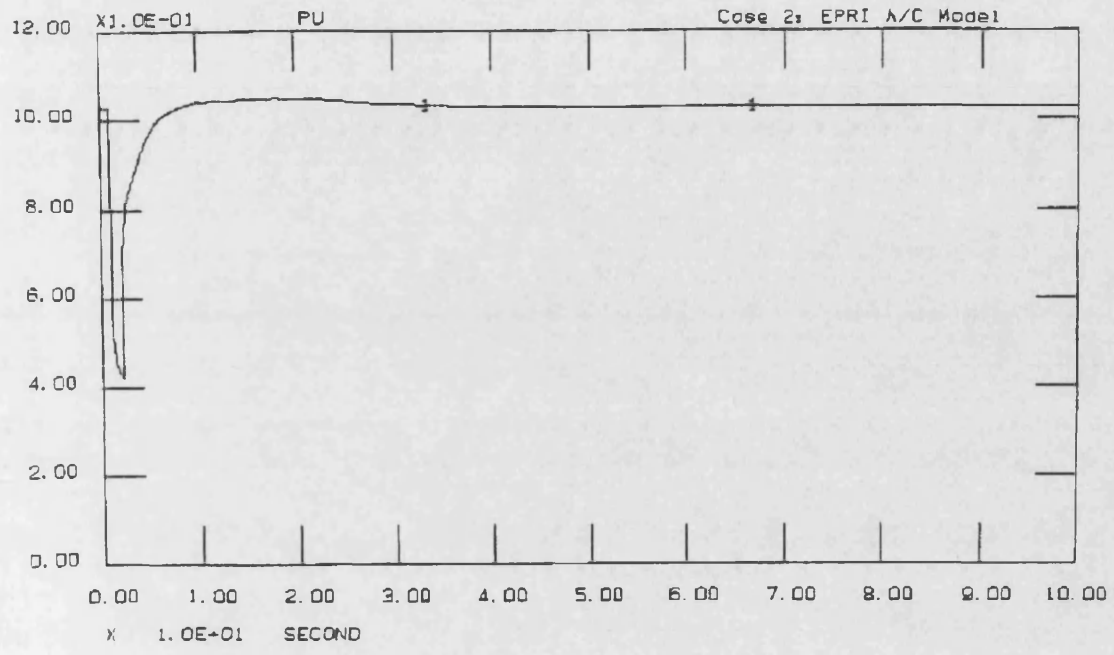

Figure (6.9) Case # 2 - Voltage simulation using the EPRI model.

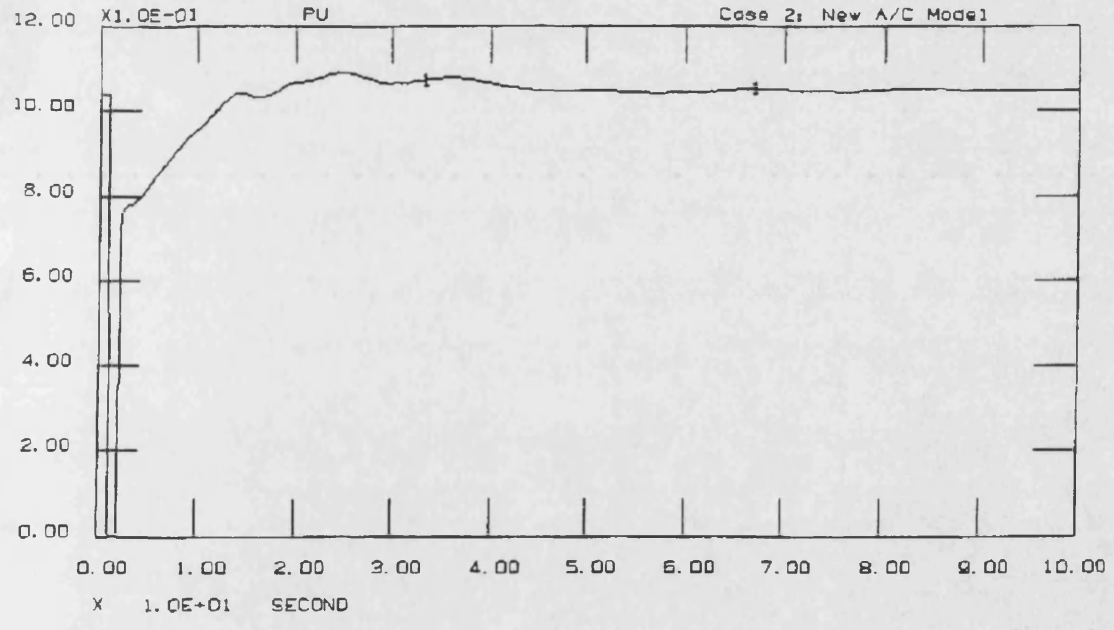

Figure (6.10) Case # 2 - Voltage simulation using the new model.

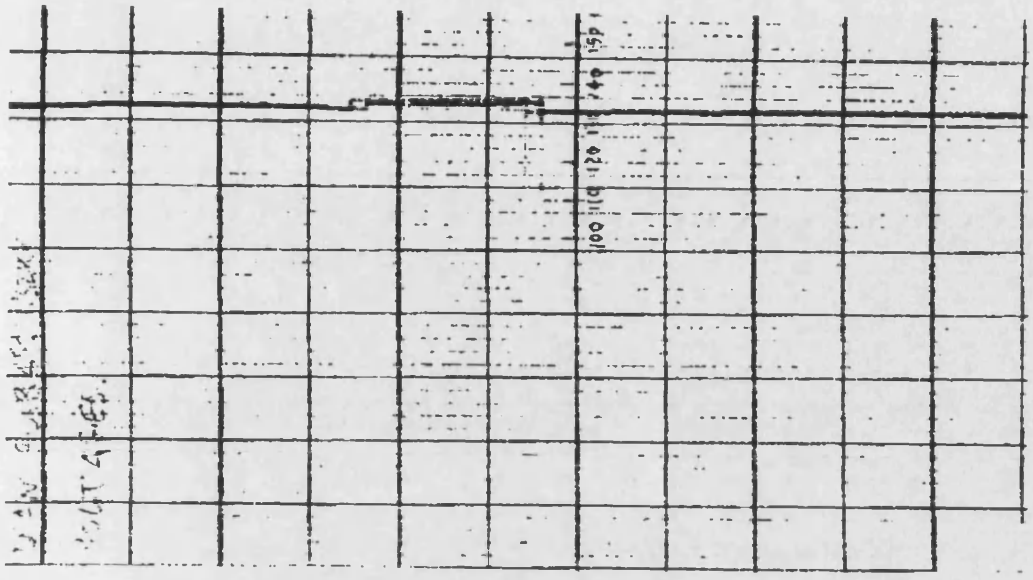

Figure (6.11) Case # 2 - System voltage recorded on 19/7/1993.

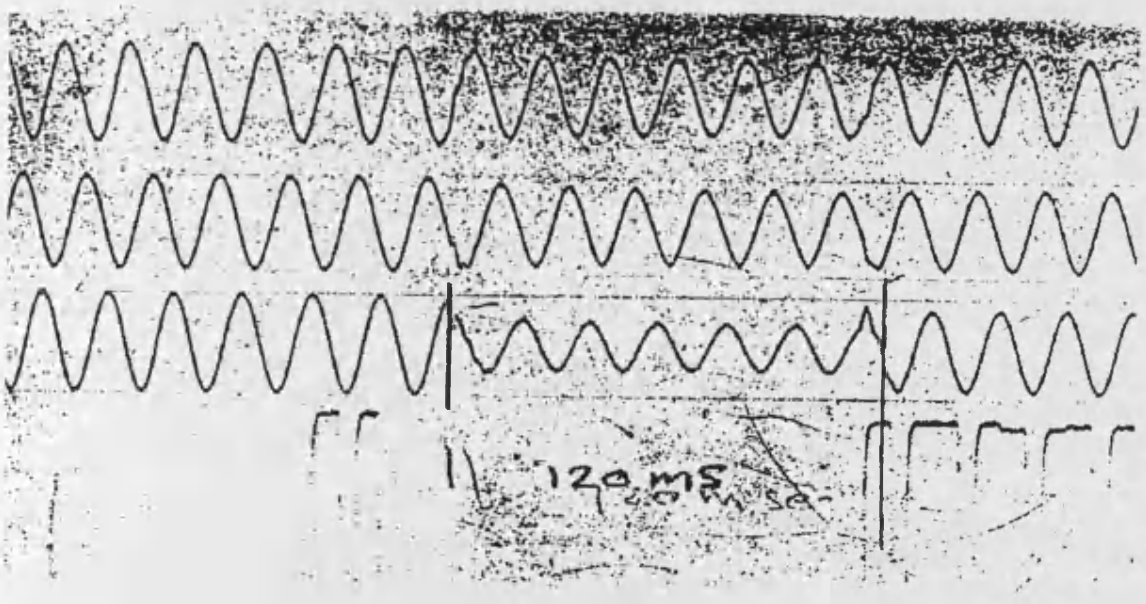

Figure (6.12) Case # 2 - Voltage recorder output showing fault duration.

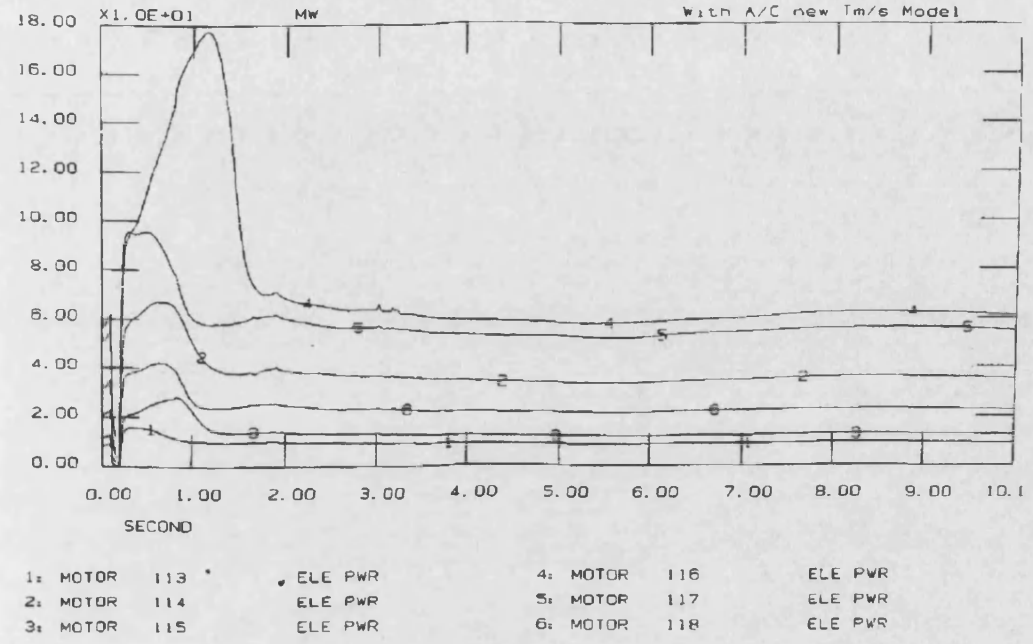

Figure (6.13) Case # 1 - Active power simulation of motors at E18 sub.(11 kV feeders)

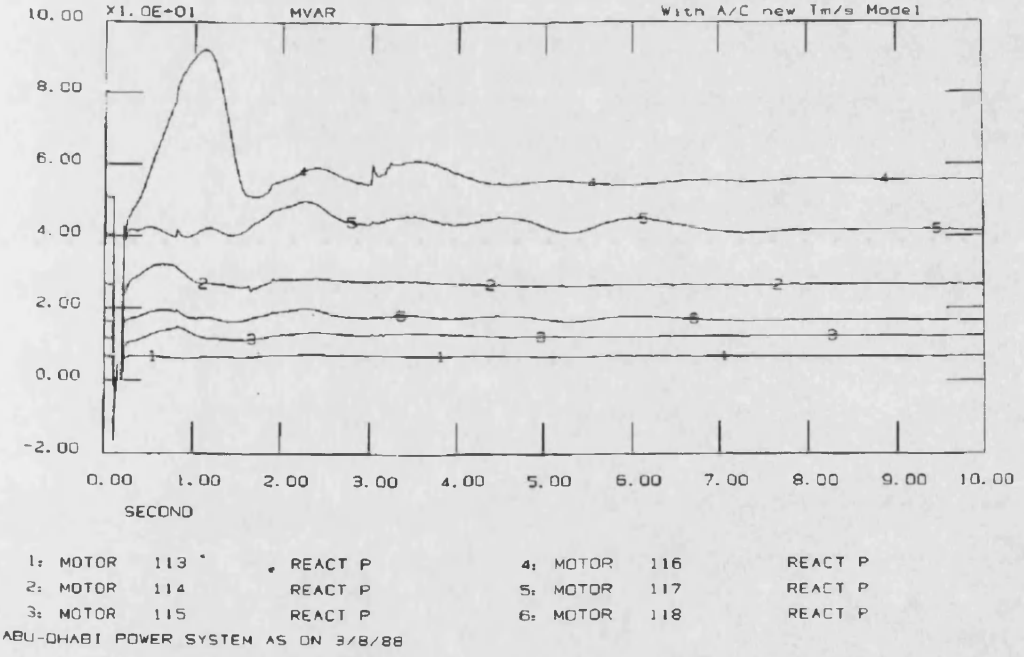

Figure (6.14) Case # 1 - Reactive power simulation of motors at E18 sub.(11 kV feeders)

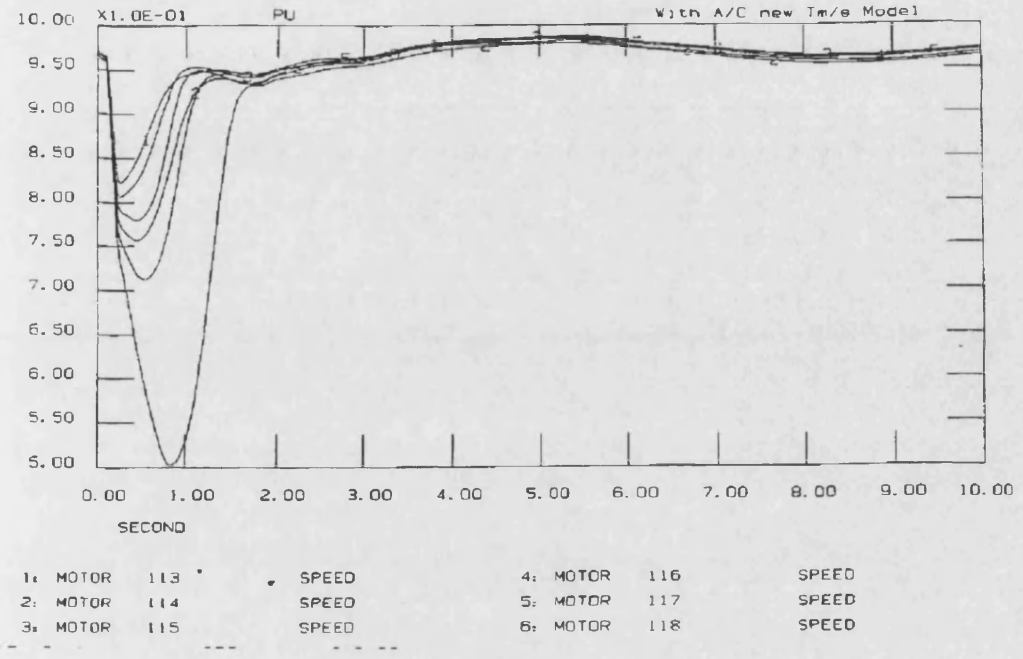

Figure (6.15) Case # 1 - Speed simulation of motors at E18 sub.(11 kV feeders)

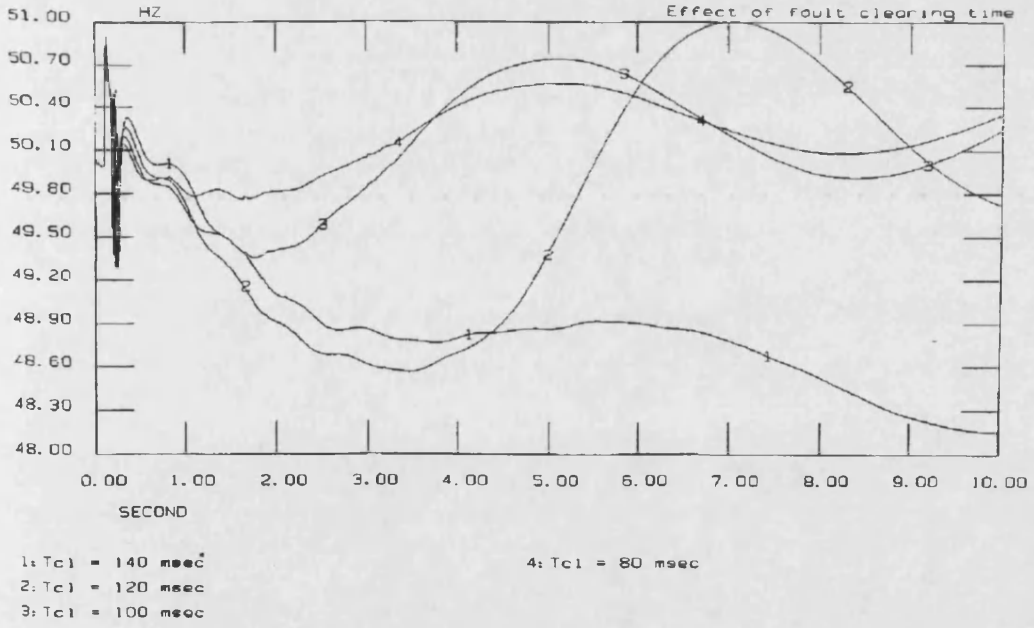

Figure (6.16) Case # 1 - Impact of fault clearing time on system frequency.

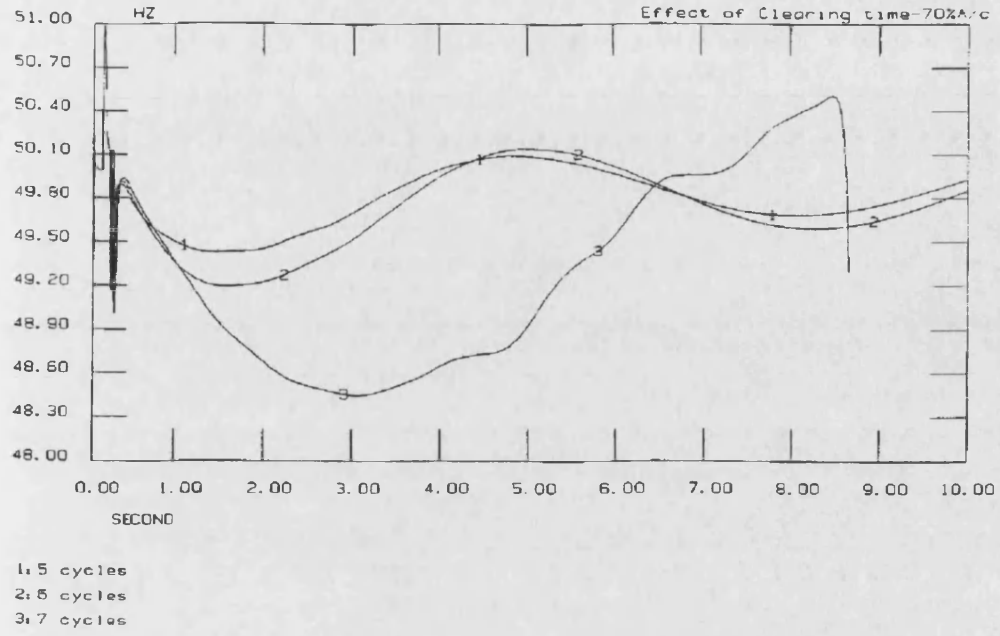

Figure (6.17) Case # 2 - Impact of fault clearing time on system frequency.

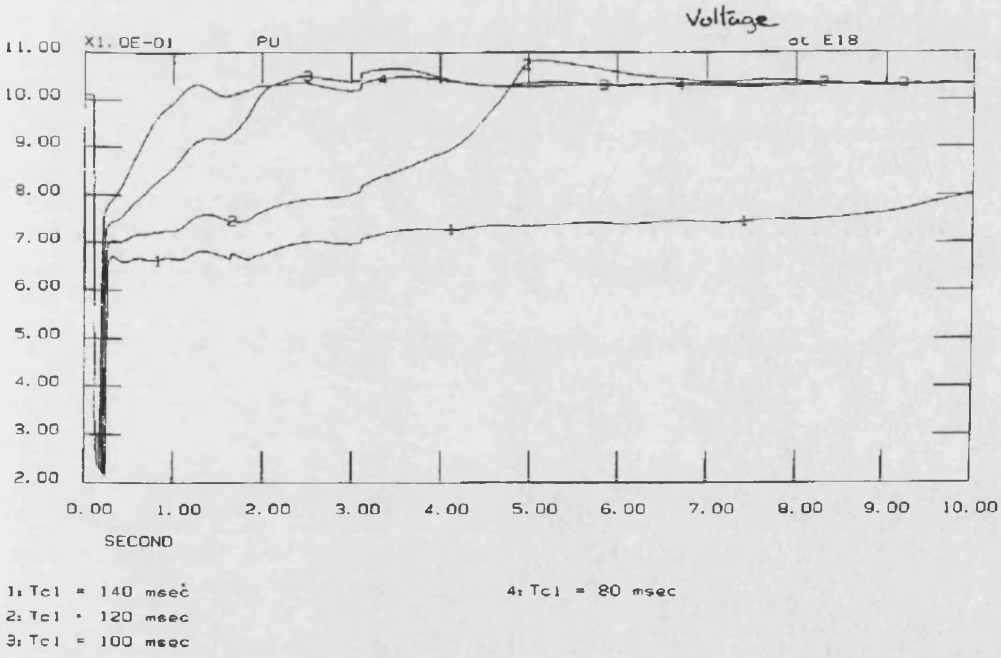

Figure (6.18) Case # 1 - Impact of fault clearing time on system voltage at Abu Dhabi.

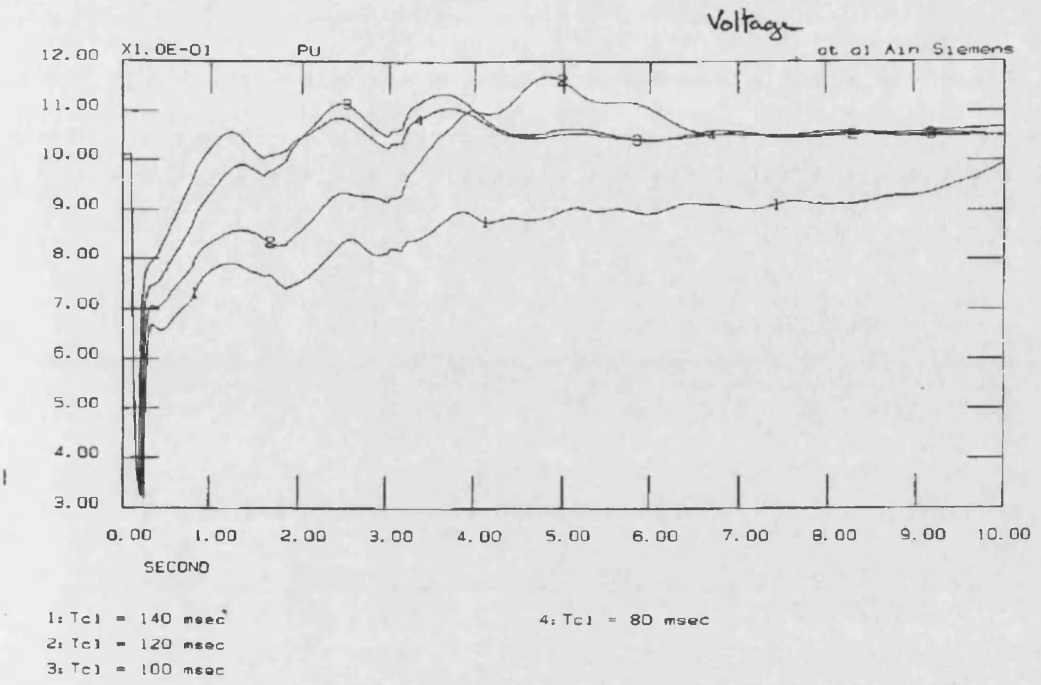

Figure (6.19) Case # 1 - Impact of fault clearing time on system voltage at Al-Ain.

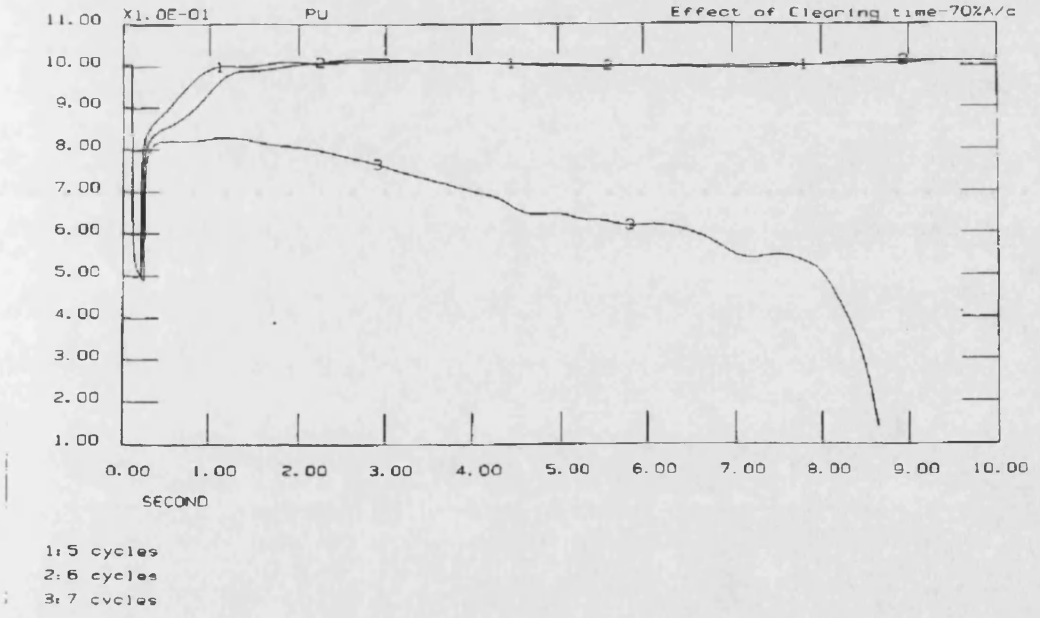

Figure (6.20) Case # 2 - Impact of fault clearing time on system voltage (70% A/C load).

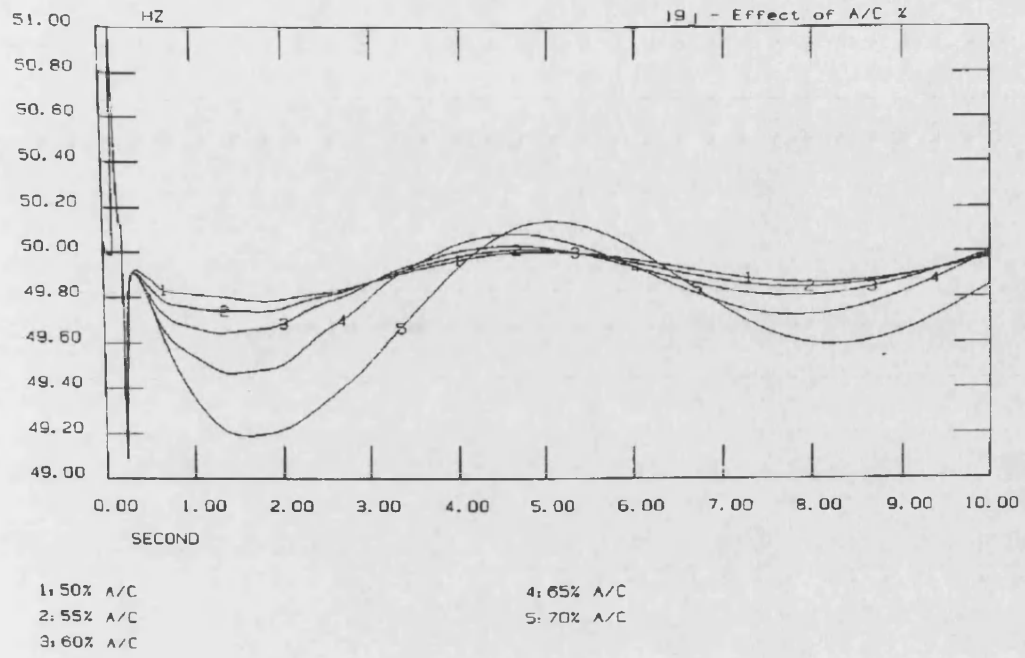

Figure (6.21) Case #2 - Impact of A/C load percentage on system frequency.

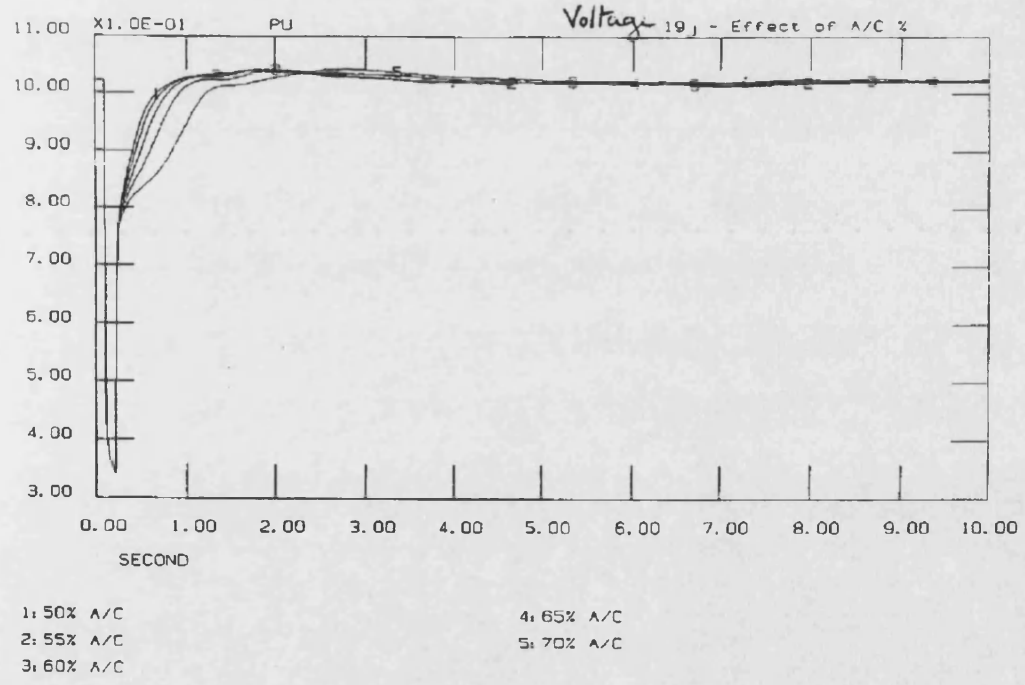

Figure (6.22) Case # 2 - Impact of A/C load percentage on system voltage.

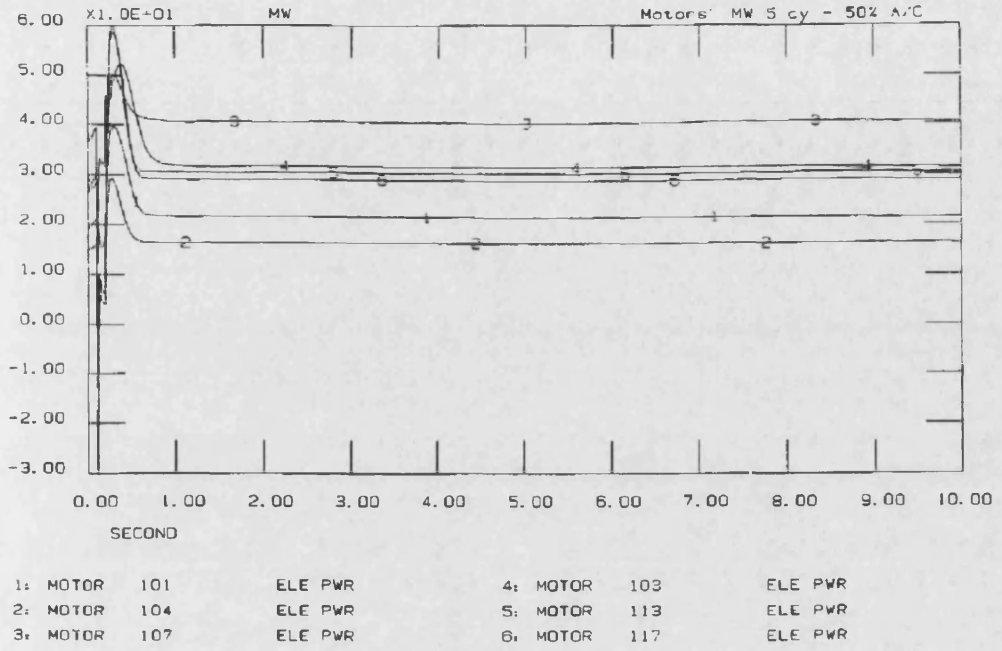

Figure (6.23) Case # 2 - Active power simulation of motors (5 cycles & 50% A/C load)

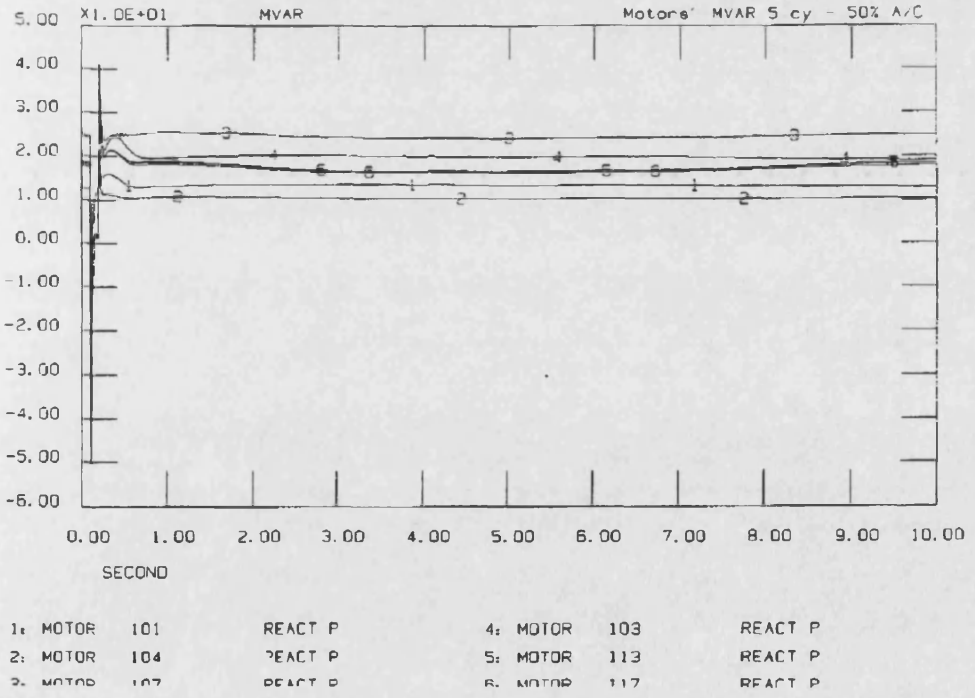

Figure (6.24) Case # 2 - Reactive power simulation of motors (5 cycles & 50% A/C load)

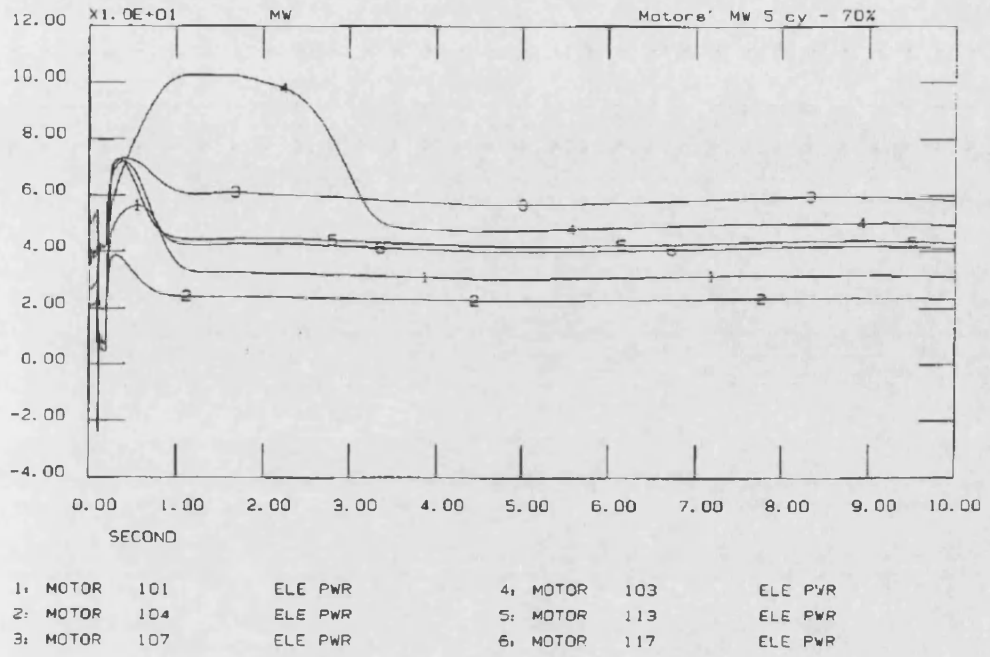

Figure (6.25) Case # 2 - Active power simulation of motors (5 cycles & 70% A/C load)

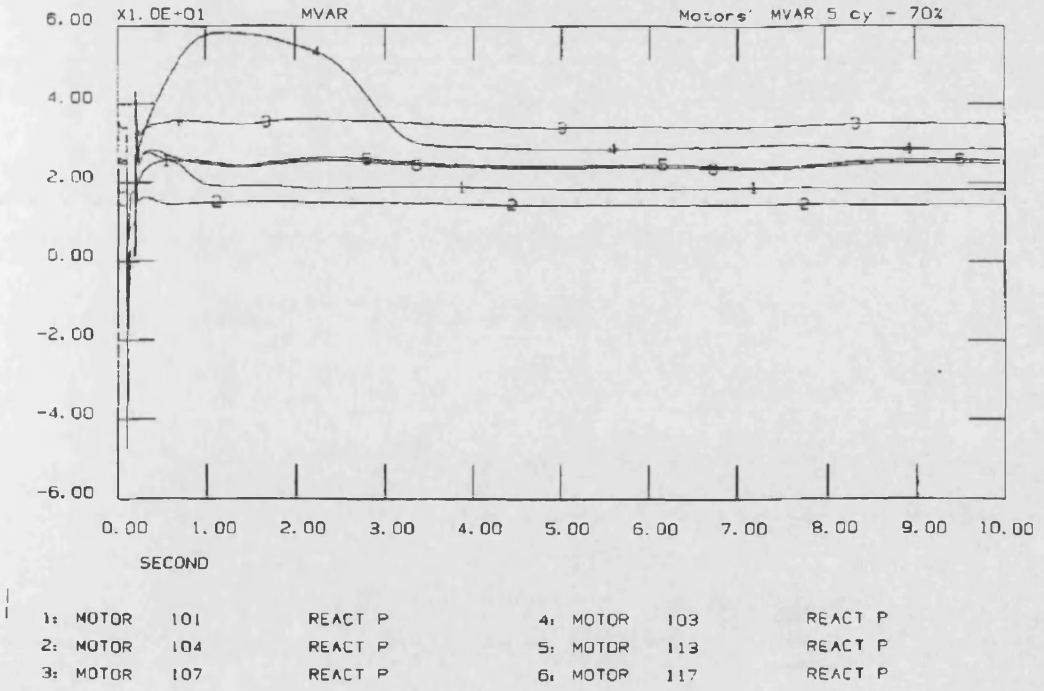

Figure (6.26) Case # 2 - Reactive power simulation of motors (5 cycles & 70% A/C load)

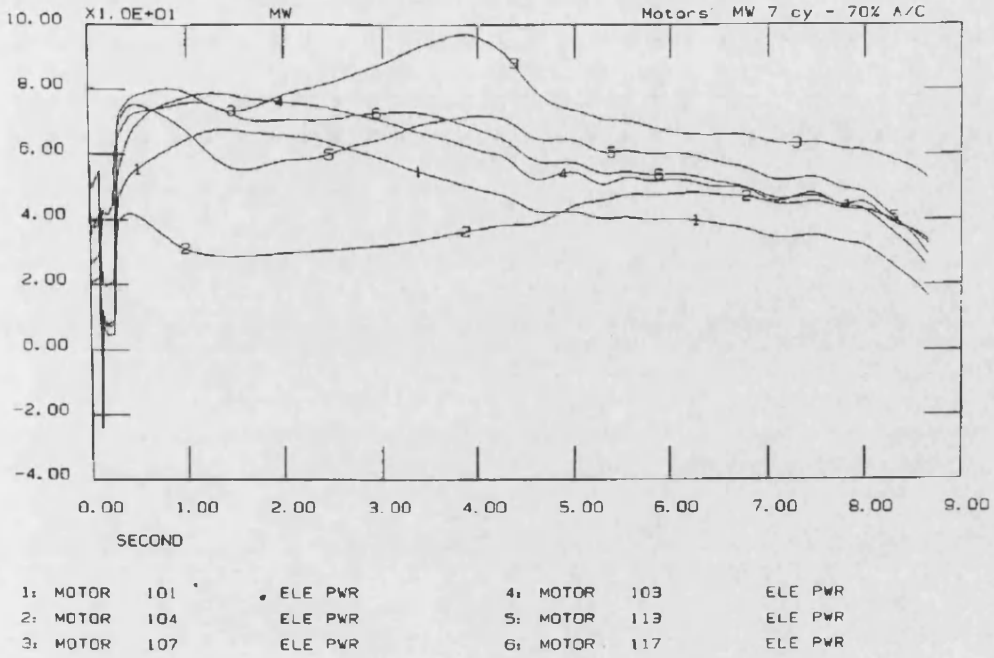

Figure (6.27) Case # 2 - Active power simulation of motors (7 cycles & 70% A/C load)

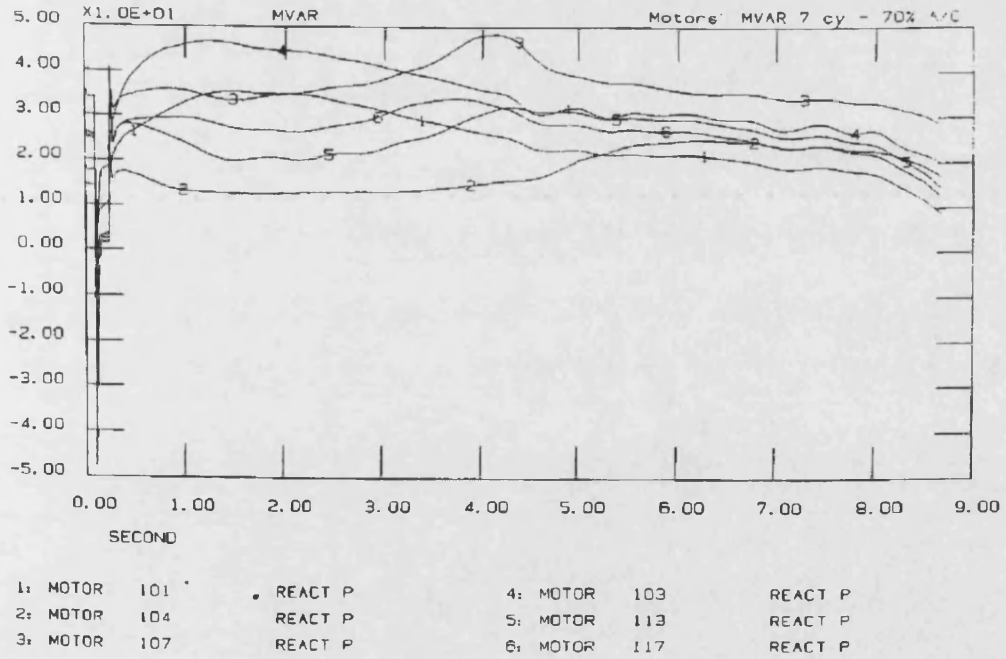

Figure (6.28) Case # 2 - Reactive power simulation of motors (7 cycles & 70% A/C load)

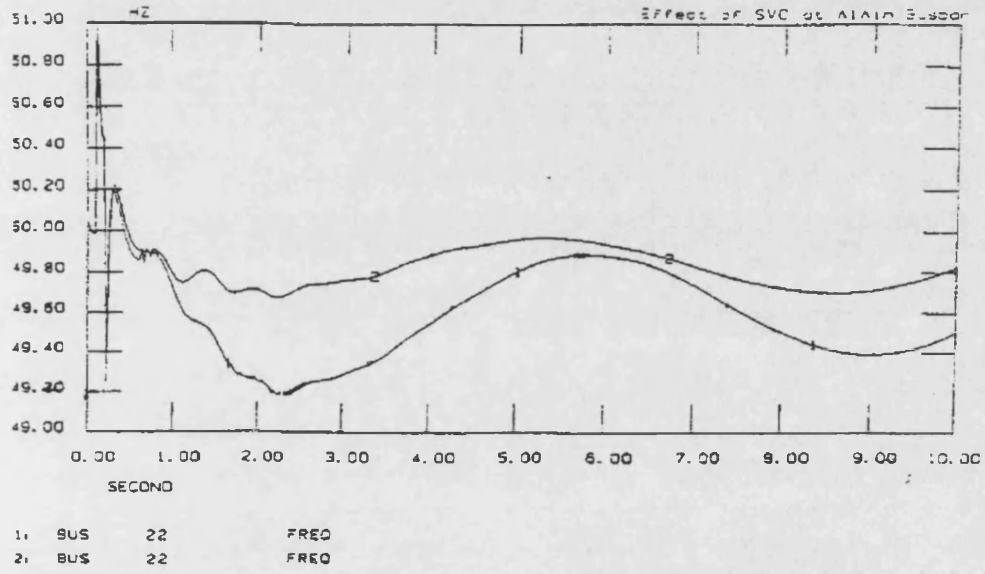

Figure (6.29) Case # 1 - Impact of Static VAR compensator (SVC =180 MVAR) on the system frequency simulation at Al-Ain substation (220 kV busbar).

CHAPTER 7

Conclusions and Recommendations

7.1 - Conclusions:

The use of simple static models in stability analysis may be adequate in cases where such models give the same results as more detailed dynamic models. Meanwhile, if the power system under study includes high percentage of dynamic load, stability studies should employ detailed dynamic load models in order to ensure simulations accuracy. Accordingly, the Abu Dhabi power utility (Water & Electricity Department) has emphasized the study of the low-voltage dynamic behavior of the single-phase A/C load, which is highly concentrated in the system, specially during the summer peak load. The main purpose was to build an efficient dynamic load model, which can accurately simulate the A/C load impact on the power system during faults.

To achieve such goal, the electrical parameters of the split-phase induction motor driving the single-phase A/C compressor, as well as the condenser fan motor of the A/C load, were identified by performing laboratory tests (DC, no-load, locked-rotor), which were detailed in most references. A special arrangement has been made while performing the locked-rotor test on the hermetic A/C compressor, since the compressor rotor was inaccessible. These tests were applied on three selected single-phase A/C compressors of different refrigeration capacities, covering the most available A/C units in the local market.

Based on the laboratory tests results, the following conclusions were reached:

1) The electrical parameters of A/C compressor load identified herein were more accurate than the parameters of earlier published works [16].

2) A mathematical formula was derived herein to determine an approximate and satisfactory value of the compressor slip, since it was impossible to measure the rotor speed of the hermetic compressor while running.

3) The mechanical torque characteristics of A/C compressor load was totally different than the mechanical load characteristics of the condenser fan motor. Despite such observed difference, earlier published works have aggregated the parameters of both A/C compressor and condenser fan motor to represent the A/C load model in stability analysis.

Accordingly, a new definition method of the single-phase A/C load mechanical torque characteristics was described in Chapter 4. The new definition method was partially derived from the measurement-based load modeling technique, where it has mainly depended on recording the compressor starting current by using a digital disturbance recorder, and calculating the corresponding dynamic compressor slip. Then, the dynamic slip curve was plotted, and the slopes $\left(\frac{dS}{dt}\right)$ were determined at starting, critical, and nominal slip values, where they were substituted in the induction motor dynamic equation, in addition to the corresponding values of the compressor electrical torque. Accordingly, the mechanical torque coefficients (A, B, and C) of each tested compressor were

determined, where they were aggregated afterwards to obtain the mechanical torque coefficients of the aggregated single-phase A/C compressor load.

Air-conditioners are likely to stall if they experienced voltage dips to less than 65% of nominal voltage, irrespective of fault clearing time [26]. An interruption in terminal voltage for longer than 0.2 seconds will result in the stalling of compressors with split phase motors [27]. The former statement has indicated the critical voltage limit of air-conditioner compressors, while neglecting a very important factor to be considered, which is the fault clearing time. Meanwhile, the latter statement has only indicated a time limit for fault clearance, regardless of the reduced terminal voltage level reached during faults.

The low-voltage dynamic behavior of the single-phase A/C compressor load was investigated by performing a transient simulation test, which has mainly subjected the compressor load to a simulated low-voltage transients for different duration. The compressor terminal voltage and stator current were recorded during the test runs by using the digital disturbance recorder, where the following conclusions have been reached:

1) Each tested compressor has stalled when the terminal voltage has reached a certain reduced level, which was called the *compressor critical voltage (V_{cr})*. This level was determined at 0.72 pu of nominal voltage for all tested compressors.

2) A mathematical formula was derived to simulate the actual test data, which related between the low terminal voltage and the maximum fault clearing time (t_{max}) needed to avoid the stalling of A/C compressor during faults. This relationship was found effective when the terminal voltage has been varied between 0.6 pu and 0.72 pu during the test, while below 0.6 pu voltage, the compressor load would stall instantaneously.

3) The distribution system reactance (X_d) had a very strong and distinctive impact on the compressor low-voltage dynamic behavior, when simulated in the test circuit. The reactance (X_d) was found to be inversely proportional with the maximum fault clearing time (t_{max}), where it has largely decreased the operational stability limits of the single-phase A/C compressor.

4) The slow-acting thermal overload relay has allowed the stalling compressor to withdraw high power from the system before being tripped, and during the consecutive reconnection intervals to the system when it was reset, while the internal gas pressure was not released yet. Therefore, the thermal overload relay equipped inside the A/C compressors has badly affected the system stability.

The new single-phase A/C load model was described by two non-linear differential equations, which were functions of the compressor stator current and slip. The newly defined mechanical torque coefficients were included in this new model, and the electrical torque was expressed in term of the compressor stator current. The new model was

simulated individually, before being adopted in the transient stability program, by applying the 4th order Runge-Kutta solution method in a commercial mathematical software (MathCAD 5.0). The model input was the compressor terminal voltage recorded during the transient simulation test, which was the forcing function exerting dynamic variations on the compressor system, while the model outputs were the compressor stator current and slip. Accordingly, the simulated compressor stator current was compared to the recorded compressor current of six selected typical test cases.

It was concluded that the new model simulations were satisfactorily matching with the actual test results, when compared to the simulations produced by an earlier published model [16]. This matching results have initially proved the improvement made in the new model, which was mainly the newly defined mechanical torque characteristics of the single-phase A/C compressor load. Sensitivity analysis performed on the new model parameters has proved the following results:

1) The fine tuning of the aggregated mechanical torque coefficients in defined narrow limits has further improved the new model simulations.

2) The new model simulations was improved when the A/C compressor load inertia constant was slightly increased. Therefore, such analysis has proved the favorable impact of robust motors transient response on the system stability.

The new A/C load model was adopted in the transient stability program to simulate two major fault cases, which have occurred in Abu Dhabi power system in recent years. When adopted in stability analysis, the new load model has produced improved system simulations compared to earlier published load model simulations, and which have greatly matched with the recorded system variables during transient.

Sensitivity analysis were performed in order to investigate the impact of the fault clearing time (t_c) and the A/C load percentage on the system and load variables. According to such analysis, the following conclusions have been reached:

1) Fast fault clearing is essential to avoid the disturbing impact of stalling A/C compressors and low-inertia motors on the system stability, due to their highly increased power requirements during faults. It has also enhanced the post-fault voltage recovery, which eliminate the probability of cascade stalling of many more A/C compressors and low-inertia motors.

2) The high percentage of A/C load had the same adverse impact of the increased fault clearing time on the system stability. For an increased A/C load percentage in the system, the expected number of stalling A/C compressors due to faults will be higher, which will consequently affect the system stability.

3) Some references [48] have claimed that voltage collapse could be prevented by the action of power transformers which are equipped with on-load tap changers. This is only true for the situations where the voltage collapse occurs

over a long time period of the order of minutes to hours. The time response of the mechanical tap changers is very slow to cope with the fast transient voltage collapse phenomena associated with loads of major induction motor content. For this situation, the injection of fast variable reactive power near the load centers, by means of fast-acting reactive power compensators (SVC), can effectively alleviate all voltage degradation and prevent any voltage collapse or instability in the system.

7.2 - Recommendations:

According to the work and conclusions detailed in the thesis, the following recommendations are emphasized to ensure enhanced stability and better performance of the power system:

7.2.1 - Improved dynamic load model:

1) It is recommended to improve the available database of dynamic load characteristics, so that new load data must be based on actual load characteristics derived from laboratory tests performed on different types of dynamic loads, such as fans, pumps, home appliances, etc. It is also recommended to study the dynamic behaviour and characteristics of rotary compressors during steady-state and transient conditions, so as to be compared with the piston-type compressors investigated in this thesis.

2) It is recommended to define the mechanical torque characteristics of different load types, specially those of high concentration in the power system, by applying the new definition procedure earlier detailed in the thesis.

3) A motor with light shaft load would run at a nearly constant speed over a considerable range of voltage [46]. This was true in the case of condenser fan motor, which did never stall when subjected to low-voltage simulated transients. Earlier published work [16] has aggregated the single-phase A/C compressor with the condenser fan motor to represent the A/C load model. As previously revealed in the thesis, there was a great difference between the mechanical torque characteristics of A/C compressor load and that of the condenser fan. Accordingly, it is recommended to represent the A/C load by the single-phase A/C compressor only, without aggregating the condenser fan motor with it.

4) It is recommended to develop the earlier published 2-motor dynamic model into a 3-motor model, by segregating the *"prone-to-stall"* motors group into two further subgroups of *"compressor"* and *"non-compressor"* motors. This was due to the high percentage of compressor load existing among the low-inertia motors connected to the power system, with its unique impact on the system transient response and stability, due to its mechanical torque characteristics different than other load types driven by small motors like fans, washing machines, dryers, etc.

5) It is recommended to include the distribution system reactance (X_d) in the system dynamic simulations, due to its important observed impact on the low-voltage dynamic behavior of A/C compressor load during test.

6) According to the sensitivity analysis previously detailed in Chapter 6, the A/C load percentage has a distinctive impact on the system dynamic simulations, and hence, on system stability. Therefore, it is recommended to define the accurate percentage of highly concentrated dynamic load while performing stability analysis of each individual power system.

7.2.2 - Improved system and load protection:

1) All three phase air-conditioners have under-voltage relays that trip the units off within 5 cycles when the supply voltage drops below (70%) [26]. Accordingly, it is recommended to back-up the thermal overload relay, equipped inside the single-phase A/C compressors, by an additional under-voltage relay with a suitable time delay. The under-voltage relay will disconnect the single-phase A/C compressor from the system when the voltage drops below a certain level during faults. The relay will not restore the supply unless the system voltage is fully recovered after a certain time delay, in order to release the refrigerant gas back pressure fully. The under-voltage trip level can be set at the earlier defined compressor critical voltage of 0.72 pu, or at the same low-voltage relay setting equipped in the three-phase A/C units of 0.70 pu.

2) Use of digital relays for fast and reliable system protection schemes.

3) Based on test results detailed earlier in Chapter 4, it is recommended to adopt an appropriate small fault clearing time setting ($t_c \leq 100$ milliseconds) in order to avoid the severe impact of stalling of A/C compressors and other low-inertia motors on the power system stability.

4) Review the setting of over-current and under-voltage protection on the 11 KV load feeders, considering the impact of stalling A/C compressors at the time of system faults.

5) Review the under-frequency load shedding scheme, based on the demonstrated phenomenon of frequency dip following to system faults.

6) Increase the voltage support on load busbars during faults by means of the static VAR compensator (SVC) in order to reduce the stalling phenomena of A/C compressors, and its impact on the system stability.

7.2.3 - Adaptive under-voltage load shedding scheme:

An adaptive under-voltage load shedding scheme is proposed herein to disconnect the heavily affected load feeders during the system abnormal conditions. The scheme is aimed to avoid the adverse impact of high reactive power consumed by the dynamic load on the system stability.

Based on test results, data of fault cases, and stability analysis, the behavior of total load reactive power at each load feeder has depended on the reduced system voltage during faults, the fault clearing time, the fault location relative to each load feeder, and on the load composition of the system feeders at the time of fault occurrence. Therefore, the proposed scheme will be based on an adaptive selection criteria, which will depend on the total load reactive power consumed by the aggregated dynamic load connected to each load feeder in the system during faults.

According to stability analysis, the load reactive power has highly increased when a relatively longer fault clearing time was combined with an increased A/C load percentage of the total load. The proposed load shedding scheme can be initiated when the system voltage drops down to 0.75 pu during faults, and which will followed by a continuous reactive power monitoring of each load feeder in the system. If the load feeder reactive power is highly sustained, then, the feeder in concern will be disconnected from the system after a certain appropriate time delay. On the other hand, if the load reactive power is quickly depressed after fault clearance, then, there will be no need to disconnect such feeder in order to avoid load over-shedding, and consequently, system instability.

The tripping time delay must mainly depend on the reached level of load reactive power at each feeder following system faults, as well as the fault clearing time. For an increased load reactive power and relatively longer fault clearing time, the tripping time delay must be reduced. Further studies are recommended in order to shed more light on the possible impact of such proposed under-voltage load shedding scheme on the system stability, as well as its interaction with the fast fault clearing aspect, the (SVC) operation, and the already adopted under-frequency load shedding scheme (UFLSS).

Appendix A

Aggregated models of a sample Residential & Industrial motors

A sample of residential and industrial motors are selected to show the procedure of motor aggregation as detailed in EPRI final report on load modeling EL-5003 Vol.1, research project 849-7, January 1987. Aggregation method "B" is used to build-up different aggregated motor models. To calculate the rotor resistance, the critical slip (slip at max. torque) is selected for all motors. All motors' data are in per-unit values.

Parameters of the aggregated models are calculated, then, their torque-slip characteristic curves are compared in order to indicate modeling improvements. Models under investigation are 1-motor, 2-motor, and 3-motor models, in addition to the composite motor model.

The selected residential & industrial load includes the following motor types:

Clothes washer	CWSH
Clothes dryer	DRYR
Refrigerator & freezer	REFR
Central A/C	RCAR
Room A/C	RRAR
Dishwasher	DWSH
Small industrial motors	SINM
Large industrial motors	LINM

Motors' Data

$i := 1..8$

$Rs_i :=$	$Xs_i :=$	$Xm_i :=$	$Rr_i :=$	$Xr_i :=$	$H_i :=$	$Lm_i :=$	$\sigma_i :=$	
0.11	0.12i	2.0i	0.11	0.13i	1.5	0.4	0.02	CWSH
0.12	0.15i	1.9i	0.13	0.14i	1.3	0.4	0.02	DRYR
0.056	0.087i	2.4i	0.053	0.082i	0.28	0.5	0.15	REFR
0.053	0.076i	2.4i	0.048	0.062i	0.28	0.6	0.4	RCAR
0.11	0.14i	2.8i	0.11	0.065i	0.28	0.5	0.01	DWSH
0.031	0.10i	3.2i	0.018	0.18i	0.7	0.6	0.1	SINM
0.10	0.10i	1.8i	0.09	0.06i	0.28	0.6	0.2	RRAR
0.013	0.067i	3.8i	0.009	0.17i	1.5	0.8	0.1	LINM

Appendix A

Aggregated 1-motor model

$Zs_i := Rs_i + Xs_i$ Stator impedance

$Zm_i := Xm_i$ Magnetizing reactance

$Zth_i := \frac{Zs_i \cdot Zm_i}{Zs_i + Zm_i}$ Thevenin's impedance

$Scr_i := \frac{Rr_i}{\sqrt{\left[Re\left(Zth_i\right)^2 + \left(Im\left(Zth_i\right) + Im\left(Xr_i\right)\right)^2\right]}}$ Critical slip

$Zr_i := \frac{Rr_i}{Scr_i} + Xr_i$ Rotor impedance

$Ysagg := \sum_i \frac{\sigma_i}{Zs_i}$ Aggregated stator admittance

$Zsagg := \frac{1}{Ysagg}$ Aggregated stator impedance

$Rsagg := Re(Zsagg)$ Aggregated stator resistance

$Xsagg := Im(Zsagg)$ Aggregated stator reactance

$Ymagg := \sum_i \frac{\sigma_i}{Zm_i}$ Aggregated magnetizing admittance

$Zmagg := \frac{1}{Ymagg}$ Aggregated magnetizing impedance

$Xmagg := Im(Zmagg)$ Aggregated magnetizing reactance

$Yragg := \sum_i \frac{\sigma_i}{Zr_i}$ Aggregated rotor admittance

$Zragg := \frac{1}{Yragg}$ Aggregated rotor impedance

$Scragg := \sum_i \sigma_i \cdot Scr_i$ Aggregated critical slip

$Rragg := Re(Zragg) \cdot Scragg$ Aggregated rotor resistance

$Xragg := Im(Zragg)$ Aggregated rotor reactance

$\sigma agg := \sum_i \sigma_i$ Aggregated weighting coefficient

$Lmagg := \sum_{i=1}^{8} \frac{\sigma_i \cdot Lm_i}{\sigma agg}$ Aggregated loading factor

Parameters:

$Rsagg = 0.053$ $Rragg = 0.055$ $Scragg = 0.308$ $\sigma agg = 1$

$Xsagg = 0.088$ $Xragg = 0.078$ $Xmagg = 2.37$ $Lmagg = 0.596$

Aggregated 2-motor model

In this model, motors are classified into 2 groups *"robust"* motors and *"prone-to-stall"* motors.

a) Robust motors:

$i := 1..2$

$Rs_i :=$	$Xs_i :=$	$Xm_i :=$	$Rr_i :=$	$Xr_i :=$	$H_i :=$	$Lm_i :=$	$\sigma_i :=$	
0.11	0.12i	2.0i	0.11	0.13i	1.5	0.4	0.02	CWSH
0.12	0.15i	1.9i	0.13	0.14i	1.3	0.4	0.02	DRYR

$Zs_i := Rs_i + Xs_i$ Stator impedance

$Zm_i := Xm_i$ Magnetizing reactance

$$Zth_i := \frac{Zs_i \cdot Zm_i}{Zs_i + Zm_i}$$ Thevenin's impedance

$$Scr_i := \frac{Rr_i}{\sqrt{\left[Re\left(Zth_i\right)^2 + \left(Im\left(Zth_i\right) + Im\left(Xr_i\right)\right)^2\right]}}$$ Critical slip

$$Zr_i := \frac{Rr_i}{Scr_i} + Xr_i$$ Rotor impedance

$$Ysr := \sum_i \frac{\sigma_i}{Zs_i}$$ Aggregated stator admittance

$$Zsr := \frac{1}{Ysr}$$ Aggregated stator impedance

$$\sigma r := \sum_i \sigma_i$$ Aggregated weighting coefficient

$$Rsr := Re(Zsr) \cdot \sigma r$$ Aggregated stator resistance

$$Xsr := Im(Zsr) \cdot \sigma r$$ Aggregated stator reactance

$$Ymr := \sum_i \frac{\sigma_i}{Zm_i}$$ Aggregated magnetizing admittance

$$Zmr := \frac{1}{Ymr}$$ Aggregated magnetizing impedance

$$Xmr := Im(Zmr) \cdot \sigma r$$ Aggregated magnetizing reactance

$$Yrr := \sum_i \frac{\sigma_i}{Zr_i}$$ Aggregated rotor admittance

$$Zrr := \frac{1}{Yrr}$$ Aggregated rotor impedance

$$Scrr := \frac{\sum_i \sigma_i \cdot Scr_i}{\sigma r}$$ Aggregated critical slip

$Rrr := Re(Zrr)\cdot\sigma r\cdot Scrr$ Aggregated rotor resistance

$Xrr := Im(Zrr)\cdot\sigma r$ Aggregated rotor reactance

$$Lmr := \frac{\sum_{i=1}^{2} \sigma_i \cdot Lm_i}{\sigma r}$$ Aggregated loading factor

Parameters:

Rsr = 0.115	Rrr = 0.119	Scrr = 0.421	σr = 0.04
Xsr = 0.134	Xrr = 0.135	Xmr = 1.949	Lmr = 0.4

b) Prone-to-stall Motors:

$i := 1..6$

$Rs_i :=$	$Xs_i :=$	$Xm_i :=$	$Rr_i :=$	$Xr_i :=$	$H_i :=$	$Lm_i :=$	$\sigma_i :=$	
0.056	0.087i	2.4i	0.053	0.082i	0.28	0.5	0.15	REFR
0.053	0.076i	2.4i	0.048	0.062i	0.28	0.6	0.4	RCAR
0.11	0.14i	2.8i	0.11	0.065i	0.28	0.5	0.01	DWSH
0.031	0.10i	3.2i	0.018	0.18i	0.7	0.6	0.1	SINM
0.10	0.10i	1.8i	0.09	0.06i	0.28	0.6	0.2	RRAR
0.013	0.067i	3.8i	0.009	0.17i	1.5	0.8	0.1	LINM

$Zs_i := Rs_i + Xs_i$ Stator impedance

$Zm_i := Xm_i$ Magnetizing reactance

$$Zth_i := \frac{Zs_i \cdot Zm_i}{Zs_i + Zm_i}$$ Thevenin's impedance

$$Scr_i := \frac{Rr_i}{\sqrt{\left[Re(Zth_i)^2 + \left(Im(Zth_i) + Im(Xr_i)\right)^2\right]}}$$ Critical slip

$$Zr_i := \frac{Rr_i}{Scr_i} + Xr_i$$ Rotor impedance

$$Ysp := \sum_i \frac{\sigma_i}{Zs_i}$$ Aggregated stator admittance

$$Zsp := \frac{1}{Ysp}$$ Aggregated stator impedance

$$\sigma p := \sum_i \sigma_i$$ Aggregated weighting coefficient

$$Rsp := Re(Zsp)\cdot \sigma p$$ Aggregated stator resistance

$$Xsp := Im(Zsp)\cdot \sigma p$$ Aggregated stator reactance

$$Ymp := \sum_i \frac{\sigma_i}{Zm_i}$$ Aggregated magnetizing admittance

$$Zmp := \frac{1}{Ymp}$$ Aggregated magnetizing impedance

$$Xmp := Im(Zmp)\cdot \sigma p$$ Aggregated magnetizing reactance

$$Yrp := \sum_i \frac{\sigma_i}{Zr_i}$$ Aggregated rotor admittance

$$Zrp := \frac{1}{Yrp}$$ Aggregated rotor impedance

$$Scrp := \frac{\sum_i \sigma_i \cdot Scr_i}{\sigma p}$$ Aggregated critical slip

$$Rrp := Re(Zrp)\cdot \sigma p \cdot Scrp$$ Aggregated rotor resistance

$$Xrp := Im(Zrp)\cdot \sigma p$$ Aggregated rotor reactance

$$Lmp := \frac{\sum_{i=1}^{6} \sigma_i \cdot Lm_i}{\sigma p}$$ Aggregated loading factor

$$\sigma 2r := \sigma r \cdot \frac{Lmr}{Lmr + Lmp}$$ Normalized weighting factor - robust motors

$$\sigma 2p := \sigma p \cdot \frac{Lmp}{Lmr + Lmp}$$ Normalized weighting factor - prone motors

Parameters:

Rsp = 0.052	Rrp = 0.053	Scrp = 0.303	σp = 0.96	σ2r = 0.016
Xsp = 0.087	Xrp = 0.077	Xmp = 2.392	Lmp = 0.604	σ2p = 0.578

Aggregated 3-motor model

a) Robust motors:

Same parameters as in the case of 2-motor model.

b) Prone-to-stall motors:

1- Compressor motors:

$i := 1..3$

$Rs_i :=$	$Xs_i :=$	$Xm_i :=$	$Rr_i :=$	$Xr_i :=$	$H_i :=$	$Lm_i :=$	$\sigma_i :=$	
0.056	0.087i	2.4i	0.053	0.082i	0.28	0.5	0.15	REFR
0.053	0.076i	2.4i	0.048	0.062i	0.28	0.6	0.4	RCAR
0.10	0.10i	1.8i	0.09	0.06i	0.28	0.6	0.2	RRAR

$Zs_i := Rs_i + Xs_i$ Stator impedance

$Zm_i := Xm_i$ Magnetizing reactance

$$Zth_i := \frac{Zs_i \cdot Zm_i}{Zs_i + Zm_i}$$ Thevenin's impedance

$$Scr_i := \frac{Rr_i}{\sqrt{\left[Re(Zth_i)^2 + \left(Im(Zth_i) + Im(Xr_i)\right)^2\right]}}$$ Critical slip

$$Zr_i := \frac{Rr_i}{Scr_i} + Xr_i$$ Rotor impedance

$$Ysc := \sum_i \frac{\sigma_i}{Zs_i}$$ Aggregated stator admittance

$$Zsc := \frac{1}{Ysc}$$ Aggregated stator impedance

$$\sigma c := \sum_i \sigma_i$$ Aggregated weighting coefficient

$$Rsc := Re(Zsc)\cdot\sigma c$$ Aggregated stator resistance

$$Xsc := Im(Zsc)\cdot\sigma c$$ Aggregated stator reactance

$$Ymc := \sum_i \frac{\sigma_i}{Zm_i}$$ Aggregated magnetizing admittance

$$Zmc := \frac{1}{Ymc}$$ Aggregated magnetizing impedance

$$Xmc := Im(Zmc)\cdot\sigma c$$ Aggregated magnetizing reactance

$$Yrc := \sum_i \frac{\sigma_i}{Zr_i}$$ Aggregated rotor admittance

$$Zrc := \frac{1}{Yrc}$$ Aggregated rotor impedance

$$Scrc := \frac{\sum_i \sigma_i \cdot Scr_i}{\sigma c}$$ Aggregated critical slip

$$Rrc := Re(Zrc)\cdot\sigma c\cdot Scrc$$ Aggregated rotor resistance

$Xrc := Im(Zrc)\cdot\sigma c$ Aggregated rotor reactance

$$Lmc := \frac{\sum_i \sigma_i \cdot Lm_i}{\sigma c}$$ Aggregated loading factor

Parameters:

$Rsc = 0.062$ $Rrc = 0.059$ $Scrc = 0.368$ $\sigma c = 0.75$

$Xsc = 0.084$ $Xrc = 0.065$ $Xmc = 2.204$ $Lmc = 0.58$

2- Non-compressor motors:

$i := 1..3$

$Rs_i :=$	$Xs_i :=$	$Xm_i :=$	$Rr_i :=$	$Xr_i :=$	$H_i :=$	$Lm_i :=$	$\sigma_i :=$	
0.11	0.14i	2.8i	0.11	0.065i	0.28	0.5	0.01	DWSH
0.031	0.10i	3.2i	0.018	0.18i	0.7	0.6	0.1	SINM
0.013	0.067i	3.8i	0.009	0.17i	1.5	0.8	0.1	LINM

$Zs_i := Rs_i + Xs_i$ Stator impedance

$Zm_i := Xm_i$ Magnetizing reactance

$$Zth_i := \frac{Zs_i \cdot Zm_i}{Zs_i + Zm_i}$$ Thevenin's impedance

$$Scr_i := \frac{Rr_i}{\sqrt{\left[Re(Zth_i)^2 + \left(Im(Zth_i) + Im(Xr_i)\right)^2\right]}}$$ Critical slip

$$Zr_i := \frac{Rr_i}{Scr_i} + Xr_i$$ Rotor impedance

$$Ysn := \sum_i \frac{\sigma_i}{Zs_i}$$ Aggregated stator admittance

$$Zsn := \frac{1}{Ysn}$$ Aggregated stator impedance

$$\sigma n := \sum_i \sigma_i$$ Aggregated weighting coefficient

$$Rsn := Re(Zsn)\cdot\sigma n$$ Aggregated stator resistance

$$Xsn := Im(Zsn)\cdot\sigma n$$ Aggregated stator reactance

$$Ymn := \sum_i \frac{\sigma_i}{Zm_i}$$ Aggregated magnetizing admittance

$$Zmn := \frac{1}{Ymn}$$ Aggregated magnetizing impedance

$$Xmn := Im(Zmn)\cdot\sigma n$$ Aggregated magnetizing reactance

$$Yrn := \sum_i \frac{\sigma_i}{Zr_i}$$ Aggregated rotor admittance

$$Zrn := \frac{1}{Yrn}$$ Aggregated rotor impedance

$$Scrn := \frac{\sum_i \sigma_i \cdot Scr_i}{\sigma n}$$ Aggregated critical slip

$$Rrn := Re(Zrn)\cdot\sigma n\cdot Scrn$$ Aggregated rotor resistance

$$Xrn := Im(Zrn)\cdot\sigma n$$ Aggregated rotor reactance

$$Lmn := \frac{\sum_i \sigma_i \cdot Lm_i}{\sigma n}$$ Aggregated loading factor

$$\sigma 3r := \sigma r\cdot\frac{Lmr}{Lmr + Lmc + Lmn}$$ Normalized weighting factor - robust motors

$$\sigma 3c := \sigma c\cdot\frac{Lmc}{Lmr + Lmc + Lmn}$$ Normalized weighting factor - compressor motors

$$\sigma 3n := \sigma n \cdot \frac{Lmn}{Lmr + Lmc + Lmn}$$

Normalized weighting factor - non-comp. motors

Parameters:

$Rsn = 0.021$	$Rrn = 0.018$	$Scrn = 0.072$	$\sigma n = 0.21$	$\sigma 3r = 0.01$
$Xsn = 0.083$	$Xrn = 0.168$	$Xmn = 3.435$	$Lmn = 0.69$	$\sigma 3c = 0.26$
				$\sigma 3n = 0.087$

Composite model

$j := 1..8$

$\sigma_j :=$

0.02
0.02
0.15
0.4
0.01
0.1
0.2
0.1

$Lm_j :=$

0.4
0.4
0.5
0.6
0.5
0.6
0.6
0.8

$$\sigma c_j := \sigma_j \cdot \frac{Lm_j}{\sum_{j=1}^{8} Lm_j}$$

Normalized weighting factor for composite model

Appendix A

Simulation of torque-speed characteristics curves of aggregated models:

$n := 1..999$ $\quad i := 1..14$

$S_n := \frac{n}{1000}$ $\quad \omega_n := 1 - S_n$

$Rs_i :=$	$Xs_i :=$	$Xm_i :=$	$Rr_i :=$	$Xr_i :=$	$\sigma_i :=$
0.11	0.12i	2.0i	0.11	0.13i	0.02
0.12	0.15i	1.9i	0.13	0.14i	0.02
0.056	0.087i	2.4i	0.053	0.082i	0.15
0.053	0.076i	2.4i	0.048	0.062i	0.4
0.11	0.14i	2.8i	0.11	0.065i	0.01
0.031	0.10i	3.2i	0.018	0.18i	0.1
0.10	0.10i	1.8i	0.09	0.06i	0.2
0.013	0.067i	3.8i	0.009	0.17i	0.1
0.053	0.088i	2.37i	0.055	0.078i	1.0
0.115	0.134i	1.949i	0.119	0.135i	0.04
0.052	0.087i	2.392i	0.053	0.077i	0.96
0.115	0.134i	1.949i	0.119	0.135i	0.04
0.062	0.084i	2.204i	0.059	0.065i	0.75
0.021	0.083i	3.435i	0.018	0.168i	0.21

σc_j

0.002
0.002
0.017
0.055
0.001
0.014
0.027
0.018

$\sigma 2r = 0.016$ $\quad \sigma 3r = 0.01$

$\sigma 2p = 0.578$ $\quad \sigma 3c = 0.26$

$\sigma 3n = 0.087$

$Zs_i := Rs_i + Xs_i$ $\quad Zm_i := Xm_i$ $\quad V := 1.0$

$Zth_i := \frac{Zs_i \cdot Zm_i}{Zs_i + Zm_i}$ $\quad Z_i := Rs_i + (Xs_i + Xm_i)$

$$Te_{i,n} := \frac{\left(\frac{Im(Xm_i)}{|Z_i|}\right)^2 \cdot \left(\frac{Rr_i}{S_n}\right) \cdot V^2}{\left(Re(Zth_i) + \frac{Rr_i}{S_n}\right)^2 + (Im(Zth_i) + Im(Xr_i))^2}$$ Electrical torque

$T11_n := \sigma_9 \cdot Te_{9,n}$ 1-motor model torque

$T22_n := \sigma 2r \cdot Te_{10,n} + \sigma 2p \cdot Te_{11,n}$ 2-motor model torque

$T33_n := \sigma 3r \cdot Te_{12,n} + \sigma 3c \cdot Te_{13,n} + \sigma 3n \cdot Te_{14,n}$ 3-motor model torque

$Tcc_n := \sum_j \sigma c_j \cdot Te_{j,n}$ Composite model torque

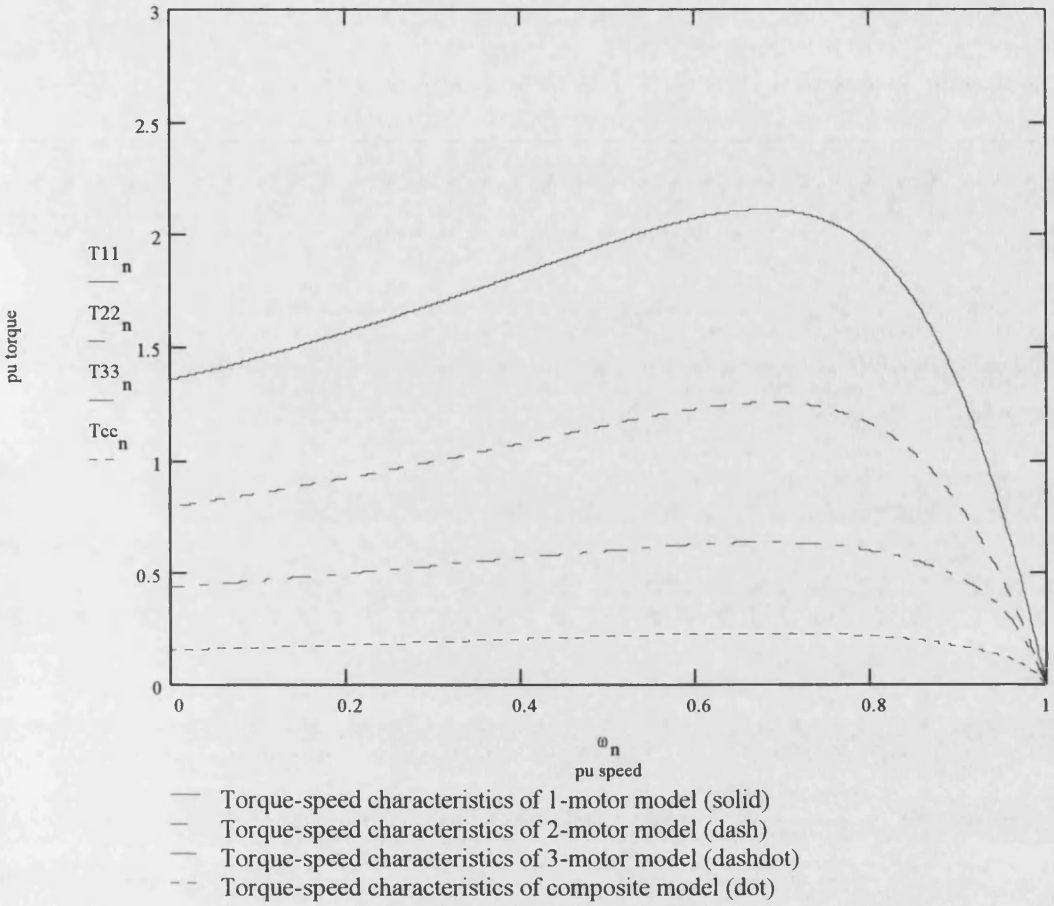

T-S characteristics of 1-motor, 2-motor, 3-motor, and composite model.

Appendix B

Digital disturbance recorder

1- Tasks and functions:

Digital disturbance recorders are a microprocessor-based data acquisition units, installed at different substations and connected to the measuring instruments of specific feeders in the power system. These recorders are mainly suitable for the monitoring, acquisition, and presentation of system transient data [18,19,20,21,28].

When fault occurs, recorders are triggered automatically, and the voltage and current signals are recorded in a digital form, then stored in local buffers. The recorded disturbance data are transmitted to a central station computer for evaluation and analysis. This could be done either automatically through an appropriate communication means, or manually off-loaded on removable storage cassettes.

Data conversion software has been developed and implemented in the central computer, to convert the recorded transient data into a suitable form for use in stability analysis. Different load characteristics over wide range of disturbance conditions can be more accurately defined. Consequently, this will lead to a better estimated load model parameters.

Appendix B

The digital disturbance recorder essentially fulfills the following functions:

1) Continuous monitoring of the connected binary and analog signals, and storage of their history.

2) Storage of these signals in a binary buffer when an event occurs. Several events can be stored temporarily. Their exact number depends on the number of signals acquired, sampling rate, and event duration.

3) Establishing and storing the exact event time, which is determined by the internal clock with a resolution of 10 ms for each event.

4) Transmission of disturbance data from RAM memory of the recorder to the mass storage memory of a remote evaluation station. The recorder should be capable of retaining data of several disturbance events before they must be transferred.

5) Optional re-recording of data from the buffer store to a magnetic cassette when required, as a record, transport medium, or as a "back-up" when transmission fails.

6) The disturbance state recognition should be based on either internally generated criteria like system variable level and rate of change of variable, or by an external triggering signal initiated manually or through a relay contact closure.

2- Hardware description:

Most of the old recorders used analog transducers for measuring active and reactive power, and then digitized their outputs. In general, (PQ) analog transducers have the following disadvantages:

1) Inherent time delay of recorded data (200 - 400 ms for slow response transducers, and 50 - 80 ms for fast response transducers).

2) Complex measuring circuit of (PQVF).

3) Additional burdens on (UPS).

Latest technology allows the direct digitization of analog voltage and current input signals, with the (PQ) computation function implemented on the central computer. Mainly, the digital disturbance recorder consists of signal isolation modules, followed by multiple voltage and current input stages.

Each analog input signal is fed through a low-pass filter for signal conditioning. All filtered signals are multiplexed and fed onto a holding circuit before passing through the analog-to-digital (A/D) converter. An advanced type of (A/D) converter can convert analog signals at high frequencies into digital amplitude samples. Typically, a 12 bit (A/D) converter can give an improved amplitude accuracy less than 0.025%. The effect of such accuracy can be easily noticed when recording high currents during faults or motors'

starting. The accuracy of (A/D) converter and the suitable data sampling rate will provide best results of the disturbance recorder.

A built-in microcomputer module controls and supervises the whole data acquisition process within the recorder. The program that determines the behavior of the recorder is stored in ROM (Read Only Memory) on the same module. The module also contains a RAM (Random Access Memory), which serves as a storage buffer for recorded data, and the serial interface for the optional cassette recorder unit. Figure (B-1) illustrates the architecture of digital disturbance recorder.

Each recorder, or data acquisition unit, has a control console which permits its manual operation. For this purpose, the control console contains the following elements:

1) A numerical display and LED's status indication for memory capacity, hardware failure, status of input channels, number of recorded events, error codes, etc.

2) Push button keys to select and enter data, such as date and time of recording, initiating test event, etc.

3) Plug-in jumpers for setting the station parameters, such as trigger settings, signals sampling rate, recording time, pre-history time, data transmission parameter, recorder designation, number of blocked input channels, etc.

4) A built-in diagnostics to test the integrity of the recorder circuitry and its operation.

The recorder must have a secure power supply (UPS), independent of station power supply. This countermeasure is very important to ensure reliable recorder operation during disturbances, and to protect recorded data.

3- Triggering condition:

Upon sensing abnormal conditions, the recorder located at each load feeder will be triggered. Only a few cycles of the normal waveforms are recorded as initial pre-trigger or pre-fault data, leaving the major part of the memory to capture the fast sub-transient and transients associated with the fault. The following options can be selected to trigger the recorder:

1) Change of the configured binary signal from 0 $\rightarrow$1 or 1$\rightarrow$ 0.

2) Manual instruction via the control console in "TEST" mode.

3) Several scanned peak values of the monitored analog channels are located outside the limits. The peak values are formed by taking into account the maximum positive value of consecutive 20 ms intervals. The peak values are observed separately according to under-run (LOW) or over-run (HIGH) of the limit. Triggering occurs when the planned number of over-runs or under-runs is achieved. During an under or over-run, a start recording signal is generated as long as the analog values are out of limits. Figure (B-2) illustrates a typical transient waveform with high and low limits and triggering signal.

4) The rate of change (gradient) of an analog input is greater than the allowed preset value. To determine the rate of change, the peak values of the monitored analog input within 20 ms intervals are compared. Figure (B-3) illustrates a typical analog waveform with peaks of different amplitudes.

4- Waveforms reproduction and sampling rate:

To reproduce accurate waveforms, the analog input signals must be derived from electromagnetic instrument transformers. Capacitor voltage transformer (CVT) should be avoided as they may suppress the flow of signals due to high frequency during disturbances, which will lead to measurement errors.

Typically, the recorder can measure and record 3-∅ currents in the range between 0.1 and 1 pu, and 3-∅ bus voltages in the range between 0.5 and 1.2 pu. In practice, the sampling rate must be programmable (500 Hz - 4000 Hz) in order to ensure proper storage and accurate reproduction of recorded waveforms.

Errors in waveforms reproduction can be caused by a non-suitable rate, or by an inadequate frequency response of input filters. The recorder should have the capability for logging windows of disturbance data with sampling rates as specified. Figure (B-4) illustrates a typical window of disturbance data with its sampling rates.

5- Recording time:

The recording time (TR) per event is composed into three parts:

1) The pre-history time (TVG), prior to the actual start signal for recording the event.

2) The actual recording time (TE) of the event, which begins with the start signal.

3) The post-history time (TNG), which follows the disappearance of the start signal.

Figure (B-5) illustrates a typical diagram showing different parts of recording time. The length of the start signal (TST) is in principle not restricted by the length of the recording time (TE). Generally, the following two recording modes are possible:

1) In recording mode (A), the recording time (TE) is determined by the length of start signal (TST).

2) In recording mode (B), the recording time (TE) is completely independent of the length of start signal (TST). It only has a pre-defined maximum limit.

A minimum recording time (Te_{min}) is required with a very short start signal. However, if the start signal (TST) is larger than the maximum limit of recording time (TE), then it's limited to (TE_{max}).

6- Data reduction:

The data reduction parameters allow to reduce the amount of data to be transferred when an event occurs. The input signals are cut into blocks of a definable length. If a block is very similar to the last block transmitted (signal difference <= allowed difference), no more data will be transmitted.

This arrangement allows to reduce transmission time considerably for stable portions of the signal. The greater the maximum allowed difference between two blocks, less data will have to be transferred. A good selected value for the maximum allowed difference is 10, which corresponds to loss of accuracy not greater than 0.5%.

The data block length is equal to the sampling rate divided by the mains frequency. If the result is an integer value, it can be used directly as a block length. On the other hand, if it contains a fraction part, a multiple of the result has to be considered to eliminate this fraction. For example, for a sampling rate of 2000 Hz and mains frequency of 50 Hz, the data block length will be directly calculated as 40. For the same sampling rate and mains frequency of 60 Hz, the calculated block length equals to 33.333. Therefore, the data block length is set at 100, which is a multiple of 33.333 in order to eliminate the fraction. Figure (B-6) illustrates a block diagram showing the data reduction process.

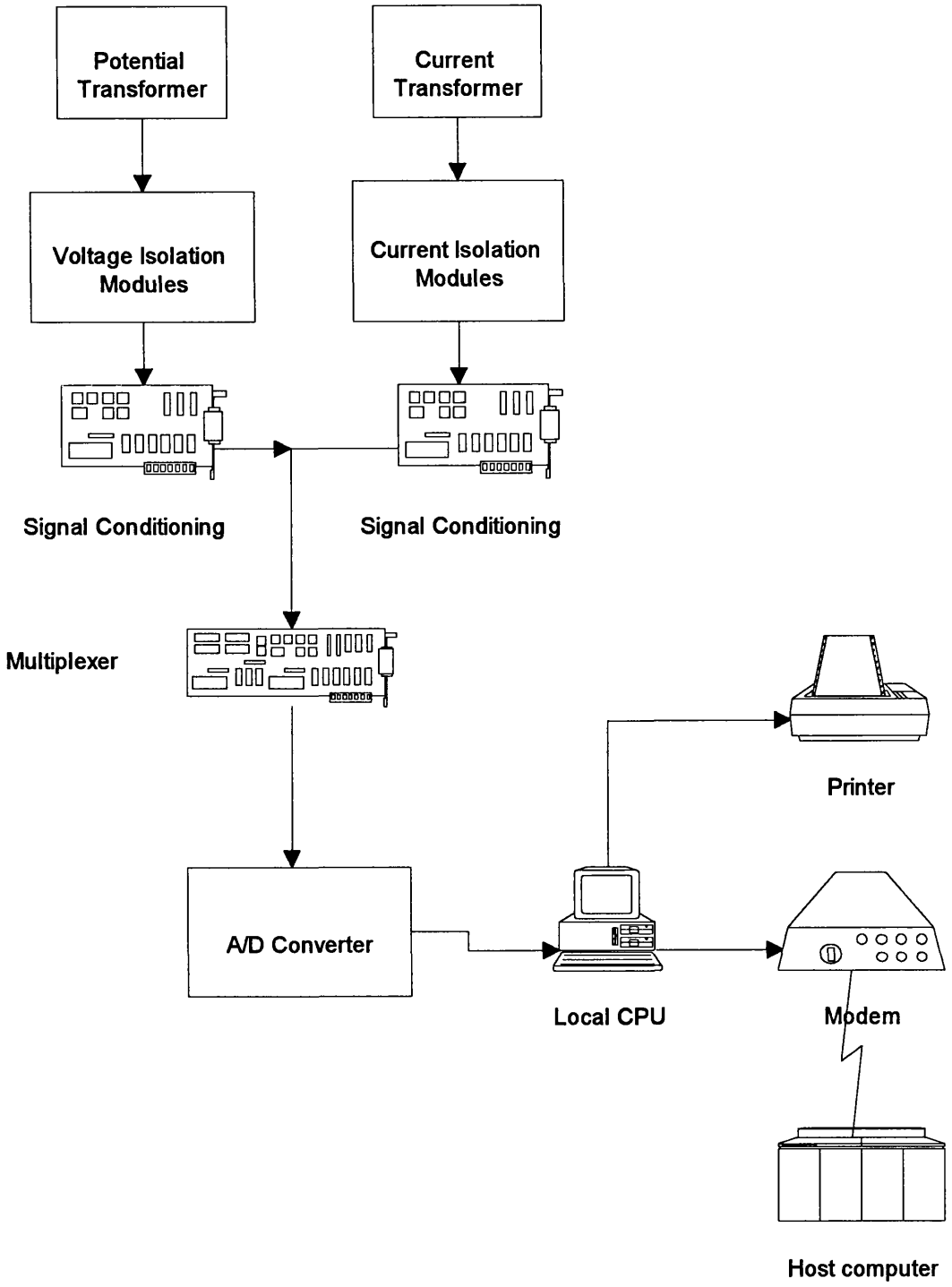

Figure (B-1) Architecture of digital disturbance recorder.

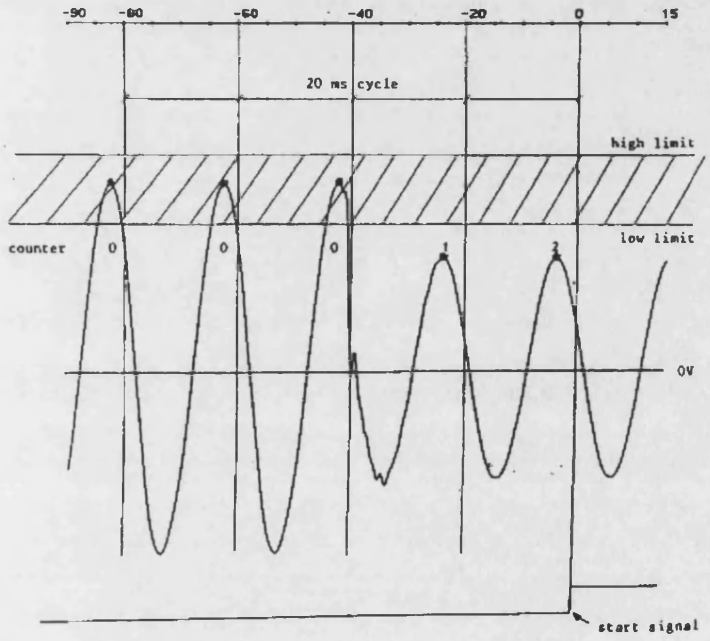

Figure (B-2) Typical transient waveform showing high and low limits.

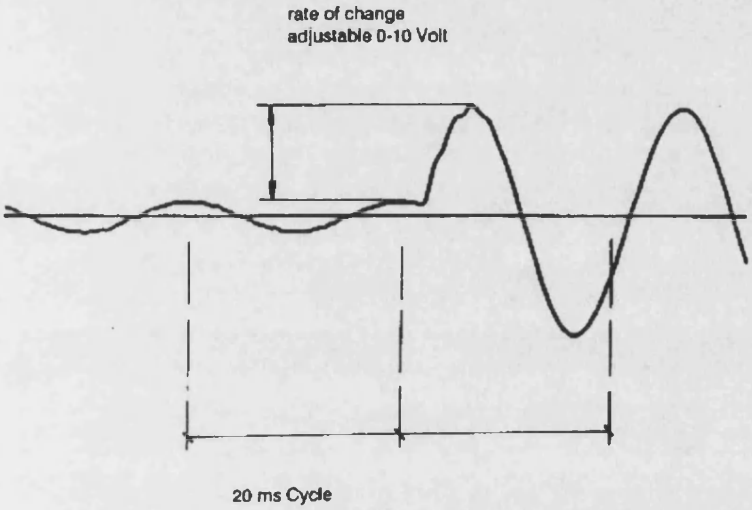

Figure (B-3) Rate of change of waveform.

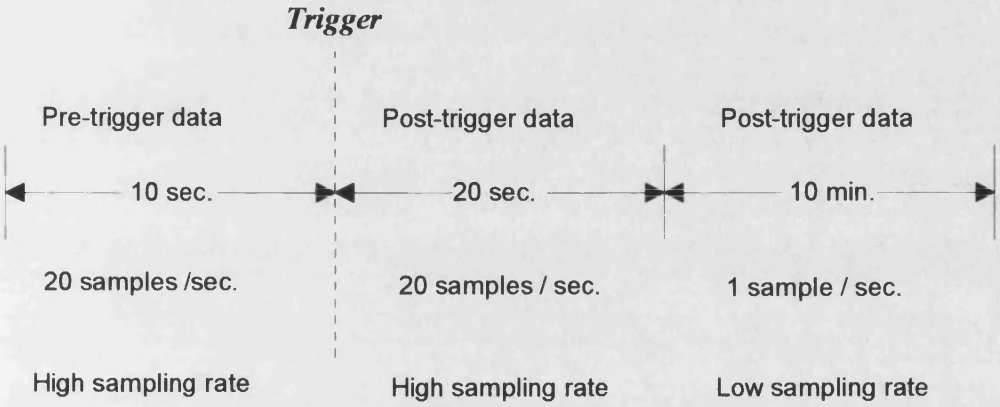

Figure (B-4) Typical window of disturbance with sampling rate.

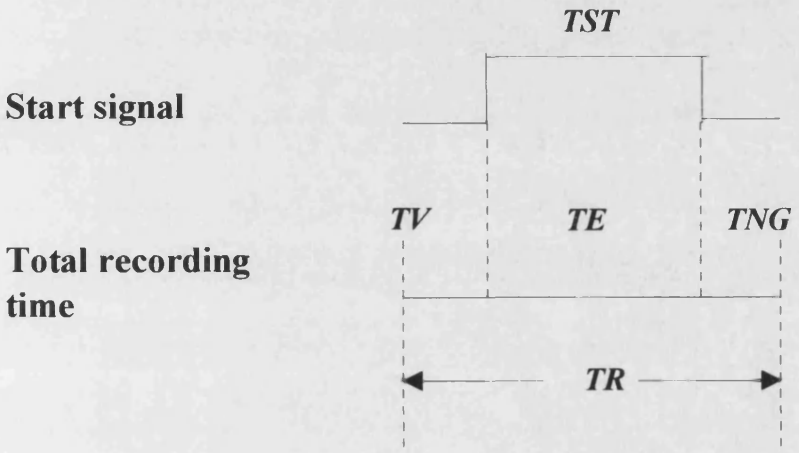

Figure (B-5) Diagram of typical recording time.

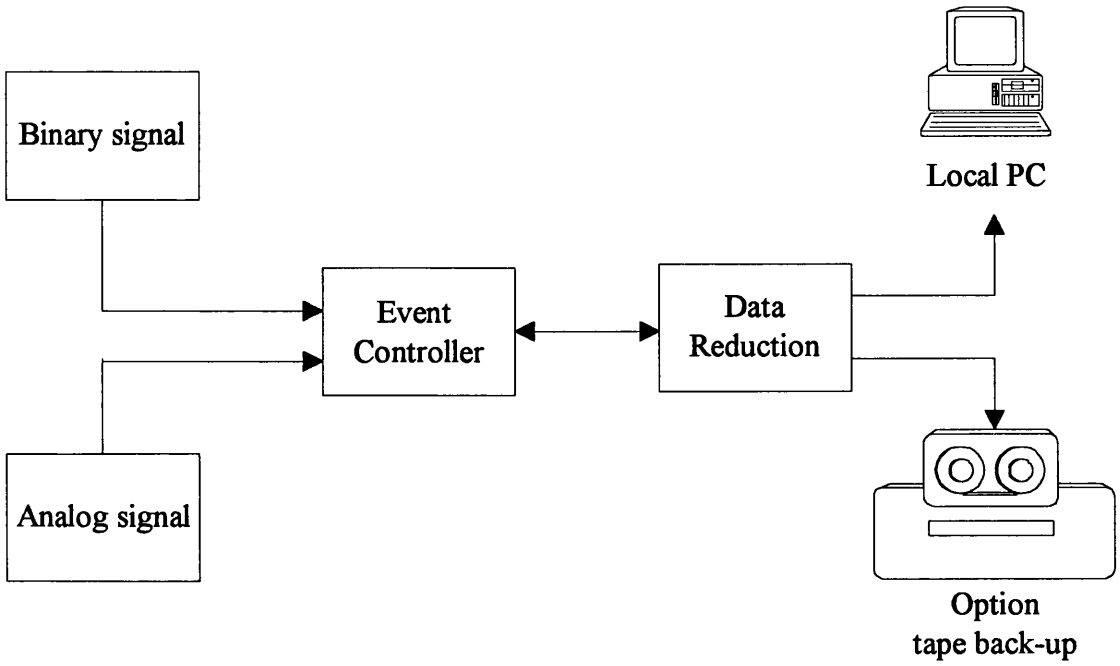

Figure (B-6) Block diagram of data reduction process.

Appendix C

A - Parameters Identification of Compressors:

1 - Manufacturers' Technical Data:

	Electrical characteristics				Mechanical characteristics			
Model	**LRA**	**RLA**	**EER**	**KVA**	**BTU/hr**	**kcal/hr**	**D (mt.)**	**G (kgs.)**
AW5520E	51.0	9.0	9.78	2.070	17,600	4435	0.12	11.3
AB5522F	50.5	10.4	8.61	2.392	18,330	4619	0.12	11.3
AW5524E	54.0	9.7	10.00	2.231	21,000	5292	0.12	11.3

LRA = locked-rotor current (amp)

RLA = rated current (amp)

EER = energy efficiency ratio

D = diameter of gyration (meter)

G = weight of rotating parts (kilograms)

2 - Tests' Data :

	DC test		No-Load test			Locked-rotor test		
Model	V_{dc}	I_{dc}	V_{nl}	I_{nl}	P_{nl}	V_{br}	I_{br}	P_{br}
AW5520E	14.8	8.85	230	3.55	640	60	11	500
AB5522F	14.0	8.32	230	5.35	600	60	13.5	440
AW5524E	14.0	9.96	230	4.30	880	60	16	640

3 - Compressors' Parameters:

Stator resistance $$r_1 = \frac{V_{dc}}{I_{dc}}$$

Core resistance $$R_c = \frac{V_{nl}^{\ 2}}{P_{nl}}$$

Magnetizing current $$I_m = \sqrt{I_{nl}^{\ 2} - \left(\frac{V_{nl}}{R_c}\right)^2}$$

Magnetizing reactance $$X_m = \frac{V_{nl}}{I_{nl}}$$

Locked-rotor impedance $$Z_{br} = \frac{V_{br}}{I_{br}}$$

Locked-rotor resistance $$R_{br} = \frac{P_{br}}{I_{br}^2}$$

Rotor resistance $$r_2 = R_{br} - r_1$$

Locked-rotor reactance $$X_{br} = \sqrt{Z_{br}^2 - R_{br}^2}$$

Stator reactance $$x_1 = 0.3 * X_{br}$$

Rotor reactance $$x_2 = 0.7 * X_{br}$$

Input power $$P_{in} = \frac{BTU}{EER}$$

Slip $$S = \frac{-\left(2 * r_1 - \frac{V_{ph}^2}{P_{in}}\right) - \sqrt{\left(2 * r_1 - \frac{V_{ph}^2}{P_{in}}\right)^2 - 4 * r_1^2}}{2 * \left(\frac{r_1^2}{r_2}\right)}$$

Inertia constant $$H = \frac{1.363 * 10^{-6} * G^2 * D^2 * (rpm)^2}{KVA}$$

Model	r_1	x_1	R_c	X_m	r_2	x_2	H	S
AW5520E	1.672	0.862	82.66	104.335	0.811	2.011	0.241	0.031
AB5522F	1.683	1.119	176.33	44.328	0.732	2.612	0.200	0.034
AW5524E	1.406	0.839	60.12	117.203	1.094	1.957	0.242	0.049

4 - Per-Unit Values:

The per-unit values of all compressors' parameters were calculated based on their KVA and voltage ratings. The base current is given by:

$$I_{base} = \frac{(KVA) * 1000}{V_{ph}}$$

and the base impedance equals to:

$$Z_{base} = \frac{V_{ph}}{I_{base}}$$

Model	r_1	x_1	X_m	r_2	x_2	H	S
AW5520E	0.065	0.034	4.083	0.032	0.079	0.251	0.031
AB5522F	0.076	0.051	2.004	0.033	0.118	0.200	0.034
AW5524E	0.059	0.035	4.943	0.046	0.083	0.242	0.049

B - Parameters Identification of Condenser Fan Motor:

1 - Manufacturer Technical Data:

Power = ¼ HP

Voltage = 1-∅ - 220/240 v

Current = 1.8 A

frequency = 50 Hz

Speed = 1100 rpm (highest)

2 - Tests' Data:

	DC Test		No-Load Test			Locked-Rotor Test		
Winding	**Vdc**	**Idc**	V_{nl}	I_{nl}	P_{nl}	V_{br}	I_{br}	P_{br}
High speed	14	1.15	230	0.90	132	70	1.30	80
Medium speed	14	0.90	230	0.70	100	70	0.95	60
Low speed	14	0.75	230	0.65	64	70	0.75	50

3 - Motor Parameters:

Winding	r_1	x_1	X_m	r_2	x_2	H	S
High speed	12.174	10.265	331.761	35.163	15.398	0.026	0.136
Medium speed	15.556	12.709	419.248	50.926	19.064	0.026	0.202
Low speed	18.667	11.383	391.538	70.222	17.075	0.026	0.287

Since the fan motor is of Design Class B, the stator and rotor reactance were calculated based on the following proportions:

$$x_1 = 0.4 * X_{br} \qquad x_2 = 0.6 * X_{br}$$

4 - Per-Unit Values:

The base impedance of condenser fan motor was calculated using its nominal voltage and current, and the parameters per-unit values are shown in the following table:

Winding	r_1	x_1	X_m	r_2	x_2	H	S
High speed	0.095	0.080	2.596	0.275	0.121	0.026	0.136
Medium speed	0.122	0.099	3.281	0.399	0.149	0.026	0.202
Low speed	0.146	0.089	3.064	0.550	0.134	0.026	0.287

Appendix D-1

Simulation of electrical torque-speed characteristics:

$i := 1..7$

$r1_i :=$	$x1_i :=$	$Xm_i :=$	$r2_i :=$	$x2_i :=$	$H_i :=$	$S_i :=$	
0.065	0.034i	4.083i	0.032	0.079i	0.241	0.031	17,600 BTU
0.076	0.051i	2.227i	0.033	0.118i	0.200	0.034	18,330 BTU
0.059	0.035i	4.943i	0.046	0.083i	0.242	0.049	21,000 BTU
0.121	0.089i	2.980i	0.408	0.135i	0.026	0.208	Fan motor
0.100	0.100i	1.800i	0.090	0.060i	0.280	0.100	EPRI
0.066	0.039i	3.293i	0.066	0.091i	0.227	0.038	Agg. compressor
0.071	0.043i	3.240i	0.156	0.096i	0.196	0.065	Agg. comp. + fan

$n := 1..999$ $\quad V := 1$ nominal voltage

$S_n := \frac{n}{1000}$ $\quad \omega_n := 1 - S_n$ speed

$Zs_i := r1_i + x1_i$ stator impedance

$Zo_i := r1_i + (x1_i + Xm_i)$ open-circuit impedance

$Zm_i := Xm_i$ magnetizing impedance

$Zth_i := \frac{Zs_i \cdot Zm_i}{Zs_i + Zm_i}$ Thevenin impedance

$Rth_i := Re(Zth_i)$ $\quad Xth_i := Im(Zth_i)$

$$Te_{i,n} := \frac{\left(\frac{Im(Xm_i)}{|Zo_i|}\right)^2 \cdot \frac{r2_i}{S_n} \cdot V^2}{\left(Rth_i + \frac{r2_i}{S_n}\right)^2 + \left(Xth_i + Im(x2_i)\right)^2}$$

Electrical torque

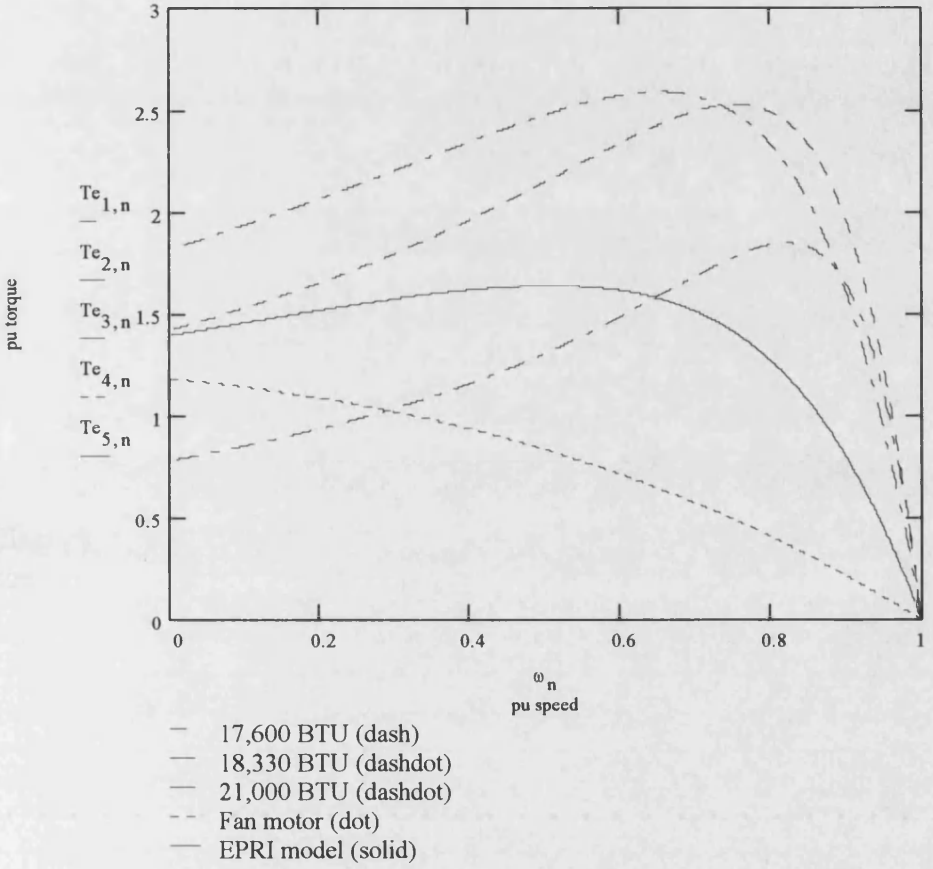

— 17,600 BTU (dash)
— 18,330 BTU (dashdot)
— 21,000 BTU (dashdot)
-- Fan motor (dot)
— EPRI model (solid)

Electical T-S characteristics of three compressors, condenser fan motor, and EPRI model.

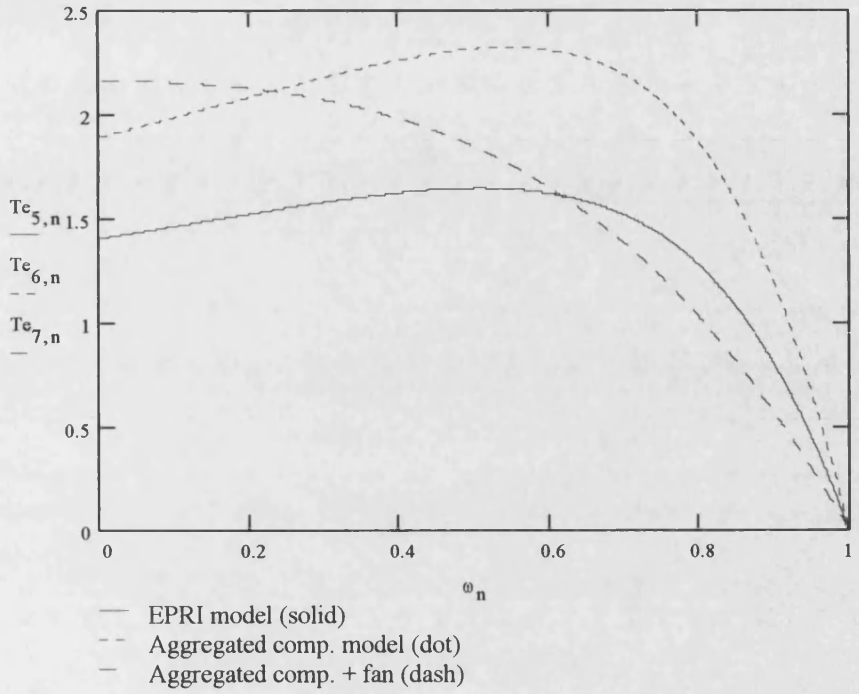

Electical T-S characteristics of EPRI model, aggregated compressor model, and aggregated compressor + fan motor model.

Appendix D-2

Mechanical torque coefficients A ,B , and C of compressor load:

a) Simulation of dynamic slip at starting - 17,600 BTU/hr compressor:

1- Read recorded starting current:

$i := 1 .. 300$

$t_i := i$

$I_i := READ\ (start17i\ )$ Read current at starting

2- Calculate actual slip:

$r2 := 0.032$ Rotor resistance

$x2 := 0.079i$ Rotor reactance

$Xm := 4.083i$ Magnetizing reactance

$P := 1$ Input power

$S := 0.031$ Nominal slip

Given

$$P = \left(I \cdot \frac{Xm}{Xm + x2 + \frac{r2}{S}} \right)^2 \cdot \frac{r2}{S}$$

$Slip(I) := Minerr\ (S)$

$S_i := Slip\left(I_i\right)$ Actual slip

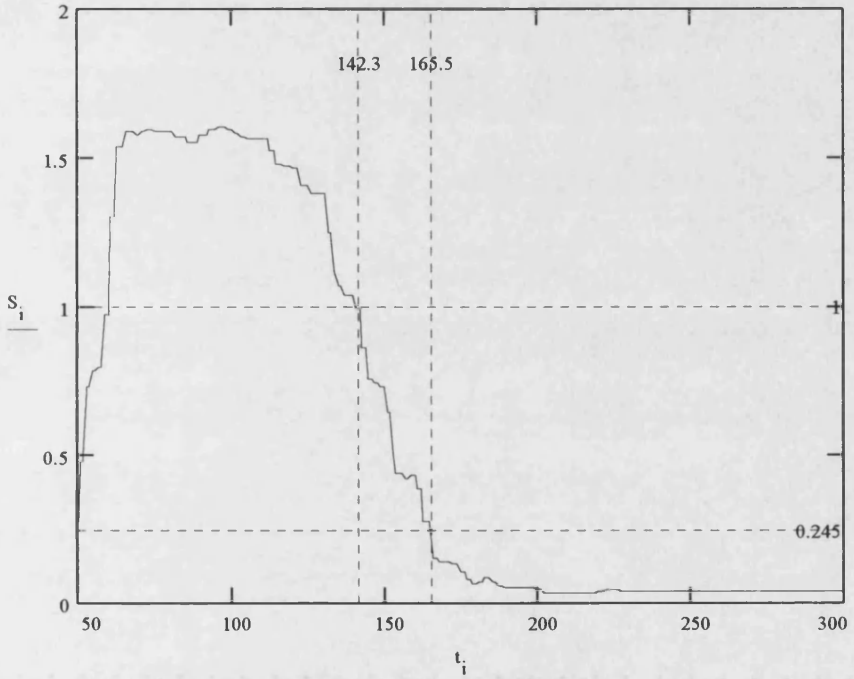

— Actual dynamic slip at starting - 17,600 BTU

3- Calculate the mechanical torque coefficients:

$j := 1..3$ $H := 0.251$ Inertia constant

$Te_j :=$	Electrical torque	$S_j :=$	Slip
1.42	starting	1	starting
2.54	critical	0.245	critical
0.97	nominal	0.031	nominal

$A := -10$ $B := 10$ $C := 5$

Given

$$-2 = \frac{\left[A\cdot\left(1-S_1\right)^2+B\cdot\left(1-S_1\right)+C\right]-Te_1}{2\cdot H}$$ Dynamic equation with S = 1

$$-1.335 = \frac{\left[A\cdot\left(1-S_2\right)^2+B\cdot\left(1-S_2\right)+C\right]-Te_2}{2\cdot H}$$ Dynamic equation with S = 0.245

$$0 = \frac{\left[A\cdot\left(1-S_3\right)^2+B\cdot\left(1-S_3\right)+C\right]-Te_3}{2\cdot H}$$ Dynamic equation with S = 0.031

$$\text{Find}(A,B,C) = \begin{pmatrix} -6.327 \\ 6.702 \\ 0.416 \end{pmatrix}$$ Mechanical torque coefficients of 17,600 BTU/hr

b) Simulation of dynamic slip at starting - 18,330 BTU/hr compressor:

1- Read recorded starting current:

$i := 1..300$

$t_i := i$

$I_i := READ(start18i)$ Read current at starting

2- Calculate actual slip:

$r2 := 0.033$ Rotor resistance

$x2 := 0.118i$ Rotor reactance

$Xm := 2.227i$ Magnetizing reactance

$P := 1$ Input power

$S := 0.034$ Nominal slip

Given

$$P = \left(I \cdot \frac{Xm}{Xm + x2 + \frac{r2}{S}}\right)^2 \cdot \frac{r2}{S}$$

$Slip(I) := Minerr(S)$

$S_i := Slip(I_i)$ Actual slip

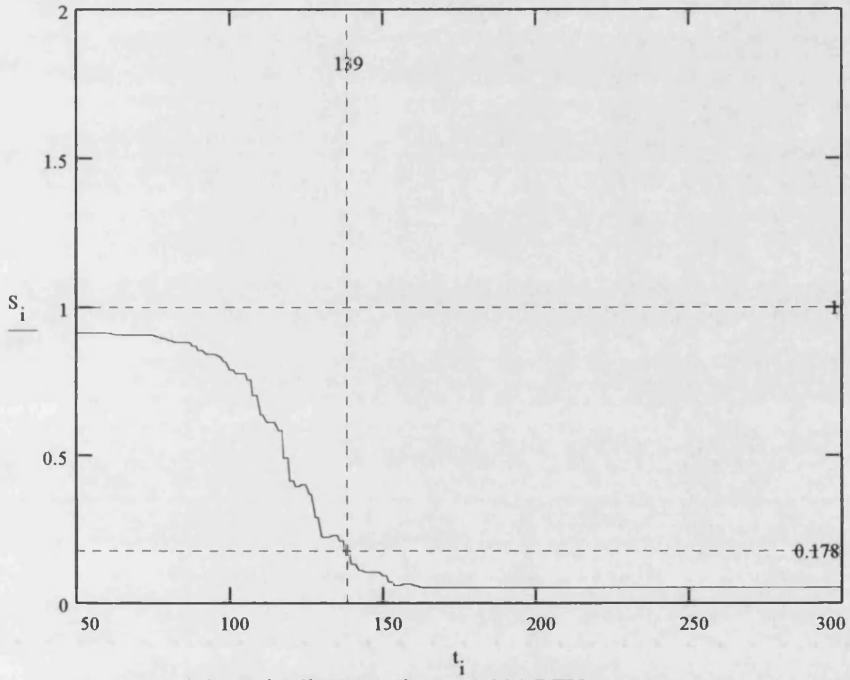

— Actual dynamic slip at starting - 18,330 BTU

3- Calculate the mechanical torque coefficients:

$j := 1..3$ $H := 0.200$ Inertia constant

$Te_j :=$	Electrical torque
0.79	starting
1.86	critical
0.97	nominal

$S_j :=$	Slip
1	starting
0.178	critical
0.034	nominal

$A := -10$ $B := 10$ $C := 5$

Given

$$0 = \frac{\left[A\cdot\left(1-S_1\right)^2+B\cdot\left(1-S_1\right)+C\right]-Te_1}{2\cdot H}$$ Dynamic equation with S = 1

$$-1.43 = \frac{\left[A\cdot\left(1-S_2\right)^2+B\cdot\left(1-S_2\right)+C\right]-Te_2}{2\cdot H}$$ Dynamic equation with S = 0.178

$$0 = \frac{\left[A\cdot\left(1-S_3\right)^2+B\cdot\left(1-S_3\right)+C\right]-Te_3}{2\cdot H}$$ Dynamic equation with S = 0.034

$$\text{Find}(A,B,C) = \begin{pmatrix} -2.913 \\ 3.001 \\ 0.79 \end{pmatrix}$$ Mechanical torque coefficients of 18,330 BTU/hr

c) Simulation of dynamic slip at starting - 21,000 BTU/hr compressor:

1- Read recorded starting current:

$i := 1..300$

$t_i := i$

$I_i := READ(start21i)$ Read current at starting

2- Calculate actual slip:

$r2 := 0.046$ Rotor resistance

$x2 := 0.083i$ Rotor reactance

$Xm := 4.943i$ Magnetizing reactance

$P := 1$ Input power

$S := 0.049$ Nominal slip

Given

$$P = \left| I \cdot \frac{Xm}{Xm + x2 + \frac{r2}{S}} \right|^2 \cdot \frac{r2}{S}$$

$Slip(I) := Minerr(S)$

$S_i := Slip(I_i)$ Actual slip

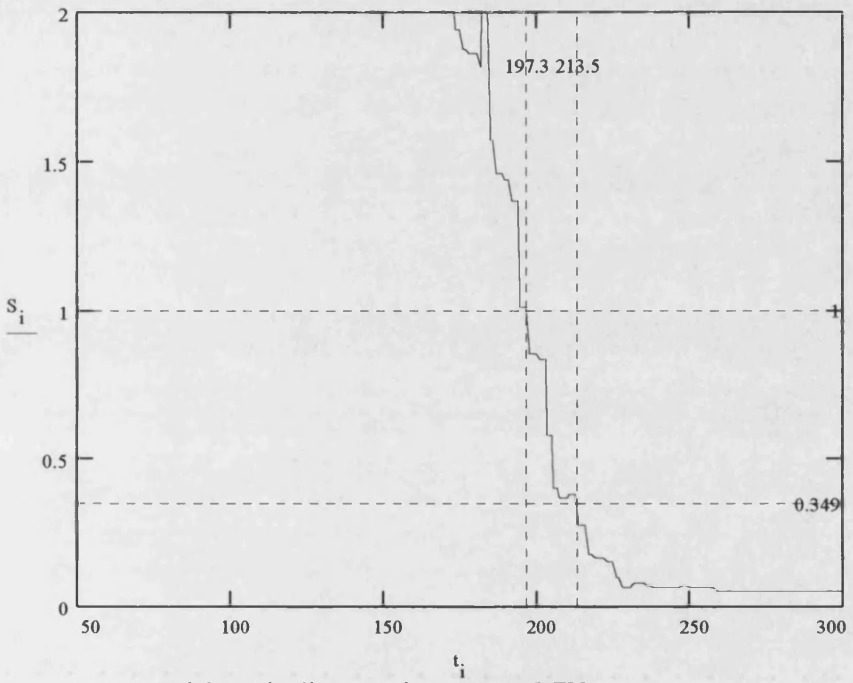

— Actual dynamic slip at starting - 21,000 BTU

3- Calculate the mechanical torque coefficients:

$j := 1..3$ $H := 0.242$ Inertia constant

$Te_j :=$	Electrical torque	$S_j :=$	Slip
1.83	starting	1	starting
2.6	critical	0.349	critical
0.97	nominal	0.049	nominal

$A := -10$ $B := 10$ $C := 5$

Given

$$-2.4 = \frac{\left[A\cdot\left(1-S_1\right)^2+B\cdot\left(1-S_1\right)+C\right]-Te_1}{2\cdot H}$$ Dynamic equation with S = 1

$$-1.241 = \frac{\left[A\cdot\left(1-S_2\right)^2+B\cdot\left(1-S_2\right)+C\right]-Te_2}{2\cdot H}$$ Dynamic equation with S = 0.349

$$0 = \frac{\left[A\cdot\left(1-S_3\right)^2+B\cdot\left(1-S_3\right)+C\right]-Te_3}{2\cdot H}$$ Dynamic equation with S = 0.049

$$\text{Find}(A,B,C) = \begin{pmatrix} -5.758 \\ 5.793 \\ 0.668 \end{pmatrix}$$ Mechanical torque coefficients of 21,000 BTU/hr

d) Simulation of electrical & mechanical torque-speed characteristics for all models:

$i := 1..5$

$r1_i :=$	$x1_i :=$	$Xm_i :=$	$r2_i :=$	$x2_i :=$	$H_i :=$	$S_i :=$	
0.065	0.034i	4.083i	0.032	0.079i	0.241	0.031	17,600 BTU
0.076	0.051i	2.227i	0.033	0.118i	0.200	0.034	18,330 BTU
0.059	0.035i	4.943i	0.046	0.083i	0.242	0.049	21,000 BTU
0.066	0.039i	3.293i	0.066	0.091i	0.227	0.100	Agg. compressor
0.100	0.100i	1.800i	0.090	0.060i	0.280	0.100	EPRI

$n := 1..999$ $\quad V := 1$

$S_n := \frac{n}{1000}$ $\quad \omega_n := 1 - S_n$

$A_i :=$	$B_i :=$	$C_i :=$	$KVA_i :=$
-6.327	6.702	0.416	2.070
-2.913	3.001	0.790	2.392
-5.758	5.793	0.668	2.231
-4.917	5.076	0.634	1.000
0.2	0	0	1.000

$Zs_i := r1_i + x1_i$

$Zo_i := r1_i + (x1_i + Xm_i)$

$Zm_i := Xm_i$

$Zth_i := \frac{Zs_i \cdot Zm_i}{Zs_i + Zm_i}$

$Rth_i := Re(Zth_i)$ $\quad Xth_i := Im(Zth_i)$

$$Te_{i,n} := \frac{\left(\frac{Im(Xm_i)}{|Zo_i|}\right)^2 \cdot \frac{r2_i}{S_n} \cdot V^2}{\left(Rth_i + \frac{r2_i}{S_n}\right)^2 + (Xth_i + Im(x2_i))^2}$$

$$Tm_{i,n} := A_i \cdot (1 - S_n)^2 + B_i \cdot (1 - S_n) + C_i$$

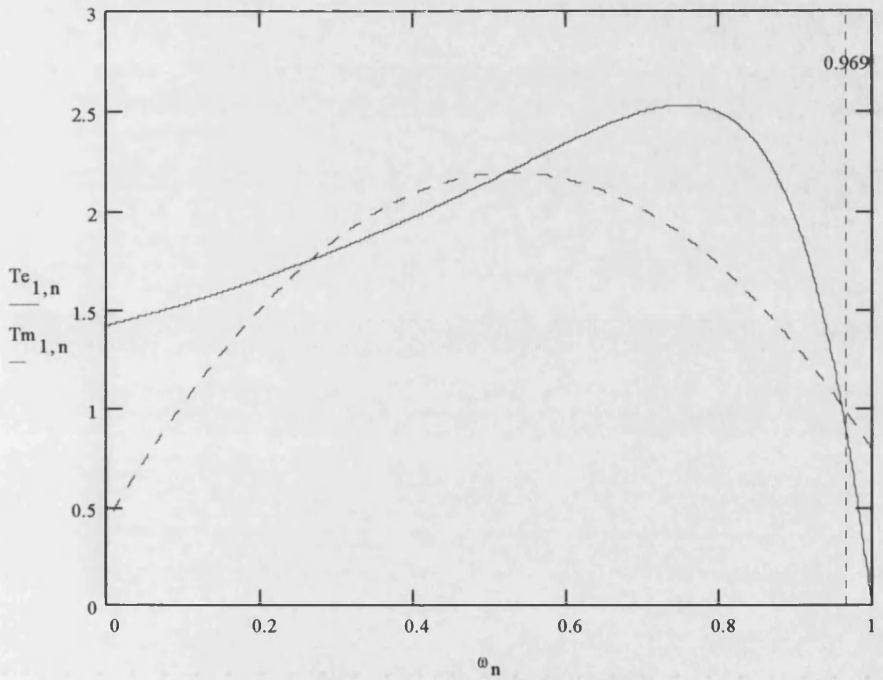

— Electrical T-S characteristics 17,600 BTU (solid)
– Mechanical T-S characteristics 17,600 BTU (dash)

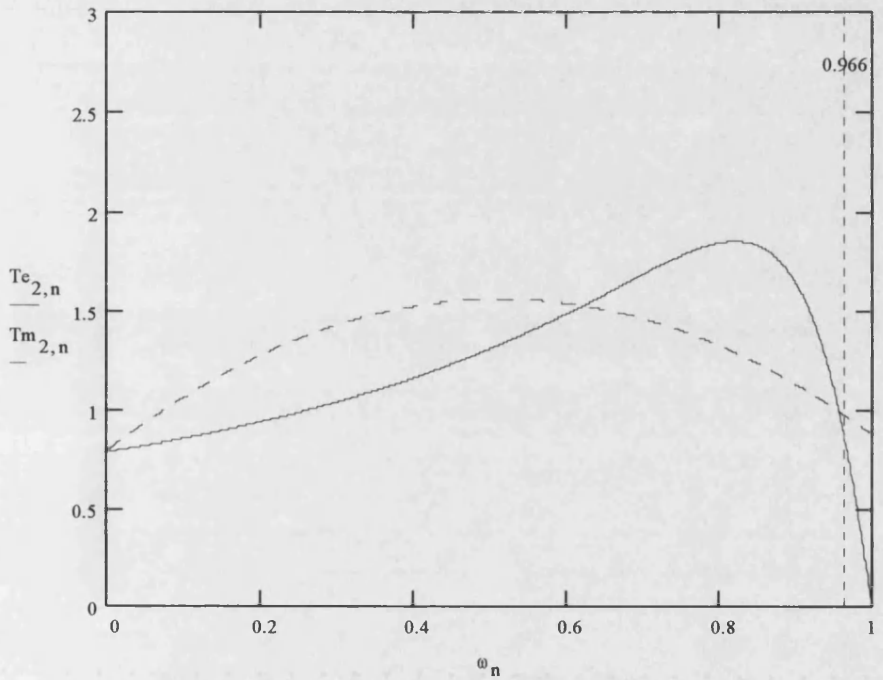

— Electrical T-S characteristics 18,330 BTU (solid)
— Mechanical T-S characteristics 18,330 BTU (dash)

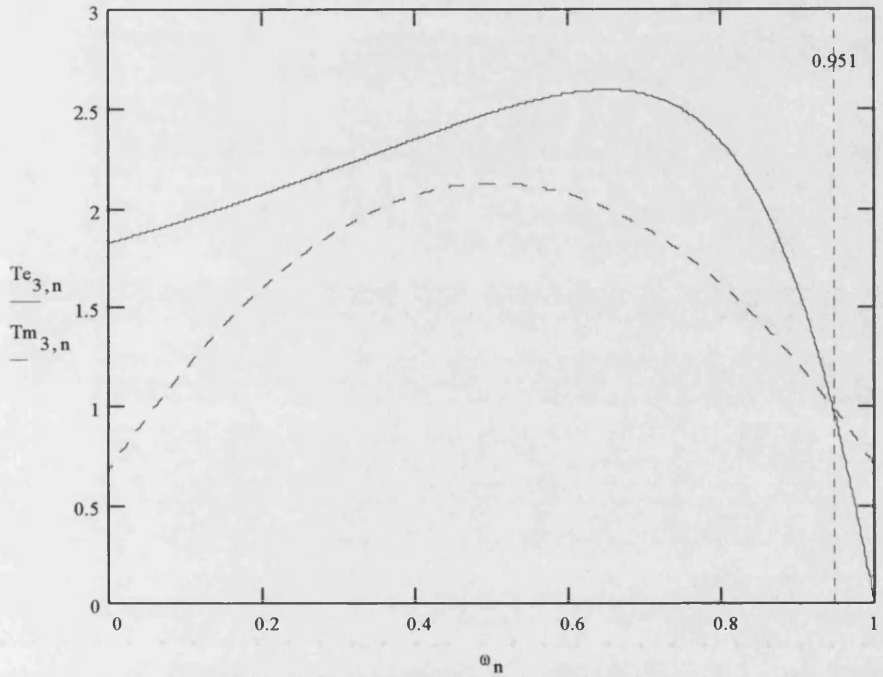

— Electrical T-S characteristics 21,000 BTU (solid)
– Mechanical T-S characteristics 21,000 BTU (dash)

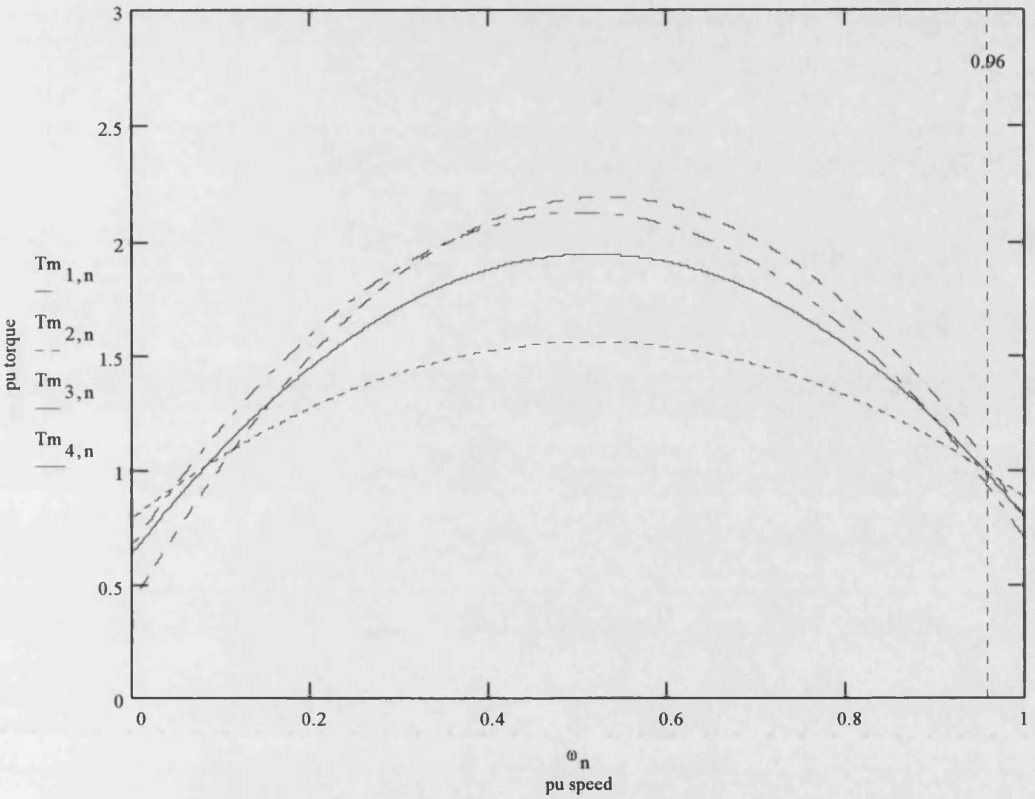

— Mechanical T-S characteristics - 17,600 BTU (dash)
– – Mechanical T-S characteristics - 18,330 BTU (dot)
— Mechanical T-S characteristics - 21,000 BTU (dashdot)
— Aggregate Mechanical T-S char. of agg. compressor (solid)

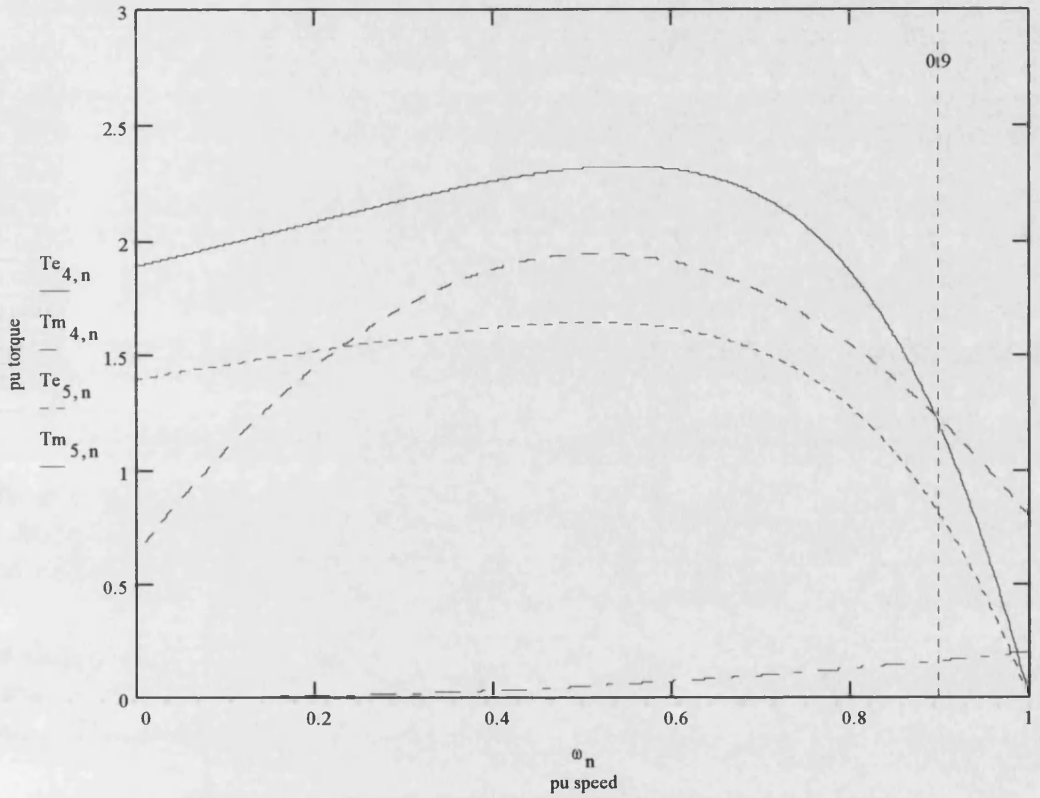

Electrical T-S characteristics of agg. compressor (solid)
Mechanical T-S characteristics of agg. compressor (dash)
Electrical T-S EPRI (dot)
Mechanical T-S EPRI (dashdot)

Appendix E

Analysis of transient simulation test results:

1- Difference between digital timer setting and actual recorded transient duration:

$i := 1..10$

$Ttimer_i :=$ Timer setting

0.370
0.380
0.210
0.200
0.110
0.100
0.050
0.040
0.030
0.020

$Tactual_i :=$ Actual recorded transient duration

0.376
0.388
0.215
0.208
0.116
0.106
0.050
0.042
0.038
0.028

The above selected data was extracted from tests performed on 21,000 BTU/hr compressor, at different low voltage levels ranging between 0.72 pu and 0.6 pu of nominal terminal voltage, and without distribution system reactance (ΔX_d) added in series.

As shown, the differences between the timer settings and corresponding actual recorded transient duration were in the range of 0-10 milliseconds only, which prove the high resolution of time settings during tests, and the reliability of contactor switching mechanism.

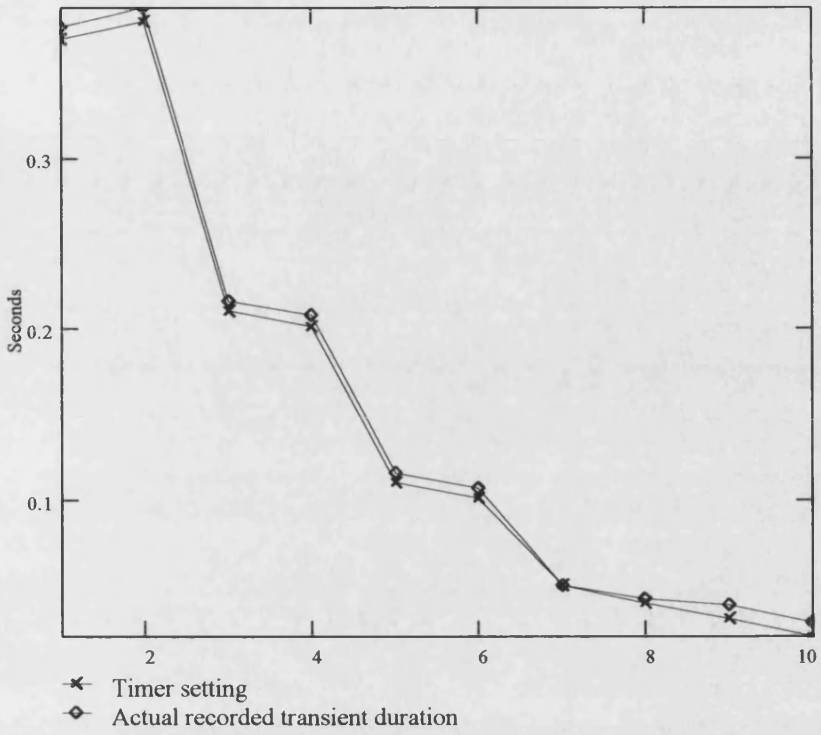

2- Definition of compressor critical voltage:

The critical stalling condition of the single-phase compressor load occurs when the maximum developed electrical torque (T_{cr}) at a certain reduced terminal voltage, called the critical voltage (V_{cr}), equals to the minimum required laod mechanical torque of 1 pu.

$i := 1..4$ $n := 1..999$

$S_n := \frac{n}{1000}$ Compressor slip

$\omega_n := 1 - S_n$ Compressor speed

Appendix E

Compressors parameters:

$r1_i :=$	$x1_i :=$	$Xm_i :=$	$r2_i :=$	$x2_i :=$	$S_i :=$	$Tecr_i :=$	
0.065	0.034i	4.083i	0.032	0.079i	0.031	1.33	17,600 BTU/hr
0.076	0.051i	2.004i	0.033	0.118i	0.034	1.00	18,330 BTU/hr
0.059	0.035i	4.943i	0.046	0.083i	0.049	1.36	21,000 BTU/hr
0.066	0.039i	3.293i	0.066	0.091i	0.038	1.23	Aggregate compressor

$Zs_i := r1_i + x1_i$ Stator impedance

$Zm_i := Xm_i$ Magnetizing impedance

$Zo_i := r1_i + (x1_i + Xm_i)$ Open-circuit impedance

$Zth_i := \frac{Zs_i \cdot Zm_i}{Zs_i + Zm_i}$ Thevenin impedance

$Rth_i := Re(Zth_i)$ Real part of Thevenin impedance

$Xth_i := Im(Zth_i)$ Imaginary part of Thevenin impedance

$V := 1$ Nominal terminal voltage

$$Vcr_i := \sqrt{\frac{\left[Rth_i + \sqrt{(Rth_i)^2 + (Xth_i + Im(x2_i))^2}\right] \cdot Tecr_i}{0.5}}$$ Critical voltage

$Vcractual := 0.72$ Actual critical voltage Vcr_i Calculated critical voltage

Vcr_i
0.719
0.717
0.719
0.719

The percentage error between actual and calculated values of compressor critical voltage is given by the following equation:

$$Error_i := \left(\frac{Vcractual - Vcr_i}{Vcractual}\right) \cdot 100$$

$Error_i$	Error % in calculated critical voltage
0.132	
0.38	
0.123	
0.11	

3- Relationship between maximum fault clearing time (t_{max}), terminal voltage, and distribution system reactance (X_d):

$j := 1..7$ $n := 1..5$ $i := 1..3$

a) Test data of 17,600 BTU/hr compressor :

Xd = 0

$V1_j :=$	$t1_j :=$
0.67	0.261
0.64	0.232
0.60	0.123
0.57	0.109
0.54	0.124
0.50	0.105
0.44	0.082

Xd = 0.067

$V2_i :=$	$t2_i :=$
0.72	0.308
0.70	0.231
0.67	0.153

Xd = 0.1

$V3_i :=$	$t3_i :=$
0.72	0.249
0.70	0.213
0.67	0.151

Xd = 0.2

$V4_i :=$	$t4_i :=$
0.72	0.193
0.70	0.184
0.67	0.133

b) Test data of 18,330 BTU/hr compressor :

Xd = 0

$V5_n :=$ $t5_n :=$

0.72	0.394
0.70	0.211
0.67	0.093
0.64	0.057
0.60	0.052

Xd = 0.067

$V6_i :=$ $t6_i :=$

0.72	0.113
0.70	0.079
0.67	0.058

Xd = 0.1

$V7_i :=$ $t7_i :=$

0.72	0.096
0.70	0.064
0.67	0.054

Xd = 0.2

$V8_i :=$ $t8_i :=$

0.72	0.083
0.70	0.069
0.67	0.043

c) Test data of 21,000 BTU/hr compressor:

Xd = 0

$V9_n :=$ $t9_n :=$

0.72	0.377
0.70	0.212
0.67	0.111
0.64	0.046
0.60	0.033

Xd = 0.067

$V10_i :=$ $t10_i :=$

0.72	0.100
0.70	0.062
0.67	0.054

Xd = 0.1

$V11_i :=$ $t11_i :=$

0.72	0.091
0.70	0.053
0.67	0.045

Xd = 0.2

$V12_i :=$ $t12_i :=$

0.72	0.048
0.70	0.033
0.67	0.025

Note:

Based on tests' data, the locus relating different levels of reduced terminal voltage and maximum fault clearing time for all three tested compressors at various values of distribution system reactance (X_d) are plotted. Since the points available are not enough to clearly show the trend of such relationship, in the next section, mathematical formulas were derived to simulate same trends.

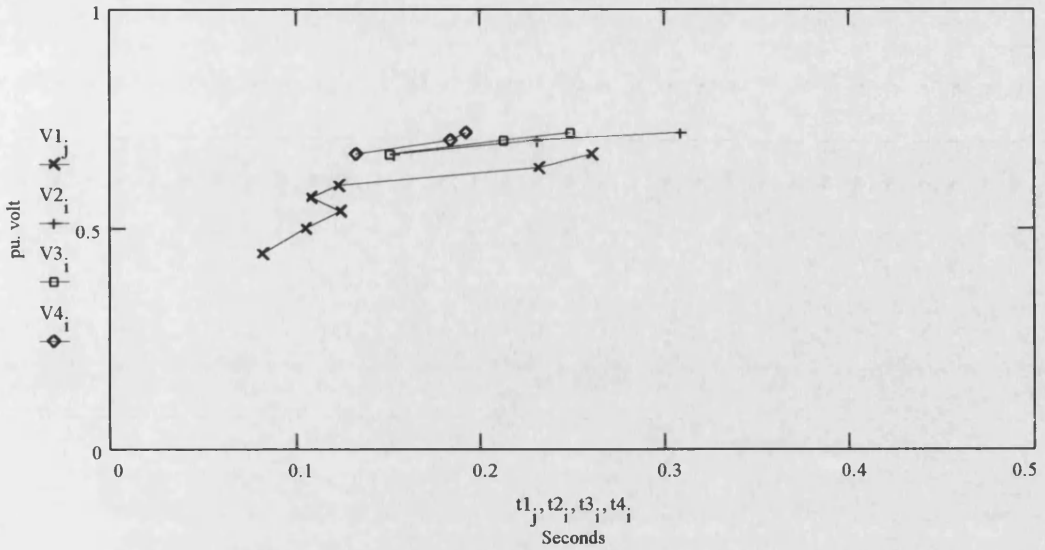

Compressor 17,600 BTU - Xd=0 pu
Compressor 17,600 BTU - Xd=0.067 pu
Compressor 17,600 BTU - Xd=0.100 pu
Compressor 17,600 BTU - Xd=0.200 pu

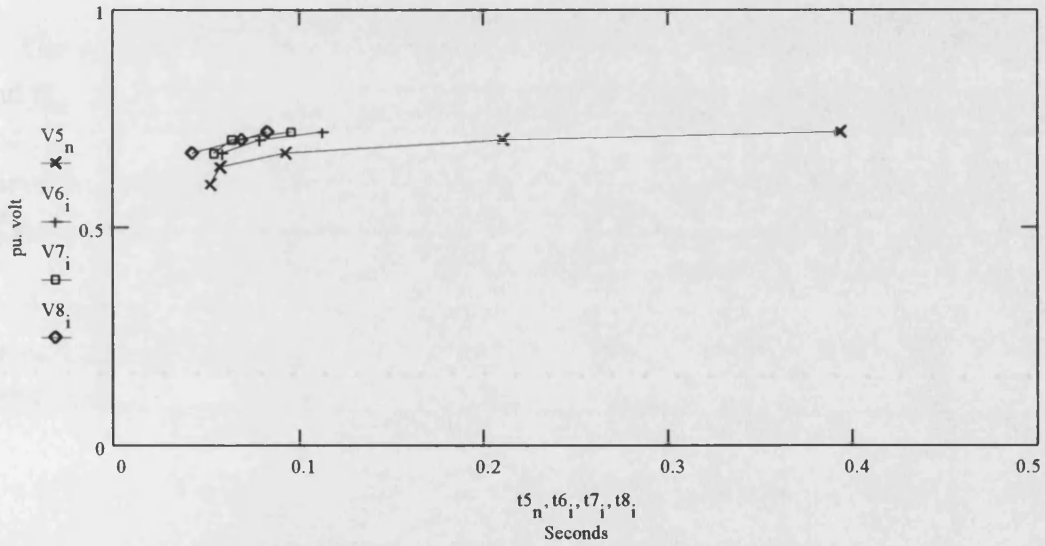

Compressor 18,330 BTU - Xd=0 pu
Compressor 18,330 BTU - Xd=0.067 pu
Compressor 18,330 BTU - Xd=0.100 pu
Compressor 18,330 BTU - Xd=0.200 pu

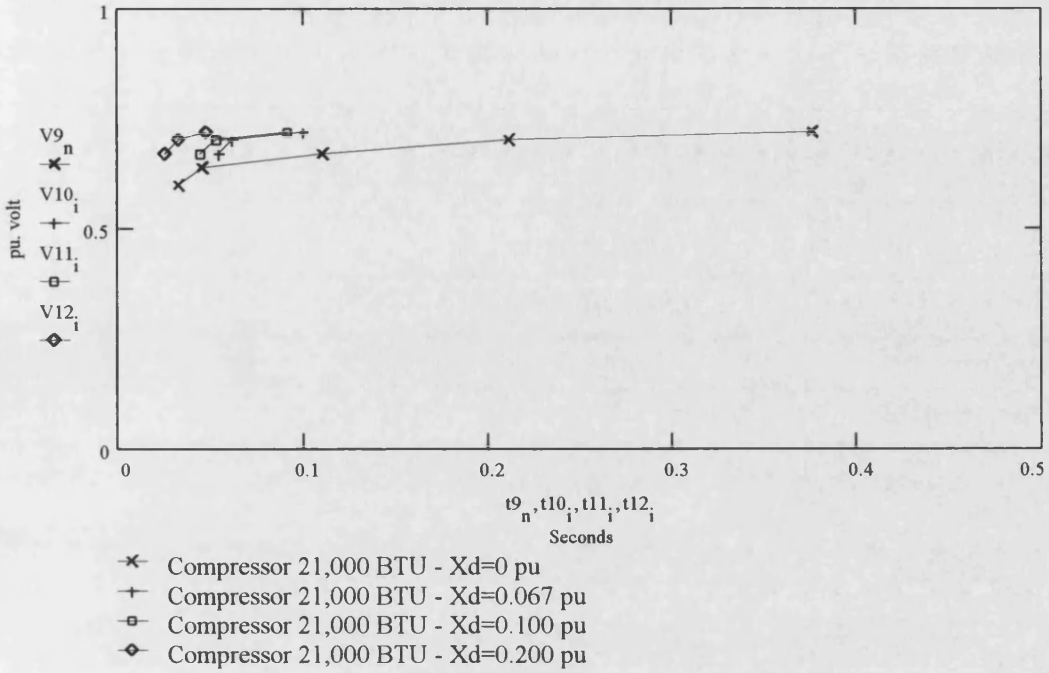

The main formula relating terminal voltage and maximum clearing time has 2 constants K_1 and K_2, which change with different values of reactance (X_d). For each compressor model and for every value of reactance (X_d), constants K_1 and K_2 are derived by tuning resulting curve from equation (3) with actual test data. Then, for each value of (X_d), an average value of these constants is calculated in order to represent one aggregate compressor.

By knowing (X_d), constants K_1 and K_2 can be calculated from equations (1) and (2), and by substituting their values in the main equation (3), the maximum fault clearing time for compressor load can be calculated at any voltage level.

Appendix E

$k := 1..500$ Simulation of 500 milliseconds

$t_k := \frac{k}{1000}$ Time in seconds

$m := 1..4$ Counter for 4 values of reactance (X_d)

$Xd_m :=$

0
0.067
0.1
0.2

Dist. reactance

$K117_m :=$ $K118_m :=$ $K121_m :=$

0.73	0.75	0.75
0.80	0.87	0.82
0.86	0.91	0.85
0.91	0.97	0.98

Constant K_1 of 3 compressors

$K217_m :=$ $K218_m :=$ $K221_m :=$

0.10	0.05	0.05
0.10	0.09	0.06
0.14	0.10	0.07
0.16	0.12	0.10

Constant K_2 of 3 compressors

$K1_m :=$

0.743
0.830
0.873
0.953

Average values of constant K_1

$K2_m :=$

0.067
0.083
0.103
0.127

Average values of constant K_2

$K1 := 0.75 + 1.14 Xd$ Equation(1) of K_1 and X_d

$K2 := 0.07 + 0.36 Xd$ Equation(2) of K_2 and X_d

$V_{k,m} := \left[K1_m \cdot \left(e^{t_k} - 1 \right)^{K2_m} \right]$ Main equation (3) relating terminal voltage (V), distribution system reactance (X_d), and maximum fault clearing time (t_{max}).

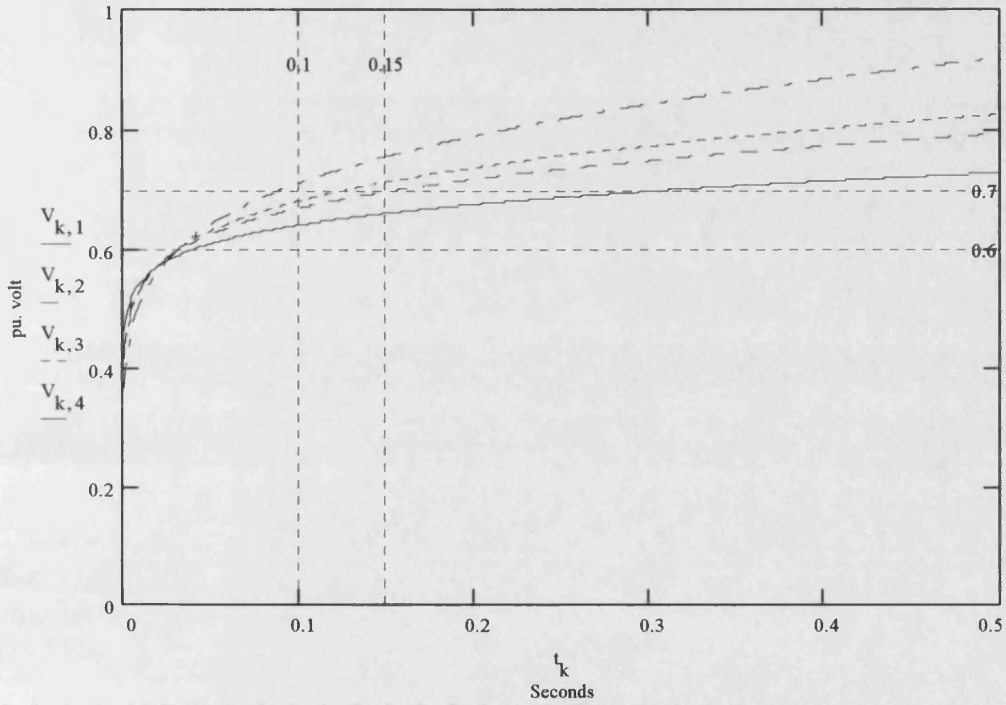

— Voltage vs. max. fault clearing time at Xd = 0 pu (solid)
— Voltage vs. max. fault clearing time at Xd = 0.067 pu (dash)
- - Voltage vs. max. fault clearing time at Xd = 0.100 pu (dot)
— Voltage vs. max. fault clearing time at Xd = 0.200 pu (dashdot

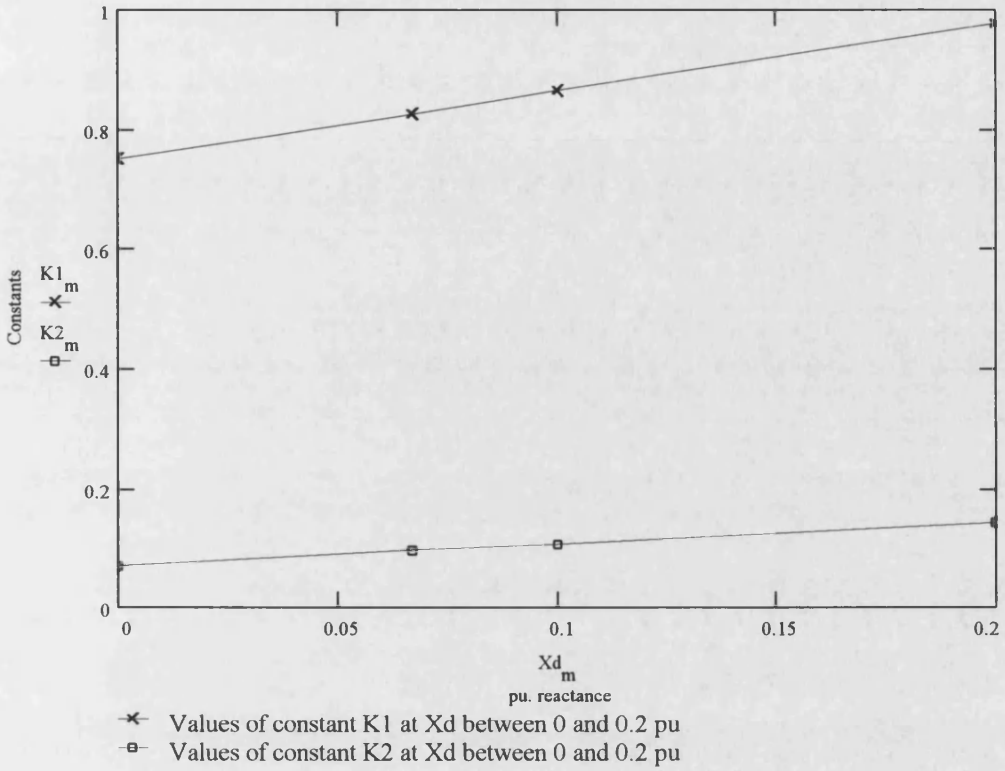

4- Effect of added distribution system reactance on maximum fault clearing time:

The test data of 17,600 BTU/hr compressor was used as shown below to simulate the effect of distribution system reactance on the maximum fault clearing time when added to the compressor circuit. The data was extracted from tests performed at low terminal voltage levels of 0.72 pu, 0.7 pu, and 0.67 pu.

The maximum fault clearing time was reduced sharply when adding reactance (X_d) ranging between 0 and 0.07pu in series to the compressor, while it had a moderate reduction when (X_d) had values ranging between 0.07 pu and 0.2 pu.

$i := 1..4$ $j := 1..3$

$Xd_i :=$ $T72_i :=$

0	0.377
0.067	0.100
0.100	0.091
0.200	0.048

$Xd_i :=$ $T70_i :=$

0	0.212
0.067	0.061
0.100	0.053
0.200	0.035

$Xd_j :=$ $T67_j :=$

0	0.111
0.067	0.054
0.100	0.040

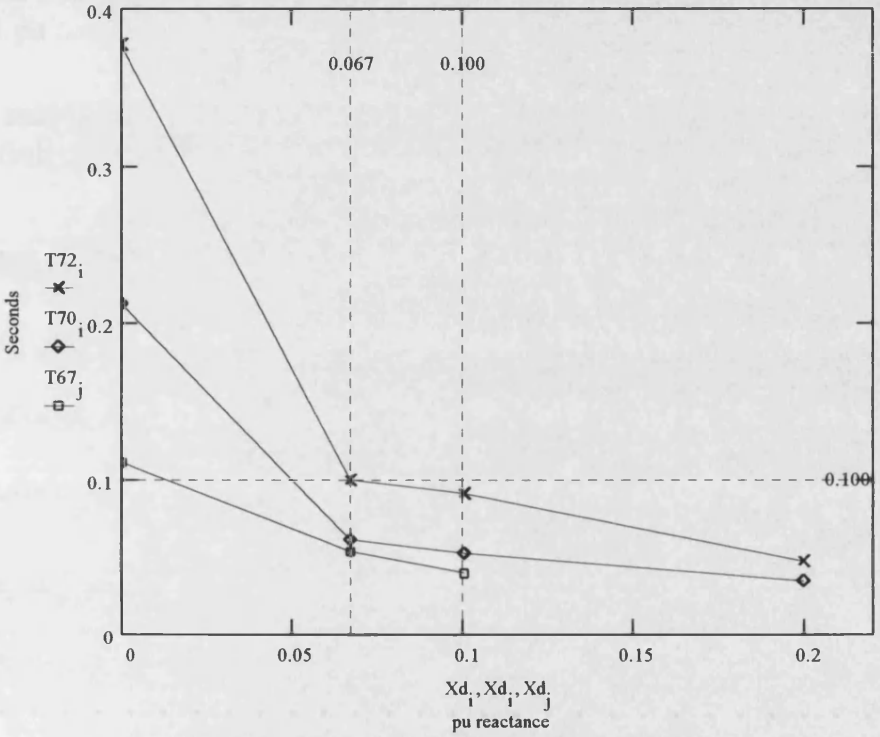

Max. fault clearing time at 0.72 pu volt
Max. fault clearing time at 0.70 pu volt
Max. fault clearing time at 0.67 pu volt

5- Simulation of P & Q in stalling and non-stalling cases of compressor :

Two typical cases of stalling and non-stalling compressor were selected out of 80 transient simulation tests performed on single-phase compressors of different capacities in order to show the trends and behavior of recorded active and reactive power during transient.

The selected test cases were of a 17,600 BTU/hr compressor, where the terminal voltage was reduced down to 0.7 pu, with the presence of a distribution system reactance (X_d) = 0.1 pu connected in series with the compressor.

In the stalling case, the fault clearing time was 0.256 seconds, while in the non-stalling case, the fault clearing time was 0.242 seconds.

Data of non-stalling case:	$i := 0..499$	***Data of stalling case:***
$Vnb_i := READ(nonblock17v491)$	compressor voltage	$Vb_i := READ(block17v488)$
$Inb_i := READ(nonblock17i491)$	compressor current	$Ib_i := READ(block17i488)$
$\Phi nb_i := READ(angle491)$	phase angle bet. V & I	$\Phi b_i := READ(angle488)$
$Pnb_i := Vnb_i \cdot Inb_i \cdot \cos(\Phi nb_i)$	compressor active power	$Pb_i := Vb_i \cdot Ib_i \cdot \cos(\Phi b_i)$
$Qnb_i := Vnb_i \cdot Inb_i \cdot \sin(\Phi nb_i)$	compressor reactive power	$Qb_i := Vb_i \cdot Ib_i \cdot \sin(\Phi b_i)$

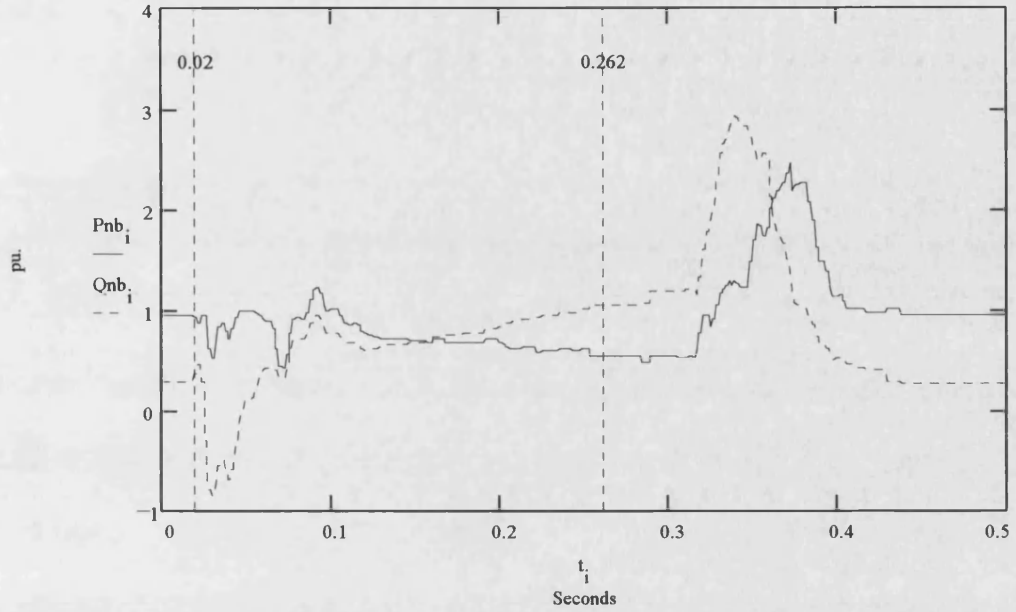

Active power (P)
Reactive power (Q)

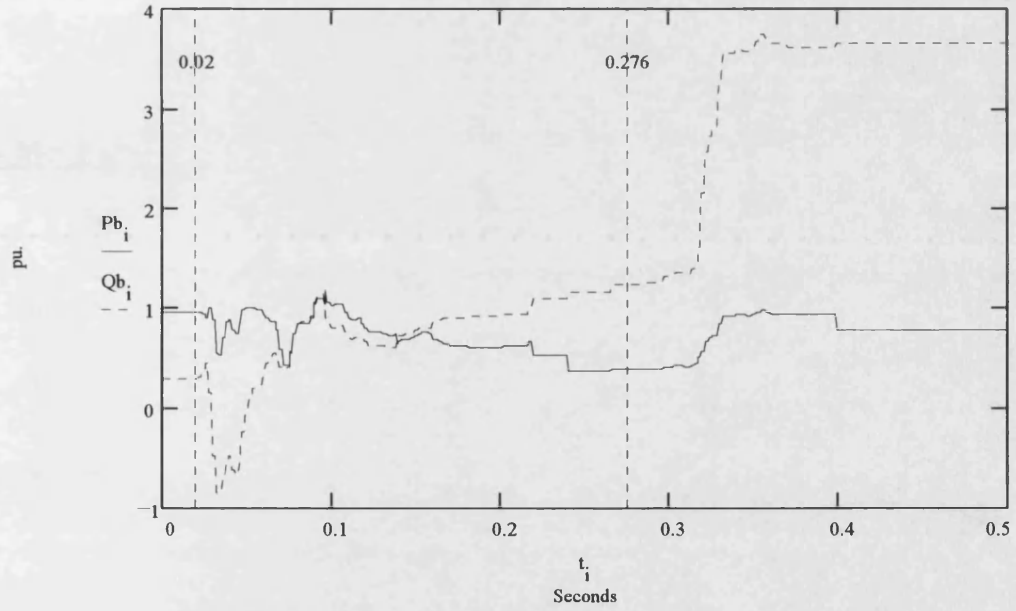

Active power (P)
Reactive power (Q)

Appendix F

Dynamic simulation of 17,600 BTU/hr. compressor test model using the Runge-Kutta method:

Test case # 465 - non-block compressor at *V = 0.72 pu & Xd = 0.2 pu*

1- Read voltage & current test data:

$i := 0..499$

$V_i := READ(nonblock17v465)$ recorded compressor voltage

$Ia_i := READ(nonblock17i465)$ recorded compressor stator current

2- Electrical parameters:

$r1 := 0.065$ $x1 := 0.034i$ stator resistance & reactance

$r2 := 0.032$ $x2 := 0.079i$ rotor resistance & reactance

$Xm := 4.083i$ magnetizing reactance

$t_i := \frac{i}{1000}$ time iteration

3- Mechanical parameters :

$A := -4.917$

$B := 5.076$ mechanical torque coefficients

$C := 0.634$

$H := 0.251$ inertia constant

4 - Seeded iteration solution of the dynamic model differential equations

$i := 0..499$ seed values of iteration

$$\begin{bmatrix} k1_0 \\ k2_0 \\ k3_0 \\ k4_0 \\ Is_0 \\ I1_0 \\ I2_0 \\ I3_0 \\ I4_0 \\ S_0 \end{bmatrix} := \begin{bmatrix} 0.358 \\ 0.356 \\ 0.356 \\ 0.355 \\ 1 \\ 0.01 \\ 0.009 \\ 0.009 \\ 0.009 \\ 0.031 \end{bmatrix}$$

Initial values of weighted average constants k_2, k_3, and k_4

Initial stator current

Initial values of weighted average constants l_2, l_3, and l_4

Initial simulated slip

$h := 0.001$ Runge-Kutta iteration step size

$$-\left[\frac{r1 + \frac{Xm^2 \cdot \frac{r2}{S_1}}{(x2 + Xm)\cdot\left(x2 + Xm + \frac{r2}{S_1}\right)}}{x1 + Xm - \frac{Xm^2}{x2 + Xm}}\right] \cdot Is_1 + \left(\frac{1}{x1 + Xm - \frac{Xm^2}{x2 + Xm}}\right) \cdot V_1$$

Diff. eq. for stator current

$$\frac{V_1}{r1 + x1 + \frac{Xm\cdot\left(x2 + \frac{r2}{S_1}\right)}{Xm + x2 + \frac{r2}{S_1}}}$$

Steady-state stator current

$$
\begin{bmatrix} k1_{I+1} \\ k2_{I+1} \\ k3_{I+1} \\ k4_{I+1} \\ ls_{I+1} \\ l1_{I+1} \\ l2_{I+1} \\ l3_{I+1} \\ l4_{I+1} \\ s_{I+1} \end{bmatrix} :=
\begin{bmatrix}
-\left|\frac{r1+\frac{Xm^2\cdot\frac{r2}{s_I}}{(x2+Xm)\cdot\left(x2+Xm+\frac{r2}{s_I}\right)}}{x1+Xm-\frac{Xm^2}{x2+Xm}}\right|\cdot\left[\frac{V_I}{\left|r1+x1+\frac{Xm\cdot\left(x2+\frac{r2}{s_I}\right)}{Xm+x2+\frac{r2}{s_I}}\right|}\right]+8.969_I \\
-\left|\frac{r1+\frac{Xm^2\cdot\frac{r2}{\left(s_I+\frac{h}{2}\cdot l1_I\right)}}{(x2+Xm)\cdot\left[x2+Xm+\frac{r2}{\left(s_I+\frac{h}{2}\cdot l1_I\right)}\right]}}{x1+Xm-\frac{Xm^2}{x2+Xm}}\right|\cdot\left[\left[\frac{V_I}{\left|r1+x1+\frac{Xm\cdot\left[x2+\frac{r2}{\left(s_I+\frac{h}{2}\cdot l1_I\right)}\right]}{Xm+x2+\frac{r2}{\left(s_I+\frac{h}{2}\cdot l1_I\right)}}\right|}\right]+\frac{h}{2}\cdot k1_I\right]+8.969_I \\
-\left|\frac{r1+\frac{Xm^2\cdot\frac{r2}{\left(s_I+\frac{h}{2}\cdot l2_I\right)}}{(x2+Xm)\cdot\left[x2+Xm+\frac{r2}{\left(s_I+\frac{h}{2}\cdot l2_I\right)}\right]}}{x1+Xm-\frac{Xm^2}{x2+Xm}}\right|\cdot\left[\left[\frac{V_I}{\left|r1+x1+\frac{Xm\cdot\left[x2+\frac{r2}{\left(s_I+\frac{h}{2}\cdot l2_I\right)}\right]}{Xm+x2+\frac{r2}{\left(s_I+\frac{h}{2}\cdot l2_I\right)}}\right|}\right]+\frac{h}{2}\cdot k2_I\right]+8.969_I \\
-\left|\frac{r1+\frac{Xm^2\cdot\frac{r2}{(s_I+h\cdot l3_I)}}{(x2+Xm)\cdot\left[x2+Xm+\frac{r2}{(s_I+h\cdot l3_I)}\right]}}{x1+Xm-\frac{Xm^2}{x2+Xm}}\right|\cdot\left[\left[\frac{V_I}{\left|r1+x1+\frac{Xm\cdot\left[x2+\frac{r2}{(s_I+h\cdot l3_I)}\right]}{Xm+x2+\frac{r2}{(s_I+h\cdot l3_I)}}\right|}\right]+h\cdot k3_I\right]+8.969_I \\
\left[\frac{V_I}{\left|r1+x1+\frac{Xm\cdot\left(x2+\frac{r2}{s_I}\right)}{Xm+x2+\frac{r2}{s_I}}\right|}\right]+\frac{h}{6}\cdot\left(k1_I+2\,k2_I+2\,k3_I+k4_I\right) \\
\frac{1}{2H}\cdot\left[\left[A\cdot\left(1-s_I\right)^2+B\cdot\left(1-s_I\right)+C\right]-\left[\left(ls_I\cdot\left|\frac{Xm}{Xm+x2+\frac{r2}{s_I}}\right|\right)^2\cdot\frac{r2}{s_I}\right]\right] \\
\frac{1}{2H}\cdot\left[\left[A\cdot\left[1-\left(s_I+\frac{h}{2}\cdot l1_I\right)\right]^2+B\cdot\left[1-\left(s_I+\frac{h}{2}\cdot l1_I\right)\right]+C\right]-\left[\left[\left(ls_I+\frac{h}{2}\cdot k1_I\right)\cdot\left|\frac{Xm}{Xm+x2+\frac{r2}{\left(s_I+\frac{h}{2}\cdot l1_I\right)}}\right|\right]^2\cdot\frac{r2}{\left(s_I+\frac{h}{2}\cdot l1_I\right)}\right]\right] \\
\frac{1}{2H}\cdot\left[\left[A\cdot\left[1-\left(s_I+\frac{h}{2}\cdot l2_I\right)\right]^2+B\cdot\left[1-\left(s_I+\frac{h}{2}\cdot l2_I\right)\right]+C\right]-\left[\left[\left(ls_I+\frac{h}{2}\cdot k2_I\right)\cdot\left|\frac{Xm}{Xm+x2+\frac{r2}{\left(s_I+\frac{h}{2}\cdot l2_I\right)}}\right|\right]^2\cdot\frac{r2}{\left(s_I+\frac{h}{2}\cdot l2_I\right)}\right]\right] \\
\frac{1}{2H}\cdot\left[\left[A\cdot\left[1-\left(s_I+h\cdot l3_I\right)\right]^2+B\cdot\left[1-\left(s_I+h\cdot l3_I\right)\right]+C\right]-\left[\left[\left(ls_I+h\cdot k3_I\right)\cdot\left|\frac{Xm}{Xm+x2+\frac{r2}{(s_I+h\cdot l3_I)}}\right|\right]^2\cdot\frac{r2}{(s_I+h\cdot l3_I)}\right]\right] \\
s_I+\frac{h}{6}\cdot\left(l1_I+2\,l2_I+2\,l3_I+l4_I\right)
\end{bmatrix}
$$

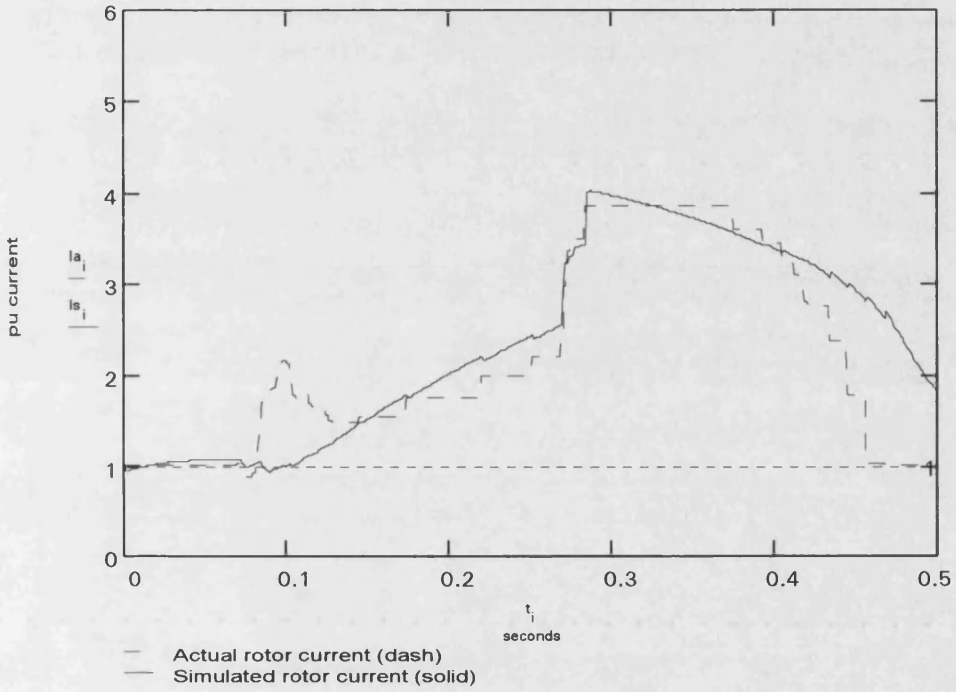
pu current
$\frac{Ia_i}{Is_i}$
6
5
4
3
2
1
0
0
0.1
0.2
0.3
0.4
0.5
t_i
seconds
Actual rotor current (dash)
Simulated rotor current (solid)

References

1. Lokay, H.E., Burtnyk, V.: ***Application of under-frequency relays for automatic load shedding,*** IEEE Trans. PAS, paper No.31 TP 67-447, pp. 525-532, March 1968.

2. Urden, E.A.: ***Applied Protective Relaying,*** Westinghouse Electric Corp., Relay-Instrument Division, Coral Springs, Fl 33065, Chapter 21, 1982.

3. Harrison, P. : ***Considerations when planning a load shedding program,*** BBC, Rev.10, pp. 593-598, 1980.

4. Fox, B., Thompson, J.G., Tindall, C.E. : ***Adaptive control of load shedding relays under generation loss conditions,*** IEE, 2nd International Conference on Power System Monitoring and Control, pp. 259-263, 1988.

5. Levy, C.P., Haupt, C.A. : ***Automatic under-frequency load shedding in ESCOM,*** Proc. Of IFAC, Power Generation, Distribution and Protection, South Africa, 1980.

6. Bigelow, R.O., Freer, F.H., Ashton, P.T. : ***Automatic load relief practices in North-Eastern United States and Province of Ontario,*** Canada, CIGRE, paper 34-06, 1972.

7. Buotin, G.D., Portnoy, M.G., Rabinovich, R.S. : ***Automatic frequency load shedding in USSR power systems,*** CIGRE, paper 34-04, 1972.

8. Olwegard, A., Norback, K., Blondell, R. : ***Load shedding in Sweden according to system requirements & frequency relay testing,*** CIGRE, paper 34-09, 1972.

9. Berntsen, T.O., Pedersen, A., Fismen, S.A. : ***Network protection schemes for emergency control in the Norwegian power system,*** CIGRE, paper 34-06, 1984.

10. Ashmole, P.H., Battlebury, D.R., Bowdler, R.K. : ***Power system model for large frequency disturbances,*** Proc. of IEE, Vol. 121, No.7, pp. 601-608, 1974.

11. Taylor, C.W., Nassief, F.R., Cresap, R.L. : ***North-West power pool transient stability and load shedding controls for generation-load imbalances,*** IEEE Trans. Vol. PAS-100, No.7, pp. 3486-3495, 1981.

12. Hicks, K.L. : ***Hybrid load shedding is frequency based,*** IEEE Spectrum, pp. 52-56, 1983.

13. Malt, A.P.J., Clarke, G. D., Robinson, P. E. : ***Computer-based supervisory control and energy management system for the city of Cape Town,*** Proc. of IEE, Vol.135, No.1, Part C, 1988.

14. El-Banhawy, M.H. : ***New adaptive load shedding scheme for the Abu Dhabi power system (UAE),*** Ph.D. Thesis, The City University, London, 1988.

15. Pal, M.K. : ***Voltage stability conditions considering load characteristics,*** IEEE Trans. PAS, Vol.7, No.1, February 1992.

16. Price, W.W. : ***Load modeling for power flow and transient stability computer studies,*** EPRI El-5003 Vol.1 &2, Research Project 849-7, Final report January 1987.

17. IEEE Task Force on Instrumentation for System Dynamic Performance : ***Instrumentation for Monitoring power system dynamic performance,*** IEEE Trans. Vol. PWRS-2, No.1, pp. 145-152, February 1987.

18. Chiew-Yann Chion et al : ***Development and application of microprocessor-based load transient data recording system,*** International Conference on High Technology in the Power Industry, pp. 289-297, 1991.

19. Dovan, T., Dillan, T.S., Berger, C.S. : ***A microcomputer-based on-line identification approach to power system dynamic load modeling,*** IEEE Trans. Vol. PWRS-2, No.3, pp. 529-536, August 1987.

20. Vaheedi, E., Zein El-Dein, H.M., Price, W.W. : ***Dynamic load modeling in large scale stability studies,*** IEEE Trans. PAS, Vol.3, No.3, pp. 1039-1045, 1988.

21. Clark, H.K. et al : ***Experience with dynamic system monitors to enhance system stability analysis,*** IEEE Trans. Vol.7, No.2, pp. 693-701, May 1992.

22. Chia-Jen Lin et al : ***Dynamic load models in power systems using the measurement approach,*** IEEE paper No. 92 WM 173-5 PWRS, 1992.

23. IEEE Task Force on Load Representation for Dynamic Performance : ***Load representation for dynamic performance analysis,*** IEEE Trans. Vol.8, No.2, pp. 472-482, May 1993.

24. Venikov, V.: ***Transient Process in Electrical Power Systems,*** Mir Publishers, Moscow, 1980.

25. Chen, M.S., Concordia, C., Nagao, T.: ***Determining the static and dynamic characteristics of power system loads,*** CIGRE, paper 31-11, 1978.

26. Williams, B.R., Schmus, W.R., Dawson, D.C.: ***Transmission voltage recovery delayed by stalled air conditioner compressors,*** IEEE Trans. Vol.7, No.3, pp. 1173-1181, August 1992.

27. Frowd, R.J., Podmore, R., Waldron, M.: ***Synthesis of dynamic load models for stability studies,*** IEEE Trans. Vol. PAS-101, No.1, pp. 127-135, January 1982.

28. Manual of fault monitoring system : ***Indactic 65C*** , ABB Industrie AG, Switzerland, 1995.

29. Chen, M.S., Schoults, R.R.: ***The effects of reduced voltage on the operation and efficiency of electric systems,*** EPRI Report EL-3591, Vol.1, research project 1419-1, 1984.

30. Taylor, C.W.: ***Power System Voltage Stability,*** McGraw-Hill, 1993.

31. GEC Measurements: ***Protective Relays Application Guide,*** UK, 3rd Edition, 1987.

32. Fitzgerald, A., Kingsley, C., Kusko, A.: ***Electric Machinery,*** 3rd Edition, McGraw-Hill, 1971.

33. Stagg, G.W., El-Abiad, A.H.: ***Computer Methods in Power System Analysis,*** McGraw-Hill, 1986.

34. Elgerd, O.I.: ***Electric Energy System Theory: An Introduction,*** McGraw-Hill , 1982.

35. Anderson, P.M., Fouad, A.A.: ***Power System Control and Stability,*** Iowa State University Press, Ames, Iowa, 1977.

36. Weedy, B.M.: ***Electric Power System,*** John Willey & Sons, 3rd Edition, 1987.

37. Arrillaga, J., Arnold, C.P.: ***Computer Analysis of Power Systems,*** John Willey & Sons, 1990.

38. Whitman, W.C., Johnson, W.M.: ***Refrigeration & Air Conditioning Technology,*** Delmar Publishers Inc., USA, 1987.

39. Fink, D.G., Beaty, H.W.: ***Standard Handbook for Electrical Engineer,*** McGraw Hill, 1978.

40. Ward, M.R., Lister, E.C.: ***Electric Circuits and Machines,*** McGraw Hill, 1980.

41. McPherson, G., Lavomore, R.D.: ***An Introduction to Electrical Machines & Transformers,*** John Willey & Sons, 1990.

42. Gray, C.B.: ***Electrical Machines & Drives Systems,*** Longman Scientific & Technical, 1989.

43. ***Air Conditioning Compressor Statistics - AW-E models*** : Tecumseh, Michigan 49286, USA.

44. Singh, L.P.: ***Advanced Power Systems Analysis & Dynamics,*** Willey Eastern Limited, 3rd Edition, 1992.

45. Shackshaft, G., Ashmole, P.H.: ***The influence of load characteristics on power system performance - A C.E.G.B. viewpoint,*** CIGRE, paper 31-02, 1978.

46. Concordia, C., Ihara, S.: ***Load representation in power system stability studies,*** IEEE Trans. Vol. PAS-101, No.4, April 1982.

47. Frantz, T. et al: ***Load behavior observed in LILCO and RG&E systems,*** IEEE Trans. Vol. PAS-103, No. 4, April 1984.

48. Hammad, A.E., El-Sadek, M.Z.: ***Prevention of transient voltage instabilities due to induction motor loads by static VAR compensators,*** IEEE Trans. Vol. 4, No.3, pp. 1182-1190, August 1989.

49. Elmore, W.A.: ***Protective Relaying - Theory and Applications,*** ABB Power T&D Company Inc., Marcel Dekker Inc., 270 Madison Avenue, New York, NY 10016, 1994.

50. Boyce, W.E., DiPrima, R.C.: ***Elementary Differential Equations and Boundary Value Problems,*** John Wiley & Sons, Fifth Edition, 1992.

51. Scheid, F.: ***2000 Solved Problems in Numerical Analysis,*** McGraw-Hill Publishing Co., 1990.

52. MathSoft Inc., ***MathCAD Plus 5.0 User's Guide,*** 101 Main street, Cambridge, Massachusetts 02142, USA, 1994.

53. El- Banhawy, M., El-Baya, A.: ***Stability analysis of short-circuit fault followed by frequency dip on August 3rd, 1988,*** report No. WED/PSG/003/1990, Power System Group, Water and Electricity Department, Abu Dhabi, 1990.

54. El- Banhawy, M., El-Baya, A.: ***Stability analysis of 132 kV cable fault incident on July 19th, 1993,*** Power System Group, Water and Electricity Department, Abu Dhabi, 1993.

55. El-Banhawy, M.: ***Impact of air conditioning load on power system security,*** Power System Group, Water and Electricity Department, Abu Dhabi, 1992.

56. Siemens Aktiengesellschaft : ***Electrical Engineering Handbook,*** Siemens AG - Berlin and Heyden & Son Limited - London, 1976.